THE UNIVERSITY *of* EDINBURGH

The Use of Acetylacetonate-Based Paramagnetic Metalloligands in the Construction of Supramolecular Magnetic Coordination Capsules

Helen O'Connor

A Thesis Submitted for the Degree of Doctor of Philosophy

School of Chemistry

Faculty of Science and Engineering

The University of Edinburgh

September 2017

For Boss, Gran, and Carol

Abstract

In molecular magnetism, rational design and serendipity have played complementary roles in the synthesis of complexes which display a breadth of interesting physical characteristics. These range from the basic understanding of magneto-structural correlations, to more complicated phenomena such as slow relaxation of the magnetisation, spin frustration effects, and tuning magnetic interactions with a view to spintronics. The inherent physical properties of these complexes has already afforded molecules which can behave as single-molecule magnets, single-chain magnets, single-ion magnets, magnetic metal-organic frameworks, magnetic refrigerants, and molecular qubits.

Even when the building blocks are well known, the rational design of magnetic clusters can be extremely difficult, with the shape and nuclearity often dominated by several internal and external factors. Metallosupramolecular processes proffer an attractive strategy to the rational design of these clusters by making use of structurally-rigid precursors which, when combined in the correct stoichiometric ratio, can be used to construct various predefined discrete two- and three-dimensional polygons and polyhedra. In particular, the use of metalloligands as structurally-rigid precursors is appealing, not only because of their often-straightforward synthesis, but because of their ability to be easily modified in order to create comparable building blocks with different chemical and physical properties. It is therefore surprising that there are limited examples of magnetic architectures built through this approach.

Each chapter of this thesis aims to exploit the use of acetylacetonate-based paramagnetic metalloligands for the synthesis of structurally analogous magnetic coordination capsules, with inherently different magnetic properties.

Chapter 2 describes the structural and magnetic studies of fourteen tetradecanuclear coordination cubes, synthesised using the paramagnetic metalloligand $[M^{III}L_3]$ (M^{III} = Cr, Fe; HL = 1-(4-pyridyl)butane-1,3-dione). The heterometallic $[M^{III}_8M^{II}_6L_{24}]^{n+}$ (M^{II} = Co, Ni, Cu, and Pd; n = 0-12) cubes formed from the reaction of $[M^{III}L_3]$ and a "naked" M^{II} salt are all topologically similar, with the M^{III} ions occupying the corners of the cubes and the M^{II} ions occupying the faces. Excluding the Pd^{II}-based cube, all of the complexes display magnetic exchange interactions at low temperatures. Due to the enormous size of these clusters and their resulting matrices, the magnetic fitting was done using the process of statistical spectroscopy.

Chapter 3 describes the structural and magnetic studies of five $[M^{III}_2M^{II}_3L_6]^{n+}$ (M^{III} = Cr, Fe, and Al; M^{II} = Co, Zn, and Pd; HL = 1-(4-pyridyl)butane-1,3-dione; n = 0-6) trigonal bipyramids, built using the diamagnetic and paramagnetic metalloligands $[M^{III}L_3]$. $[Fe^{III}_2Co^{II}_3L_6Cl_6]$ represents the first

magnetic trigonal bipyramid synthesised through the pyridyl-based metalloligand approach. SQUID magnetometry studies show a weak antiferromagnetic exchange interactions between the Fe^{III} and Co^{II} ions, while EPR spectroscopy measurements demonstrate a small increase in the zero-field splitting parameter of the Fe^{III} ion upon coordination of $[Fe^{III}L_3]$ to a M^{II} ion. Complete active space self-consistent field (CASSCF) calculations show the axial zero-field splitting parameter of Co^{II} to be ≈-14 cm^{-1}, which is consistent with the magnetothermal and spectroscopic data.

Chapter 4 describes the synthesis and characterisation of six magnetic trigonal bipyramids, synthesised through dynamic covalent reactions of the metalloligand $[Fe^{III}L^{NH2}{}_3]$ (HL^{NH2} = 1-(4-aminophenyl)butane-1,3-dione) with either a dialdehyde or diacyl dichloride. The three $[Fe^{III}{}_2M^{II}{}_3L^{im}{}_3]^{n+}$ (M^{II} = Co, Ni; n = 0-6) imine-based cages are formed from the reaction of the metalloligand with 2,6-pyridinedicarboxaldehyde in the presence of a templating M^{II} salt and a catalytic amount of acid, whereas the three $[Fe^{III}{}_2L^{am}{}_3]$ amide-based cages are formed from the reaction of the metalloligand with isophthaloyl chloride in the presence of a base. The $[Fe^{III}{}_2Ni^{II}{}_3L^{im}{}_3]^{n+}$ trigonal bipyramid displays weak antiferromagnetic interactions between Fe^{III} and Ni^{II} ions, with $J_{Fe\text{-}Ni}$ = -0.12 cm^{-1} and D_{Ni} = 8.93 cm^{-1}, while the $[Fe^{III}{}_2L^{am}{}_3]$ amide-based cages display interesting configurational features dominated by the enthalpic gain from a series of intermolecular interactions.

Lay Summary

This thesis aims to exploit the use of "negatively" charged predefined building blocks, known as metalloligands, to build discrete magnetic three-dimensional structures. In order to create these structures the predefined metalloligands seek out "positively" charged predefined acceptors (Fig. 1). The majority of these building blocks comprise of magnetic metal centres which contain unpaired electrons and depending on the identity, proximity, and orientation of the building blocks, these electrons can interact—either reinforcing each other to make highly magnetic structures, or cancelling each other out to essentially make the structure non-magnetic. By changing the identity of the metal centres in both the metalloligand and the acceptor, we can make structures that look very similar, but will behave completely differently magnetically.

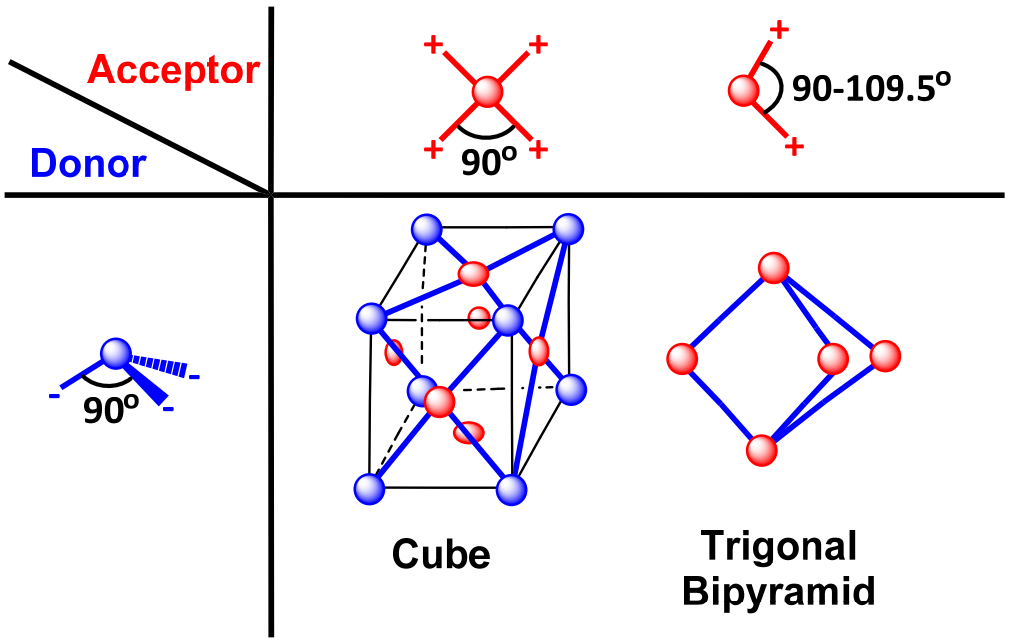

Figure 1 How the combination of a metalloligand donor (red) and an acceptor (blue) can be used to make discrete three-dimensional structures.

Table of Contents

Acknowledgements

It would be difficult write my acknowledgements without mentioning the big man up the stairs, Professor Euan K. Brechin. Thank you for giving me, a young Irish girl who still thinks the only whiskey worth having is spelled with an 'e', the opportunity to join your group. In particular, thank you for the endless opportunities, freedom, encouragement, and support I've experienced throughout, and for continuously pushing me out of my comfort zone in order so that I can become the best researcher that I can be.

To Sergio Joaquin Sanz Calvo, now officially “Papa Sanz”—it's hard to convey how much I’m thankful for everything you've helped me with, and I couldn't have imagined this experience without you. Not only have I learned a lot from you from inside of lab 251, but the friendship, guidance, and, in particular, the non-stop support I have experienced along the way has meant that I have obtained someone who is a pretty good lifelong friend, eh?

To Ross Inglis, the Premier Leaugue 2016/17's best predictor, for always being up for going for a pint or to the rugby or to the snooker. Although I still don't remember Scotland ever beating Ireland in the 6 Nations, I'll always remember finding world class bars like Café Peterpan or Nirvana with you.

To Julia Vallejo Navarret, for not only helping me to get my head around some tricky chemistry, but also for being a personal trainer, therapist, and most importantly an amazing friend. Yo como manzanas.

To the other members of the Brechin and Inglis group past and present: Hector Fraser, Robbie McNab, Anders Hjordt Pedersen, Priyanka Comar, Jose Lillo, and Jamie Frost—I couldn't have imagined a more inviting and supportive group of people to be a part of.

To Gary Nichol and Mateusz Pitak, thank you for always being willing to try my crystals, and thank you for your endless patience in solving the structures that make up this thesis. To Paul Lusby and Vicente Martí-Centelles for your help with the organic side of things and the NMRs, and to all of our collaborators in Copenhagen and Manchester for their help with the magnetic measurements. To Murray Low, Michael Seery, and the inorganic teaching lab technicians, thank you for your support and hard work which has helped make teaching at Edinburgh a great experience.

To the other two teaching muskateers Amy and Euan, it's been a rollercoaster but I'll look back on our shared teaching experiences with very fond memories. Without PCDS I might not have had

the privilage of gaining two amazing friends, and I look forward to keeping in contact and seeing the amazing things you'll do.

To Rebecca, Steph, Cath, Cowleys, Claire, and Mary, thank you for always being up for a well needed cuppa tea or beer. To Stefan, we've come a long way since Belfield, I'll always remember our days in Ratcliffe Terrace with a warm heart and a cold everything else.

To everyone I have had the pleasure of meeting over the last three years, it's been a crazy experience but your friendly faces and forever willingness to go for a pint have helped make my PhD something I will never forget.

To all of my friends back home—Aoife, Lisa, Nicola, Paddy, Patrice, Ruth, Sara, and Siobhán. My trips back will always remind me how special, supportive, and strong, friendships can be.

Finally, to all of my family, and especially to Mary, Jim, and Kevin—your ability to provide belief, guidance, support, and enthusiasm from all the way across the Irish sea has meant a great deal to me. I am forever grateful for you sparking my interest in science (even if this thesis isn't based on Trichoptera!).

Chíonn beirt rud nach bhfeiceann duine amháin.

Declaration

I hereby declare that except where specific reference is made to other sources, the work contained in this thesis is the original work of the author. It has been composed by the candidate and has not been submitted, in whole or in part, for any other degree, diploma, or other qualification.

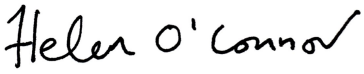

Helen O'Connor

Format of the Thesis

Each chapter of this thesis, with the exception of Chapter 1, is made up of contributions to peer-reviewed papers, which have already been published or submitted for publication. To fulfil the requirements of The University of Edinburgh regarding the preparation and submission of a thesis for the degree of PhD, they have been reformatted accordingly.

Chapter 1: Introduction

- The rational design of discrete magnetic complexes

Chapter 2: $[M^{III}_8M^{II}_6L_{24}]^{n+}$ Coordination Cubes

- Structural and magnetic investigation of fourteen tetradecanuclear coordination cubes, built using the paramagnetic metalloligands $[Cr^{III}L_3]$ and $[Fe^{III}L_3]$, and a "naked" M^{II} salt

Chapter 3: $[M^{III}_2M^{II}_3L_6]^{n+}$ Pyridyl-Based Trigonal Bipyramids

- Structural and magnetic invesitgation of five pentanuclear trigonal bipyramids built from $[Al^{III}L_3]$, $[Cr^{III}L_3]$, and $[Fe^{III}L_3]$, and a tetrahedral or *cis*-capped square planar M^{II} salt

Chapter 4: Imine-Based $[M^{III}_2M^{II}_3L^{im}_3]^{n+}$ and Amide-Based $[M^{III}_2L^{am}_3]$ Trigonal Bipyramids

- Investigation of six trigonal bipyramids based on the dynamic covalent reactions of $[Fe^{III}L^{NH2}_3]$ with either 2,6-pyrdinedicarboxaldehyde or isophthaloyl chloride

Chapter 5: Conclusions and Future Outlook

External Contributions

X-ray Crystallography: Dr Mateusz Pitak and Prof. Simon Coles (University of Southampton)
CASSCF Calculations: Dr Nicholas Chilton (The University of Manchester)
Magnetic Fitting: Dr Høgni Weihe and Dr Stergios Piligkos (University of Copenhagen)
EPR Measurements: Dr Amga Baldansuren, Dr Eufemio Moreno Pineda, Dr Nicholas Chilton and Prof. Eric McInnes (The University of Manchester)
Heat Capacity Measurements: Dr Marco Evangelisti (University of Zaragoza)

Publications

In Preparation

8. "Dynamic Covalent $[Fe^{III}_2M^{II}_3]^{n+}$ and $[Fe^{III}_2]$ Magnetic Trigonal Bipyramids"
Helen M. O'Connor, Sergio Sanz, Mateusz B. Pitak, Gary S. Nichol, Vincente Martí-Centelles, Stergios Piligkos, Paul J. Lusby, and Euan K. Brechin, *CrystEngComm*, 2017, To Be Submitted

7. "$[Cr^{III}_8Ni^{II}_6]$ Coordination Cubes"
Helen M. O'Connor, Sergio Sanz Mateusz B. Pitak, Simon J. Coles, Ole Mønsted, Høgni Weihe, Stergios Piligkos, Eric J. L. McInnes, Paul J. Lusby, and Euan K. Brechin, *Dalton Trans.*, 2017, To Be Submitted

6. "Modular $[Fe^{III}_8M^{II}_6]^{12+}$ (M^{II} = Pd, Fe, Co, Ni, Cu) Coordination Cages"
Sergio Sanz, **Helen M. O'Connor**, Priyanka Comar, Mateusz B. Pitak, Simon J. Coles, Ole Mønsted, Høgni Weihe, Stergios Piligkos, Eric J. L. McInnes, Paul J. Lusby, and Euan K. Brechin, *Inorg. Chem.*, 2017, Submitted

2017

5. "$[M^{III}_2M^{II}_3]^{n+}$ trigonal bipyramids based on diamagnetic and paramagnetic metalloligands"
Helen M. O'Connor, Sergio Sanz, Vincente Martí-Centelles, Priyanka Comar, Mateusz B. Pitak, Simon J. Coles, Giulia Lorusso, Elias Palacios, Marco Evangelisti, Amgalanbaatar Baldansuren, Nicholas F. Chilton, Høgni Wiehe, Eric J. L. McInnes, Paul J. Lusby, Stergios Piligkos, and Euan K. Brechin, *Chem. Sci.*, 2017, **8**, 5526. **DOI:** 10.1039/C7SC00487G

4. "Developing laboratory skills by incorporating peer-review and digital badges" (Note: Authors listed alphabetically)
Michael K. Seery, Hendra Y. Agustian, Euan D. Doidge, Maciej M. Kurcharski, **Helen M. O'Connor**, Amy N. Price, *Chem. Educ. Res. Pract.*, 2017, **18**, 403. **DOI:** 10.1039/C7RP00003K

2016

3. "$[Cr^{III}_8M^{II}_6]^{n+}$ (M^{II} = Cu, Co) face-centred, metallosupramolecular cubes" (Front Cover)
Helen M. O'Connor, Sergio Sanz, Mateusz B. Pitak, Simon J. Coles, Gary S. Nichol, Stergios Piligkos, Paul J. Lusby, and Euan K. Brechin, *CrystEngComm*, 2016, **18**, 4914. **DOI:** 10.1039/C6CE00654J

2015

2. "$[Cr^{III}_8M^{II}_6]^{12+}$ Coordination Cubes (M^{II}= Cu, Co)"
Sergio Sanz, **Helen M. O'Connor**, Eufemio Moreno Pineda, Kasper S. Pedersen, Gary S. Nichol, Ole Mønsted, Høgni Weihe, Stergios Piligkos, Eric J. L. McInnes, Paul J. Lusby, and Euan K. Brechin, *Angew. Chem. Int. Ed.*, 2015, **127**, 6865. **DOI:** 10.1002/ange.201501041

1. "A room temperature spin crossover ionic liquid"
Anthony J. Fitzpatrick, **Helen M. O'Connor**, and Grace G. Morgan, *Dalton Trans.*, 2015, **44**, 20839. **DOI:** 10.1039/C5DT04264J

Conferences Attended

2017

4th EuCheMS Inorganic Chemistry Conference (EICC), Copenhagen, Denmark—2nd–5th July 2017
Participation: Poster Presentation

3rd Annual Joseph Black Chemistry Conference, The University of Edinburgh, UK—1st June 2017
Participation: Oral Communication

RSC Sir Geoffrey Wilkinson Dalton Poster Symposium, London, UK—27th March 2017
Participation: Poster Presentation

2016

15th International Conference on Molecule-Based Magnets (ICMM), Sendai, Japan—4th–8th September 2016
Participation: Poster Presentation

Inaugural EastCHEM Conference for Early-Career Researchers (ECECR), The University of Edinburgh, UK—25th August 2016

Universities of Scotland Inorganic Conference (USIC), University of Strathclyde, UK—11th and 12th August 2016
Participation: Poster Presentation

42nd International Conference on Coordination Chemistry (ICCC), Brest, France—3rd–8th July 2016
Participation: Oral Communication

2nd Annual Joseph Black Chemistry Conference, The University of Edinburgh, UK—26th May 2016
Participation: Poster Presentation

2015

5th European Conference on Molecular Magnetism (ECMM), Zaragoza, Spain—6th–10th September 2015
Participation: Poster Presentation

1st Annual Joseph Black Chemistry Conference, The University of Edinburgh, UK—27th May 2015

Prizes and Awards

HEA (Fellow): Awarded Fellowship Status of the Higher Education Academy through Level 2 of the Edinburgh Teaching Award—October 2017

Student Bursary for EuCheMS Inorganic Chemistry Conference (EICC): Covered €150 towards registration fee—June 2017

Student Poster Prize: 15th International Conference on Molecule-Based Magnets (ICMM), Sendai, Japan—September 2016

Institute for Academic Development (IAD Edinburgh) Principal Teaching Award Scheme: Successful application for funding as a co-investigator for the project "Peer Assessing Laboratory Skills"—October 2015

Fellowship for European Conference Molecular Magnetism (ECMM): Covered cost of registration fee for the ECMM 2015—June 2015

High Ryan Memorial Gold Medal, University College Dublin: Awarded annually to the top graduating Chemistry BSc (Hons.) student—June 2014

Principal's Career Development Scholarship, The University of Edinburgh: Teaching-based scholarship awarded to students undertaking postgraduate studies within the School of Chemistry—Covers the UK/EU rate of tuition fees as well as a stipend of £14,000 for three years—March 2014

List of Complexes

The following table provides a quick reference guide for all of the complexes presented in this thesis. Solvent molecules of crystallisation and additional counterions have been removed for clarity.

Number	Chapter	Complex
1	2	$[Cr^{III}_8Cu^{II}_6L_{24}Cl_{12}]$
2	2	$[Cr^{III}_8Cu^{II}_6L_{24}(H_2O)_{10}(NO_3)_2](NO_3)_{10}$
3	2	$[Cr^{III}_8Cu^{II}_6L_{24}(H_2O)_{12}](SO_4)_6$
4	2	$[Cr^{III}_8Co^{II}_6L_{24}Cl_{12}]$
5	2	$[Cr^{III}_8Co^{II}_6L_{24}(H_2O)_{12}](ClO_4)_{12}$
6	2	$[Cr^{III}_8Co^{II}_6L_{24}(SCN)_{12}]$
7	2	$[Cr^{III}_8Ni^{II}_6L_{24}Cl_{12}]$
8	2	$[Cr^{III}_8Ni^{II}_6L_{24}(H_2O)_{12}](NO_3)_{12}$
9	2	$[Cr^{III}_8Ni^{II}_6L_{24}(MeCN)_7(H_2O)_5](ClO_4)_{12}$
10	2	$[Fe^{III}_8Cu^{II}_6L_{24}(H_2O)_4Br_4]Br_8$
11	2	$[Fe^{III}_8Cu^{II}_6L_{24}(H_2O)_{10}](NO_3)_{12}$
12	2	$[Fe^{III}_8Co^{II}_6L_{24}(SCN)_{10}(H_2O)_2]Cl_2$
13	2	$[Fe^{III}_8Ni^{II}_6L_{24}(SCN_{11})Cl]$
14	2	$[Fe^{III}_8Pd^{II}_6L_{24}]Cl_{12}$
15	3	$[Fe^{III}_2Co^{II}_3L_6Cl_6]$
16	3	$[Fe^{III}_2Zn^{II}_3L_6Br_6]$
17	3	$[Cr^{III}_2Zn^{II}_3L_6Br_6]$
18	3	$[Cr^{III}_2Pd^{II}_3L_6(dppp)_3](OTf)_6$
19	3	$[Al^{III}_2Pd^{II}_3L_6(dppp)_3](OTf)_6$
20	4	$[Fe^{III}_2Ni^{II}_3L^{im}_3(H_2O)_9]Cl_6$
21	4	$[Fe^{III}_2Co^{II}_3L^{im}_3(H_2O)_9](BF_4)(OTf)$
22	4	$[Fe^{III}_2Co^{II}_3L^{im}_3(H_2O)_9][CoCl_4]$
23	4	$[Fe^{III}_2L^{am}_3]\bullet Cl_2$
24	4	$[Fe^{III}_2L^{am}_3]$
25	4	$[Fe^{III}_2L^{am}_3]\bullet Cl_3$

Chapter 1: Introduction

1.1 The Rational Design of Discrete Magnetic Complexes

The increased fascination in the field of molecular magnetism in recent years has been as a result of the development of polymetallic clusters that exhibit a breadth of interesting magnetic behaviours. These range from the understanding of basic magneto-structural correlations to more complicated phenomena such as spin frustration effects,[1–3] slow relaxation of the magnetisation,[4–6] and tuning magnetic interactions with a view to molecular spintronics.[7,8] These phenomena have already afforded complexes that can behave as single-molecule magnets,[9,10] single-chain magnets,[11] single-ion magnets,[12] magnetic metal-organic frameworks,[13] magnetic refrigerants,[14] and molecular qubits.[15] With the field encompassing so many sub disciplines it is possible to comprehend why a range of synthetic strategies towards the construction of these magnetic materials has been employed.

In the past, the synthetic strategies for their construction have relied heavily on serendipity, utilising ligands capable of bridging metal centres through a variety of coordination modes, and metal ions in different oxidation states with geometrical flexibility.[16] Not only are the choice of metals and terminal/bridging ligands important in the development of these clusters, but the topology of the cluster can also be impacted by "external factors" such as the choice of solvent, pH, temperature and the use of various counterions.[17] The final structure is therefore often a fine balance of all these competing factors, making structural prediction extremely difficult, even if the building blocks of the cluster are well known.

Fundamental to the formation of these magnetic clusters is the inclusion of metal centres with a non-zero spin ground state. The spin state of the paramagnetic ion relies on both the geometrical preferences of the metal ion and careful consideration of the type of ligand sphere that surrounds it. An example of such an influence can be seen when considering a Co^{II} centre. Tetrahedral Co^{II} has a configuration of $e^4 t_2^3$, while octahedral Co^{II} in a weak field has a configuration of $t_{2g}^5 e_g^2$, and octahedral Co^{II} in a strong field has electronic configuration $t_{2g}^6 e_g^1$ (Fig. 1.1). The resulting magnetic moment, and anisotropy, of each complex will differ due to the presence of a quartet state, a triply degenerate quartet state, and a doublet state, respectively.

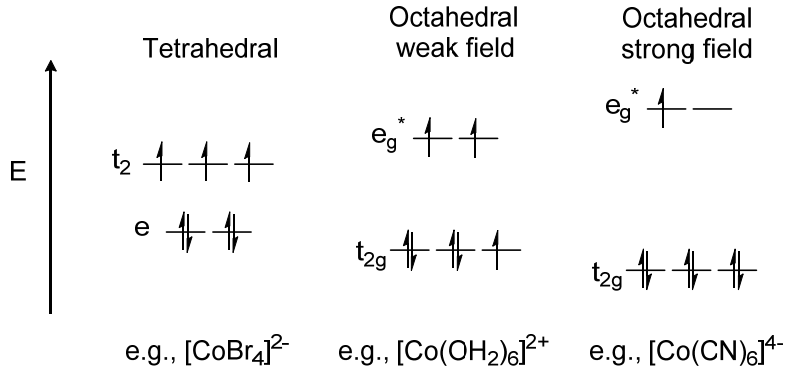

Figure 1.1 The energy level diagrams for Co^{II} showing the dependence of the spin state on the ligand field in which the metal ion is placed.

The smallest change in coordination sphere not only affects the magnetic properties of the ion but also its ability to exchange magnetic information. Magnetic exchange interactions generally occur by the process of superexchange, in which diamagnetic *p*-block (mostly oxygen, nitrogen, and sulfur) based bridging ligands allow magnetic communication between metal ions. The magnetic orbitals, the orbitals in which the unpaired electrons are housed, interact with the bonding orbitals of the diamagnetic ligand, and depending on the orientation of the second magnetic orbital, a ferromagnetic or antiferromagnetic interaction can be observed.[18] The ability of chemists to exploit these exchange interactions in the rational design of magnetic clusters is perhaps best exemplified though the use of octahedral metal centres and the small and linear cyano-ligand (Fig. 1.2).[19]

If the magnetic orbitals are positioned orthogonally with respect to one another, such as that found in orbitals with incompatible symmetry (t_{2g} + e_g^*), Hund's first rule will dictate a ferromagnetic exchange, resulting in maximum spin multiplicity. Conversely, the use of symmetry-compatible orbitals (t_{2g} + t_{2g}) will lead to an antiferromagnetic exchange *via* the Pauli Exclusion Principle. If both ferro- and antiferromagnetic pathways are present, antiferromagnetic interactions will dominate due to their increased strength compared with that of ferromagnetic interactions.[20]

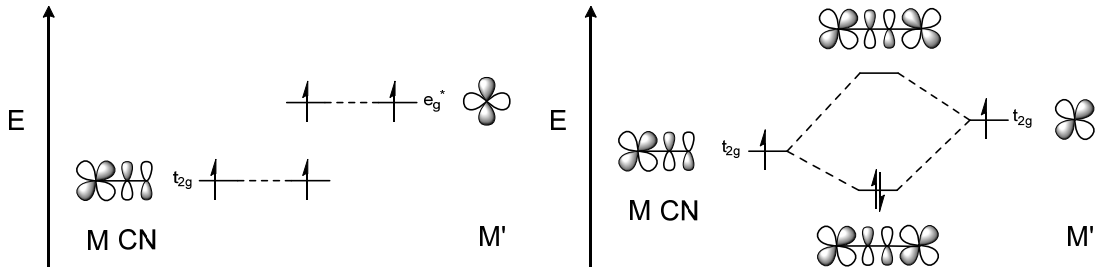

Figure 1.2 Cyano-bridged *d*-orbitals displaying ferromagnetic (left) and antiferromagnetic exchange interactions (right).

Most noteworthy of the cyano-based clusters is the well-known Prussian blue ($KFe^{III}[Fe^{II}(CN)_6]$), a face centred cubic three-dimensional bulk ferromagnet (Fig. 1.3), built through the combination of $K_4[Fe^{II}(CN)_6]$ and an unprotected or "naked" Fe^{III} salt.[21] Prussian blue and analogous materials, where the metal centres have been exchanged for other paramagnetic ions, have seen ferromagnetic ordering at room temperature, but unfortunately their low solubility has meant their characterisation has been hindered and their applications limited.[22] The use of specific co-ligands to protect and limit the available donor or acceptor sites on a metal centre prevents the growth of these three-dimensional networks, and more importantly helps increase the solubility of these materials for the examination of their properties.[23] Their exploitation has resulted in the creation of one-dimensional chains,[24] two-dimensional polymers,[25] and discrete three-dimensional (or zero-dimensional) polygons and polyhedra.[26,27]

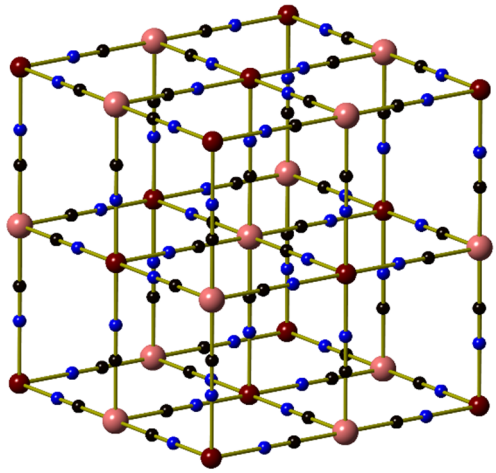

Figure 1.3 Partial structure of $Fe^{III}[Fe^{II}(CN)_6]^-$ with potassium ions removed for clarity. Colour code: Fe^{III} – Maroon, Fe^{II} – Salmon, N – Blue, C – Black.

The use of hexacyanometallate ions with protected metal centres allows for the creation of discrete structures through supramolecular processes, arising from the fact these anions tend to bridge the acceptors in a *cis*- or *fac*-orientation.[28] An example of this phenomenon can be seen in Murray and co-workers ferromagnetically coupled trigonal bipyramid, $[Fe^{III}(CN)_6]_2[Ni^{II}(bpm)_2]_3{\cdot}7H_2O$ (Fig. 1.4, bpm = *bis*(1-pyrazolyl)methane),[29] and in Dunbar and co-workers systematic study of trigonal bipyramids based on the first-row transition metals.[30]

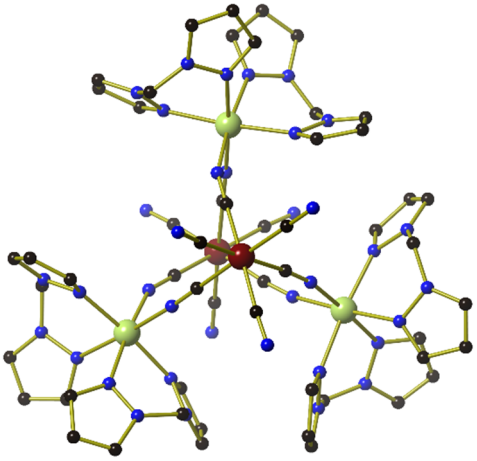

Figure 1.4 Structure of $[Fe^{III}(CN)_6]_2[Ni^{II}(bpm)_2]_3 \cdot 7H_2O$. Hydrogen atoms have been removed for clarity. Colour code: Fe^{III} – Maroon, Ni^{II} – Green, N – Blue, C – Black.

The use of protecting groups is not limited to the acceptor, with many examples of tricyanometallates, which contain three cyano-donor sites, forming discrete molecular clusters. Long and co-workers have used the tridentate ligands 1,4,7-triazacyclononane (tacn) or 1,3,5-triaminocyclohexane (tach) to limit the donor sites to the *fac*-positions of an octahedral metal centre.[31–33] Through this method they have been able to create a series of heterometallic magnetic capsules, including $[M^{III}_2M^{II}_3]$ trigonal bipyramidal structures (M^{III} = Fe, Cr; M^{II} = Ni, Cu), and the magnetic $[Fe^{III}_4Ni^{II}_4(tach)_4(H_2O)_{12}(CN)_{12}]^{8+}$ cube (Fig. 1.5), all of which show ferromagnetic exchange interactions at low temperature.

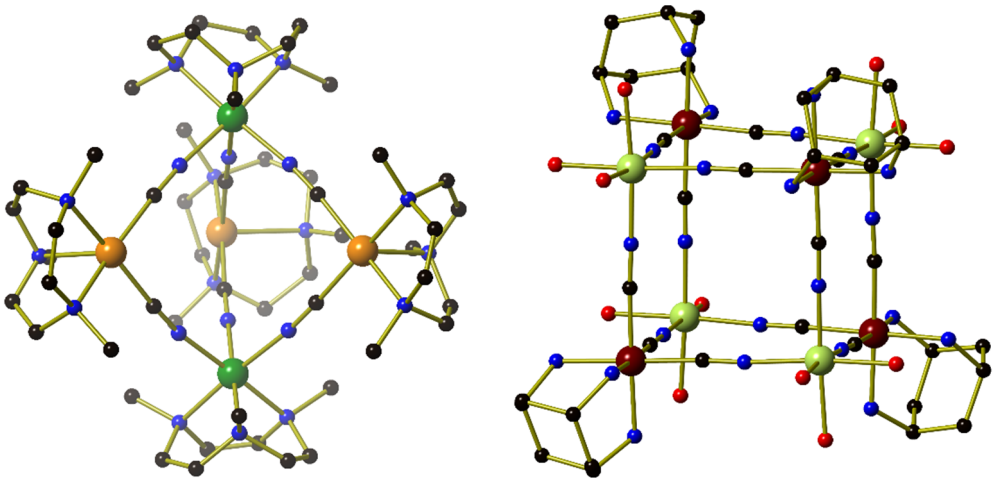

Figure 1.5 Structure of $[Cr^{III}_2Cu^{II}_3Tp_2(Me_3tacn)_3(CN)_6]^{4+}$ (left) and $[Fe^{III}_4Ni^{II}_4(tach)_4(H_2O)_{12}(CN)_{12}]^{8+}$ (right) with hydrogen atoms and counterions removed for clarity. Colour code: Fe^{III} – Maroon, Cr^{III} – Medium Green, Cu^{II} – Orange, Ni^{II} – Light Green, N – Blue, O – Red, C – Black.

An attempt to add paramagnetic centres to the faces of the cubic structures in order to increase the total spin ground state was explored through the reaction of the $[Cr^{III}(Me_3tacn)(CN)_3]$ building block with $[Ni^{II}(H_2O)_6]^{2+}$ in boiling aqueous media. The structure $[Cr^{III}_8Ni^{II}_6(Me_3tacn)_8(CN)_{24}]^{12+}$ (Fig. 1.6) indicated a rearrangement of the Cr^{III}-C≡N moiety so that the carbon end of the cyano-ligand coordinated to the Ni^{II} in a Cr^{III}-N≡C-Ni^{II} fashion. Unfortunately, the strong ligand field effect of the carbon on the Ni^{II} ion caused a diamagnetic square planar geometry, and thus no magnetic exchange interactions are present within the tetradecanuclear structure. Interestingly, at lower temperature the colour of the crystals obtained were green as opposed to orange, possibly indicating the presence of an isomeric Cr^{III}-C≡N-Ni^{II} cage, and further highlighting the need for control over external reaction conditions in the rational design of magnetic cages.[34–36]

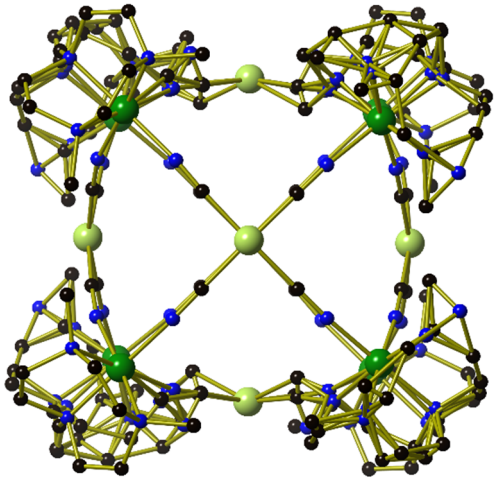

Figure 1.6 Structure of $[Cr^{III}_8Ni^{II}_6(Me_3tacn)_8(CN)_{24}]^{12+}$ with hydrogen atoms and counterions removed for clarity. Colour code: Cr^{III} – Medium Green, Ni^{II} – Light Green, N – Blue, C – Black.

Although cyano-ligands have been heavily used in the rational design of magnetic clusters, they are not the only synthetic pathway that has been employed. Compartmental ligands, a subclass of polytopic ligands in which the metal ions share at least one donor atom, have been used for the construction of rows of closely spaced magnetic ions. A prime example of this is the use of phenol-*bis*(β-diketone)-derived ligands for the synthesis of linear clusters such as the tetranuclear $[Mn^{II}_4(H_2L)_2(OAc)_2(dmf)_4]$ (Fig. 1.7), formed from the reaction of 1,3-*bis*(3-oxo-3-(2-hydroxyphenyl)-propionyl)-2-methoxybenzene (H_5L), and Mn^{II} acetate tetrahydrate, in dimethylformamide.[37] Similar structures have been synthesised using Cu^{II}, Ni^{II}, and Co^{II}, with the simple phenoxo-bridge allowing for antiferromagnetic exchange interactions between neighbouring paramagnetic centres.[38,39] Further alteration of reaction conditions through the addition of sodium acetate allows for the introduction of sodium ions within the structure, creating the paddlewheel-type cluster $[Mn^{II}_2Na_2(H_2L)_3]^{3-}$ (H_5L= (2-hydroxy-1,3-*bis*(3-oxo-3-(2-hydroxyphenyl)-propionyl)-benzene).[40] This strategy of introducing diamagnetic ions into

magnetic clusters is not uncommon within the field of molecular magnetism, as it not only allows for detailed studies to be carried out on specifically targeted ions, but also allows for the enhancement of magnetisation relaxation barriers.[56]

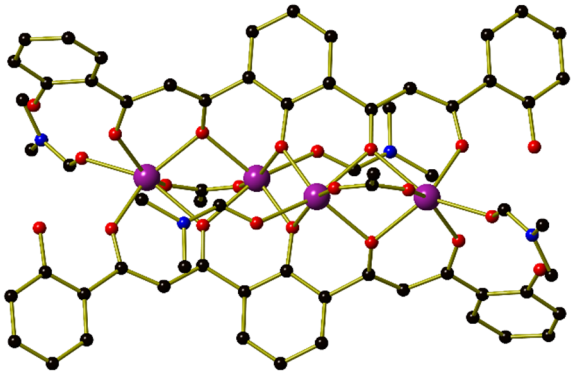

Figure 1.7 Structure of $[Mn^{II}_4(H_2L)_2(AcO)_2(dmf)_4]$. Hydrogen atoms have been removed for clarity. Colour code: Mn^{II} – Purple, N – Blue, O – Red, C – Black.

Similarly rigid polytopic ligands have been employed in the construction of magnetic grid assemblies, the simplest of which makes use of *bis*(bidentate) ditopic ligands to make two dimensional [2 x 2] square grids. The ligand 3,6-*bis*(2-pyridyl)-1,2,4,5-tetrazine (L) was used in conjunction with either Ni^{II} tetrafluoroborate or Ni^{II} perchlorate salts to create the [2 x 2] square grids $[Ni^{II}_4(L)_4(CH_3CN)_8](BF_4)_8$ and $[Ni^{II}_4(L)_4(CH_3CN)_8](ClO_4)_8$, respectively, both of which display antiferromagnetic exchange interactions at low temperature.[41] Interestingly, the use of a larger templating anion, such as hexafluoroantimonate as opposed to tetrafluoroborate or perchlorate, resulted in the formation of a pentagonal ring (Fig. 1.8), once again further highlighting the need for careful selection of reaction conditions in the rational design of polymetallic architectures.[42]

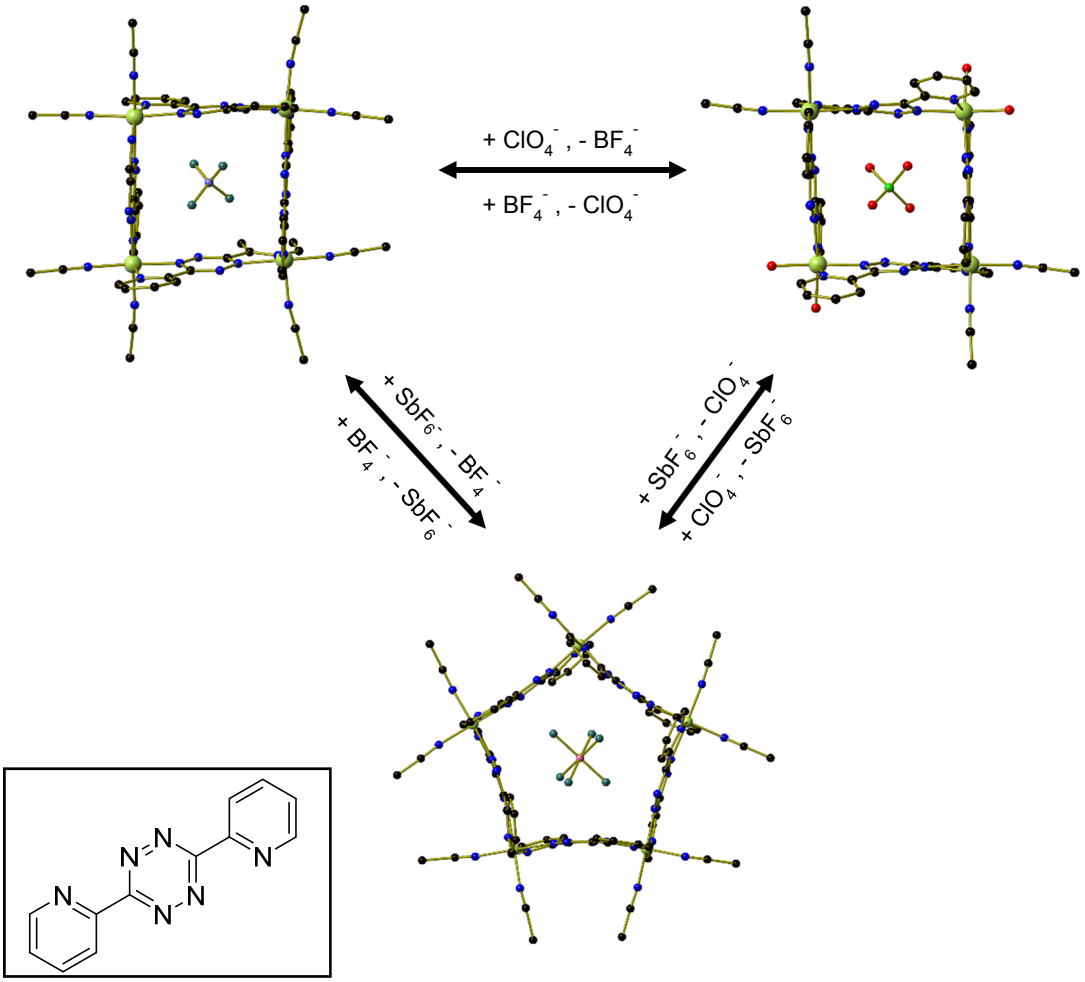

Figure 1.8 The transformations between the $[\{Ni^{II}_4(L)_4(CH_3CN)_8\}(BF_4)]^{7+}$ and $[\{Ni^{II}_4(L)_4(CH_3CN)_8\}(ClO_4)]^{7+}$ squares (top left and right, respectively) and the $[\{Ni^{II}_4(L)_5(CH_3CN)_{10}\}\{SbF_6\}]^{9+}$ pentagonal ring (bottom), made using L (inset). Hydrogen atoms and additional counterions have been removed for clarity. Colour code: Ni^{II} – Light Green, Sb – Pink, F^- – Turquoise, Cl^- – Bright Green, B – Medium Slate Blue, N – Blue, O – Red, C – Black.

Another strategy used for the creation of magnetic clusters is the exploitation of the ligand sphere preferences of different metal ions. Schiff-base ligands have been used for the formation of 3*d*-4*f* clusters in which the 3*d*- and 4*f*-metals occupy the nitrogen- and oxygen-based pockets of the ligand, respectively. These polymetallic clusters have played a crucial role in understanding the nature of exchange interactions between lanthanides and various 3*d*-metal ions (Cu^{II}, Ni^{II}, Fe^{II}, Co^{II}, and $V^{IV}O$),[43] and have even been used as building blocks for the construction of high nuclearity clusters,[44,45] or coordination polymers,[46,47] through careful consideration of appropriate linkers. The trinuclear complex, $[(Cu^{II}L)_2Gd^{III}(H_2O)(NO_3)_3]\cdot 2EtNO_2$, {$H_2L$ = *N,N'*-1,3-propylene-*bis*(salicylaldimine)}, which shows ferromagnetic coupling at low temperature, is a pivotal example for the efficiency of the construction of these complexes (Fig. 1.9).[48]

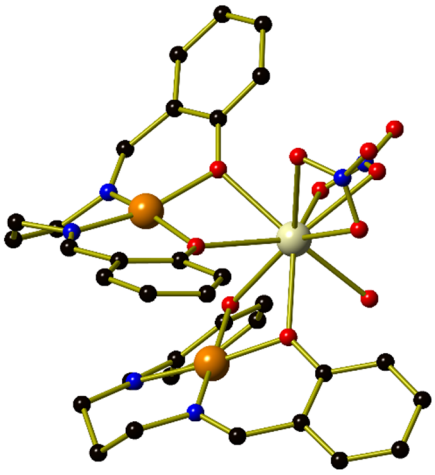

Figure 1.9 Structure of $[Gd^{III}Cu^{II}_2L_2(H_2O)(NO_3)_2]^+$ with the hydrogen atoms and the third nitrate ion removed for clarity. Colour code: Gd^{III} – Yellow, Cu^{II} – Orange, N – Blue, O – Red, C – Black.

Schiff-base ligands have been commonly employed in the design of magnetic clusters, with their properties allowing for their application in other areas such as catalysis,[49] supramolecular chemistry,[50] and chemical biology.[51] The reversible condensation reaction of a primary amine and an aldehyde to form a secondary aldimine is simple, reliable, and often high-yielding—its equilibrium easily pushed away from hydrolysis of the imine through the use of a catalytic amount of acid or a templating ion.[50] Within supramolecular chemistry Schiff-base reactions belong to dynamic covalent chemistry (DCvC), and their inherently reversible nature has been exploited to create a range of discrete structures.[52,53] Nitschke and co-workers have made use of 2-pyridinecarboxaldehyde and a range of amines to create coordination capsules, including Co^{II} or Ni^{II} magnetic tetrahedra (Fig. 1.10).[54,55] Again, the inclusion of different counterions allows for the 6,6′-diformyl-3,3′-bipyridine and *p*-toluidine-based $[Co^{II}_4L_6]$ tetrahedron to rearrange into a $[Co^{II}_{10}L_{15}]$ pentagonal prism, a structure which has a chloride ion encapsulated in the centre of the cage.

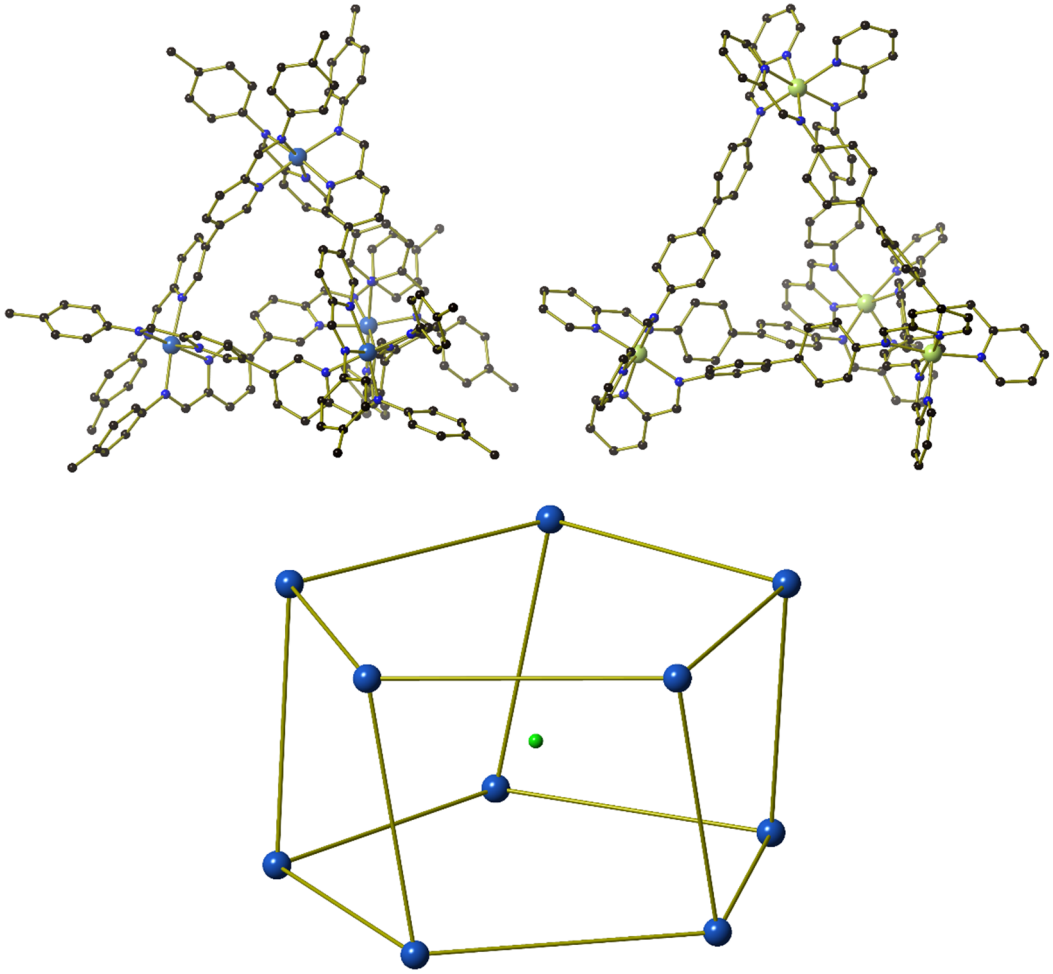

Figure 1.10 Structures of the $[Co^{II}_4L_6]^{8+}$ (left) and $[Ni^{II}_4L_6]^{8+}$ (right) tetrahedra, and a simplified structure of the $[\{Co^{II}_{10}L_{15}\}Cl]^{19+}$ pentagonal prism, with a chloride ion located in the centre of the cage. Hydrogen atoms and additional counterions have been removed for clarity. Colour code: Ni^{II} – Light Green, Co^{II} – Royal Blue, Cl^- – Bright Green, N – Blue, C – Black.

The increased interest in these type of supramolecular cages is as a result of Pedersen, Lehn and Cram claiming the 1987 Nobel Prize "for their development and use of molecules with structure-specific interactions of high selectivity". Supramolecular chemistry relies on a self-assembly process through which molecular building blocks organise themselves into rigidly defined structures spontaneously. From a coordination chemistry approach, the directional bonding by metal centres is widely used as a supramolecular technique, treating metal centres as highly directional corners with predefined angles and symmetry preferences. The combination of various complementary building blocks allows for a plethora of discrete two- and three-dimensional polygons and polyhedra to be built, as long as the structurally rigid precursor units are combined in the correct stoichiometric ratios (Fig. 1.11).[56]

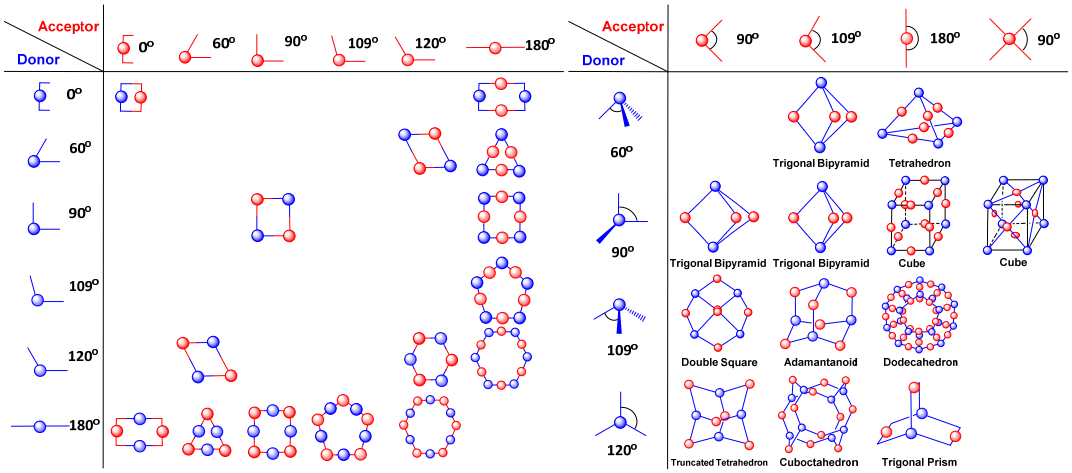

Figure 1.11 Discrete two- (left) and three- (right) dimensional architectures formed from the combination of complementary ditopic and tritopic building blocks, respectively.[56]

In more recent years, researchers such as Stang, Fujita, and Ward have continued the work of these pioneers, utilising supramolecular processes for the rational design of two- and three-dimensional polymetallic architectures.[57–59] One of the most celebrated diamagnetic examples is perhaps Fujita's square complex $[(en)Pd^{II}(4,4'\text{-bpy})]_4(NO_3)_8$, formed from the reaction of 4,4'-bipyridine and the *cis*-capped (ethylenediamine)palladium(II) nitrate (Fig. 1.12).[60]

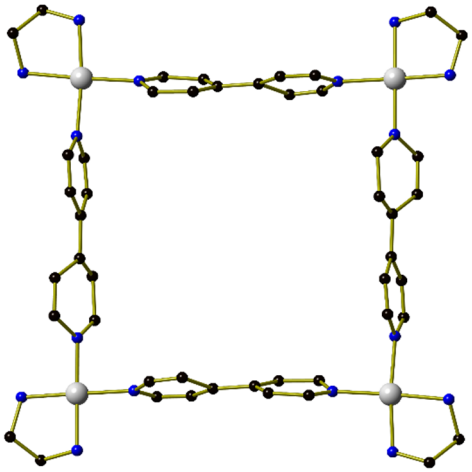

Figure 1.12 Structure of $[(en)Pd^{II}(4,4'\text{-bpy})]_4^{8+}$ obtained through inclusion of naphthalene within the square complex.[61] Hydrogen atoms, naphthalene molecules, counterions, and water of crystallisation have been removed for clarity. Colour code: Pd^{II} – Grey, N – Blue, C – Black.

The substitution of 4,4'-bipyridine with larger bridging ligands such as *bis*(4-pyridyl)acetylene unexpectedly leads to the formation of a molecular triangle, which is in equilibrium with the expected square complex.[61] Rationalised thermodynamically, the square has less total strain and thus is enthalpically favoured, while the triangle has fewer components and is therefore

entropically favoured. In accordance with Le Chatelier's principle, the addition of heat to the reaction allows for the enthalpic penalty of forming the more strained triangle to be compensated by the increased entropy and lower Gibbs free energy. Similarly, an increase in component concentration shifts the square-triangle equilibrium away from the triangle and towards the square due to the loss of entropy. This careful thermodynamic balance can also be manipulated by the presence of a guest, with Raymond and co-workers using the ligand 1,5-*bis*(2,3-dihydroxybenzamido)naphthalene (H_4L) to form either a $[Ti^{IV}_2L_3]^{4-}$ triple helicate or a $[Ti^{IV}_4L_6]^{8-}$ tetrahedron. The inclusion of a tetramethylammonium ion allows for the entropic penalty of forming a tetrahedron to be compensated by intermolecular interactions between the host and guest (Fig. 1.13).[62]

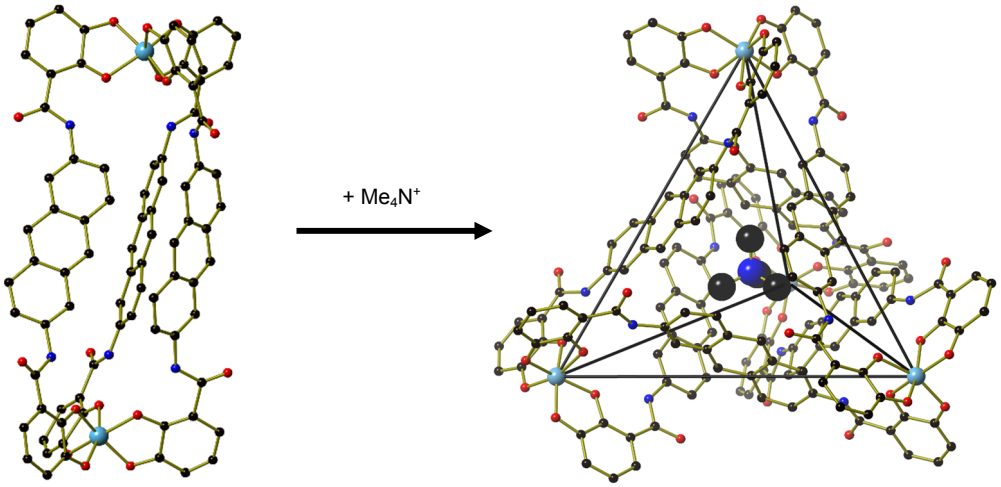

Figure 1.13 Transformation of the $[Ti^{IV}_2L_3]^{4-}$ triple helicate (left) into a $[(NMe_4)\{Ti^{IV}_4L_6\}]^{7-}$ tetrahedron (right) through the inclusion of a tetramethylammonium ion. Hydrogen atoms and additional counterions have been removed for clarity. Colour code: Ti^{IV} – Light Blue, N – Blue, O – Red, C – Black.

Compared to simple two-dimensional polygons, supramolecular polyhedra, or coordination capsules, proffer themselves as more attractive functional motifs arising from their ability to perform this type of host-guest chemistry.[63] These host-guest interactions have helped see supramolecular capsules used in areas such as catalysis,[64] photochemistry,[65] and stabilisation of reactive species.[66] Ward and co-workers have used Co^{II} and *bis*(pyrazolyl-pyridine)-based magnetic capsules for the encapsulation of small organic guests,[67] catalysis of the Kemp elimination reaction,[68] and the stabilisation of alkyl-phosphonate chemical warfare agent simulants (Fig. 1.14).[69] The limited use of paramagnetic ions in the development of these type of supramolecular architectures is perhaps unsurprising due to the fact that paramagnetic species give rise to a wide chemical shift range and broadened signals in solution-based NMR studies. This need not hinder the use of paramagnetic ions however, with Ward's work showing that this phenomenon can actually greatly facilitate the analysis of host-guest binding, spreading the

proton signals of the host out over a range of 200 ppm, and resulting in large complexation-induced shifts in the guest after encapsulation.[67]

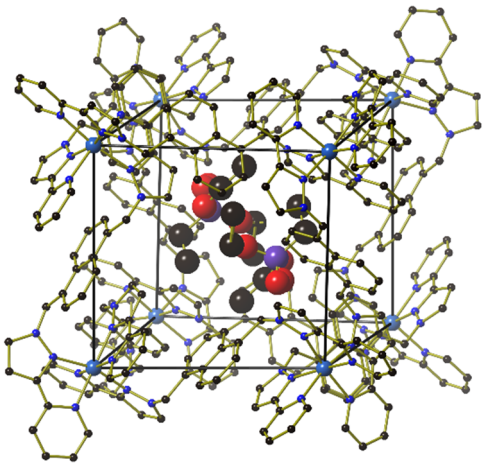

Figure 1.14 Structure of the $[Co^{II}_8L_{12}]^{16+}$ cubic cage showing the inclusion of diethyl methylphosphonate. Hydrogen atoms and counterions have been removed for clarity. Colour code: Co^{II} – Royal Blue, P – Mauve, N – Blue, O – Red, C – Black.

The interactions present between host and guest can range from strong ion-dipole interactions to weaker dispersion forces,[70] and manipulation of simple reaction conditions can lead to the inclusion or removal of a guest. Although these interactions play a major role in the stabilisation of the host-guest adduct, it is perhaps more crucial to take into consideration the size of the guest that is to be included. Allowing for the thermal motion of molecules, Rebek and co-workers have estimated optimal guest inclusion will occur in the liquid state when the packing coefficient, that is, the ratio of the guest volume to the host volume, is in the range 0.55 ± 0.09. Higher packing coefficients up to 0.70 may be observed when favourable interactions such as hydrogen bonding compensate the loss of entropy through a gain in enthalpy.[71]

Many of the examples thus far have shown supramolecular cages which make use of large organic ligands, compounds which are often synthesised by difficult low yielding multistep reactions. Metalloligands proffer an attractive alternative strategy towards the creation of magnetic cages due to their often-straightforward synthesis and their potential to add more magnetic ions within structurally analogous motifs. These building blocks can be defined as metal complexes with external functional groups capable of interacting or coordinating with other entities, including, but not limited to, other metalloligands or secondary metal ions. In order for metalloligands to be used as building blocks for the construction of capsules, the external functional groups must have a predefined orientation, but this can be easily generated from the choice of the central transition metal and its resulting geometry.[72]

Reichel et al. used the neutral metalloligand [$Fe^{III}L$] (H_3L = *tris*{[2-{(imidazole-4-yl)methylidene}amino]ethyl}amine) and Cu^{II} perchlorate in methanol to synthesise the imidazolate-bridged magnetic $[Fe^{III}_8Cu^{II}_6L_8]^{12+}$ heterometallic cube (Fig. 1.15).[73] Although magnetic studies have yet to be carried out on the cage, it is interesting to note that each cage complex is chiral, with either ΛΛΛΛΛΛΛΛ or ΔΔΔΔΔΔΔΔ configuration at the Fe^{III} centres. This chirality is communicated through the imidazolate-ligands which act like propellers around the Cu^{II} centres, the twisting of which ensures that all the Fe^{III} centres have the same configuration. This "soft" approach of chiral self-sorting is common within supramolecular magnetic cages, especially tetrahedra, and arises from the structural rigidity of the ligands which helps communicate the chirality between metal centres.[55,74–80] A racemic mixture of Λ and Δ capsules is usually formed, but these racemates can be resolved through the introduction of chiral auxiliary molecules or guest molecules.[81]

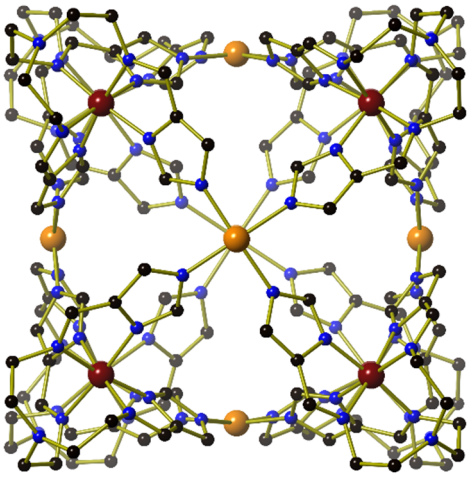

Figure 1.15 Structure of $[Fe^{III}_8Cu^{II}_6L_8]^{12+}$. Hydrogen atoms and counterions have been removed for clarity. Colour code: Fe^{III} – Maroon, Cu^{II} – Orange, N – Blue, C – Black.

These type of negatively charged polydentate ligands have been heavily employed within the metalloligand approach—their chelating nature allowing a stable and often neutral building block to be formed. This stability is crucial for the metalloligand's integrity during further reaction and it is perhaps for this reason that simple β-diketone and acetylacetonate-based ligands have been utilised for the design of metalloligands. There are limited examples of paramagnetic metalloligands using these oxygen-based donors, with acetylacetonate-based ligands more commonly employed because they have the advantage of being able to be functionalised at several positions.[75] This feature initially results in the creation of structurally similar metalloligands with different donor angles, and ultimately translates itself into the synthesis of topologically-varied cages.

Furthermore, pyridyl-acetylacetonate-based metalloligands have been used heavily in the creation of polynuclear coordination capsules. These donors have been employed due to the labile metal-nitrogen bond which allows for the self-correction needed within the self-assembly process. 1-(4-Pyridyl)butane-1,3-dione (HL) has been used by Wang et al. to make Al^{III} or Ga^{III} metalloligands, building blocks which were subsequently reacted with different *cis*-capped Pt^{II} salts to form a series of trigonal bipyramids in which the Al^{III} or Ga^{III} ions occupy the axial positions, and the Pt^{II} ions occupy the equatorial sites.[82] Wu and Wang have also used this Al^{III} metalloligand with Zn^{II} bromide to make an $[Al^{III}_2Zn^{II}_3L_6Br_6]$ trigonal bipyramid (Fig. 1.16). In addition to this structure they also showed how the reaction of the metalloligand with the *cis*-capped (ethylenediamine)palladium(II) nitrate leads to the loss of the ethylenediamine ligand and the formation of a $[Al^{III}_8Pd^{II}_6L_{24}](NO_3)_{12}$ coordination cube (Fig. 1.16).

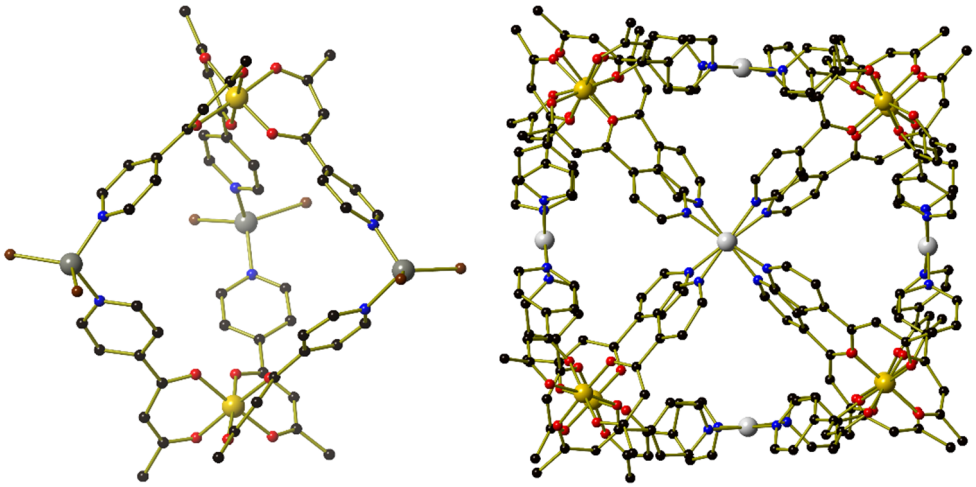

Figure 1.16 Structures of $[Al^{III}_2Zn^{II}_3L_6Br_6]$ (left) and $[Al^{III}_8Pd^{II}_6L_{24}]^{12+}$ (right). Hydrogen atoms and additional counterions have been removed for clarity. Colour code: Al^{III} – Gold, Pd^{II} – Light Grey, Zn^{II} – Dark Grey, Br^- – Brown, N – Blue, O – Red, C – Black.

Supramolecular chemistry proffers itself as an appealing rational design strategy towards the synthesis of coordination capsules as it allows for total control of the nuclearity and form of the complex. Within molecular magnetism, the ability to design structures could be transposed into the ability to predetermine any resultant magnetic behaviour. For this reason it is surprising that only a small number of groups have used supramolecular chemistry to rationally design magnetic architectures, and even fewer groups have specifically employed the metalloligand approach. The stability and applicability of these functional complexes should lead to a straightforward method for the development of high-nuclearity magnetic structures, with predictable magnetic behaviour.

1.2 References

(1) Müller, A.; Sarkar, S.; Shah, S. Q. N.; Bögge, H.; Schmidtmann, M.; Sarkar, S.; Kögerler, P.; Hauptfleisch, B.; Trautwein, A. X.; Schünemann, V. *Angew. Chemie Int. Ed.* **1999**, *38* (21), 3238.

(2) Schröder, C.; Nojiri, H.; Schnack, J.; Hage, P.; Luban, M.; Kögerler, P. *Phys. Rev. Lett.* **2005**, *94* (1), 1.

(3) Kögerler, P.; Tsukerblat, B.; Müller, A. *Dalton Trans.* **2010**, *39* (1), 21.

(4) Amjad, A.; Madalan, A. M.; Andruh, M.; Caneschi, A.; Sorace, L. *Chem. - A Eur. J.* **2016**, *22* (36), 12849.

(5) Upadhyay, A.; Singh, S. K.; Das, C.; Mondol, R.; Langley, S. K.; Murray, K. S.; Rajaraman, G.; Shanmugam, M. *Chem. Commun.* **2014**, *50* (64), 8838.

(6) Upadhyay, A.; Das, C.; Vaidya, S.; Singh, S. K.; Gupta, T.; Mondol, R.; Langley, S. K.; Murray, K. S.; Rajaraman, G.; Shanmugam, M. *Chem. - A Eur. J.* **2017**, *23* (20), 4903.

(7) Dei, A.; Gatteschi, D. *Angew. Chem. Int. Ed.* **2011**, *50* (50), 11852.

(8) Bogani, L.; Wernsdorfer, W. *Nat. Mater.* **2008**, *7* (3), 179.

(9) Sessoli, R.; Gatteschi, D.; Caneschi, A.; Novak, M. A. *Nature* **1993**, *365* (6442), 141.

(10) Milios, C. J.; Vinslava, A.; Wernsdorfer, W.; Moggach, S.; Parsons, S.; Perlepes, S. P.; Christou, G.; Brechin, E. K. *J. Am. Chem. Soc.* **2007**, *129* (10), 2754.

(11) Gatteschi, D.; Vindigni, A. In *Molecular Magnets: Physics and Applications*; Bartolomé, J., Fernando, L., Fernández, J. F., Eds.; Springer: New York, 2014; pp 191–220.

(12) Craig, G. A.; Murrie, M. *Chem. Soc. Rev.* **2015**, *44* (8), 2135.

(13) Kurmoo, M. *Chem. Soc. Rev.* **2009**, *38* (5), 1353.

(14) Evangelisti, M.; Candini, A.; Ghirri, A.; Affronte, M.; Brechin, E. K.; McInnes, E. J. L. *Appl. Phys. Lett.* **2005**, *87* (7), 1.

(15) Lehmann, J.; Gaita-Ariño, A.; Coronado, E.; Loss, D. *Nat. Nanotechnol.* **2007**, *2* (5), 312.

(16) Winpenny, R. E. P. *J. Chem. Soc. Dalt. Trans.* **2002**, *6* (1), 1.

(17) Fielden, J.; Cronin, L. In *Encyclopedia of Supramolecular Chemistry*; Atwood, J. L., Steed, J. W., Eds.; CRC Press: Florida, 2004; pp 1–10.

(18) Kahn, O.; Tola, P.; Galy, J.; Coudanne, H. *J. Am. Chem. Soc.* **1978**, *100* (12), 3931.

(19) Rebilly, J.-N.; Mallah, T. In *Single-Molecule Magnets and Related Phenomena*; Winpenny, R. E. P., Ed.; Springer-Verlag: Berlin Heidelberg, 2006; pp 103–131.

(20) Mallah, T.; Marvilliers, A.; Riviere, E. *Philos. Trans. R. Soc. A Math. Phys. Eng. Sci.* **1999**, *357* (1762), 3139.

(21) Keggin, J. F.; Miles, F. D. *Nature* **1936**, *137* (3466), 577.

(22) Ferlay, S.; Mallah, T.; Ouahès, R.; Veillet, P.; Verdaguer, M. *Nature* **1995**, *378* (6558), 701.

(23) Lefebvre, J.; Leznoff, D. B. In *Macromolecules Containing Metal and Metal-Like Elements*; Abd-El-Aziz, A. S., Carraher, C. E., Pittman, C. U., Zeldin, M., Eds.; John Wiley & Sons, Inc.: New Jersey, 2005; pp 155–208.

(24) Yao, M.-X.; Wei, Z.-Y.; Gu, Z.-G.; Zheng, Q.; Xu, Y.; Zuo, J.-L. *Inorg. Chem.* **2011**, *50* (17), 8636.

(25) Alexandru, M.-G.; Visinescu, D.; Shova, S.; Lloret, F.; Julve, M.; Andruh, M. *Inorg. Chem.* **2013**, *52* (19), 11627.

(26) Liu, W.; Wang, C.; Li, Y.; Zuo, J.; You, X. *Inorg. Chem.* **2006**, *45* (25), 10058.

(27) Beltran, L. M. C.; Long, J. R. *Acc. Chem. Res.* **2005**, *38* (4), 325.

(28) Smith, J. A.; Galán-Mascarós, J.-R.; Clérac, R.; Sun, J.-S.; Ouyang, X.; Dunbar, K. R. *Polyhedron* **2001**, *20* (11–14), 1727.

(29) Van Langenberg, K.; Batten, S. R.; Berry, K. J.; Hockless, D. C. R.; Moubaraki, B.; Murray, K. S. *Inorg. Chem.* **1997**, *36* (22), 5006.

(30) Shatruk, M.; Chambers, K. E.; Prosvirin, A. V.; Dunbar, K. R. *Inorg. Chem.* **2007**, *46* (13), 5155.

(31) Yang, J. Y.; Shores, M. P.; Sokol, J. J.; Long, J. R. *Inorg. Chem.* **2003**, *42* (5), 1403.

(32) Bartlett, B. M.; Harris, T. D.; DeGroot, M. W.; Long, J. R. *Zeitschrift für Anorg. und Allg. Chemie* **2007**, *633* (13–14), 2380.

(33) Wang, C. F.; Zuo, J. L.; Bartlett, B. M.; Song, Y.; Long, J. R.; You, X. Z. *J. Am. Chem. Soc.* **2006**, *128* (22), 7162.

(34) Berseth, P. a.; Sokol, J. J.; Shores, M. P.; Heinrich, J. L.; Long, J. R. *J. Am. Chem. Soc.* **2000**, *122* (40), 9655.

(35) Heinrich, J. L.; Berseth, P. A.; Long, J. R. *Chem. Commun.* **1998**, *4* (11), 1231.

(36) Sokol, J. J.; Shores, M. P.; Long, J. R. *Angew. Chemie Int. Ed.* **2001**, *40* (1), 236.

(37) Aromí, G.; Gamez, P.; Krzystek, J.; Kooijman, H.; Spek, A. L.; MacLean, E. J.; Teat, S. J.; Nowell, H. *Inorg. Chem.* **2007**, *46* (7), 2519.

(38) Aromí, G.; Ribas, J.; Gamez, P.; Roubeau, O.; Kooijman, H.; Spek, A. L.; Teat, S.; MacLean, E.; Stoeckli-Evans, H.; Reedijk, J. *Chem. - A Eur. J.* **2004**, *10* (24), 6476.

(39) Aromí, G.; Gamez, P.; Boldron, C.; Kooijman, H.; Spek, A. L.; Reedijk, J. *Eur. J. Inorg. Chem.* **2006**, *2006* (10), 1940.

(40) Barrios, L. A.; Borilovic, I.; Salinas Uber, J.; Aguilà, D.; Roubeau, O.; Aromí, G. *Dalton Trans.* **2013**, *42* (34), 12185.

(41) Campos-Fernández, C. S.; Clérac, R.; Dunbar, K. R. *Angew. Chemie Int. Ed.* **1999**, *38* (23), 3477.

(42) Campos-Fernández, C. S.; Schottel, B. L.; Chifotides, H. T.; Bera, J. K.; Bacsa, J.; Koomen, J. M.; Russell, D. H.; Dunbar, K. R. *J. Am. Chem. Soc.* **2005**, *127* (37), 12909.

(43) Andruh, M. *Chem. Commun.* **2011**, *47* (11), 3025.

(44) Andruh, M.; Ramade, I.; Codjovi, E.; Guillou, O.; Kahn, O.; Trombe, J. C. *J. Am. Chem. Soc.* **1993**, *115* (5), 1822.

(45) Benelli, C.; Caneschi, A.; Gatteschi, D.; Guillou, O.; Pardi, L. *Inorg. Chem.* **1990**, *29* (9), 1750.

(46) Patrascu, A. A.; Calancea, S.; Cassaro, R. A. A.; Soriano, S.; Madalan, A. M.; Maxim, C.; Novak, M. A.; Vaz, M. G. F.; Andruh, M. *CrystEngComm* **2016**, *18* (25), 4779.

(47) Im, H. J.; Lee, S. W. *Polyhedron* **2016**, *110* (3), 24.

(48) Bencini, A.; Benelli, C.; Caneschi, A.; Dei, A.; Gatteschi, D. *Inorg. Chem.* **1986**, *25* (4), 572.

(49) Cozzi, P. G. *Chem. Soc. Rev.* **2004**, *33* (7), 410.

(50) Belowich, M. E.; Stoddart, J. F. *Chem. Soc. Rev.* **2012**, *41* (6), 2003.

(51) Kumar, S.; Dhar, D. N.; Saxena, P. N. *J. Sci. Ind. Res. (India).* **2009**, *68* (3), 181.

(52) Granzhan, A.; Riis-Johannessen, T.; Scopelliti, R.; Severin, K. *Angew. Chemie Int. Ed.* **2010**, *49* (32), 5515.

(53) Granzhan, A.; Schouwey, C.; Riis-Johannessen, T.; Scopelliti, R.; Severin, K. *J. Am. Chem. Soc.* **2011**, *133* (18), 7106.

(54) Riddell, I. A.; Smulders, M. M. J.; Clegg, J. K.; Hristova, Y. R.; Breiner, B.; Thoburn, J. D.; Nitschke, J. R. *Nat. Chem.* **2012**, *4* (10), 860.

(55) Ronson, T. K.; Giri, C.; Kodiah Beyeh, N.; Minkkinen, A.; Topić, F.; Holstein, J. J.; Rissanen, K.; Nitschke, J. R. *Chem. - A Eur. J.* **2013**, *19* (10), 3374.

(56) Chakrabarty, R.; Mukherjee, P. S.; Stang, P. J. *Chem. Rev.* **2011**, *111* (11), 6810.

(57) Cook, T. R.; Zheng, Y.-R.; Stang, P. J. *Chem. Rev.* **2013**, *113* (1), 734.

(58) Fujita, M.; Tominaga, M.; Hori, A.; Therrien, B. *Acc. Chem. Res.* **2005**, *38* (4), 369.

(59) Liu, Y.; Hu, C.; Comotti, A.; Ward, M. D. *Science.* **2011**, *333* (6041), 436.

(60) Fujita, M.; Yazaki, J.; Ogura, K. *J. Am. Chem. Soc.* **1990**, *112* (14), 5645.

(61) Fujita, M.; Sasaki, O.; Mitsuhashi, T.; Fujita, T.; Yazaki, J.; Yamaguchi, K.; Ogura, K. *Chem. Commun.* **1996**, *20* (13), 1535.

(62) Scherer, M.; Caulder, D. L.; Johnson, D. W.; Raymond, K. N. *Angew. Chemie Int. Ed.* **1999**, *38* (11), 1587.

(63) Riddell, I. A.; Ronson, T. K.; Clegg, J. K.; Wood, C. S.; Bilbeisi, R. A.; Nitschke, J. R. *J. Am. Chem. Soc.* **2014**, *136* (26), 9491.

(64) Zhao, C.; Toste, F. D.; Raymond, K. N.; Bergman, R. G. *J. Am. Chem. Soc.* **2014**, *136* (41), 14409.

(65) Chepelin, O.; Ujma, J.; Wu, X.; Slawin, A. M. Z.; Pitak, M. B.; Coles, S. J.; Michel, J.; Jones, A. C.; Barran, P. E.; Lusby, P. J. *J. Am. Chem. Soc.* **2012**, *134* (47), 19334.

(66) Mal, P.; Breiner, B.; Rissanen, K.; Nitschke, J. R. *Science.* **2009**, *324* (5935), 1697.

(67) Turega, S.; Whitehead, M.; Hall, B. R.; Meijer, A. J. H. M.; Hunter, C. A.; Ward, M. D. *Inorg. Chem.* **2013**, *52* (2), 1122.

(68) Cullen, W.; Misuraca, M. C.; Hunter, C. A.; Williams, N. H.; Ward, M. D. *Nat. Chem.* **2016**, *8* (3), 231.

(69) Taylor, C. G. P.; Piper, J. R.; Ward, M. D. *Chem. Commun.* **2016**, *52* (37), 6225.

(70) Mugridge, J. S. Supramolecular Host-Guest Interactions, Dynamics and Structure, University of California, Berkeley, 2010.

(71) Mecozzi, S.; Rebek, Jr., J. *Chem. - A Eur. J.* **1998**, *4* (6), 1016.

(72) Kumar, G.; Gupta, R. *Chem. Soc. Rev.* **2013**, *42* (24), 9403.

(73) Reichel, F.; Clegg, J. K.; Gloe, K.; Gloe, K.; Weigand, J. J.; Reynolds, J. K.; Li, C.-G.; Aldrich-Wright, J. R.; Kepert, C. J.; Lindoy, L. F.; Yao, H.-C.; Li, F. *Inorg. Chem.* **2014**, *53* (2), 688.

(74) Saalfrank, R. W.; Stark, A.; Bremer, M.; Hummel, H.-U. *Angew. Chem. Int. Ed. Engl.* **1990**, *29* (3), 311.

(75) Saalfrank, R. W.; Hörner, B.; Stalke, D.; Salbeck, J. *Angew. Chem. Int. Ed. Engl.* **1993**, *32* (8), 1179.

(76) Fleming, J. S.; Mann, K. L. V; Carraz, C.-A.; Psillakis, E.; Jeffery, J. C.; McCleverty, J. A.; Ward, M. D. *Angew. Chemie Int. Ed.* **1998**, *37* (9), 1279.

(77) Caulder, D. L.; Powers, R. E.; Parac, T. N.; Raymond, K. N. *Angew. Chemie Int. Ed.* **1998**, *37* (13–14), 1840.

(78) Beissel, T.; Powers, R. E.; Raymond, K. N. *Angew. Chem. Int. Ed. Engl.* **1996**, *35* (10), 1084.

(79) Clegg, J. K.; Lindoy, L. F.; Moubaraki, B.; Murray, K. S.; McMurtrie, J. C. *Dalton Trans.* **2004**, *4* (16), 2417.

(80) Clegg, J. K.; Li, F.; Jolliffe, K. A; Meehan, G. V; Lindoy, L. F. *Chem. Commun.* **2011**, *47* (21), 6042.

(81) Davis, A. V; Fiedler, D.; Ziegler, M.; Terpin, A.; Raymond, K. N. *J. Am. Chem. Soc.* **2007**, *129* (49), 15354.

(82) Wang, M.; Vajpayee, V.; Shanmugaraju, S.; Zheng, Y.-R.; Zhao, Z.; Kim, H.; Mukherjee, P. S.; Chi, K.-W.; Stang, P. J. *Inorg. Chem.* **2011**, *50* (4), 1506.

Chapter 2: $[M^{III}_8M^{II}_6L_{24}]^{n+}$ Coordination Cubes

2.1 Introduction

The choice of the central metal ion in the design of a metalloligand has crucial consequences over both the chemical and physical properties of the resultant architecture. Chemically, the geometrical preferences of the central ion will affect the number of functional ligands available for further donation, thus impacting the shape of the final assembly. 1-(4-Pyridyl)butane-1,3-dione is capable of forming *tris*(bidentate) complexes, and its coordination to a metal ion capable of octahedral geometry should lead to the creation of a $[M^{III}L_3]$ building block that is functionalised with three *p*-pyridyl donor groups. In the case of the *fac*-isomer, the N-donor groups are aligned in a tripodal array, such that combining it with a square-planar connector should lead to the formation of a cubic system (Fig. 1.11). This enables us to use pre-designed self-assembly to position a paramagnetic ion, from the $[M^{III}L_3]$, at the eight vertices of the cube, with another metal ion at the centre of the six faces. We have chosen to focus our studies on two paramagnetic metalloligands of this type, namely, $[Cr^{III}L_3]$ (Fig. 2.1), and $[Fe^{III}L_3]$. These two ions possess isotropic $S = 3/2$ and $S = 5/2$ spin states, respectively, and their interaction with various secondary metal ions will have a profound influence on the magnetic behaviour of the resultant cluster. Therefore, through the careful selection of M^{III} and M^{II} building blocks, we can predictably design the magnetic properties of the final assembly.

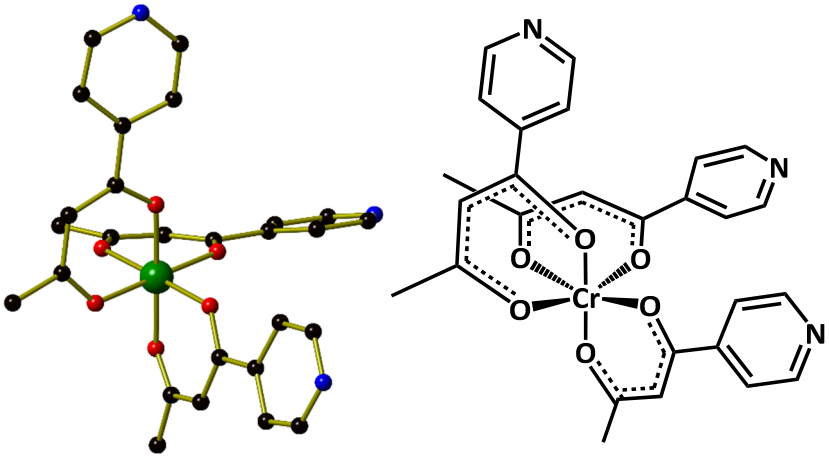

Figure 2.1 The molecular structure of *fac*-$[Cr^{III}L_3]$ (left), with a skeletal representation for clarity (right). Hydrogen atoms have been removed for clarity. Colour code: Cr^{III} – Green, O – Red, N – Blue, C – Black.

Herein, we present the synthesis and characterisation of fourteen new heterometallic tetradecanuclear coordination cubes of the general formula $[M^{III}_8M^{II}_6L_{24}]^{n+}$ (M^{III} = Cr, Fe; M^{II} = Cu, Co, Ni, Pd; n = 0-12), formed from the reaction of the paramagnetic metalloligands $[Cr^{III}L_3]$ or $[Fe^{III}L_3]$ and a "naked" M^{II} salt.

2.2 Experimental

Materials and Instrumentation

All reactions were performed under aerobic conditions. Solvents and reagents were used as received from commercial suppliers. Elemental analyses were carried out by Medac Ltd. Magnetisation measurements were carried out on a Quantum Design SQUID MPMS-XL magnetometer, operating between 1.8 and 300 K for dc applied magnetic fields ranging from 0 to 5 T. X-, Q- and W-band EPR spectra were collected on powdered microcrystalline samples of [$Cr^{III}L_3$] and compounds **2**, **5**, **10**, **11**, **13**, and **14** at the National EPR Facility at The University of Manchester.

Syntheses

Preparation of 1-(4-pyridyl)butane-1,3-dione (HL)

1-(4-Pyridyl)butane-1,3-dione was prepared according to previously published procedures.[1] Methyl isonicotinate (196 mL, 1.45 mol) was placed into a mixture of acetone (350 mL) and THF (1 L). The mixture was heated to 30 °C, before sodium methoxide (81.00 g, 1.50 mol) was added slowly. The solution was heated to 60 °C for 24 hours and the resultant yellow precipitate was filtered under vacuum, before being washed with THF (20 mL) and diethyl ether (20 mL). The dried yellow solid was dissolved in water and the pH was adjusted to 7 using acetic acid. The solution was filtered and the product extracted with CH_2Cl_2 before being dried over anhydrous $MgSO_4$. CH_2Cl_2 was removed under reduced pressure to afford the product as a yellow oil which solidified upon cooling (135.79 g, 57%). ^{1}H NMR spectroscopy (CD_3OD, 500 MHz): δ 8.67 (m, 2H, Ar-*H*), 7.84 (m, 2H, Ar-*H*), 5.48 (s, 1H, COC*H*CO), 2.24 (s, 3H, CH_3) ppm.

Synthesis of *tris*{1-(4-pyridyl)acetylacetonato}chromium(III), [$Cr^{III}L_3$]

The synthesis of [$Cr^{III}L_3$] was adapted from previously published procedures.[2]

$CrCl_3 \cdot 6H_2O$ (0.530 g, 2.0 mmol) and urea (0.500 g, 8.0 mmol) were dissolved in distilled water (50 mL). To this solution, HL (1.07 g, 6.6 mmol) was added, and the solution was stirred for 2 days at 90 °C. A light-brown precipitate resulted which was filtered and washed with water (10 mL). The crude product was extracted with CH_2Cl_2 and dried over anhydrous $MgSO_4$. CH_2Cl_2 was removed under reduced pressure to afford the product as a light-brown solid (0.703 g, 65%). Elemental analysis (%) calculated (found) for $C_{27}H_{24}N_3O_6Cr$ (538.50 g mol^{-1}): C 60.22 (60.06), H 4.49 (4.19), N 7.80 (7.68). ESI TOF HRMS m/z calculated (found) for [$Cr^{III}L_3$]: [$C_{27}H_{25}CrN_3O_6$]$^+$: 539.1143 (539.1173), [$C_{27}H_{24}CrN_3O_6Na$]$^+$ 561.0963 (561.0978).

Synthesis of *tris*{1-(4-pyridyl)acetylacetonato}iron(III), [$Fe^{III}L_3$]

The synthesis of [$Fe^{III}L_3$] was adapted from previously published procedures.[3]

$FeCl_3$ (0.162 g, 1 mmol), HL (0.570 g, 3.5 mmol) and sodium methoxide (0.189 g, 3.5 mmol) were dissolved in MeOH/H_2O (1:1 v/v, 100 mL), and left to stir until a red product precipitated (≈24 h). The precipitate was filtered and washed with water. The crude product was extracted with CH_2Cl_2 and dried over anhydrous $MgSO_4$. The CH_2Cl_2 was removed under reduced pressure to afford the product as a red solid (0.460 g, 85 %). Elemental analysis (%) calculated (found) for $C_{27}H_{24}N_3O_6Fe$ (542.34 g mol^{-1}): C 59.79 (59.53), H 4.46 (4.39), N 7.75 (7.67). ESI TOF HRMS *m/z* calculated (found) for [$Fe^{III}L_3$]: $[C_{27}H_{25}FeN_3O_6]^+$ 543.1088 (543.1051), $[C_{27}H_{24}FeN_3O_6Na]^+$ 565.0907 (565.0865).

[$Cr^{III}_8Cu^{II}_6L_{24}Cl_{12}$] (1)

To a solution of [$Cr^{III}L_3$] (108 mg, 0.2 mmol) in CH_2Cl_2/MeOH (1:1 v/v, 20 mL), was added a solution of $CuCl_2{\cdot}2H_2O$ (34 mg, 0.2 mmol) in water (2 mL). The solution was stirred for 5 minutes, before being filtered and allowed to stand. Green X-ray quality crystals were obtained from room temperature evaporation of the mother liquor after 5 days. Yield (109 mg, 85 %). Elemental analysis (%) calculated (found) for $C_{216}H_{192}N_{24}O_{48}Cl_{12}Cr_8Cu_6$ (5114.68 g mol^{-1}): C 50.72 (50.43), H 3.78 (3.45), N 6.57 (6.64).

[$Cr^{III}_8Cu^{II}_6L_{24}(H_2O)_{10}(NO_3)_2$]$(NO_3)_{10}$ (2)

To a solution of [$Cr^{III}L_3$] (108 mg, 0.2 mmol) in CH_2Cl_2 (10 mL), was added a solution of $Cu(NO_3)_2{\cdot}3H_2O$ (48 mg, 0.2 mmol) in MeOH (10 mL). The solution was stirred for 1 hour, before being filtered and allowed to stand. Dark-red X-ray quality crystals were obtained from room temperature evaporation of the mother liquor after 5 days. Yield (91 mg, 68 %). Elemental analysis (%) calculated (found) for $C_{216}H_{208}N_{36}O_{92}Cr_8Cu_6$ (5325.32 g mol^{-1}): C 48.72 (48.57), H 3.94 (3.86), N 4.73 (4.58).

[$Cr^{III}_8Cu^{II}_6L_{24}(H_2O)_{12}$]$(SO_4)_6$ (3)

To a solution of [$Cr^{III}L_3$] (108 mg, 0.2 mmol) in CH_2Cl_2/MeOH (1:1 v/v, 20 mL), was added a solution of $Cu(SO_4){\cdot}5H_2O$ (50 mg, 0.2 mmol) in water (3 mL). The solution was stirred for 1 hour, before being filtered and allowed to stand. Brown X-ray quality crystals were obtained from room temperature evaporation of the mother liquor after 2 days. Yield (112 mg, 82 %). Elemental analysis (%) calculated (found) for $C_{216}H_{216}N_{24}O_{84}S_6Cr_8Cu_6$ (5481.79 g mol^{-1}): C 47.33 (47.12), H 3.97 (3.83), N 6.13 (5.97), S 3.51 (3.44).

[$Cr^{III}_8Co^{II}_6L_{24}Cl_{12}$] (4)

To a solution of [$Cr^{III}L_3$] (108 mg, 0.2 mmol) in CH_2Cl_2/THF (1:1 v/v, 20 mL), was added $CoCl_2$ (20 mg, 0.15 mmol). The solution was stirred for 14 hours, before being filtered and allowed to stand.

Dark-orange X-ray quality crystals were obtained from room temperature evaporation of the mother liquor after 4 days. Yield (78 mg, 61 %). Elemental analysis (%) calculated (found) for $C_{216}H_{192}N_{24}O_{48}Cl_{12}Cr_8Co_6$ (5087.00 g mol^{-1}): C 51.00 (51.11), H 3.80 (3.69), N 6.61 (6.54).

$[Cr^{III}_8Co^{II}_6L_{24}(H_2O)_{12}](ClO_4)_{12}$ (5)

To a solution of $[Cr^{III}L_3]$ (108 mg, 0.2 mmol) in CH_2Cl_2 (10 mL), was added a solution of $Co(ClO_4)_2{\cdot}6H_2O$ (73 mg, 0.2 mmol) in MeOH/$MeNO_2$ (1:1 v/v, 10 mL). The solution was stirred for 1 hour, before being filtered and allowed to stand. Brown X-ray quality crystals were obtained from room temperature evaporation of the mother liquor after 5 days. Yield (100 mg, 66 %). Elemental analysis (%) calculated (found) for $C_{216}H_{216}N_{24}O_{108}Cl_{12}Cr_8Co_6$ (6071.13 g mol^{-1}): C 42.73 (42.47), H 3.59 (3.43), N 5.54 (5.31).

$[Cr^{III}_8Co^{II}_6L_{24}(SCN)_{12}]$ (6)

To a solution of $[Cr^{III}L_3]$ (108 mg, 0.2 mmol) in CH_2Cl_2/MeOH (1:1 v/v, 20 mL), was added $Co(SCN)_2$ (35 mg, 0.2 mmol). The solution was stirred for 2 hours, before being filtered and allowed to stand. Light-brown X-ray quality crystals were obtained from room temperature evaporation of the mother liquor after 5 days. Yield (106 mg, 79 %). Elemental analysis (%) calculated (found) for $C_{228}H_{192}N_{36}O_{48}S_{12}Cr_8Co_6$ (5358.46 g mol^{-1}): C 53.63 (53.26), H 3.79 (3.51), N 4.94 (5.13).

$[Cr^{III}_8Ni^{II}_6L_{24}Cl_{12}]$ (7)

To a solution of $[Cr^{III}L_3]$ (108 mg, 0.2 mmol) in CH_2Cl_2 (10 mL), was added a solution of $NiCl_2$ (20 mg, 0.15 mmol) in THF (10 mL). The solution was stirred for 12 hours, before being filtered and allowed to stand. Brown X-ray quality crystals were obtained from room temperature evaporation of the mother liquor after 5 days. Yield (78 mg, 61 %). Elemental analysis (%) calculated (found) for $C_{216}H_{192}N_{24}O_{48}Cr_8Ni_6$ (5085.58 g mol^{-1}): C 50.99 (51.08), H 3.81 (3.93), N 6.61 (6.70).

$[Cr^{III}_8Ni^{II}_6L_{24}(H_2O)_{12}](NO_3)_{12}$ (8)

To a solution of $[Cr^{III}L_3]$ (54 mg, 0.1 mmol) in CH_2Cl_2 (10 mL), was added a solution of $Ni(NO_3)_2{\cdot}6H_2O$ (30 mg, 0.1 mmol) and pyrazine (32 mg, 0.4 mmol) in MeOH (10 mL). The solution was stirred for 3 hours, before being filtered and allowed to stand. Dark-orange X-ray quality crystals were obtained from room temperature evaporation of the mother liquor after 7 days. Yield (41 mg, 67 %). Elemental analysis (%) calculated (found) for $C_{216}H_{216}N_{24}O_{60}Cr_8Ni_6$ (4876.38 g mol^{-1}): C 53.20 (53.01), H 4.46 (4.39), N 6.89 (6.78). Note: Pyrazine was added in an attempt to join coordination cubes. Crystallisation of **8** was not possible without its addition.

$[Cr^{III}_8Ni^{II}_6L_{24}(MeCN)_7(H_2O)_5](ClO_4)_{12}$ (9)

To a solution of $[Cr^{III}L_3]$ (108 mg, 0.2 mmol) in CH_2Cl_2 (10 mL), was added a solution of $Ni(ClO_4)_2{\cdot}6H_2O$ (73 mg, 0.2 mmol) and TEMPO (31 mg, 0.2 mmol) in MeCN (10 mL). The solution was stirred for 3 days, before being filtered and allowed to stand. Brown X-ray quality crystals were obtained after 5 days from diffusion of hexane into the mother liquor. Yield (95 mg, 75 %). Elemental analysis (%) calculated (found) for $C_{230}H_{223}N_{31}O_{54}Cr_8Ni_6$ (5053.64 g mol^{-1}): C 54.65 (54.78), H 4.45 (4.56), N 8.59 (8.68). Note: Host-guest chemistry was attempted through the addition of TEMPO. Crystallisation of **9** was not possible without its addition.

$[Fe^{III}_8Cu^{II}_6L_{24}(H_2O)_4Br_4]Br_8$ (10)

To a solution of $[Fe^{III}L_3]$ (108 mg, 0.2 mmol) in CH_2Cl_2 (10 mL), was added $CuBr_2$ (45 mg, 0.2 mmol) in MeOH (10 mL). The mixture was stirred for 3 hours, before being filtered and allowed to stand. Red X-ray quality crystals were obtained from room temperature evaporation of the mother liquor after 2 days. Yield (69 mg, 48 %). Elemental analysis (%) calculated (found) for $C_{216}H_{200}N_{24}O_{52}Br_{12}Fe_8Cu_6$ (5750.98 g mol^{-1}): C 45.11 (45.01), H 3.51 (3.24) N 5.85 (6.04).

$[Fe^{III}_8Cu^{II}_6L_{24}(H_2O)_{10}](NO_3)_{12}$ (11)

To a solution of $[Fe^{III}L_3]$ (54 mg, 0.1 mmol) in CH_2Cl_2/EtOH (1:1 v/v, 20 mL), was added $Cu(NO_3)_2{\cdot}3H_2O$ (24 mg, 0.1 mmol) and pyrazine (32 mg, 0.4 mmol). The mixture was stirred for 3 hours, before being filtered and allowed to stand. Red X-ray quality crystals were obtained from room temperature evaporation of the mother liquor after 2 days. Yield (46 mg, 65 %). Elemental analysis (%) calculated (found) for $C_{216}H_{212}N_{36}O_{94}Fe_8Cu_6$ (5644.21 g mol^{-1}): C 45.96 (45.49), H 3.79 (3.68), N 8.93 (8.54). Note: Pyrazine was added in an attempt to join coordination cubes. Crystallisation of **11** was not possible without its addition.

$[Fe^{III}_8Co^{II}_6L_{24}(SCN)_{10}(H_2O)_2]Cl_2$ (12)

To a solution of $[Fe^{III}L_3]$ (108 mg, 0.2 mmol) in CH_2Cl_2/MeOH (1:1 v/v, 20 mL), was added $CoCl_2$ (26 mg, 0.2 mmol). After 20 minutes of stirring, KSCN (39 mg, 0.4 mmol) in water (2 mL) was added, and the solution was allowed to stir for a further 30 minutes. The solution was filtered and allowed to stand. Red X-ray quality crystals were obtained from room temperature evaporation of the mother liquor after 3 days. Yield (83 mg, 62 %). Elemental analysis (%) calculated (found) for $C_{226}H_{196}N_{34}O_{50}S_{10}Cl_2Fe_8Co_6$ (5380.08 g mol^{-1}): C 50.45 (50.81), H 3.67 (3.70), N 8.85 (9.21).

$[Fe^{III}_8Ni^{II}_6L_{24}(SCN_{11})Cl]$ (13)

To a solution of $[Fe^{III}L_3]$ (108 mg, 0.2 mmol) in CH_2Cl_2/MeOH (1:1 v/v, 20 mL), was added $NiCl_2$ (26 mg, 0.2 mmol). After 20 minutes KSCN (39 mg, 0.4 mmol) in water (2 mL) was added, and the solution was allowed to stir for a further 30 minutes. The solution was filtered and allowed to stand. Red X-ray quality crystals were obtained from room temperature evaporation of the

mother liquor after 4 days. Yield (95 mg, 71 %). Elemental analysis (%) calculated (found) for $C_{227}H_{192}N_{35}O_{48}S_{11}ClFe_8Ni_6$ (5365.24 g mol^{-1}): C 50.82 (50.13), H 3.61 (3.70), N 9.14 (9.27).

$[Fe^{III}_8Pd^{II}_6L_{24}]Cl_{12}$ (14)

A solution of $AgNO_3$ (28 mg, 0.16 mmol) and [Pd(benzonitrile)$_2Cl_2$] (32 mg, 0.08 mmol) in $CHCl_3$/MeOH (1:1, 10 mL) was stirred for 30 minutes at room temperature. The solution was filtered, added to a solution of [$Fe^{III}L_3$] (30 mg, 0.055 mmol) in MeOH (10 mL), stirred for a further 30 minutes, before being filtered and allowed to stand. Dark-red X-ray quality crystals were obtained from room temperature evaporation of the mother liquor after 3 days. Yield (32 mg, 87 %). Elemental analysis (%) calculated (found) for $C_{216}H_{192}N_{24}O_{48}Cl_{12}Fe_8Pd_6$ (5402.67 g mol^{-1}): C 48.02 (48.31), H 3.58 (3.31), N 6.22 (6.12). Note: $AgNO_3$ was added in an attempt to perform a salt metathesis reaction. Crystallisation of **14** was not possible without its addition.

Crystal Structure Information

[$Fe^{III}L_3$], [$Cr^{III}L_3$], $[Cr^{III}_8Cu^{II}_6L_{24}Cl_{12}]$ (1), $[Cr^{III}_8Cu^{II}_6L_{24}(H_2O)_{12}](SO_4)_6$ (3), $[Cr^{III}_8Co^{II}_6L_{24}Cl_{12}]$ (4), $[Cr^{III}_8Co^{II}_6L_{24}(SCN)_{12}]$ (6), $[Cr^{III}_8Ni^{II}_6L_{24}Cl_{12}]$ (7), $[Cr^{III}_8Ni^{II}_6L_{24}(H_2O)_{12}](NO_3)_{12}$ (8), $[Cr^{III}_8Ni^{II}_6L_{24}Cl_{12}]$ (9), $[Fe^{III}_8Cu^{II}_6L_{24}(H_2O)_4Br_4]Br_8$ (10), $[Fe^{III}_8Cu^{II}_6L_{24}(H_2O)_{10}](NO_3)_{12}$ (11), $[Fe^{III}_8Co^{II}_6L_{24}(SCN)_{10}(H_2O)_2]Cl_2$ (12), $[Fe^{III}_8Ni^{II}_6L_{24}(SCN_{11})Cl]$ (13), $[Fe^{III}_8Pd^{II}_6L_{24}]Cl_{12}$ (14)

For compounds [$Fe^{III}L_3$], **1**, **4**, **6**, **7**, **8**, **9**, **10**, **11**, **12**, and **14** single-crystal X-ray diffraction data were collected at T = 100 K on a Rigaku AFC12 goniometer equipped with an enhanced sensitivity (HG) Saturn 724+ detector mounted at the window of an FR-E+ Superbright MoKα rotating anode generator with HF Varimax optics (70 μm focus).[8] For [$Cr^{III}L_3$] and compound **3**, single crystal X-ray diffraction data were measured on a Rigaku Oxford Diffraction SuperNova diffractometer using Mo (for [$Cr^{III}L_3$]) or Cu (for **3**) radiation at T = 120 K. The CrysalisPro software package was used for instrument control, unit cell determination and data reduction for [$Fe^{III}L_3$], **1**, **4**, **6**, **7**, **8**, **9**, **10**, **11**, **12**, and **14**,[4] whereas Rigaku Crystal Clear and CrysalisPro software was used for the data collection and reduction of [$Cr^{III}L_3$] and **3**.[9,10]

Due to very weak scattering power, single-crystal X-ray diffraction data for **8**, **9** and **11** were collected at T = 30.15 K using a synchrotron source (λ = 0.6889 Å) on the I19 beam line at Diamond Light Source on an undulator insertion device with a combination of double crystal monochromator, vertical and horizontal focussing mirrors and a series of beam slits. The same software as above was used for data refinement. Crystals of all samples were very sensitive to solvent loss, which resulted in rapid crystal delamination and poor quality X-ray diffraction data. To slow down this crystal degradation, crystals of [$Fe^{III}L_3$], **1**, **4**, **6**, **7**, **8**, **9**, **10**, **11**, **12**, and **14** were "cold mounted" on MiTeGen Micromounts™ at T = 203 K using Sigma-Aldrich Fomblin Y® LVAC

(3300 mol. wt.) with the X-Temp 2 crystal cooling system attached to the microscope.[12] This procedure protected crystal quality and permitted collection of usable X-ray data. Unit cell parameters in all cases were refined against all data.

The crystal structures of [$Cr^{III}L_3$], [$Fe^{III}L_3$], **1**, **4**, **6**, and **12** were solved using the charge flipping method implemented in SUPERFLIP,[11] whereas **10**, **11**, **13**, and **14** were solved using the dual space algorithm as implemented in SHELXT,[15] **7**-**9** were solved using Intristic Phasing as implemented in SHELXT,[15] and **3** was solved using direct methods with ShelXS. All structures were refined on F_o^2 by full-matrix least-squares refinements using ShelXL,[5] within the OLEX2 suite.[6] All non-hydrogen atoms were refined with anisotropic displacement parameters, and all hydrogen atoms were added at calculated positions and refined using a riding model with isotropic displacement parameters based on the equivalent isotropic displacement parameter (U_{eq}) of the parent atom.

All crystal structures (except [$Cr^{III}L_3$] and [$Fe^{III}L_3$]) contain large accessible voids and channels that are filled with diffuse electron density belonging to uncoordinated solvent, whose electron contribution was accounted for by the SMTBX solvent masking routine as implemented in OLEX2 software (**1**, **3**, **4**, **6**, **7**, **10**-**14**) or by the PLATON/SQUEEZE routine (**8** and **9**).[6] The crystal structure of **4** exhibits a significant amount of positional disorder, whereby part of the complex adopts two positions along the Cl3-Co2-Cl4 axis. This disorder has been modelled over two sites with a 60:40 ratio. Several geometrical constraints (DFIX, AFIX 66, FLAT) have been used to maintain sensible molecular geometry. Crystal structures **1** and **6** (both in the tetragonal $I4_122$ space group) have been refined as two-component inversion twins with 81:19 and 58:42 ratios, respectively. To maintain reasonable molecular geometry, DFIX restraints were used in **7**-**11**, and **13**, whereas SIMU, DELU and RIGU restraints were applied to model appropriately atomic displacement parameters (ADP).

For **3**, the structure has been modelled as far as is reasonable and practical, given the poor quality of the data set. The ShelX weighting scheme could not be optimized. The [$Cr^{III}_8Cu^{II}_6$] cage was identified easily from the initial structure solution and refines well without restraints. Overall the cube carries a total charge of 12+, which is is balanced by six sulfate ions. Peaks in the difference map corresponding to three crystallographically inequivalent sulfate anions per asymmetric unit were identified. Of these, two are inside the cube (S2 and S3) and one (S1) is outside of the cube. The geometry of the S1 anion is the most stable, and thus S2 and S3 anions were modelled to have similar geometries to S1. S1 and S2 were refined anisotropically with displacement ellipsoid restraints; S3 was refined using an isotropic model. Each sulfate anion was modelled as half-occupied, and each is disordered around a crystallographic four-fold rotation axis so that the charges balance. Bond distance and displacement similarity restraints (SADI and RIGU) were

used, as shown in the .res file embedded within the CIF shelx_res_file. Close O···O contacts between sulfate anions are flagged by PLATON; this is inevitable given the disordered nature of the anions. The copper centres are assumed to have axially coordinated water molecules, with the H atoms on these ligands placed for the sake of chemical completeness.

$[Cr^{III}_8Cu^{II}_6L_{24}(H_2O)_{10}(NO_3)_2](NO_3)_{10}$ (2), and $[Cr^{III}_8Co^{II}_6L_{24}(H_2O)_{12}](ClO_4)_{12}$ (5)

In each case a suitable crystal was selected and mounted on a MITIGEN holder in Paratone oil on an Agilent Technologies SuperNova diffractometer using CuK_α radiation. The crystal was kept at T = 120.01(10) K during data collection. Using Olex2 the structure was solved with the ShelXT structure solution program, using the Direct Methods solution method. The model was refined with version 2014/6 of ShelXL using Least Squares minimisation.[13,14]

The molecular formulae for complexes **1**-**14** are tabulated below for convenience (Table 2.1), and a crystallographic summary with structure refinement details for $[Cr^{III}L_3]$, $[Fe^{III}L_3]$, and complexes **1**-**14** are presented in Tables 2.2, 2.3, 2.4, and 2.5.

Table 2.1 Molecular formulae for complexes **1**-**14**. Additional solvent molecules of crystallisation have been removed from the molecular formulae for clarity.

Complex	Molecular formula
1	$[Cr^{III}_8Cu^{II}_6L_{24}Cl_{12}]$
2	$[Cr^{III}_8Cu^{II}_6L_{24}(H_2O)_{10}(NO_3)_2](NO_3)_{10}$
3	$[Cr^{III}_8Cu^{II}_6L_{24}(H_2O)_{12}](SO_4)_6$
4	$[Cr^{III}_8Co^{II}_6L_{24}Cl_{12}]$
5	$[Cr^{III}_8Co^{II}_6L_{24}(H_2O)_{12}](ClO_4)_{12}$
6	$[Cr^{III}_8Co^{II}_6L_{24}(SCN)_{12}]$
7	$[Cr^{III}_8Ni^{II}_6L_{24}Cl_{12}]$
8	$[Cr^{III}_8Ni^{II}_6L_{24}(H_2O)_{12}](NO_3)_{12}$
9	$[Cr^{III}_8Ni^{II}_6L_{24}(MeCN)_7(H_2O)_5](ClO_4)_{12}$
10	$[Fe^{III}_8Cu^{II}_6L_{24}(H_2O)_4Br_4]Br_8$
11	$[Fe^{III}_8Cu^{II}_6L_{24}(H_2O)_{10}](NO_3)_{12}$
12	$[Fe^{III}_8Co^{II}_6L_{24}(SCN)_{10}(H_2O)_2]Cl_2$
13	$[Fe^{III}_8Ni^{II}_6L_{24}(SCN_{11})Cl]$
14	$[Fe^{III}_8Pd^{II}_6L_{24}]Cl_{12}$

Table 2.2 Crystallographic details for $[Cr^{III}L_3]$, $[Fe^{III}L_3]$, and complexes **1** and **2**.

Complex	$[Cr^{III}L_3]$	$[Fe^{III}L_3]$	1	2
Empirical formula	$C_{27}H_{24}N_3O_6Cr$	$C_{27}H_{24}N_3O_{10}Fe$	$C_{216}H_{192}N_{24}O_{48}Cl_{12}Cr_8Cu_6$	$C_{216}H_{208}N_{36}O_{92}Cr_8Cu_6$
Formula weight	538.49	606.34	5114.56	5325.32
Colour	Red	Red	Green	Dark Red
Shape	Block	Column	Prism	Block
Temperature, K	120.0	100.0	100.0	120.0
Crystal system	Trigonal	Trigonal	Tetragonal	Orthorhombic
Space group	*R*-3	*P*-3	$I4_122$	$Pca2_1$
***a*, Å**	17.6411(3)	14.8322(3)	41.329(14)	38.1763(6)
***b*, Å**	17.6411(3)	14.8322(3)	41.329(14)	31.3516(5)
***c*, Å**	27.0463(4)	7.5892(3)	31.056(10)	29.1087(7)
α, °	90.0	90.0	90.0	90.0
β, °	90.0	90.0	90.0	90.0
γ, °	120.0	120.0	90.0	90.0
Volume, Å^3	7289.3(2)	1445.89(9)	53046(40)	34839.9(10)
Z	12	2	4	4
Density (calculated), mg m^{-3}	1.472	1.393	0.640	1.205
Absorption coefficient, mm^{-1}	0.520	0.581	0.486	3.717
Reflections collected	102466	27017	115032	171353
Unique reflections	5148	2666	23152	33419
Data/restraints/parameters	5148/0/225	2666/0/125	23152/1461/656	33419/1281/3240
Goodness-of-fit	1.199	1.072	0.767	0.983
R_{int}	0.0473	0.0626	0.1250	0.0805
Final R_1	0.0561	0.0655	0.0424	0.0538
Final wR_2	0.1096	0.1855	0.1118	0.1385
CCDC Number	1457380	1522561	1457379	1026379

Table 2.3 Crystallographic details for **3**-**6**.

Complex	3	4	5	6
Empirical formula	$C_{216}H_{216}N_{24}O_{84}S_6Cr_8Cu_6$	$C_{216}H_{192}N_{24}O_{48}Cl_{12}Cr_8Co_6$	$C_{216}H_{216}N_{24}O_{108}Cl_{12}Cr_8Co_6$	$C_{228}H_{192}N_{36}O_{48}S_{12}Cr_8Co_6$
Formula weight	5481.79	5087.00	5481.79	5358.46
Colour	Brown	Dark Orange	Brown	Light Brown
Shape	Block	Block	Plate	Prism
Temperature, K	120.0	100.0	120.0	100.2
Crystal system	Tetragonal	Triclinic	Tetragonal	Tetragonal
Space group	$P4/n$	*P*-1	$P4/n$	$I4_122$
***a*, Å**	28.79166(19)	28.265(4)	30.5293(4)	41.7282(5)
***b*, Å**	28.79166(19)	29.830(4)	30.5293(4)	41.7282(5)
***c*, Å**	24.4854(3)	31.2900(5)	20.7384(4)	30.6665(7)
α, °	90.0	72.023(16)	90.0	90.0
β, °	90.0	71.093(15)	90.0	90.0
γ, °	90.0	63.981(13)	90.0	90.0
Volume, Å^3	20297.4(4)	21995(7)	19328.9(7)	53397.9(18)
Z	2	2	2	4
Density (calculated), mg m^{-3}	0.896	0.812	1.043	0.667
Absorption coefficient, mm^{-1}	2.781	0.526	5.072	0.422
Reflections collected	124342	235211	124556	135815
Unique reflections	16958	73957	9954	23556
Data/restraints/parameters	16958/103/828	73957/3929/2995	9954/4/723	23556/1501/772
Goodness-of-fit	1.525	1.669	1.068	0.780
R_{int}	0.0762	0.0635	0.1317	0.1250
Final R_1	0.1209	0.1495	0.0672	0.0506
Final wR_2	0.3937	0.4388	0.1922	0.1021
CCDC Number	1457378	1457376	1026380	1457377

Table 2.4 Crystallographic details for **7**-**10**.

Complex	7	8	9	10
Empirical formula	$C_{216}H_{192}Cl_{12}N_{24}O_{48}Cr_8Ni_6$	$C_{216}H_{216}N_{24}O_{60}Cr_8Ni_6$	$C_{230}H_{223}N_{31}O_{54}Cr_8Ni_6$	$C_{216}H_{192}N_{24}O_{52}Br_4Fe_8Cu_6$
Formula weight	5085.58	4876.38	5053.64	5103.60
Colour	Brown	Dark Orange	Brown	Red
Shape	Block	Block	Block	Block
Temperature, K	100.0	100.2	100.0	100.0
Crystal system	Triclinic	Monoclinic	Monoclinic	Tetragonal
Space group	*P*-1	$P2_1/n$	$P2_1/n$	*P4/nnc*
***a*, Å**	28.171(16)	25.754(3)	25.788(6)	20.076(3)
***b*, Å**	30.225(16)	41.336(5)	41.606(9)	20.076(3)
***c*, Å**	31.40(2)	43.217(5)	45.869(11)	37.225(3)
***α*, °**	72.27(6)	90.0	90	90.0
***β*, °**	72.08(6)	90.6450(10)	90.785(2)	90.0
***γ*, °**	64.04(6)	90.0	90	90.0
Volume, Å^3	22417(27)	46004(9)	49210(20)	15.003(5)
Z	2	4	4	2
Density (calculated), mg m^{-3}	0.753	0.704	0.682	1.130
Absorption coefficient, mm^{-1}	0.543	0.426	0.412	1.383
Reflections collected	134344	374116	391200	95000
Unique reflections	66105	81102	85136	8612
Data/restraints/parameters	66105/6137/2233	81102/0/2839	85136/0/2641	8612/0/353
Goodness-of-fit	1.632	0.977	1.113	1.123
R_{int}	0.1446	0.1902	0.2374	0.1407
Final R_1	0.2722	0.1251	0.1545	0.0998
Final wR_2	0.5868	0.3344	0.4292	0.3260
CCDC Number				1522563

Table 2.5 Crystallographic details for **11**-**14**.

Complex	11	12	13	14
Empirical formula	$C_{216}H_{208}N_{24}O_{58}Fe_8Cu_6$	$C_{230}H_{200}N_{34}O_{58}S_{10}Cl_{10}Fe_8Co_6$	$C_{227}H_{192}N_{35}O_{48}S_{11}ClFe_8Ni_6$	$C_{216}H_{194}N_{24}O_{54}Cl_4Fe_8Pd_6$
Formula weight	4896.09	5843.71	5365.31	5216.94
Colour	Red	Red	Red	Dark Red
Shape	Prism	Prism	Prism	Prism
Temperature, K	30.0	100.0	100.0	100.0
Crystal system	Orthorhombic	Tetragonal	Tetragonal	Orthorhombic
Space group	*Pcca*	*P4/n*	*P4/n*	*Pcca*
***a*, Å**	29.6051(6)	29.5218(3)	29.644(12)	30.4249(5)
***b*, Å**	31.3962(4)	29.5218(3)	29.644(12)	31.3338(4)
***c*, Å**	38.0783(6)	26.6262(5)	26.851(10)	38.6462(5)
***α*, °**	90.0	90.0	90.0	90.0
***β*, °**	90.0	90.0	90.0	90.0
***γ*, °**	90.0	90.0	90.0	90.0
Volume, Å^3	35393.3(10)	23205.8(7)	23596(21)	36842.5(9)
Z	4	2	2	4
Density (calculated), mg m^{-3}	0.919	0.836	0.755	0.941
Absorption coefficient, mm^{-1}	0.667	0.598	0.567	0.669
Reflections collected	463483	152412	91153	197847
Unique reflections	31234	20482	21002	42278
Data/restraints/parameters	31234/99/1425	31165/1590/820	21002/1661/791	42278/2736/1418
Goodness-of-fit	1.085	1.257	1.107	1.077
R_{int}	0.2527	0.0460	0.0862	0.0780
Final R_1	0.1122	0.1041	0.1010	0.0790
Final wR_2	0.3358	0.3552	0.3280	0.2685
CCDC Number	1522564	1522566	1522565	1522562

2.3 Results and Discussion

For clarity, the results and discussion section will be separated into the two families of coordination cubes, namely the $[Cr^{III}_8M^{II}_6L_{24}]^{n+}$ complexes, and the $[Fe^{III}_8M^{II}_6L_{24}]^{n+}$ complexes.

2.3.1 $[Cr^{III}_8M^{II}_6L_{24}]^{n+}$ Coordination Cubes

2.3.1.1 Solid-State Structural Descriptions

The heterometallic cubes $[Cr^{III}_8Cu^{II}_6L_{24}Cl_{12}]$ (**1**), $[Cr^{III}_8Cu^{II}_6L_{24}(H_2O)_{10}(NO_3)_2](NO_3)_{10}$ (**2**), $[Cr^{III}_8Cu^{II}_6L_{24}(H_2O)_{12}](SO_4)_6$ (**3**), $[Cr^{III}_8Co^{II}_6L_{24}Cl_{12}]$ (**4**), $[Cr^{III}_8Co^{II}_6L_{24}(H_2O)_{12}](ClO_4)_{12}$ (**5**), $[Cr^{III}_8Co^{II}_6L_{24}(SCN)_{12}]$ (**6**), $[Cr^{III}_8Ni^{II}_6L_{24}Cl_{12}]$ (**7**), $[Cr^{III}_8Ni^{II}_6L_{24}(H_2O)_{12}](NO_3)_{12}$ (**8**), and $[Cr^{III}_8Ni^{II}_6L_{24}(MeCN)_7(H_2O)_5](ClO_4)_{12}$ (**9**), were all prepared in a similar manner by the reaction of $[Cr^{III}L_3]$ with the corresponding M^{II} salt, in a range of solvents. Each complex is described by a *pseudo*-cubic $[Cr^{III}_8M^{II}_6L_{24}]^{n+}$ structure where the Cr^{III} ions occupy the corners of the cube and the M^{II} ions occupy the faces, approximately positioned 1.17-1.95 Å above the $Cr^{III}\cdots Cr^{III}\cdots Cr^{III}\cdots Cr^{III}$ plane (Fig 2.2). The approximate dimensions of the *pseudo*-cubes are $Cr^{III}\cdots M^{II}$ (8.75-9.06 Å), $Cr^{III}\cdots Cr^{III}$ (11.42-13.00 Å), and $M^{II}\cdots M^{II}$ (14.87-16.52 Å).

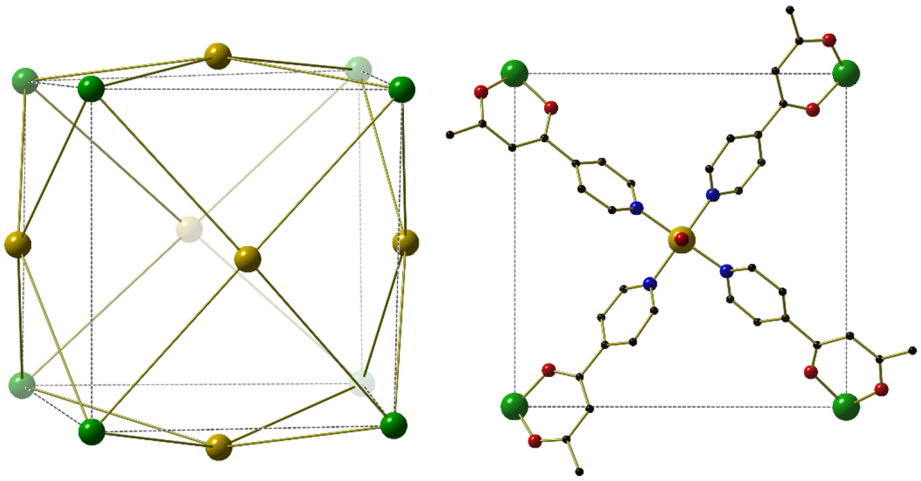

Figure 2.2 Metallic skeleton of a $[Cr^{III}_8M^{II}_6]^{n+}$ complex (left), with a representation of one of the six faces of the cube (right), which highlights the coordination geometry of the M^{II} ion. Hydrogen atoms and anions have been removed for clarity. Colour code: Cr^{III} – Green, M^{II} – Gold, N – Blue, O – Red, C – Black.

The free metalloligand is six-coordinate, and is of regular $\{CrO_6\}$ octahedral geometry, with Cr^{III}-O distances 1.95 Å, and O-Cr^{III}-O *cis*/*trans* angles in the range 88.41-91.42° and 179.52-179.58°, respectively. Upon coordination to the M^{II} ions, there is a considerable distortion to the geometry of the metalloligand, with the O-Cr^{III}-O *cis*/*trans* angles widening to 82.72-97.01° and 171.39-179.57°, respectively.

Complexes **1**, **2**, and **3** (Fig. 2.3) were prepared by the combination of $[Cr^{III}L_3]$ with $CuCl_2{\cdot}2H_2O$, $Cu(NO_3)_2{\cdot}3H_2O$, or $Cu(SO_4){\cdot}5H_2O$, respectively. The Cu^{II} sites in all three structures are described by a six-coordinate Jahn-Teller distorted $\{Cu^{II}N_4O_2\}$ or $\{Cu^{II}N_4Cl_2\}$ coordination geometry (Cu^{II}-N 1.97-2.11 Å), with the Cl-Cu^{II}-Cl or O-Cu^{II}-O vector (Cu^{II}-Cl ≈2.83 Å or Cu^{II}-O ≈2.53 Å, respectively), describing the elongated axis (d_{z2}), perpendicular to the equatorial $Cu^{II}N_4$ plane (d_{x2-y2}) in the face of the cube.

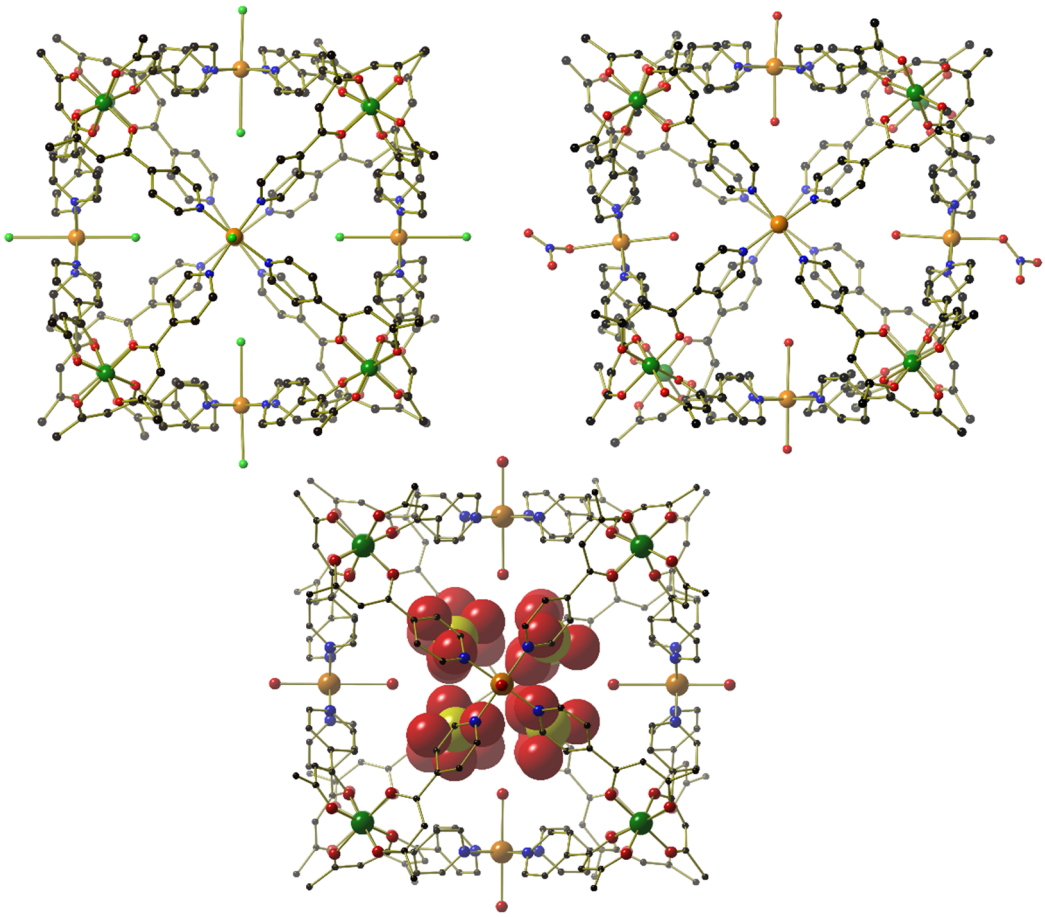

Figure 2.3 Structure of **1** (left), **2** (right), and **3** (bottom). Hydrogen atoms and some counterions have been removed for clarity. Colour code: Cr^{III} – Medium Green, Cu^{II} – Orange, Cl^- – Bright Green, S – Yellow, N – Blue, O – Red, C – Black.

Complex **1** is neutral, with twelve coordinating chloride ions located on the axial positions of the Cu^{II} ions. The neighbouring cubes interact through a series of close inter-cluster contacts between the L^- ligands: H_2C-H···Cl ≈2.73 Å, Ar-H···O ≈2.36 Å and H-C···H-CH_2 ≈2.85 Å. While complex **1** is neutral, complexes **2** and **3** are 10+ and 12+, respectively. Complex **2** has ten water molecules coordinated to the Cu^{II} ions, with the remaining two sites, on opposing sides of the cube, occupied by coordinated nitrate ions. The anions link neighbouring cubes, creating a formation of a square sheet of cubes in the *bc*-plane (Fig. 2.4). These anions also interact with the aromatic system of the pyridyl-groups, the shortest distance being 2.53 Å. The remaining anions and solvent

molecules of crystallisation are located both within the cavity of the cage, and within the void spaces between cubes. Complex **3** has twelve water molecules coordinated to the Cu^{II} ions, with six charge balancing sulfate ions, four located inside, and two located outside, the cube (Fig. 2.4). The external sulfate ions link the cubes along the *c*-axis and hydrogen bond to the water molecules on the Cu^{II} ions, with HO-H···O-SO_3 distances in the range 1.76-2.30 Å.

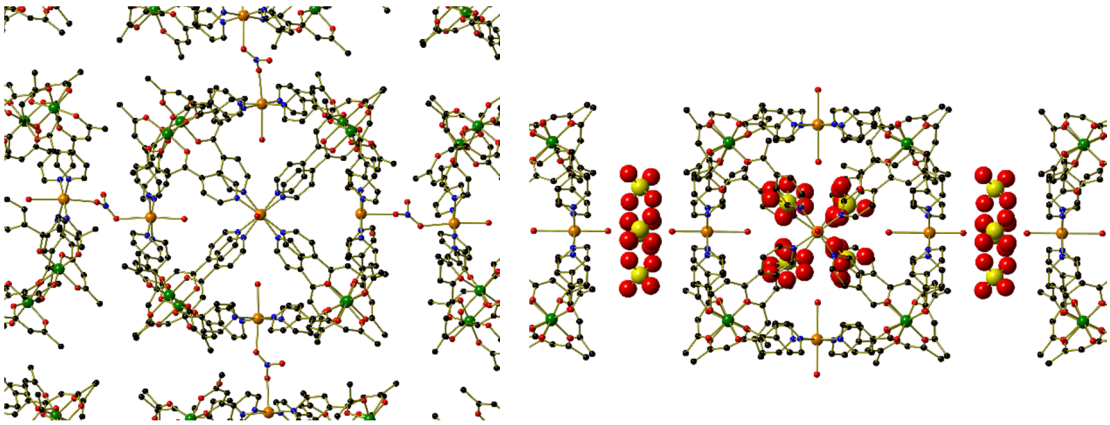

Figure 2.4 Example of how the anions link neighbouring cages in **2** (left), and **3** (right). Hydrogen atoms and some counterions have been removed for clarity. Colour code: Cr^{III} – Green, Cu^{II} – Orange, S – Yellow, N – Blue, O – Red, C – Black.

Complexes **4**, **5**, and **6** (Fig. 2.5), were prepared by the combination of $[Cr^{III}L_3]$ with $CoCl_2$, $Co(ClO_4)_2{\cdot}6H_2O$, or $Co(SCN)_2$ respectively, and are described by an octahedral Co^{II} ion located on the face of the cube, with Co^{II}-N distances in the range 2.09-2.26 Å. Complexes **4** and **6** are neutral, with coordinating chloride (Co^{II}-Cl ≈2.45 Å) or thiocyanate ions (Co^{II}-N ≈2.06 Å) located in the axial positions of Co^{II}. Complex **5** is 12+, with twelve water molecules occupying the axial positions of Co^{II} and twelve charge balancing perchlorate anions located both inside and outside the cavity. The closest inter-cluster contacts for **4**-**6** are between the L^- ligands of neighbouring cubes: Ar-H···Cl ≈2.73 Å, H_2C-H···Cl ≈2.86 Å, and C-H···Cl ≈2.65 Å for **4**; Ar-H···O ≈2.32 Å and H_2C-H···CHC_4H_4N ≈2.84 Å for **5**; Ar-H···O ≈2.34 Å and Ar-H···CH_3 ≈2.81 Å for **6**.

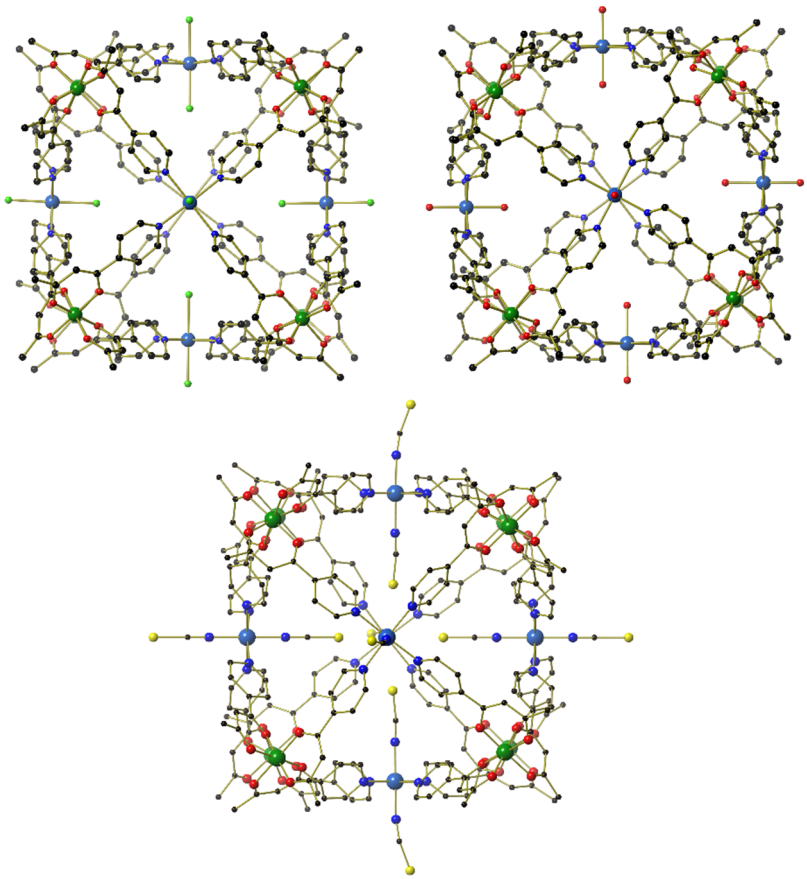

Figure 2.5 Structure of **4** (left), **5** (right), and **6** (bottom). Hydrogen atoms and some counterions have been removed for clarity. Colour code: Cr^{III} – Medium Green, Co^{II} – Royal Blue, Cl^- – Bright Green, S – Yellow, N – Blue, O – Red, C – Black.

Complexes **7**, **8**, and **9** (Fig. 2.6) were prepared by the combination of $[Cr^{III}L_3]$ with $NiCl_2$, $Ni(NO_3)_2{\cdot}6H_2O$, or $Ni(ClO_4)_2{\cdot}6H_2O$ respectively, and are described by an octahedral Ni^{II} ion located on the face of the cube with Ni^{II}-N distances in the range 2.05-2.18 Å. For **7**, the axial positions of the Ni^{II} ions are occupied by twelve chloride anions (Ni^{II}-Cl ≈2.47 Å), making complex **7** neutral. Conversely, complexes **8** and **9** both have a charge of 12+, with water or acetonitrile/water molecules occupying the axial positions of the Ni^{II} ions, respectively. The charge balancing nitrate ions for **8**, and perchlorate ions for **9**, are located both within the cavity and in the void spaces between cubes. Again, there are several close inter-cluster contacts between neighbouring cubes: Ar-H···Cl ≈2.69 Å and C-H···Cl ≈2.76 Å for **7**; Ar-H···O ≈2.47 Å and C-H···O ≈2.72 Å for **8**; H_2C-H···O ≈2.49 Å and H_2O···H-CH_2 ≈2.66 Å for **9**.

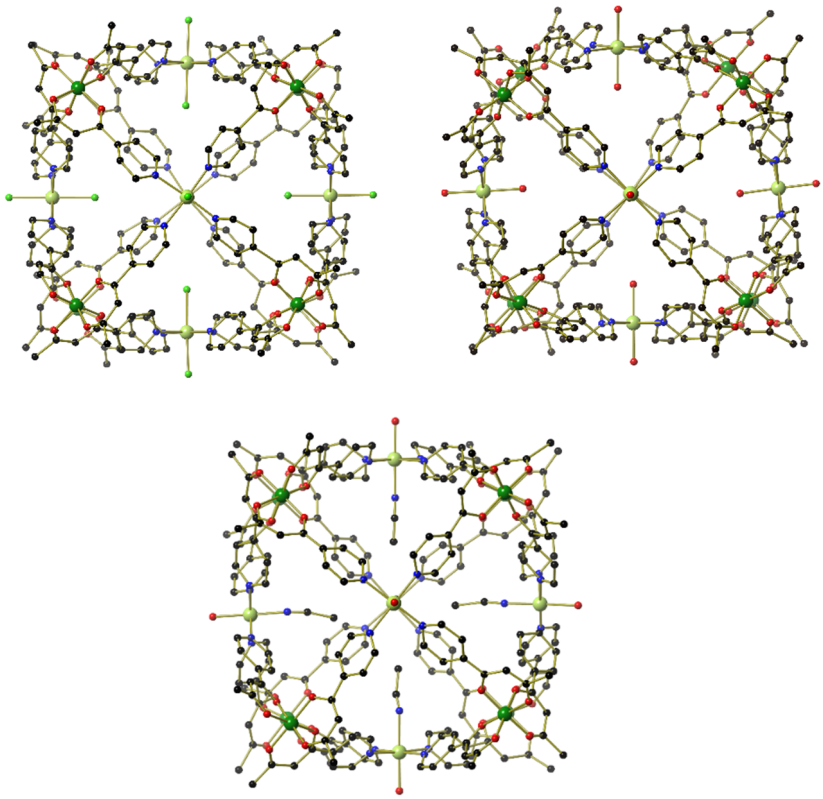

Figure 2.6 Structure of **7** (left), **8** (right), and **9** (bottom). Hydrogen atoms and some counterions have been removed for clarity. Colour code: Cr^{III} – Medium Green, Ni^{II} – Light Green, Cl^{-} – Bright Green, S – Yellow, N – Blue, O – Red, C – Black.

2.3.1.2 Magnetic Studies

SQUID Magnetometry

Quantitatively analysing the magnetic behaviour of such large heterometallic species using traditional matrix diagonalisation techniques is non-trivial, and often impossible, due to the enormous dimensions of the associated spin-Hamiltonian matrices. The associated matrices of complexes **1**-**3** are calculated to be 4,194,304, a value that increases exponentially for complexes **4**-**9** due to the additional terms introduced by the anisotropic Co^{II} or Ni^{II} ions present. Even the total spin, *S*, block matrices used in approaches based on Irreducible Tensor Operator algebra are of larger dimension than what is realistic for numerical matrix diagonalisation. In order to model these complexes therefore, we have had to employ computational techniques known in theoretical nuclear physics as statistical spectroscopy,[16] a technique that exploits the moments of the Hamiltonian to calculate relevant thermodynamic properties.

The dc (direct current) molar magnetic susceptibility, χ_M, of polycrystalline samples of **1**-**6** and **8** were measured in an applied magnetic field, B, of 0.1 T, over the 5-300 K temperature, T, range. The experimental results are shown in Fig. 2.7 in the form of the $\chi_M T$ product, where $\chi_M = M/B$, and M is the magnetisation of the sample.

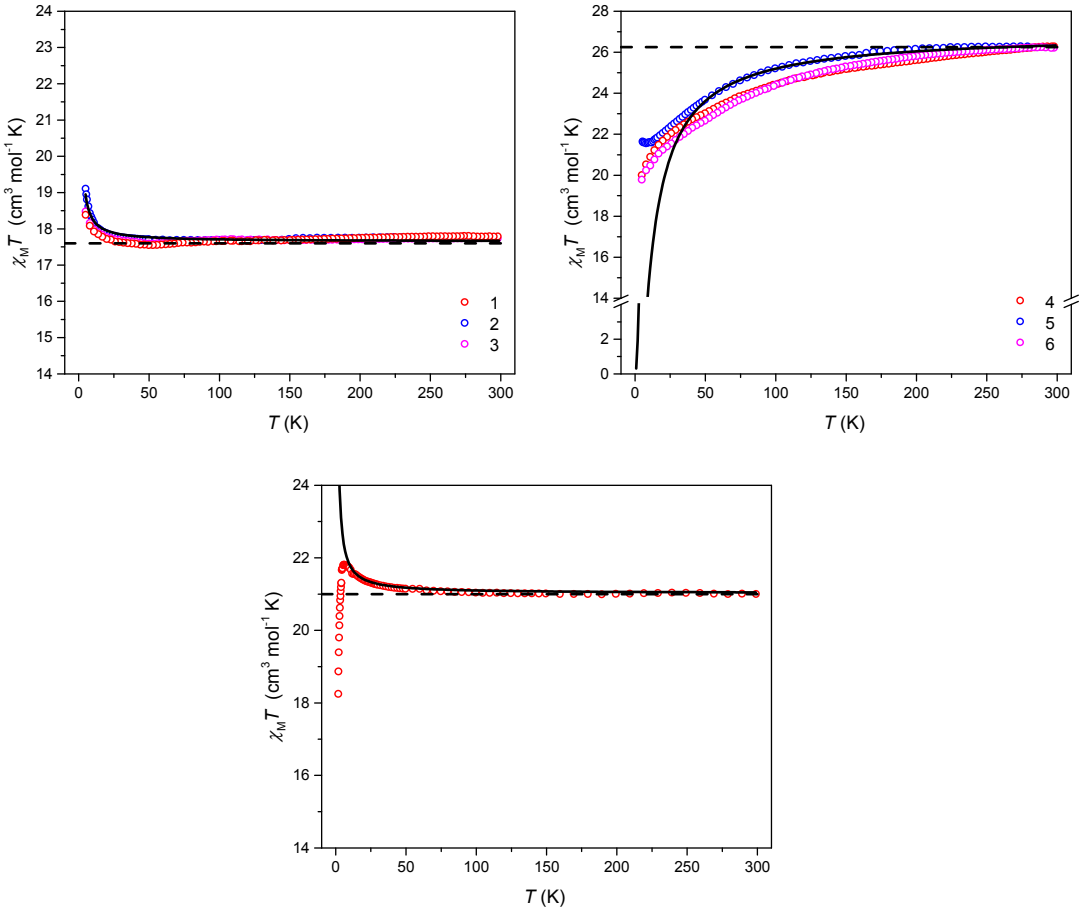

Figure 2.7 Plot of $\chi_M T$ vs T for **1**-**3** (left), **4**-**6** (right), and **8** (bottom), with experimental data (•), the sum of the Curie constants of uncorrelated ions (---), and the best-fit data (**-**).

Due to the loss of lattice solvent during the evacuation of the sample chamber of the SQUID magnetometer, leading to an uncertainty in the molar mass of the measured sample, the 300 K $\chi_M T$ products of **1**-**3**, **4**-**6**, and **8** were scaled to values 17.60 cm^3 mol^{-1} K, 26.25 cm^3 mol^{-1} K, and 21.00 cm^3 mol^{-1} K, respectively. These are the expected values from the sum of Curie constants for [$Cr^{III}_8Cu^{II}_6$], [$Cr^{III}_8Co^{II}_6$], and [$Cr^{III}_8Ni^{II}_6$] units, respectively, with $g_{Cr} = g_{Cu} = g_{Co} = g_{Ni} = 2.0$, where g_{Cr}, g_{Cu}, g_{Co}, and g_{Ni} are the g-factors of Cr^{III}, Cu^{II}, Co^{II}, and Ni^{II}, respectively. It should be noted that these rescaled values have maximum deviations of the order of 15 % from the unscaled ones.

Upon cooling, the values of $\chi_M T$ for **1**-**3** remain essentially constant down to approximately 25 K, where they begin to increase, reaching a maximum of ≈19.00 cm^3 mol^{-1} K at 5 K. This behaviour is indicative of weak ferromagnetic exchange interactions between the Cr^{III} and Cu^{II} ions. There

are also ferromagnetic exchange interactions between the Cr^{III} and Ni^{II} ions in **8**, with an increase in the value of $\chi_M T$ observed at approximately 60 K, reaching a maximum of ≈21.83 $cm^3\ mol^{-1}\ K$ at 6 K. The decrease in the value of $\chi_M T$ below 6 K is attributed to antiferromagnetic intermolecular interactions between neighbouring cages and/or zero-field splitting of the Ni^{II} ions. The behaviour of complexes **4**-**6** initially appears different to that of **1**-**3** and **8**, with a continuous decrease in the value of $\chi_M T$ upon cooling. For complex **5**, the value of $\chi_M T$ reaches a plateau value of 21.50 $cm^3\ mol^{-1}\ K$ at 8 K, before slightly increasing upon further cooling to 21.65 $cm^3\ mol^{-1}\ K$ at 5 K. Analysis of this behaviour is made complicated both by weak exchange interactions and the crystal-field splitting of the Co^{II} ion. One can assume that the low temperature increase in the value of $\chi_M T$ for **5** is indicative of ferromagnetic Cr^{III}-Co^{II} interactions and that the decrease in the value of $\chi_M T$ is due to the highly anisotropic Co^{II} ion. The tetragonal symmetry crystal field of the $\{Co^{II}(py)_4(H_2O)_2\}$ site removes the degeneracy of the $^4T_{1g}$ term breaking it into ^4E and $^4A_2$ terms, with the latter lower in energy.[17,18] Second-order spin-orbit coupling (SOC) then further removes the degeneracy of the $^4A_2$ term breaking it into two Kramers doublets, the energy splitting of which can be parameterised as a zero-field splitting (D) of the of the $^4A_2$ term (Fig 2.8). The fact that the high temperature $\chi_M T$ product of **2** agrees well with the expected spin-only value, supports the dominance of the axial crystal field splitting over first-order SOC.

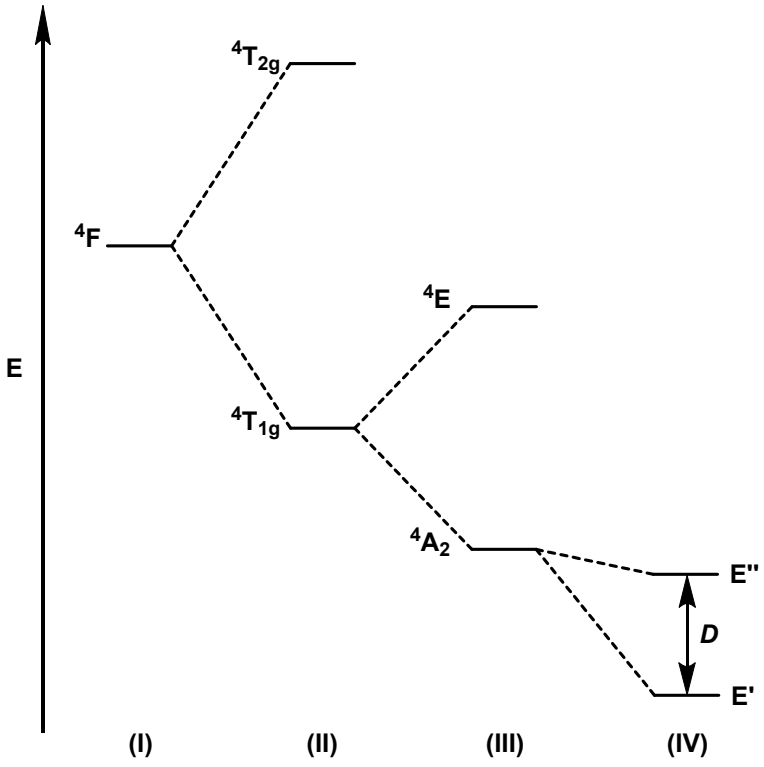

Figure 2.8 Scheme showing the: (I) ground state of the free Co^{II} ion, (II) an octahedral field splitting the ground state, (III) a tetragonal distortion of the octahedral field splitting the ground state further, and (IV) second order spin-orbit coupling giving rise to Kramers doublets, the energy splitting of which is parameterised by the zero-field splitting parameter, *D*.

Complexes **1**-**3**, **4**-**6**, and **7**-**9** are structurally similar with comparable magnetic properties and therefore we need only consider the quantitative interpretation of one of each of the complex-type (**2**, **5**, and **8**).

In order to quantitatively interpret the magnetic properties of **2** we can apply the isotropic spin-Hamiltonian (1):

$$\widehat{H}_{iso} = -2J_{\text{Cr-M}} \sum_{\text{all Cr–M pairs}} \widehat{S}_{\text{Cr}} \cdot \widehat{S}_{\text{M}} + \mu_{\text{B}} Bg \sum_{\text{i}} \widehat{S}_{\text{i}}^{Z} \qquad (1)$$

with i running over all constitutive metal centres, g the isotropic g-factor common to both Cr^{III} and M^{II}, $\hat{S}$ a spin-operator, $J_{\text{Cr-M}}$ the isotropic exchange parameter between Cr^{III} and M^{II} centres, and μ_{B} the Bohr magneton. We can neglect any $J_{\text{Cr-Cr}}$ and $J_{\text{M-M}}$ terms as these centres are not connected as first neighbours.

We calculate the temperature-dependent magnetic susceptibility of **2** by use of the Van Vleck equation (2), derived from (1):

$$\chi = \frac{N_A g^2 \mu_B^2}{k_B T} \frac{\sum_S (2S+1) \frac{S(S+1)}{3} \exp(-\frac{E_S}{k_B T})}{\sum_S (2S+1) \exp(-\frac{E_S}{k_B T})} \qquad (2)$$

with N_{A} Avogadro's number, k_{B} the Boltzmann constant, and T the temperature.

We approximate the energy dependence of the $(2S+1)$ factor in the denominator by a continuous density of states, $\rho(\text{E})$. Similarly, we approximate the energy dependence of the $(2S+1)S(S+1)/3$ factor on the numerator, by a continuous density, $\rho_{\text{C}}(\text{E})$, which we designate the Curie-constant density, thus obtaining (3):

$$\chi = \frac{N_A g^2 \mu_B^2}{k_B T} \frac{\sum_S \rho_{c(E)} \exp(-\frac{E_S}{k_B T})}{\sum_S \rho_{(E)} \exp(-\frac{E_S}{k_B T})} \qquad (3)$$

These two densities may be obtained from moments of an appropriate Hamiltonian, here (1), with the moments related to the traces of powers of the Hamiltonian.[19] The density $\rho(\text{E})$ is determined from the moments of a Hamiltonian containing only the Heisenberg terms of (1), whereas the density $\rho_{\text{C}}(\text{E})$ is determined from the bivariate moments of (1), *i.e.* those obtained from a Hamiltonian containing both Heisenberg and Zeeman terms. Once these moments, up to order 14 in our case, have been computed, the densities are conveniently determined.[20–22]

Using this approach, and by successive simulations of the temperature dependence of the $\chi_{\text{M}}T$ product of complex **2**, $J_{\text{Cr-Cu}}$ was determined to be 0.09 cm^{-1}, with a common isotropic g-factor of

g = 2.021. These results are in excellent agreement with the experimental data, as validated by the calculation of the $\chi_M T$ product of **2** by full matrix diagonalization of the blocked spin-Hamiltonian matrix using the determined spin-Hamiltonian parameters (solid black line in Fig. 2.7). Similarly good agreement was obtained with complex **8**, with $J_{Cr\text{-}Ni}$ determined to be 0.045 cm^{-1}, with an isotropic g-factor of g = 2.0. Although Ni^{II} is anisotropic, the influence of zero-field splitting only takes effect in the very low temperature region, and thus the use of (1) is enough to model the exchange interactions between Cr^{III} and Ni^{II} ions.

For complex **5**, we again used (1) in order to fit the experimental data, obtaining an exchange parameter of $J_{Cr\text{-}Co}$ = -0.55 cm^{-1}, with a common isotropic g-factor of g = 2.0. These parameters appear to agree well with the experimental data down to approximately 45 K, where they begin to deviate significantly. This deviation could be attributed to the lack of anisotropy terms in (1) and therefore we can apply a slightly different model to help fit the magnetic data, where $J_{Cr\text{-}Co}$ = 0 and $D_{Co} \neq 0$. In this limiting model we can neglect the anisotropy of Cr^{III}, D_{Cr}, as this is usually of the order of 0.1 cm^{-1}.[23]

From the experimental $\chi_M T$ product of **5** we have subtracted the calculated $\chi_M T$ value (15 cm^3 mol^{-1} K) for eight uncoupled Cr^{III} ions and divided the result by six, to generate the $\chi_M T$ curve for an "isolated" Co^{II} site (Fig. 2.9).

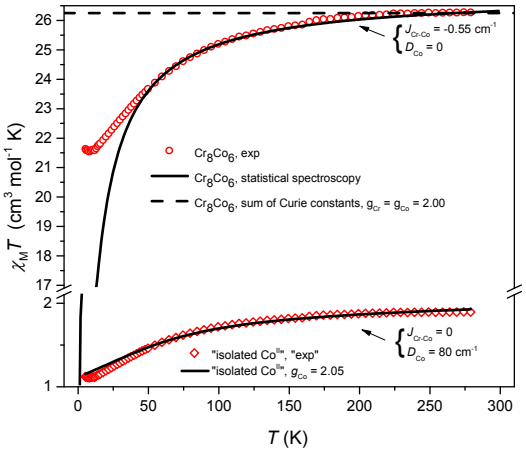

Figure 2.9 Plot of $\chi_M T$ vs T for **5** (top) and an "isolated Co^{II} ion" (bottom), with experimental data (•), the sum of the Curie constants of uncorrelated ions (---), and the best-fit data (**-**).

We attempted to fit the $\chi_M T$ product of the "isolated" Co^{II} site to the anisotropic single-ion spin-Hamiltonian (4):

$$\hat{H}_{aniso} = D_{Co}\left[\hat{S}_{Co}^2 - S_{Co}(S_{Co}+1)/3\right] + \mu_B B g_{Co} \hat{S}_{Co} \qquad (4)$$

with $S_{Co} = 3/2$, reflecting the $^4A_2$ ground term of Co^{II}.

A reasonable, but not perfect, agreement is found for $g_{Co} = 2.0$ and $D_{Co} = 80$ cm^{-1} (Fig. 2.9). With these parameters only the ground ($|m| = 1/2$) Kramers doublet would be populated at low temperatures. Given that the observed low temperature $\chi_M T$ value for an "isolated" Co^{II} is of the order of 1.1 cm^3 mol^{-1} K, the calculated low temperature paramagnetic $\chi_M T$ limit for **5** would be about 21.6 cm^3 mol^{-1} K, in good agreement with the observed low temperature plateau value of 21.5 cm^3 mol^{-1} K, at 8 K. In short, we can assign the initial decrease in the $\chi_M T$ product of **5** to the large zero-field splitting of the Co^{II} ions, with the low temperature ($T < 10$ K) plateau/rise ascribed to weak ferromagnetic exchange interactions between the Cr^{III} and Co^{II} ions.

Variable-temperature-and-variable-field (VTVB) magnetisation studies of complexes **2** and **5** at 2 K (Fig. 2.10) are consistent with weak exchange in both cases. For **2**, the saturation magnetic moment of 30.8 μ_B at 5 T and 2 K, is as expected for full spin alignment. In the case of **5**, the magnetic moment is also 30.8 μ_B at 5 T and 2 K. If only the lower Kramers doublet of Co^{II} (which has $g_{eff} = g_x = 4, g_y = 4, g_z = 2$) is populated in this regime ($D_{Co} >> kT$), then the theoretical maximum magnetisation is 34 μ_B, in reasonable agreement with the experimental data, given the simplicity of the model.

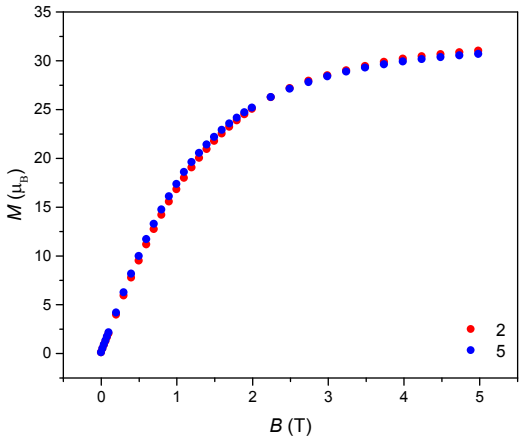

Figure 2.10 VTVB magnetisation data of **2** (•) and **5** (•) at 2 K and in the field ranges 0 to 5 T.

EPR Spectroscopy

The nature of the weak exchange interactions in complexes **2** and **5** was further probed by Q- and W-band EPR spectroscopy (34 and 94 GHz, respectively). Measurements of [$Cr^{III}L_3$] at 5 K give spectra relating to an $S_{Cr} = 3/2$ ($g_{Cr} = 1.97$), with near axial zero-field splitting parameters of D_{Cr} = -0.55 and E_{Cr} = 0.025 cm^{-1}, with $|E/D|$ = 0.045. These values are in the range found for other [Cr(diketonate)$_3$] complexes (Fig. 2.11 and 2.12; simulations were carried out using the EasySpin program, with a Gaussian linewidth of 60 mT, and a 10% D-strain).[23,24]

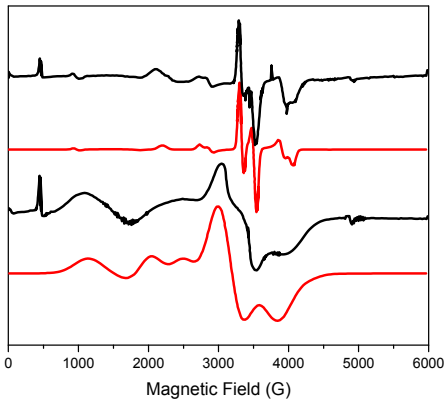

Figure 2.11 W-band EPR spectra of [$Cr^{III}L_3$] (top) and **5** (bottom) in the solid-state and 5 K (**-**). Calculated spectra (**-**) for: (i) S_{Cr} = 3/2, g_{Cr} = 1.97, D_{Cr} = +0.55 and E_{Cr} = 0.025 cm^{-1} (top), (ii) for a Cr^{III}-Co^{II} dimer, with S_{Cr} = S_{Co} = 3/2, g_{Cr} = 1.97, g_{Co} = 2.05, D_{Cr} = -0.55 cm^{-1}, E_{Cr} = 0.025 cm^{-1}, D_{Co} = +80 cm^{-1}, $J_{Cr\text{-}Co}$ = -0.3 cm^{-1} and an angle between the D_{zz}^{Cr} and D_{zz}^{Co} vectors of 54.7° (bottom; 400 mT Gaussian linewidth).

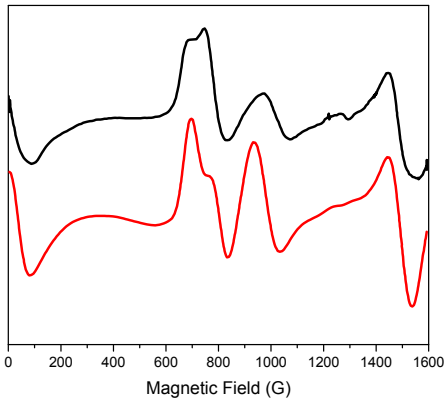

Figure 2.12 Q-band EPR spectra of [$Cr^{III}L_3$] in the solid-state and 5 K (**-**). Calculated spectra (**-**) with S_{Cr} = 3/2, g_{Cr} = 1.97, D_{Cr} = +0.55 and E_{Cr} = 0.025 cm^{-1}, with a 60 mT Gaussian linewidth and a 10% D-strain.

Spectra of **2** at 5 K are severely broadened compared with [$Cr^{III}L_3$], with linewidths approaching 400 mT (Fig. 2.13), consistent with $|J_{Cr\text{-}Cu}|$ being smaller than $|D_{Cr}|$. The lack of structure prevents any further analysis.

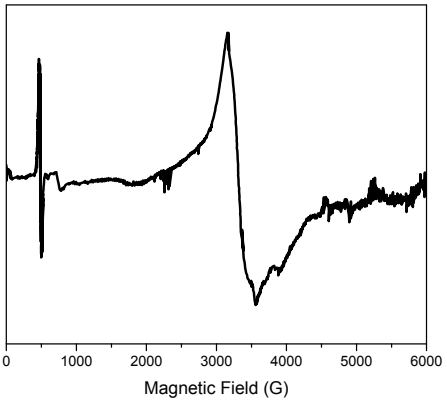

Figure 2.13 W-band EPR spectrum of **2** in the solid-state at 5 K.

Spectra of **5** are also broadened, but structured (Fig. 2.11), and resemble those of $[Cr^{III}L_3]$, with noticeable shifts in resonance fields and new resonances at ≈1400 mT (at W-band) arising from the Co^{II} sites. This implies $|J_{Cr\text{-}Co}|$ is smaller than $|D_{Cr}|$. The matrix dimension of **5** is far too large for simulation using the full $[Cr^{III}_8Co^{II}_6]$ spin system, while the weak exchange limit precludes handling the problem *via* low energy subspace methods.[25] Hence, the modelling of the spectra of **5** has been attempted through considering the system as a simple Cr^{III}-Co^{II} dimer, where the parameters for Cr^{III} are defined experimentally from $[Cr^{III}L_3]$, and those for Co^{II} are fixed from the "isolated" $S_{Co} = 3/2$ Co^{II} model (Fig. 2.9). We also fixed the relative orientation of the principal axes of the $\mathbf{D}_{Cr}$ and $\mathbf{D}_{Co}$ zero-field splitting tensors to 54.7°, being the angle between a C_4 (face-normal, defining the unique axis of Co^{II} in **5**) and C_3 (body-diagonal, defining the unique axis of Cr^{III} in **5**) axes of a cube. Thus, the only variable is $J_{Cr\text{-}Co}$. The calculated spectra are very sensitive to small $J_{Cr\text{-}Co}$ (e.g., Fig. 2.14), and we can reproduce the experimental resonances reasonably with $J_{Cr\text{-}Co} = -0.3$ cm^{-1} (Fig. 2.11, bottom, and 2.14). Note that the determined $J_{Cr\text{-}Co}$ value is *not* that of **5** but the one for the fictitious Cr^{III}-Co^{II} dimer. The isotropic exchange parameter, $J_{Cr\text{-}Co}$, of **5** is likely smaller in magnitude.

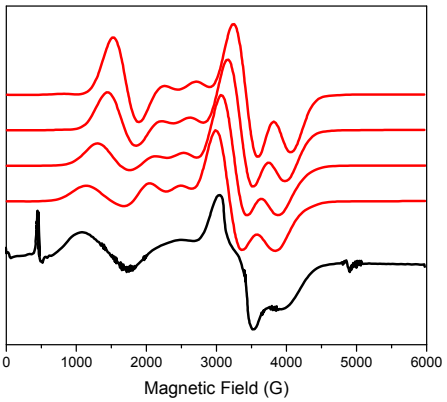

Figure 2.14 W-band EPR spectrum of **5** in the solid-state at 5 K (-), and calculated spectra (-) for a Cr^{III}-Co^{II} dimer, with $S_{Cr} = S_{Co} = 3/2$, $g_{Cr} = 1.97$, $g_{Co} = 2.05$, $D_{Cr} = -0.55$ cm^{-1}, $E_{Cr} = 0.025$ cm^{-1}, $D_{Co} = +80$ cm^{-1} and an angle between the D_{zz}^{Cr} and D_{zz}^{Co} vectors of 54.7°. From top-to-bottom, $J_{Cr\text{-}Co} = 0$, -0.1, -0.2 and -0.3 cm^{-1}. A Gaussian linewidth of 400 mT was used.

2.3.1.3 Volume calculations

The $Cr^{III}\cdots Cr^{III}$ distances between nearest neighbours along the edges of the cubes measure approximately 12 Å, creating an internal volume of ≈1400 $Å^3$. Volume calculations through the use of the *³V Volume Assessor* program confirm this,[26] and a representation of the available internal cavity space in **3** is shown as the purple surface in Fig. 2.15.

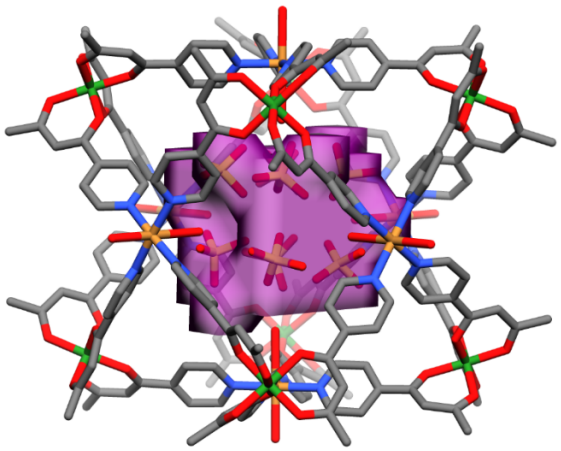

Figure 2.15 Representation of the available internal cavity space in complex **3** (purple), calculated using an outer probe of 8.0 Å and an internal probe of 2 Å.[26] Hydrogen atoms and external counterions have been removed for clarity. Colour code: Cr^{III} – Green, Cu^{II} – Orange, S – Yellow, N – Blue, O – Red, C – Grey.

The binding of molecules of suitable dimensions inside the cage should be expected when the packing coefficient is approximately 0.55,[27] suggesting a total guest volume of ≈770 $Å^3$ could be accommodated. Indeed, this is in accordance with the encapsulation of four sulfate anions, with total volume of 668 $Å^3$, inside the cavity of complex **3**. It is envisaged that encapsulation of magnetic and/or redox-active guests could allow for control over (switching on and off) magnetic exchange interactions between metal ions in the host framework and between the host and guest(s). For this reason encapsulation of magnetic and redox active anions, such as ReX_2^{2-} (X = Cl, Br) and $Mo_6O_{19}^{2-}$, respectively, were attempted. Unfortunately, even though the crystal colour and morphology were different from that of the empty cages, the large nature of the "host-guest adducts" meant that the resolution of the diffraction was very poor, and thus no structure could be determined.

2.3.2 $[Fe^{III}_8M^{II}_6L_{24}]^{n+}$ Coordination Cubes

2.3.2.1 Solid-State Structural Descriptions

The heterometallic cubes $[Fe^{III}_8Cu^{II}_6L_{24}(H_2O)_{10}Br_4]Br_8$ (**10**), $[Fe^{III}_8Cu^{II}_6L_{24}(H_2O)_{10}](NO_3)_{12}$ (**11**), $[Fe^{III}_8Co^{II}_6L_{24}(H_2O)_2(SCN)_{10}]Cl_2$ (**12**), $[Fe^{III}_8Ni^{II}_6L_{24}Cl(SCN)_{11}]$ (**13**), and $[Fe^{III}_8Pd^{II}_6L_{24}]Cl_{12}$ (**14**), were all prepared in a similar manner by the reaction of $[Fe^{III}L_3]$ with the corresponding M^{II} salt, in a range of solvents. Each complex is described by a *pseudo*-cubic $[Fe^{III}_8M^{II}_6L_{24}]^{n+}$ structure analogous to that of the $[Cr^{III}_8M^{II}_6L_{24}]^{n+}$ structures, where the Fe^{III} ions occupy the corners of the cube, and the M^{II} ions occupy the faces. The free metalloligand is of regular $\{FeO_6\}$ octahedral geometry, with Fe^{III}-O distances 1.98 Å, and O-Fe^{III}-O *cis*/*trans* angles in the range 87.02-94.21° and 174.13-174.18° respectively. Upon coordination to the M^{II} ions the metalloligand distorts, with O-Fe^{III}-O *cis*/*trans* angles in the ranges 85.40-96.82° and 170.86-176.65°, respectively.

Complexes **10** and **11** (Fig. 2.16) are of a $[Fe^{III}_8Cu^{II}_6L_{24}]^{n+}$ structure-type and were prepared from the combination of $[Fe^{III}L_3]$ with $CuBr_2$ or $Cu(NO_3)_2{\cdot}3H_2O$, respectively. Analogous to the $[Cr^{III}_8Cu^{II}_6L_{24}]^{n+}$ structures, the Cu^{II} ions are Jahn-Teller active, with elongation of the axis (d_{z^2}), perpendicular to the $Cu^{II}N_4$ plane ($d_{x^2-y^2}$) in the face of the cube (Cu^{II}-N ≈2.04 Å).

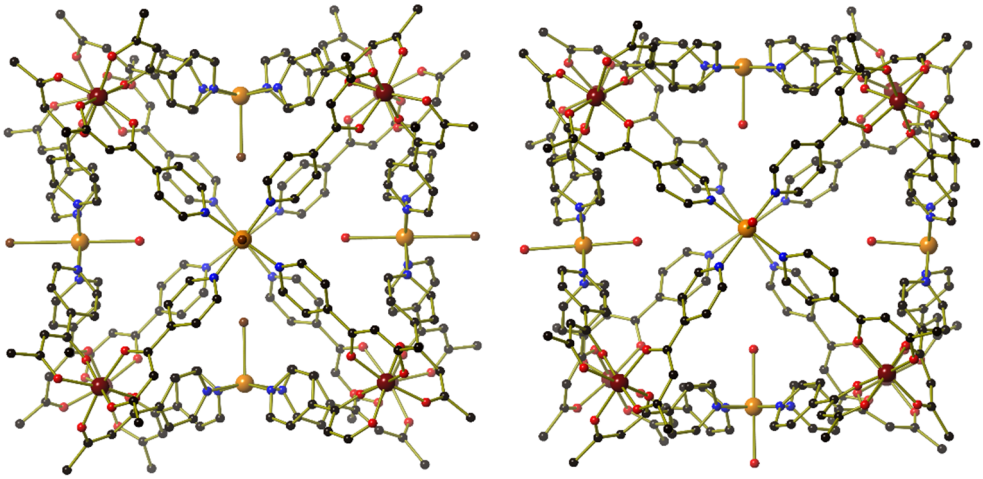

Figure 2.16 Structure of **10** (left) and **11** (right). Hydrogen atoms and some counterions have been removed for clarity. Colour code: Fe^{III} – Maroon, Cu^{II} – Orange, Br^- – Brown, N – Blue, O – Red, C – Black.

Complex **10** is 8+, with two internally (Cu^{II}-Br 2.64 Å), and four externally (Cu^{II}-Br 3.02 Å) coordinated bromide ions, the latter of which links cubes along the *ab*-plane (Fig. 2.17). As opposed to **10**, complex **11** is 10+, with eight fully-, and four half-occupied water molecules coordinated to the Cu^{II} ions (Cu^{II}-O ≈2.47 Å). The shortest inter-cluster distance in **11** is between

the L^- ligands of neigbouring cubes, with H_2C-H···Ar ≈2.86 Å. The charge balancing nitrate ions in **11**, and remaining bromide ions in **10**, are located both within the internal cavity and in the external void spaces between neighbouring clusters.

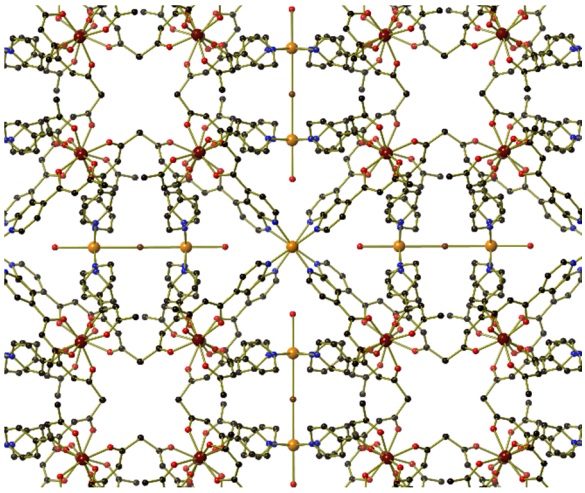

Figure 2.17 Example of how the bromide ions link neighbouring cages in **10**. Hydrogen atoms and some counterions have been removed for clarity. Colour code: Fe^{III} – Maroon, Cu^{II} – Orange, Br^- – Brown, N – Blue, O – Red, C – Black.

Complexes **12** and **13** were both prepared from thiocyanate metal salts, generated *in-situ* through the addition of aqueous KSCN to a solution of $[Fe^{III}L_3]$ and $CoCl_2$ (**12**) or $NiCl_2$ (**13**), in dichloromethane and methanol. The salt metathesis reaction was incomplete and some chloride ions remain in both structures. Complex **12** has four chloride ions, all of which are half-occupied, within the internal cavity of the cage. These chloride ions interact with the carbon atoms of the pyridyl-group, with C···Cl distances ≈3.43 Å (Fig. 2.18). In complex **13**, there is one chloride which is coordinated to the Ni^{II} ion, with a Ni^{II}-Cl distance of 2.60 Å. There is also disorder over four positions of the sulfur atom of one of the thiocyanate ligands coordinated to Ni^{II}, which can be seen in Fig. 2.18. There are several short inter-cluster contacts between the L^- ligands of neighbouring cubes in both **12** and **13**: Ar-H···O ≈2.55 Å and OC(π)···(π)CO ≈3.34 Å for **12**; Ar···O ≈3.21 Å and OC(π)···(π)CO ≈3.39 Å for **13**.

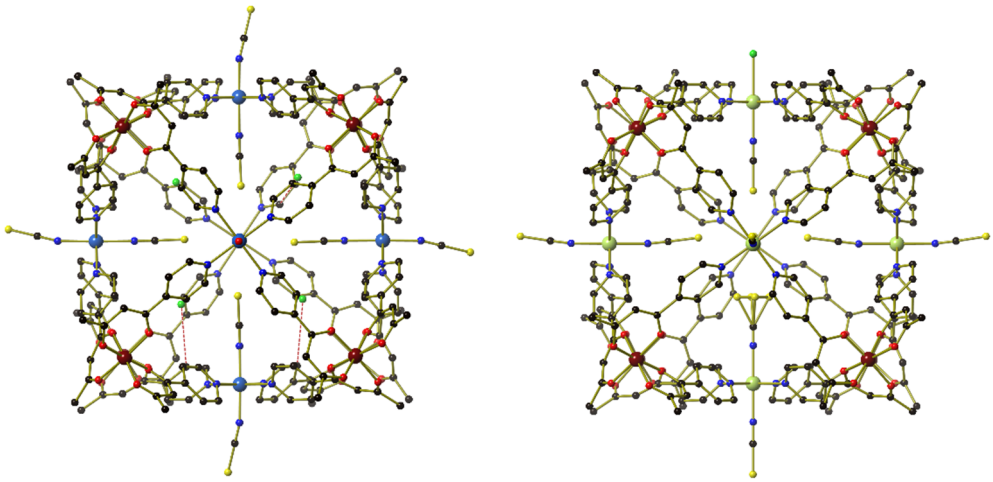

Figure 2.18 Structure of **12** (left), with interacting chloride ions (---), and **13** (right). Hydrogen atoms have been removed for clarity. Colour code: Fe^{III} – Maroon, Co^{II} – Royal Blue, Ni^{II} – Light Green, Cl^{-} – Bright Green, S – Yellow, N – Blue, O – Red, C – Black.

Complex **14** represents the only cube with diamagnetic M^{II} centres, making use of [Pd(benzonitrile)$_2$Cl$_2$] to add Pd^{II} ions to the faces of the cube. The Pd^{II} ions on first glance appear to be square planar, with Pd^{II}-N distances ≈2.02 Å (Fig. 2.19), however, some of the counterbalancing chloride ions interact with the Pd^{II} ions, "linking" neighbouring clusters, and creating a *pseudo*-square pyramidal geometry about Pd^{II}, with $Pd^{II}\cdots Cl$ distances 3.24-3.44 Å (Fig. 2.19).

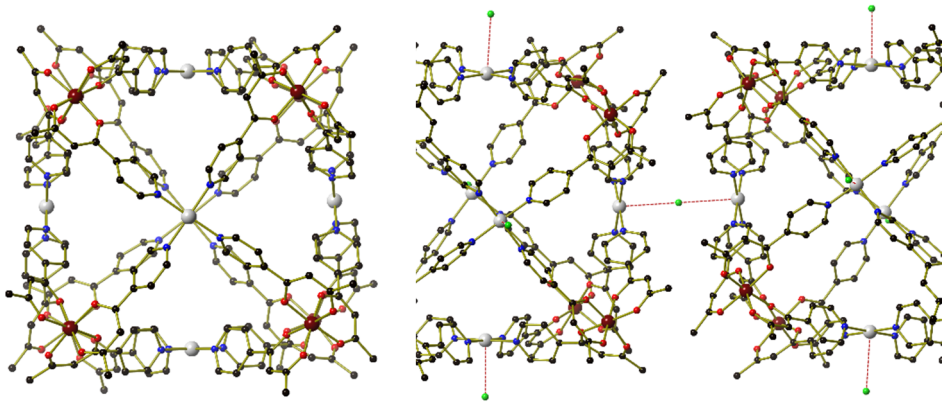

Figure 2.19 Structure **14** (left) and an example of how the clusters are "linked" through interacting chloride ions (---), as viewed down the *c*-axis (right). Colour code: Fe^{III} – Maroon, Pd^{II} – Grey, Cl^{-} – Green, N – Blue, O – Red, C – Black.

It should be noted that all fourteen $[M^{III}_8M^{II}_6L_{24}]^{n+}$ structures presented crystallise as homochiral (ΔΔΔΔΔΔΔΔ or ΛΛΛΛΛΛΛΛ) racemates with respect to the M^{III} centre. A representation of two of the chiral corner units from structure **14** is shown in Fig. 2.20.

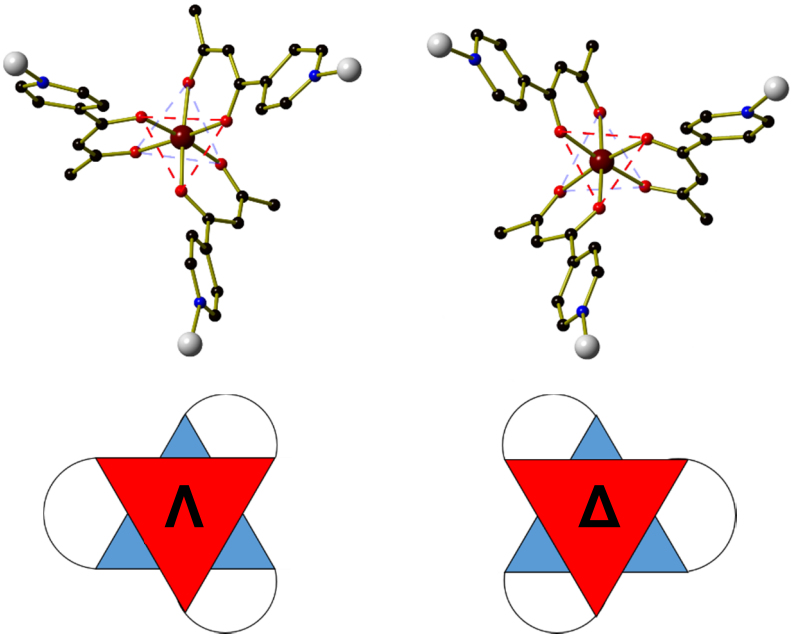

Figure 2.20 Example of the Λ enantiomer (left), and Δ enantiomer (right), of neighbouring $[Fe^{III}L_3]$ corner-units from structure **14**. Colour code: Fe^{III} – Maroon, Pd^{II} – Grey, N – Blue, O – Red, C – Black.

While it is possible that this could be simply a solid-state packing effect, solution-based self-sorting of assemblies that contain polymetallic stereocenters is a common, if not universal, occurence.[28–30] The stereochemical information in these structures is communicated by the twisting of the pyridyl group of the metalloligand, which act like propellers about the M^{II} centre.

2.3.1.2 Magnetic Studies

SQUID Magnetometry

The dc (direct current) molar magnetic susceptibility, χ_M, of polycrystalline samples of **11**-**13** were measured in an applied magnetic field, B, of 0.1 T, over the 5-290 K temperature, T, range. The experimental results are shown in Fig. 2.21 in the form of the $\chi_M T$ product, where $\chi_M = M/B$, and M is the magnetisation of the sample. The loss of lattice solvent from the $[Fe^{III}_8M^{II}_6]$ structures during evacuation of the sample chamber of the SQUID magnetometer is comparable to that of the $[Cr^{III}_8M^{II}_6]$ samples, and thus the 290 K $\chi_M T$ products of **11**, **12** and **13** were scaled to the values 37.25 $cm^3\ mol^{-1}\ K$, 46.25 $cm^3\ mol^{-1}\ K$, and 41.00 $cm^3\ mol^{-1}\ K$, respectively. These are the expected

values from the sum of Curie constants for $[Fe^{III}_8Cu^{II}_6]$, $[Fe^{III}_8Co^{II}_6]$, and $[Fe^{III}_8Ni^{II}_6]$ units, respectively, with $g_{Fe} = g_{Cu} = g_{Co} = g_{Ni} = 2.0$, where g_{Fe}, g_{Cu}, g_{Co}, and g_{Ni} are the g-factors of Fe^{III}, Cu^{II}, Co^{II}, and Ni^{II}, respectively. Upon cooling, the $\chi_M T$ product of **11** and **13** remain essentially constant until about 50 K, upon which a sharp decrease is observed, indicating weak antiferromagnetic exchange interactions. For **12**, this decrease begins at about 180 K due to the weakly antiferromagnetic nature of the interaction, and the additional zero-field splitting of the Co^{II} ion.

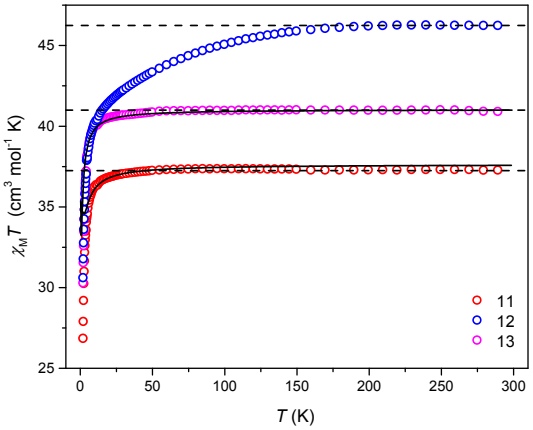

Figure 2.21 Plot of $\chi_M T$ vs T for **11** (•), **12** (•), and **13** (•), with experimental data (•), the sum of the Curie constants of uncorrelated ions (---), and the best-fit data (-).

Again, the quantitative analysis of this magnetic behaviour is complicated by the large matrices generated by the tetradecanuclear systems. In a similar methodology to that of the $[Cr^{III}_8M^{II}_6]$ systems, the magnetic properties of **11** and **13** are described by the isotropic spin-Hamiltonian (5):

$$\hat{H}_{iso} = -2J_{\text{Fe-M}} \sum_{\text{all Fe–M pairs}} \hat{S}_{\text{Fe}} \cdot \hat{S}_{\text{M}} + \mu_B B g \sum_{i} \hat{S}_i^Z \qquad (5)$$

with i running over all constitutive metal centres, g the isotropic g-factor common to both Fe^{III} and M^{II}, $\hat{S}$ a spin-operator, $J_{\text{Fe-M}}$ the isotropic exchange parameter between Fe^{III} and M^{II} centres, and μ_B the Bohr magneton. We can neglect any $J_{\text{Fe-Fe}}$ and $J_{\text{M-M}}$ terms as these centres are not connected as first neighbours.

Using the same approach as the $[Cr^{III}_8M^{II}_6]$ systems, $J_{\text{Fe-Cu}}$ and $J_{\text{Fe-Ni}}$ were determined to be -0.05 cm^{-1} and -0.0125 cm^{-1} for **11** and **13**, respectively, with a common isotropic g-factor of g = 2.0 for both complexes.

EPR Spectroscopy

The nature of the weak exchange interactions in complexes **10**, **11**, **13** and **14** was further probed by Q-band EPR spectroscopy (34 GHz). The results are shown in Fig. 2.22, where the black lines represent the experimental data, and the red lines represent the simulations, calculated using the EasySpin program (simulated with a Gaussian linewidth of 60 mT and a 10 % *D*-strain).[24]

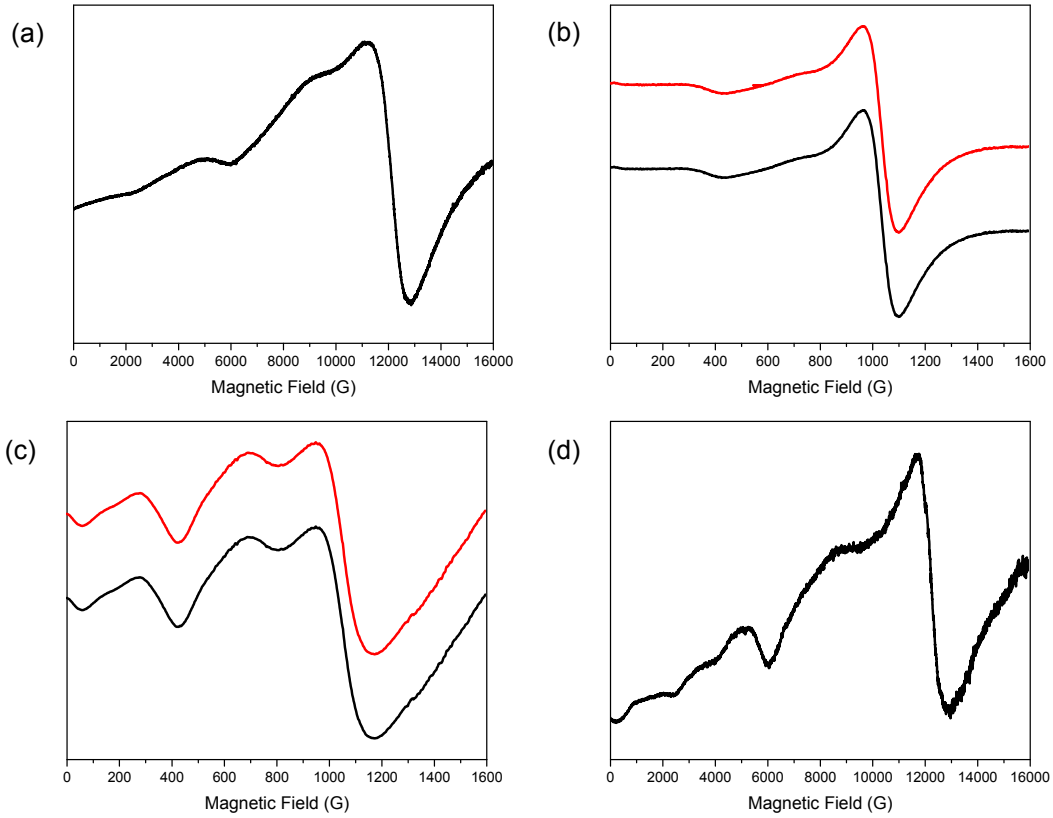

Figure 2.22 Q-band EPR spectra of (a) **10** at 5 K, (b) **11** at 8 K, (c) **13** at 8 K, and (d) **14** at 5 K (-), and calculated spectra (-), with D_{Fe} = 0.17 cm^{-1}, and a Gaussian linewidth of 60 mT.

The spectra are all very similar, with severely broadened peaks, thus limiting their accuracy. The simulations for **11** and **13** show a small, but measurable, increase in the zero-field splitting parameter of $|D_{Fe}|$ compared to that of $[Fe^{III}L_3]$. This value (≈0.2 cm^{-1}) is very similar to that of the $[Fe^{III}_2M^{II}_3]$ trigonal bipyramidal family (*vide infra*), and a detailed discussion of the distortion imposed on the metalloligand, in terms of the measureable zero-field splitting parameter, will be presented in Chapter 3.

2.4 Conclusions

The two paramangetic metalloligands $[Cr^{III}L_3]$ and $[Fe^{III}L_3]$ were successfully employed for the creation of fourteen structurally analogous $[M^{III}_8M^{II}_6L_{24}]^{n+}$ (M^{III} = Cr, Fe; M^{II} = Cu, Co, Ni, Pd; n = 0-12) coordination cubes. The choice of M^{II} ion has profound consquences on the physical properties of the cubes, whilst the choice of anion affects the chemical properties, including the charge of the cubes, their extended structures, and their ability to interact with other clusters in order to create different networks of coordination cubes.

Of these fourteen structures, nine have eight Cr^{III} ions situated at the vertices of the cubes, with either Cu^{II}, Co^{II}, or Ni^{II} ions occupying the six faces. The Cr^{III}-Cu^{II} (**1**-**3**), Cr^{III}-Co^{II} (**4**-**6**), and Cr^{III}-Ni^{II} (**8**) cubes all show ferromagnetic exchange interactions at low temperatures, with the Cr^{III}-Co^{II} cubes displaying the effects of the large zero-field splitting of the $^4A_2$ term of the Co^{II} ion. Due to the large associated matrices of these cubes, specialised computational techniques, known as statistical spectrocopy, were employed to model the susceptibility data. Through the use of an isotropic spin-Hamiltonian, simulations of the data for **2** and **5** afford $J_{Cr\text{-}Cu}$ = 0.09 cm^{-1} and $J_{Cr\text{-}Ni}$ = 0.045 cm^{-1}, respectively. An anisotropic spin-Hamiltonian was used to model the zero-field splitting of an "isolated" Co^{II} ion, suggesting $|D_{Co}|$ = 80 cm^{-1}. Q- and W-band EPR spectroscopic measurements were carried out on $[Cr^{III}L_3]$, and complexes **2** and **5**. The spectra of $[Cr^{III}L_3]$ are comparable to other *tris*(acac)-type complexes, while the complicated nature of the cubes have made analysis of associated spectra difficult. Volume calculations using the *³V Volume Assessor* program confirm an internal volume of **3** of ≈1400 $Å^3$. Inclusion of guests can be expected when the total volume of the guest are ≈770 $Å^3$ which corresponds with the inclusion of four sulfate ions (668 $Å^3$) encapsulated inside **3**.

The structurally similar $[Fe^{III}_8M^{II}_6L_{24}]^{n+}$ complexes have either Cu^{II}, Co^{II}, Ni^{II}, or Pd^{II} ions occupying the faces of the cubes. These structures show different magnetic properties to that of the Cr^{III} cubes, with studies on **11** and **13** revealing antiferromagnetic exchange interactions between the Fe^{III}-Cu^{II} and Fe^{III}-Ni^{II} ions, respectively. Q-band EPR spectroscopic studies reveal a small increase in the zero-field splitting parameter of Fe^{III} upon coordination of the metalloligand to the M^{II} ion, which is comparable to that of the trigonal bipyramidal structures that will be presented in Chapter 3.

The ability to easily vary the M^{III} or M^{II} ion in order to generate structurally similar cages with different magnetic properties highlights the versatility and applicability of the metalloligand approach in the creation of a large family of high-nuclearity magnetic clusters.

2.5 References

(1) Singh, B.; Lesher, G. Y.; Pluncket, K. C.; Pagani, E. D.; Bode, D. C.; Bentley, R. G.; Connell, M. J.; Hamel, L. T.; Silver, P. J. *J. Med. Chem.* **1992**, *35* (26), 4858.

(2) Fernelius, W. C.; Blanch, J. E.; Bryant, B. E.; Terada, K.; Drago, R. S.; Stille, J. K. In *Inorganic Syntheses*; John Wiley & Sons, Inc., 2007; pp 130–131.

(3) Chaudhuri, M. K.; Ghosh, S. K. *J. Chem. Soc. Dalt. Trans.* **1983**, No. 4, 839.

(4) Rigaku Oxford Diffraction. In *CrysAlisPro*; 2016.

(5) Sheldrick, G. M. *Acta Crystallogr. Sect. C Struct. Chem.* **2015**, *71* (1), 3.

(6) Dolomanov, O. V.; Blake, A. J.; Champness, N. R.; Schröder, M. *J. Appl. Crystallogr.* **2003**, *36* (5), 1283.

(7) Spek, A. L. *Acta Crystallogr. Sect. C Struct. Chem.* **2015**, *71* (1), 9.

(8) Coles, S. J.; Gale, P. A. *Chem. Sci.* **2012**, *3*, 683.

(9) Rigaku Oxford Diffraction. In *CrystalClear-SM Expert 3.1 b27*; 2012.

(10) Rigaku Oxford Diffraction. In *CrysAlisPro 1.171.38.41*; 2015.

(11) Palatinus, L.; Chapuis, G. *J. Appl. Crystallogr.* **2007**, *40* (4), 786.

(12) Kottke, T.; Stalke, D. *J. Appl. Crystallogr.* **1993**, *26* (4), 615.

(13) Dolomanov, O. V.; Bourhis, L. J.; Gildea, R. J.; Howard, J. A. K.; Puschmann, H. *J. Appl. Crystallogr.* **2009**, *42* (2), 339.

(14) Sheldrick, G. M. *Acta Crystallogr. Sect. A Found. Crystallogr.* **2007**, *64* (1), 112.

(15) Sheldrick, G. M. *Acta Crystallogr. Sect. A Found. Adv.* **2015**, *71* (1), 3.

(16) Wong, S. S. M. *Nuclear statistical spectroscopy*; Oxford Science Publications; Oxford University Press, Incorporated, 1986.

(17) Lohr, L. L.; Miller, J. C.; Sharp, R. R. *J. Chem. Phys.* **1999**, *111* (22), 10148.

(18) Bencini, A.; Benelli, C.; Gatteschi, D.; Zanchini, C. *Inorg. Chem.* **1980**, *19* (5), 1301.

(19) Rushbrooke, G. S.; Wood, P. J. *Mol. Phys.* **1958**, *1* (3), 257.

(20) Mead, L. R.; Papanicolaou, N. *J. Math. Phys.* **1984**, *25* (8), 2404.

(21) Grimes, S. M.; Massey, T. N. *Fusion Eng. Des.* **1997**, *37* (1), 89.

(22) Grimes, S. M.; Massey, T. N. *Phys. Rev. C* **1995**, *51* (2), 606.

(23) Elbers, G.; Remme, S.; Lehmann, G. *Inorg. Chem.* **1986**, *25* (7), 896.

(24) Stoll, S.; Schweiger, A. *J. Magn. Reson.* **2006**, *178* (1), 42.

(25) Piligkos, S.; Bill, E.; Collison, D.; McInnes, E. J. L.; Timco, G. A.; Weihe, H.; Winpenny, R. E. P.; Neese, F. *J. Am. Chem. Soc.* **2007**, *129* (4), 760.

(26) Voss, N. R.; Gerstein, M. *Nucleic Acids Res.* **2010**, *38* (SUPPL. 2), 555.

(27) Mecozzi, S.; Rebek, Jr., J. *Chem. - A Eur. J.* **1998**, *4* (6), 1016.

(28) Chen, L.-J.; Yang, H.-B.; Shionoya, M. *Chem. Soc. Rev.* **2017**, *46* (9), 2555.

(29) Castilla, A. M.; Ramsay, W. J.; Nitschke, J. R. *Acc. Chem. Res.* **2014**, *47* (7), 2063.

(30) Chepelin, O.; Ujma, J.; Wu, X.; Slawin, A. M. Z.; Pitak, M. B.; Coles, S. J.; Michel, J.; Jones, A. C.; Barran, P. E.; Lusby, P. J. *J. Am. Chem. Soc.* **2012**, *134* (47), 19334.

Chapter 3: $[M^{III}_2M^{II}_3L_6]^{n+}$ Pyridyl-Based Trigonal Bipyramids

3.1 Introduction

In the previous chapter we showed how combination of a 90° tritopic donor with a "naked" octahedral or square planar M^{II} acceptor led to the formation of $[M^{III}_8M^{II}_6L_{24}]^{n+}$ heterometallic coordination cubes. The replacement of this acceptor with a tetrahedral or *cis*-capped square planar metal salt should allow us to access $[M^{III}_2M^{II}_3]^{n+}$ trigonal bipyramidal cages (Fig. 3.1).[1] There are few diamagnetic anaologues of this skeletal-type,[2–5] and even fewer magnetic examples, with previous work employing exclusively cyano-based bridging ligands.[6–9]

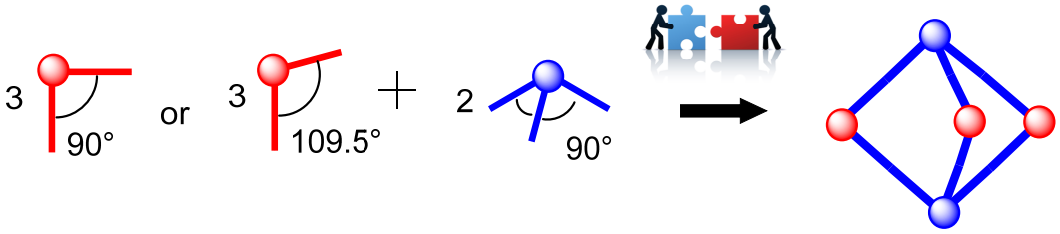

Figure 3.1 Formation of a trigonal bipyramid from three 90-109.5° ditopic (blue), and two 90° tritopic (red), building blocks.

Although it could be perceived that the $[M^{III}_2M^{II}_3L_6]^{n+}$ structure should be readily accessible through the use of any acceptor with the relevant angle, it is still necessary to carefully consider the identity of all reaction components. Previous work has shown that reaction of the $[Al^{III}L_3]$ metalloligand with the archetypal 90° acceptor complex $[(en)Pd(NO_3)_2]$ in fact yields the $[Al^{III}_8Pd^{II}_6L_{24}]^{12+}$ cube, and not the $[Al^{III}_2Pd^{II}_3L_6]^{6+}$ structure.[10,11] The replacement of this bidentate ethylenediamine ligand with a stronger bidentate donor, such as 1,3-*bis*(diphenylphosphino)propane (dppp), should prevent this dispacement, giving rise to the required angularity, and allowing for the generation of the desired pentanuclear structure.

Herein, we present the synthesis and characterisation of five new $[M^{III}_2M^{II}_3L_6]^{n+}$ (M^{III} = Cr, Fe, and Al; M^{II} = Co, Zn, and Pd; HL = 1-(4-pyridyl)butane-1,3-dione; n = 0-6) trigonal bipyramids, built using the diamagnetic and paramagnetic metalloligands $[M^{III}L_3]$.

3.2 Experimental

3.2.1 Materials and Instrumentation

All reactions were performed under aerobic conditions. Solvents and reagents were used as received from commercial suppliers. Elemental analyses were carried out by Medac Ltd. Electrospray Ionization (ESI) mass spectra of were measured on a Bruker MicroToF 2 for [$Al^{III}L_3$], and on a Waters Synapt G2 Q-TOF for compounds **18** and **19**. NMR spectra were recorded on a 500 MHz Bruker Advance NMR spectrometer. Magnetisation measurements were carried out on a Quantum Design SQUID MPMS-XL magnetometer, operating between 1.8 and 300 K for dc applied magnetic fields ranging from 0 to 5 T. Microcrystalline samples were dispersed in eicosane in order to avoid torquing of the crystallites. Heat capacity measurements were carried out for temperatures down to ≈0.3 K by using a Quantum Design 9T-PPMS, equipped with a ^{3}He cryostat. The experiments were performed on thin pressed pellets (≈1 mg) of a polycrystalline sample, thermalised by ≈0.2 mg of Apiezon N grease, whose contribution was subtracted by using a phenomenological expression. X- and Q-band EPR spectra were collected on powdered microcrystalline samples of [$Fe^{III}L_3$] and compounds **15**-**18** at the UK National EPR Facility at The University of Manchester.

3.2.2 Syntheses

Preparation of 1-(4-pyridyl)butane-1,3-dione (HL)

HL was prepared according to the same procedure as in Chapter 2.

Synthesis of *tris*{1-(4-pyridyl)acetylacetonato}chromium(III), [$Cr^{III}L_3$]

[$Cr^{III}L_3$] was prepared according to the same procedure as in Chapter 2.

Synthesis of *tris*{1-(4-pyridyl)acetylacetonato}iron(III), [$Fe^{III}L_3$]

[$Fe^{III}L_3$] was prepared according to the same procedure as in Chapter 2.

Synthesis of *tris*{1-(4-pyridyl)acetylacetonato}aluminium(III), [$Al^{III}L_3$]

$Al(NO_3)_3{\cdot}9H_2O$ (0.375 g, 1.0 mmol), HL (0.570 g, 3.5 mmol) and sodium methoxide (0.189 g, 3.5 mmol) were dissolved in MeOH/H_2O (1:1 v/v, 100 mL), and left to stir until a white product precipitated (≈1 h). The precipitate was filtered and washed with water. The crude product was extracted with CH_2Cl_2 and dried over anhydrous $MgSO_4$. CH_2Cl_2 was removed under reduced pressure to afford the product as a white solid (0.390 g, 76 %). Elemental analysis (%) calculated (found) for $C_{27}H_{24}N_3O_6Al$ (513.49 g mol^{-1}): C 63.16 (63.06), H 4.71 (4.53), N 8.18 (8.11). ESI TOF

HRMS *m/z* calculated (found) for [$Al^{III}L_3$]: [$C_{27}H_{25}AlN_3O_6$]$^+$ 540.1553 (514.1544). ^{1}H NMR spectroscopy (500 MHz; CD_3CN): δ 8.66 (m, 8H, Ar-*H*), 7.69 (m, 8H, Ar-*H*), 6.44 (m, 4H, COC*H*CO), 2.18 (m, 12H, C*H*$_3$) ppm.

[$Fe^{III}_2Co^{II}_3L_6Cl_6$] (15)

To a solution of [$Fe^{III}L_3$] (108 mg, 0.2 mmol) in acetone (35 mL), was added $CoCl_2$ (39 mg, 0.3 mmol). The solution was stirred for 30 minutes, before being filtered and layered with Et_2O. Orange X-ray quality crystals were obtained after 20 days. Yield (98 mg, 67 %). Elemental analysis (%) calculated (found) for $C_{54}H_{48}N_6O_{12}Cl_6Fe_2Co_3$ (1474.17 g mol^{-1}): C 44.00 (44.12), H 3.28 (3.39), N 5.70 (5.77).

[$Fe^{III}_2Zn^{II}_3L_6Br_6$] (16)

To a solution of [$Fe^{III}L_3$] (108 mg, 0.2 mmol) in CH_2Cl_2/acetone (1:1 v/v, 35 mL), was added $ZnBr_2$ (67 mg, 0.3 mmol). The solution was stirred for 30 minutes, before being evaporated to dryness. The dark-red product was dissolved in nitromethane, filtered and allowed to stand. Dark-red X-ray quality crystals were obtained from room temperature evaporation of the mother liquor after 10 days. Yield (133 mg, 76 %). Elemental analysis (%) calculated (found) for $C_{54}H_{48}N_6O_{12}Br_6Fe_2Zn_3$ (1876.29 g mol^{-1}): C 36.85 (36.97), H 2.75 (2.87), N 4.77 (4.91).

[$Cr^{III}_2Zn^{II}_3L_6Br_6$] (17)

To a solution of [$Cr^{III}L_3$] (108 mg, 0.2 mmol) in CH_2Cl_2 (35 mL), was added $ZnBr_2$ (67 mg, 0.3 mmol). The solution was stirred for 1 hour, in which time a precipitate was formed. The dark-red solid product was isolated by filtration, dissolved in DMF, and layered with MeOH. Dark-red X-ray quality crystals were obtained after 10 days. Yield (142 mg, 81 %). Elemental analysis (%) calculated (found) for $C_{54}H_{48}N_6O_{12}Br_6Cr_2Zn_3$ (1816.57 g mol^{-1}): C 37.01 (36.92), H 2.76 (2.67), N 4.80 (4.67).

[$Cr^{III}_2Pd^{II}_3L_6$(dppp)$_3$](OTf)$_6$ (18)

To a solution of [$Cr^{III}L_3$] (108 mg, 0.2 mmol) in MeOH (35 mL), was added [Pd(dppp)$_2$(CF_3SO_3)$_2$] (245 mg, 0.3 mmol; dppp = 1,3-*bis*(diphenylphosphino)propane). The solution was stirred for 30 minutes, before being filtered and allowed to stand. Orange X-ray quality crystals were obtained from room temperature evaporation of the mother liquor after 5 days. Yield (275 mg, 78 %). Elemental analysis (%) calculated (found) for $C_{141}H_{126}O_{30}N_6F_{18}P_6S_6Cr_2Pd_3$ (4072.56 g mol^{-1}): C 48.00 (47.89), H 3.60 (3.47), N 2.38 (2.27). ESI TOF HRMS m/z calculated (found) for [$Cr^{III}_2Pd^{II}_3L_6$(dppp)$_3$](OTf)$_6$: [$C_{138}H_{126}Cr_2F_9N_6O_{21}P_6Pd_3S_3$]$^{3+}$ 1026.7461 (1026.7236).

$[Al^{III}_2Pd^{II}_3L_6(dppp)_3](OTf)_6$ (19)

To a solution of $[Al^{III}L_3]$ (103 mg, 0.2 mmol) in MeCN (35 mL), was added $[Pd(dppp)_2(CF_3SO_3)_2]$ (245 mg, 0.3 mmol). The solution was stirred for 15 hours at 50 °C, before being filtered, cooled, and layered with diethyl ether. Colourless X-ray quality crystals were obtained after 5 days. Yield (288 mg, 83%).^{1}H NMR (500 MHz, CD_3CN): δ 8.61 (bs, 12H, H_d), 7.79 – 7.67 (m, 12H, Ph), 7.48 – 7.44 (m, 12H, Ph), 7.42 – 7.39 (m, 12H, Ph), 7.34 – 7.27 (m, 12H, Ph), 7.26 – 7.22 (m, 12H, Ph), 7.18 (d, J = 6.5 Hz, 12H, H_c), 6.13 (s, 6H, H_b), 3.28 – 3.11 (m, 6H, H_e), 3.10 – 2.92 (m, 6H, H_e), 2.60 – 2.36 (m, 3H, H_f), 2.15 (s, 18H, H_a), 1.93 – 1.75 (m, 3H, H_f) ppm. ^{13}C NMR (126 MHz, CD_3CN): δ 198.79, 177.61, 151.26, 147.79, 134.91–134.82 (m, 2 signals), 133.70, 133.07–132.99 (m, 3 signals), 130.60–130.51 (m, 2 signals), 130.42–130.33 (m, 2 signals), 127.58–126.88 (m), 125.52–124.82 (m), 124.37, 122.06 (q, J = 321.0 Hz), 99.58, 28.10, 22.25–21.92 (m), 18.30 ppm. ^{31}P NMR (202 MHz, CD_3CN) δ 6.97 ppm. ^{19}F NMR (471 MHz, CD_3CN) δ -79.05 ppm. Diffusion coefficient (DOSY, 500 MHz, CD_3CN, 298 K) 5.99 × 10^{-10} m^2/s, hydrodynamic radius 9.9 Å. ESI TOF HRMS m/z calculated (found) for $[Al^{III}_2Pd^{II}_3L_6(dppp)_3](OTf)_6$: $[C_{138}H_{126}Al_2F_9N_6O_{21}P_6Pd_3S_3]^{3+}$ 1010.1069 (1010.1238). Elemental analysis (%) calculated (found) for $C_{141}H_{126}O_{30}N_6F_{18}P_6S_6Al_2Pd_3$ (3724.13 g mol^{-1}): C 48.69 (48.42), H 3.65 (3.57), N 2.42 (2.35).

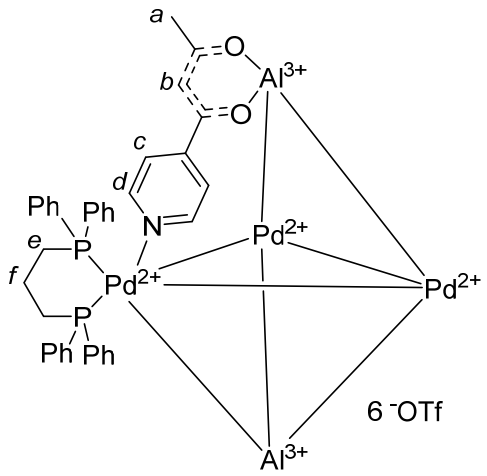

3.2.3 CASSCF Methodology

Complete active space self-consistent field (CASSCF) calculations were performed on **15** with MOLCAS 8.0,[12] where each Co^{II} site was treated independently and the other Co^{II} sites were replaced with the closed shell Zn^{II} ion. The active space consisted of seven electrons in the five 3*d* orbitals, where ten quartets and forty doublets were considered both in the orbital optimisation (RASSCF) and the spin-orbit mixing (RASSI) procedures. The zero-field splitting of the S = 3/2 ground state was extracted from the spin-orbit mixed states (SINGLE_ANISO). Basis sets from the ANO-RCC library of VTZP (Co^{II}), VDZP (coordinated N and Cl) and VDZ (all other atoms) quality were employed,[13] along with Cholesky decomposition of the two-electron integrals.

3.2.4 Crystal Structure Information

For compounds **15**, **16** and **17** single-crystal X-ray diffraction data were collected at T = 100 K on a Rigaku AFC12 goniometer equipped with an enhanced sensitivity (HG) Saturn 724+ detector mounted at the window of an FR-E+ Superbright MoKα rotating anode generator with HF Varimax optics (70 μm focus),[14] using Rigaku Crystal Clear and CrysalisPro software for data collection and reduction.[15,16] The crystals were sensitive to solvent loss and were therefore "cold-mounted" using an X-Temp 2 System apparatus at T = 70°C and then quickly transferred to the diffractometer. For compounds **18** and **19** single crystal X-ray diffraction data were measured on a Rigaku Oxford Diffraction SuperNova diffractometer using Cu radiation at T = 120 K. The CrysalisPro software package was used for instrument control, unit cell determination and data reduction.[17]

Unit cell parameters in all cases were refined against all data. Crystal structures were solved using the charge flipping method implemented in SUPERFLIP (**15**, **16**, and **17**),[18] or by direct methods with ShelXS (**18** and **19**).[19] All structures were refined on F_o^2 by full-matrix least-squares refinements using ShelXL within the OLEX2 suite.[20,21] All non-hydrogen atoms were refined with anisotropic displacement parameters, and all hydrogen atoms were added at calculated positions and refined using a riding model with isotropic displacement parameters based on the equivalent isotropic displacement parameter (U_{eq}) of the parent atom. All five structures contain accessible voids and channels that are filled with diffuse electron density belonging to uncoordinated solvent, and triflate ions in the case of compounds **18**-**19**. The SQUEEZE routine of PLATON was used to remove remaining electron density corresponding to solvent and anions not reported in the calculated formula.[22]

The molecular formulae for complexes **15**-**19** are tabulated below for convenience (Table 3.1), and a crystallographic summary with structure refinement details are presented in Tables 3.2 and 3.3.

Table 3.1 Molecular formulae for complexes **15**-**19**. Additional solvent molecules of crystallisation have been removed from the molecular formulae for clarity.

Complex	Molecular formula
15	$[Fe^{III}_2Co^{II}_3L_6Cl_6]$
16	$[Fe^{III}_2Zn^{II}_3L_6Br_6]$
17	$[Cr^{III}_2Zn^{II}_3L_6Br_6]$
18	$[Cr^{III}_2Pd^{II}_3L_6(dppp)_3](OTf)_6$
19	$[Al^{III}_2Pd^{II}_3L_6(dppp)_3](OTf)_6$

Table 3.2 Crystallographic details for **15**-**17**.

Complex	15	16·2MeNO$_2$	17·2MeOH
Empirical formula	$C_{54}H_{48}N_6O_{12}Cl_6Fe_2Co_3$	$C_{56}H_{48}Br_6N_8O_{16}Fe_2Zn_3$	$C_{56}H_{48}Br_6N_6O_{14}Cr_2Zn_3$
Formula weight	1474.17	1876.29	1816.57
Colour	Orange	Dark Red	Dark Red
Shape	Plate	Prism	Prism
Temperature, K	100.0	100.0	100.0
Crystal system	Trigonal	Trigonal	Trigonal
Space group	$P3_221$	$P3_221$	$P3_221$
***a*, Å**	12.7708(5)	12.8153(16)	13.2429(10)
***b*, Å**	12.7708(5)	12.8153(16)	13.2429(10)
***c*, Å**	39.0709(12)	12.8153(16)	38.380(3)
α, °	90.0	90.0	90.0
β, °	90.0	90.0	90.0
γ, °	120.0	120.0	120.0
Volume, Å^3	5518.5(5)	5520.9(16)	5829.1(10)
Z	3	3	3
Density (calculated), mg m^{-3}	1.333	1.693	1.546
Absorption coefficient, mm^{-1}	1.318	4.668	4.322
Reflections collected	21773	32005	8827
Unique reflections	8331	6717	8827
Data/restraints/parameters	8331/324/378	8454/32/403	8827/2/394
Goodness-of-fit	1.006	0.990	0.971
R_{int}	0.1233	0.0627	0.0356
Final R_1	0.0647	0.0321	0.0521
Final wR_2	0.1692	0.0791	0.1467
CCDC Number	1520427	1520428	1520429

Table 3.3 Crystallographic details for **18** and **19**.

Complex	18·17MeOH	19·6CH$_3$CN
Empirical formula	$C_{158}H_{194}F_{18}N_6O_{47}P_6S_6Cr_2Pd_3$	$C_{153}H_{144}N_{12}O_{30}F_{18}P_6S_6Al_2Pd_3$
Formula weight	4072.56	3724.13
Colour	Orange	Colourless
Shape	Rod	Prism
Temperature, K	120.0	120.0
Crystal system	Triclinic	Cubic
Space group	*P*-1	*I*-43*d*
***a*, Å**	18.4407(9)	43.73712(7)
***b*, Å**	22.0037(9)	43.73712(7)
***c*, Å**	27.1925(10)	43.73712(7)
α, °	104.146(3)	90.0
β, °	109.298(4)	90.0
γ, °	95.522(4)	90.0
Volume, Å^3	9907.3(8)	83666.3(4)
Z	2	16
Density (calculated), mg m^{-3}	1.365	1.183
Absorption coefficient, mm^{-1}	4.843	3.770
Reflections collected	66752	498156
Unique reflections	12021	14608
Data/restraints/parameters	12021/697/1484	14608/7/676
Goodness-of-fit	1.037	1.084
R_{int}	0.0871	0.0934
Final R_1	0.0806	0.0869
Final wR_2	0.2423	0.2282
CCDC Number	1520426	1520425

3.3 Results and Discussion

3.3.1 Solid-State Structural Descriptions

The heterometallic $[M^{III}_2M^{II}_3]^{n+}$ trigonal bipyramidal cages $[Fe^{III}_2Co^{II}_3L_6Cl_6]$ (**15**), $[Fe^{III}_2Zn^{II}_3L_6Br_6]$ (**16**), $[Cr^{III}_2Zn^{II}_3L_6Br_6]$ (**17**), $[Cr^{III}_2Pd^{II}_3L_6(dppp)_3](OTf)_6$ (**18**), and $[Al^{III}_2Pd^{II}_3L_6(dppp)_3](OTf)_6$ (**19**) were all prepared in a similar manner by the reaction of a $[M^{III}L_3]$ metalloligand with a tetrahedral (**15**, **16**, and **17**) or *cis*-capped square planar (**18** and **19**) M^{II} salt. Each $[M^{III}_2M^{II}_3]^{n+}$ skeleton is described by two M^{III} ions and three M^{II} ions occupying the axial and equatorial sites of the trigonal bipramid, respectively (Fig. 3.2). The approximate dimensions of the trigonal bipyramidal structures are $M^{III}\cdots M^{II}$ (8.77-8.99 Å), $M^{III}\cdots M^{III}$ (10.75-11.20 Å), and $M^{II}\cdots M^{II}$ (11.72-12.80 Å).

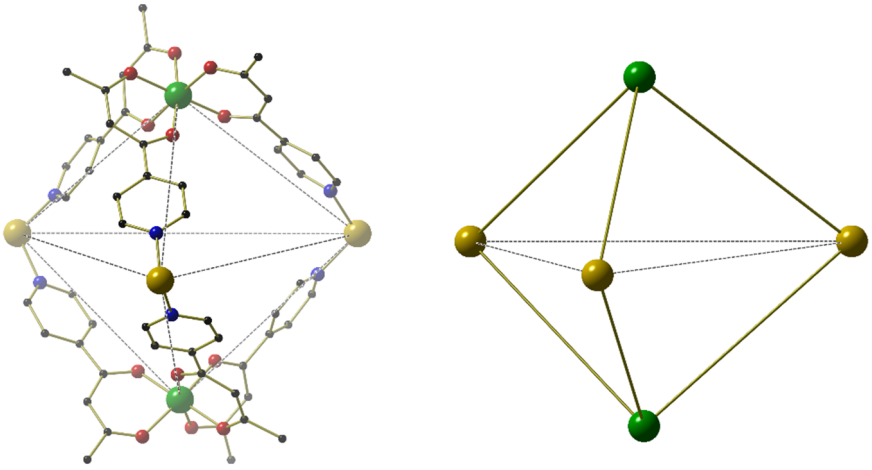

Figure 3.2 Example of a $[M^{III}_2M^{II}_3L_6]^{6+}$ trigonal bipyramid (left), with the ligands removed to show the metallic skeleton (right). All hydrogen atoms, counterions, and solvent molecules have been removed for clarity. Colour code: M^{III} – Green, M^{II} – Gold, N – Blue, O – Red, C – Black.

Upon coordination of the metalloligand to form the trigonal bipyramid, there is a slight distortion of the metalloligand's $\{MO_6\}$ coordination sphere, with M^{III}-O distances approximately 1.98-2.02 Å ($[Fe^{III}L_3]$), 1.91-1.98 Å ($[Cr^{III}L_3]$), or 1.86-1.89 Å ($[Al^{III}L_3]$), and O-M^{III}-O *cis*/*trans* angles between 83.48-95.17° and 169.99-178.40° ($[Fe^{III}L_3]$), 86.82-94.04° and 176.35-179.85° ($[Cr^{III}L_3]$), and 88.84-91.43° and 179.03-179.54° ($[Al^{III}L_3]$), respectively. The metalloligands are coordinated to the M^{II} ions through the N-donor of the pyridyl groups, with the N-M^{II}-N angles of **15**-**17**, and **18**-**19**, lying in the ranges 90.63-103.57° and 84.40-85.39°, respectively.

For clarity, the remaining structural descriptions will be separated into the two types of trigonal bipyramids, namely the structures which employ tetrahedral M^{II} salts (**15**-**17**), and those which employ *cis*-capped square planar M^{II} salts (**18** and **19**).

Complexes **15**-**17** are neutral with the M^{II} ions counterbalanced by coordinating chloride (**15**; Fig. 3.3), or bromide ions (**16** and **17**; Fig. 3.3). The Co^{II} and Zn^{II} ions of **15**-**17** are of distorted tetrahedral geometry with bond distances in the range 2.05-2.35 Å (Co^{II}-Cl ≈2.23 Å, Co^{II}-N ≈2.05 Å, Zn^{II}-Br ≈2.35 Å and Zn^{II}-N ≈2.06 Å), and bond angles ranging from 90.62-120.08°.

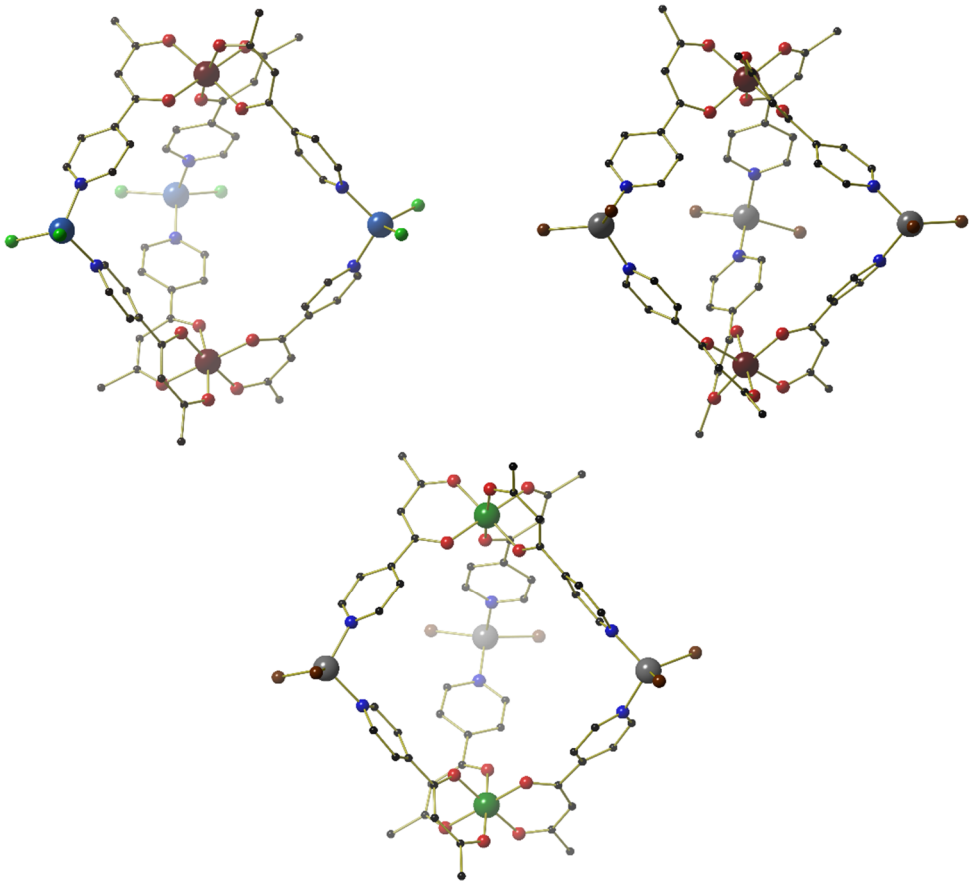

Figure 3.3 Structure of **15** (top), **16** (left), and **17** (right) with solvent molecules and hydrogen atoms removed for clarity. Colour code: Cr^{III} – Medium Green, Fe^{III} – Maroon, Co^{II} – Royal Blue, Zn^{II} – Grey, Cl^{-} – Bright Green, Br^{-} – Brown, N – Blue, O – Red, C – Black.

Complexes **15**-**17** crystallise in the space group $P3_221$ (Fig. 3.4). There are numerous intercluster interactions, including hydrogen bonding between the coordinated halide ions and the pyridyl group on the neighbouring trigonal bipyramid (C···Cl ≈3.41 Å and C-H···Cl ≈2.88 Å for **15** {Fig. 3.4}; C···Br ≈3.47 Å and C-H···Br ≈2.98 Å for **16** and **17**). There are also intercluster interactions between the halogen atoms and the L^{-} of the metalloligand (C-H···Cl ≈2.93 Å; H_2C-H···Cl ≈2.88 Å for **15**, and H_2C-H···Cl ≈2.85 Å for **16** and **17**), with nitromethane and methanol solvent molecules also "linking" the cages in **16** (≈2.67 Å) and **17** (≈2.12 Å), respectively.

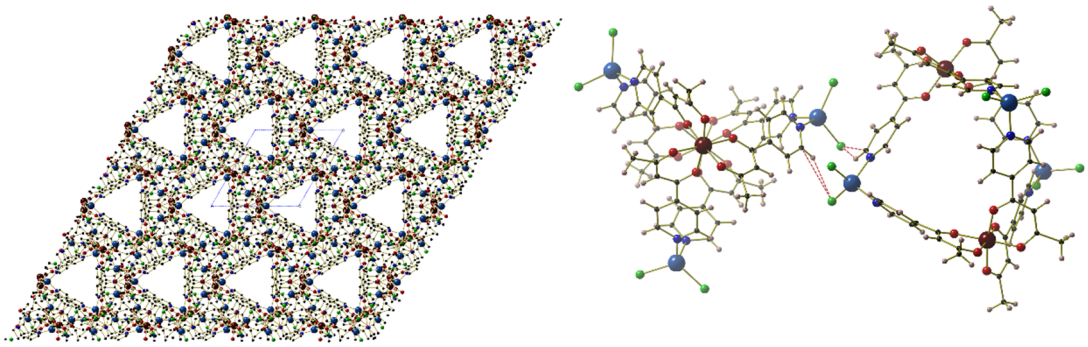

Figure 3.4 The packing of **15** as viewed down the *c*-axis (left), with an example of intercluster interactions (---) between neighbouring trigonal bipyramids (right). Colour code: Fe^{III} – Maroon, Co^{II} – Royal Blue, Cl^{-} – Green, N – Blue, O – Red, C – Black, H – Pale Pink.

In complexes **18** and **19**, the Pd^{II} ion is *cis*-protected by the dppp ligand with Pd^{II}-P bond distance ≈2.27 Å. The coordination of the metalloligand to the Pd^{II} ion through the N atom of the pyridyl donor (Pd^{II}-N ≈2.08-2.14 Å) creates a distorted square planar geometry around the Pd^{II} centre, with *cis*/*trans* bond angles in the range 84.40-93.50° and 165.49-178.57°, respectively.

Complexes **18** and **19** (Fig. 3.5) are both 6+, with charge balancing triflate ions located outside the cage. There are also several intercluster short contacts in **18** and **19**, with the shortest contacts between H_2C-H···O of neighbouring L^{-} being ≈2.57 Å. The anions also help mediate intermolecular contacts between clusters, with the shortest contacts being F_2C-F···H-Ar (≈2.45 Å) and O_2S-O···H-Ar (≈2.60 Å).

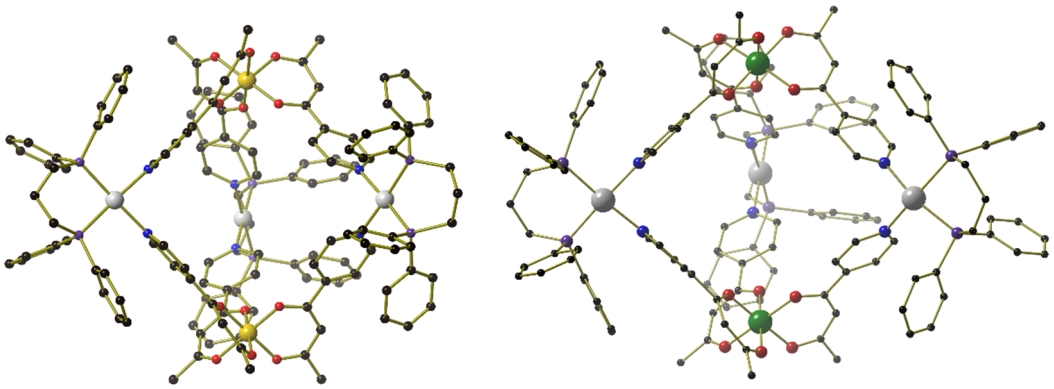

Figure 3.5 Structures of the cations of **18** and **19** with hydrogen atoms and counterions removed for clarity. Colour code: Al^{III} – Gold, Cr^{III} – Green, Pd^{II} – Grey, P – Mauve, N – Blue, O – Red, C – Black.

While on initial inspection it appears that structures **15**-**19** are structurally analogous, there are distinct diastereomeric differences between **15**-**17**, and **18** and **19** (Fig. 3.6). Structures **15**-**17** crystallise as the energetically preferred homochiral racemates,[23] in which both the M^{III} ions possess the same Λ or Δ configuration. This is comparable to the $[M^{III}_8M^{II}_6L_{24}]^{n+}$ structures presented in Chapter 2, with the stereochemical information communicated through the twisting of the pyridyl groups upon coordination to the M^{II} ions. In contrast to this, **18** and **19** both crystallise as the achiral heterodiastereomer, with the introduction of the $[Pd^{II}(dppp)]$ unit causing a small change in angle between the pyridyl-donors at each M^{II} site, and/or introducing intramolecular interactions between the dppp ligand and the $[M^{III}L_3]$ donor.

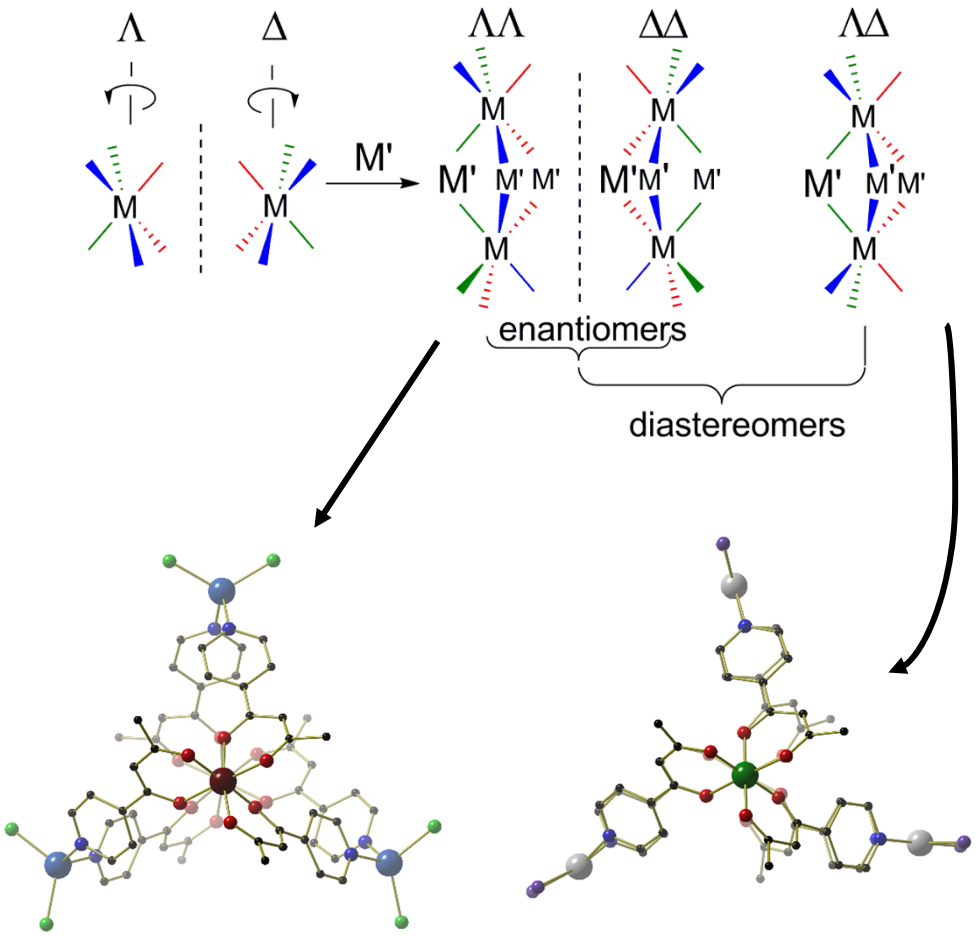

Figure 3.6 Examples of the different configurations that $[M^{II}L_3]$ can adopt (top) with an example of a homochiral ΛΛ cage (**15**, left) and a heterochiral ΛΔ cage (**18**, right), as viewed down the M^{III}-M^{III} axis. The ΔΛ cage is not shown for clarity. Hydrogen atoms, counterions, and the majority of the dppp ligand have been removed for clarity. Colour code: Fe^{III} – Maroon, Cr^{III} – Medium Green, Co^{II} – Royal Blue, Pd^{II} – Grey, Cl^- – Bright Green, P – Mauve, N – Blue, O – Red, C – Black.

3.3.2 Solution-Based Self-Assembly and Structure

NMR Spectroscopy

Complex **19** is the only fully diamagnetic trigonal bipyramidal structure and thus NMR spectroscopy was employed to examine its behaviour in solution. It is well-known that *tris*(bidentate) octahedral complexes can exist as both the *fac*- and *mer*-geometrical isomers, with the *mer*-isomer statistically favoured in a 3:1 *mer*:*fac* ratio.[24] [$Al^{III}L_3$] is no exception to this kinetic phenomenon and clearly displays both *fac*- and *mer*-isomerism, evidenced by the multiplet for the -CH and -CH_3 groups of L^- in the ^{1}H NMR spectrum (Fig. 3.7). Upon coordination there is rearrangement of the *mer*-isomer to the *fac*-isomer, as indicated by the disappearance of the multiplet and the introduction of a singlet in the crude reaction mixture (Fig. 3.7). This dynamic behaviour is not wholly unexpected because, although *mer*-*tris*(bidentate) octahedral complexes have been used previously to generate discrete metallosupramolecular cages,[25] these systems are generally large and entropically disfavoured when compared to small trigonal bipyramidal structures. In order to test if this amplification was a solid-state or solution-based effect, a crystalline sample of **19** was dissolved in CD_3CN, and the ^{1}H NMR spectrum was obtained. The spectrum (Fig. 3.7) matches that of the crude reaction solution, which was obtained by treating a slight excess of [$Pd(dppp)(OTf)_2$] with [$Al^{III}L_3$] in CD_3CN, proving the amplification of the *fac*-isomer on formation of **19** is a solution-based effect.

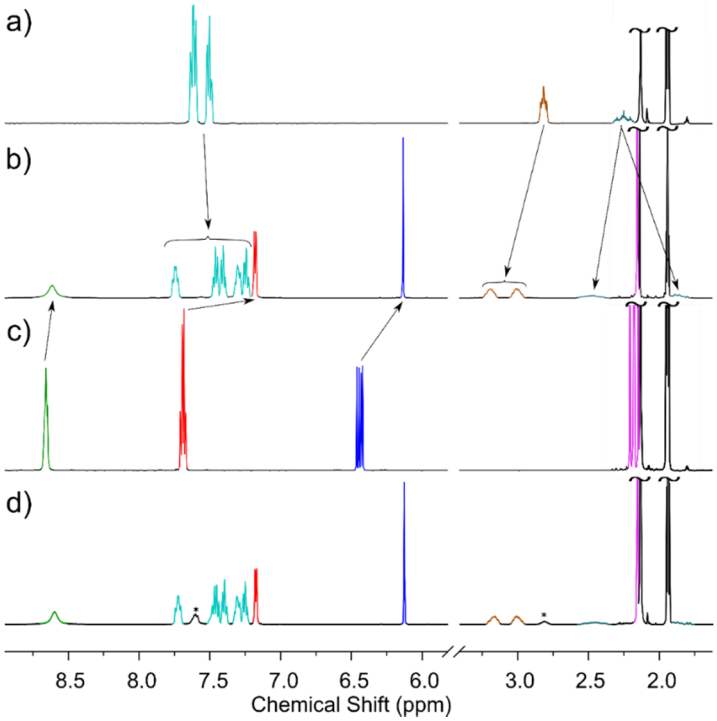

Figure 3.7 Partial ^{1}H NMR spectra (CD_3CN, 500 MHz, 300 K) of a) [$Pd(dppp)(CF_3SO_3)_2$]; b) **19** (dissolved crystalline material) c) [$Al^{III}L_3$]; d) the crude self-assembly reaction between a slight excess of [$Pd(dppp)(CF_3SO_3)_2$] and [$Al^{III}L_3$] in CD_3CN (signals for excess [$Pd(dppp)(CF_3SO_3)_2$] marked *). Colour code: *o*-py – Green, *m*-py – Red, dppp Ar*H* – Turquoise, acac-C*H* – Blue, dppp-CH_2 – Brown and Pale Blue, acac-CH_3 – Magenta.

The ^{1}H diffusion-ordered NMR spectroscopy (DOSY) spectrum (Fig. 3.8) also indicates the formation of **19** in solution, with all resonances possessing the same diffusion coefficient. The hydrodynamic radius, that is, the radius of a hypothetical sphere that diffuses with the same speed as the particle under examination, was calculated to be 9.9 Å using the Stokes-Einstein equation (6),[26] where k_B is the Boltzmann constant, T the absolute temperature, η the viscosity, and r_H the hydrodynamic radius of the species under investigation.

$$D = \frac{k_B T}{6\pi\eta\, r_H} \qquad (6)$$

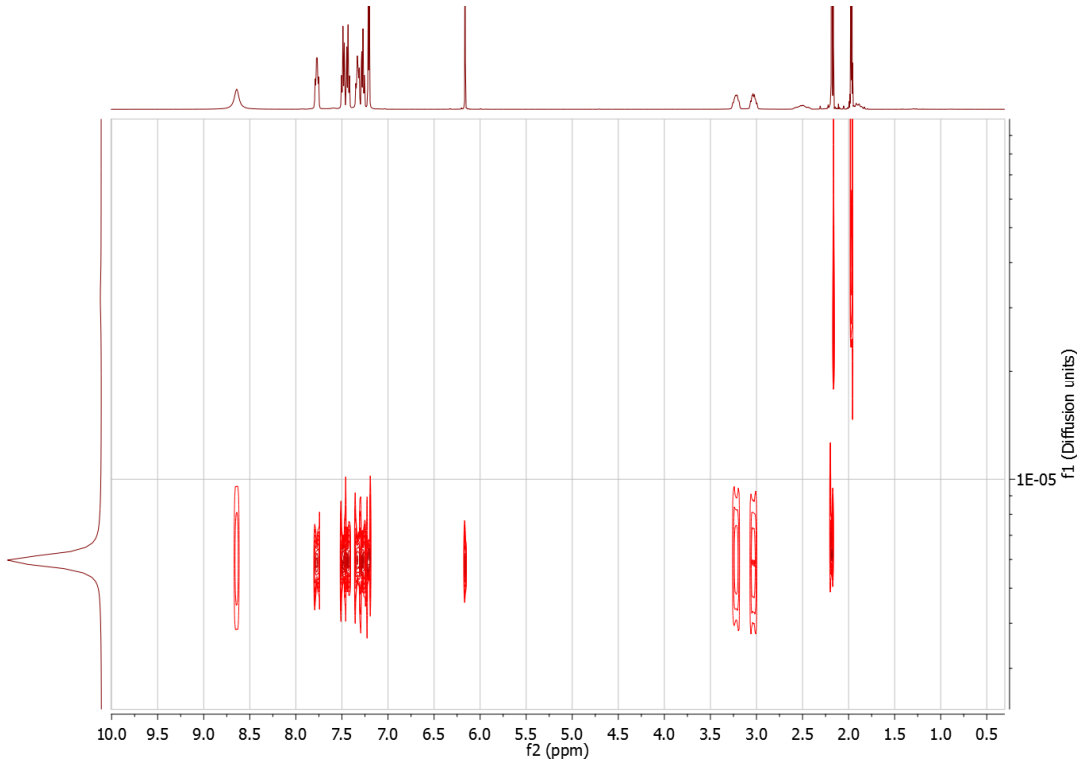

Figure 3.8 DOSY spectrum (500 MHz, CD_3CN, 298 K) of **19**. The diffusion coefficient is measured to be 5.99 × 10^{-10} m^2/s, with a hydrodynamic radius of 9.9 Å.

Mass Spectrometry

Electrospray ionisation mass spectrometry (ESI-MS) was carried out on **18** and **19** to further confirm their formation in solution (Fig. 3.9 and Table 3.4). A partial spectrum is shown as the inset in Fig. 3.9, with the 3+ charge state, corresponding to [**18**-3OTf]$^{3+}$ and [**19**-3OTf]$^{3+}$, matching the expected isotropic distribution.

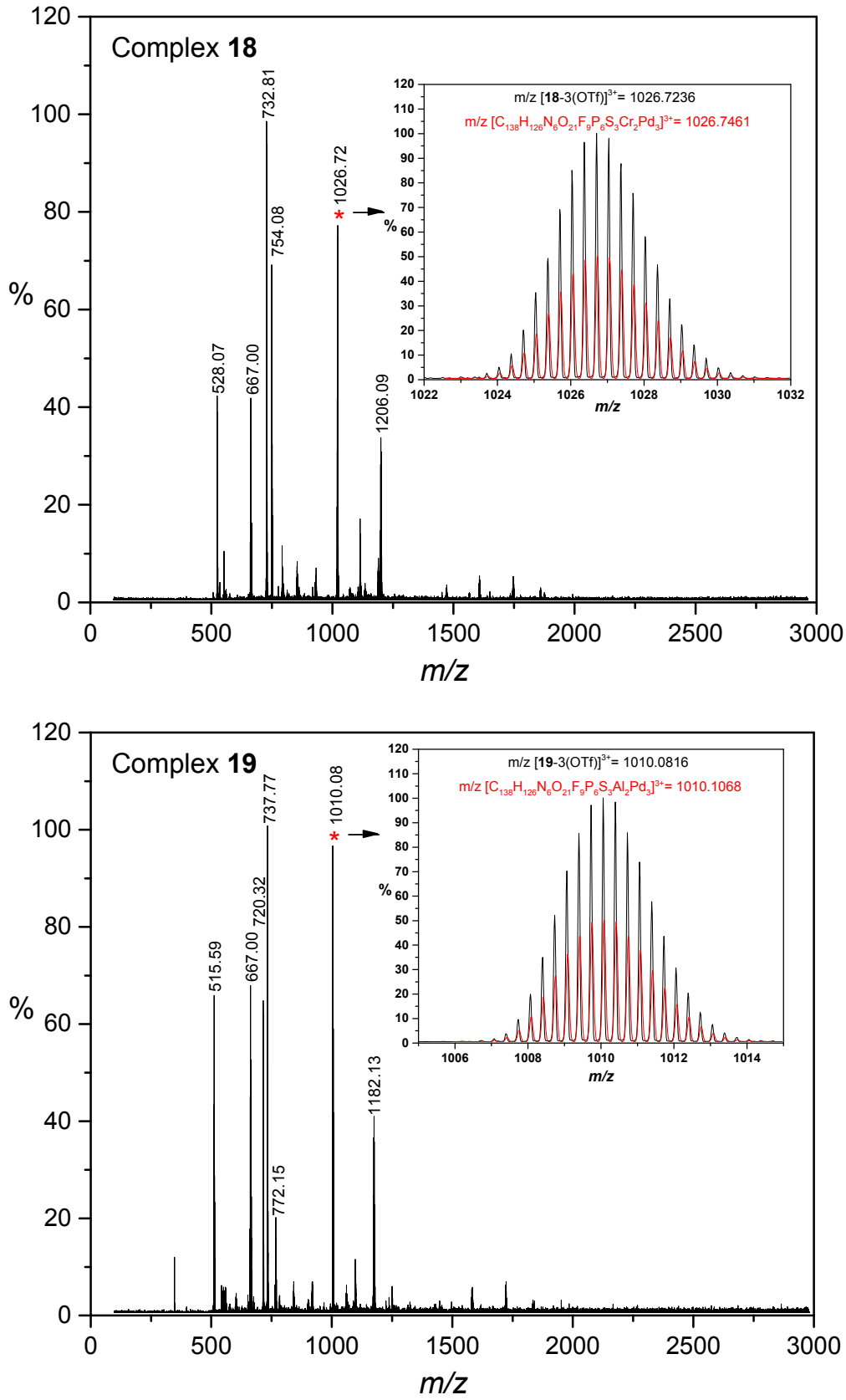

Figure 3.9 ESI-MS of **18** (top) and **19** (bottom) showing the isotopic distribution of the [**18**-3OTf]$^{3+}$ and [**19**-3OTf]$^{3+}$ charge state (insets), respectively. Experimental values (**-**) are compared against theoretical values (**-**).

Table 3.4 Table of peaks with corresponding molecular species for Fig. 3.9.

18		19	
528.07	$\{[Cr^{III}_2Pd^{II}_2L_6(dppp)_2](OTf)_2\}^{4+}$	**515.59**	$\{[Al^{III}_2Pd^{II}_2L_6(dppp)_2](OTf)_2\}^{4+}$
667.00	$\{[Pd^{II}(dppp)](OTf)\}^{+}$	**667.00**	$\{[Pd^{II}(dppp)](OTf)\}^{+}$
732.81	$\{[Cr^{III}_2Pd^{II}_3L_6(dppp)_3](OTf)_2\}^{4+}$	**720.32**	$\{[Al^{III}_2Pd^{II}_3L_6(dppp)_3](OTf)_2\}^{4+}$
754.08	$\{[Cr^{III}_2Pd^{II}_2L_6(dppp)_2](OTf)_3\}^{3+}$	**737.77**	$\{[Al^{III}_2Pd^{II}_2L_6(dppp)_2](OTf)_3\}^{3+}$
1026.72	$\{[Cr^{III}_2Pd^{II}_3L_6(dppp)_3](OTf)_3\}^{3+}$	**772.15**	$\{[Al^{III}_2Pd^{II}L_6(dppp)](OTf)_4\}^{2+}$
1206.09	$\{[Cr^{III}_2Pd^{II}_2L_6(dppp)_2](OTf)_4\}^{2+}$	**1010.08**	$\{[Al^{III}_2Pd^{II}_3L_6(dppp)_3](OTf)_3\}^{3+}$
		1182.13	$\{[Al^{III}_2Pd^{II}_2L_6(dppp)_2](OTf)_4\}^{2+}$

3.3.3 Magnetic Studies

SQUID Magnetometry

The dc (direct current) molar magnetic susceptibility, χ_M, of a polycrystalline sample of **15** was measured in an applied magnetic field, B, of 0.1 T, over the 2-300 K temperature, T, range. The experimental results are shown in Fig. 3.10 in the form of the $\chi_M T$ product, where $\chi_M = M / B$, and M is the magnetisation of the sample. At room temperature, the value of $\chi_M T$ is 14.4 $cm^3\ mol^{-1}\ K$, which is in excellent agreement with the sum of the Curie constants for a $[Fe^{III}_2Co^{II}_3]$ unit (14.375 $cm^3\ mol^{-1}\ K$, $g_{Fe} = g_{Co} = 2.0$). Note that the estimation of the g-value of the Co^{II} ions is an approximation and subject to error (e.g., lattice solvent lost upon sample drying will result in a variation of the samples diamagnetism), and a better measure comes from the EPR spectroscopy, which is consistent with $g = 2.3$ (*vide infra*). Upon cooling, the value of $\chi_M T$ remains essentially constant down to approximately 100 K, where it begins to decrease, reaching a minimum of 14.375 $cm^3\ mol^{-1}\ K$ at 2 K. This decrease in the value of $\chi_M T$ can be attributed to the large single-ion magnetic anisotropy of the Co^{II} ions and/or antiferromagnetic exchange interactions between the Fe^{III} and Co^{II} ions.

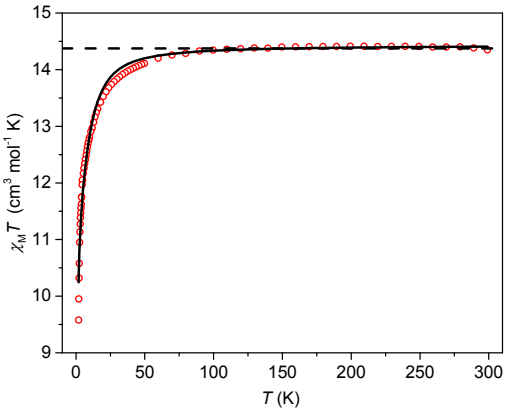

Figure 3.10 Plot of $\chi_M T$ vs T for **15**, with experimental data (•), the sum of the Curie constants of uncorrelated ions (---), and the best-fit data (**-**).

In order to further probe the low temperature magnetic properties of **15**, variable-temperature-and-variable-field (VTVB) measurements were carried out (Fig. 3.11). The magnetisation of **15** is 13.7 μ_B (μ_B is the Bohr magneton) at the highest investigated field and temperature, 5 T and 2 K, respectively. When the VTVB data of **15** is plotted against the reduced quantity $\mu_B B/kT$ (Fig. 3.11) we can see that the lines do not completely superimpose. This is indicative of a small value of anisotropy within the system, with respect to the temperature of the measurement.

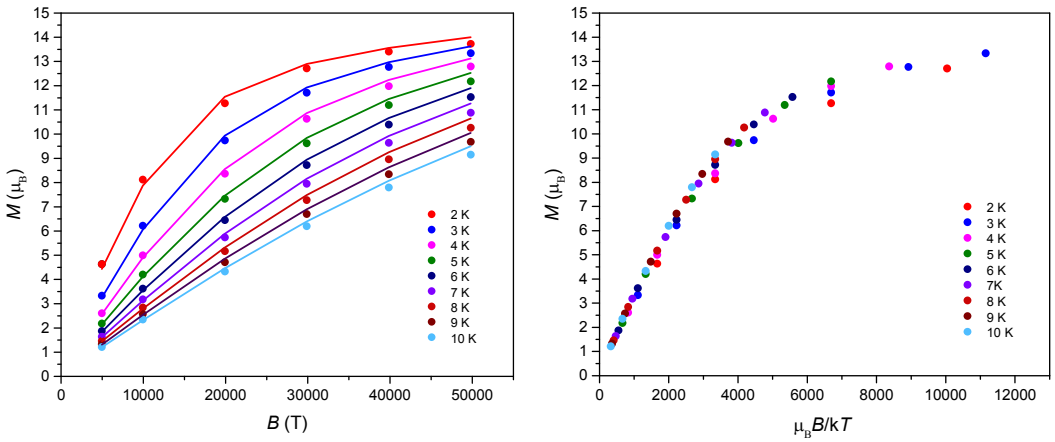

Figure 3.11 VTVB magnetisation data of **15** (left) in the field and temperature ranges 0.5 to 5 T and 2 to 10 K, respectively, with reduced magnetisation curves (right).

In order to fit the magnetisation data we used the spin-Hamiltonian (7):

$$\hat{H} = -2\sum_{i,j<i} J_{ij}\hat{S}_i \cdot \hat{S}_j + \mu_B B\sum_i g_i \hat{S}_i + \sum_i D_i\left[\hat{S}_{i,z}^2 - S_i(S_i+1)/3\right] \qquad (7)$$

where the summation indexes i, j run through the constitutive metal centres, g_i is the g-factor of the i^{th} centre, $\hat{S}$ is a spin operator, J is the isotropic exchange interaction parameter, D is the uniaxial anisotropy parameter, and S is the total spin.

For simplicity, we assume that $g_{Co} = g_{Fe} = 2$, $S_{Fe} = 5/2$, $S_{Co} = 3/2$, and $D_{Fe} = 0$ ($D_{Fe} << D_{Co}$), and from the EPR spectroscopy and theoretical studies (*vide infra*), we fix D_{Co} = -14 cm^{-1}. The only free parameter, therefore, is the isotropic exchange between Fe^{III} and Co^{II}, given by $J_{Fe\text{-}Co}$. The $\chi_M T$ product of **15** was fitted to spin-Hamiltonian (7) by full matrix numerical diagonalisation of the spin-Hamiltonian of the full system of dimension 2304 by 2304, through use of the Levenberg-Marquardt algorithm,[27] resulting in the best fit parameter of $J_{Fe\text{-}Co}$ = -0.04 cm^{-1}. In order to validate this model, we fixed $J_{Fe\text{-}Co}$ = -0.04 cm^{-1}, and D_{Co} = -14 cm^{-1}, and simulated the VTVB behaviour using (7), the results of which are shown as the solid lines in Fig. 3.10. The simulated data matches that of the experimental, thus validating our model.

Using these parameters we were able to generate the energy spectrum of **15** which consists of four groups of densely packed states, each separated by ≈2D_{Co} (Fig. 3.12). The D_{Fe} values obtained from EPR spectroscopy (*vide infra*) would have a negligible effect on the global level structure in Fig. 3.12, because both $|D_{Fe}|$ and $|J_{Fe\text{-}Co}|$ are << $|D_{Co}|$. However, it would affect the detail of the states within each of the densely packed multiplets of Fig. 3.12, because $|D_{Fe}|$ and $|J_{Fe\text{-}Co}|$ are of similar magnitude. It is also interesting to note that multiple ground level crossings simultaneously occur at approximately 0.47 T when the magnetic field is applied parallel to the quantisation axis.

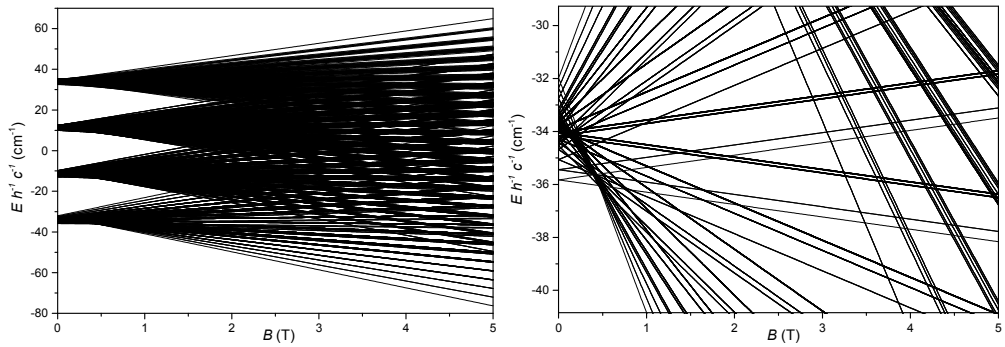

Figure 3.12 Energy spectrum of **15** determined using the best-fit parameters and the magnetic field applied along the quantisation axis (left). The low-lying states of the energy spectrum of **15**.

EPR Spectroscopy

In Chapter 2 the EPR spectrum of [$Cr^{III}L_3$] was reported, giving the zero-field splitting of the S = 3/2 ion as D = -0.55 cm^{-1}, with a small rhombicity of $|E/D|$ = 0.045. Q-band spectra of **17** and **18** are similar to that of [$Cr^{III}L_3$], giving D = -0.64 and -0.61 cm^{-1}, respectively (Fig. 3.13; $|E/D|$ = 0.03-0.04). Although, the crystallographic parameters of the {CrO_6} coordination sphere do not appear to drastically change on coordination to the M^{II} ion, there is nonetheless a small distortion imposed, which results in a small, but measurable, increase in the zero-field splitting parameter at Cr^{III}.

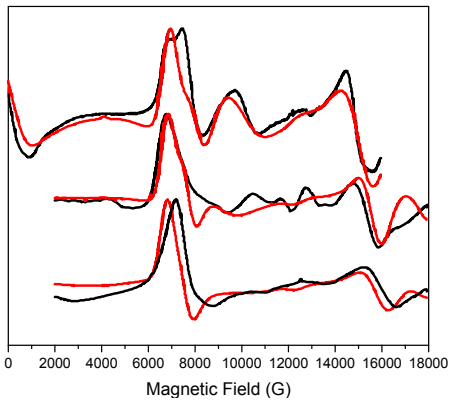

Figure 3.13 Q-band EPR spectra of (from top to bottom) [$Cr^{III}L_3$], **18**, and **17** at 10 K (-), and calculated spectra (-) with D = -0.55 cm^{-1} ($|E/D|$ = 0.045) for [$Cr^{III}L_3$], D = -0.61 cm-1 ($|E/D|$ = 0.036) for **18**, and D = -0.64 cm^{-1} ($|E/D|$ = 0.03) for **17** (with 400 G Gaussian linewidths and 5-10% D-strain).

This increase in the zero-field splitting parameter is comparable to that of the Fe^{III} systems. For $[Fe^{III}L_3]$ ($S = 5/2$), X- and Q-band spectra reveal a rather small zero-field splitting of $D = 0.08$ cm^{-1}, with $|E/D| = 1/3$ (Fig 3.14; note the sign of D has no significance with a fully rhombic $\boldsymbol{D}$-tensor). These values are comparable to previous studies on the similar Fe^{III} complexes $[Fe(acac)_3]$ ($|D| = 0.16$ cm^{-1}, $E/D = 0.3$),[28] and $[Fe(dpm)_3]$ (dpm = dipivaloylmethane; $D = -0.20$ cm^{-1}, $|E/D| = 0.25$),[29] which show D to be sensitive to any trigonal distortion at Fe^{III}. Compared with the Cr^{III} systems, we see a richer EPR spectrum upon formation of **16** (Fig. 3.14), with the increase in the Fe^{III}-O bonds and O-Fe^{III}-O angles of the $\{FeO_6\}$ coordination sphere resulting in an increase in the zero-field splitting parameter ($D = 0.20$ cm^{-1}; $E/D = 1/3$).

Complex **15** gives an EPR spectrum with very broad features at ≈5, 9 and 12 kG that line up with the main features of the spectrum of **16**, meaning the zero-field splitting at Fe^{III} must be similar. Both our theoretical measurements (*vide infra*), and the lack of additional features in the Q-band EPR spectrum, help confirm the small value of $J_{Fe\text{-}Co}$ obtained from our magnetisation measurements (-0.04 cm^{-1}). The very large value of D_{Co} obtained from our measurements also suggests that only transitions within the ground Kramers doublet of this ion are observed (the microwave energy, $h\nu << |D_{Co}|$), and there must be a significant rhombicity in order for these transitions to fall within the observed features.

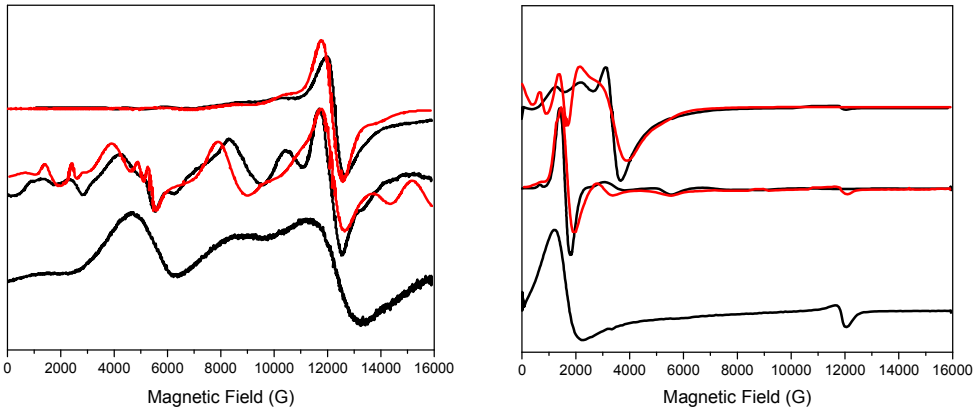

Figure 3.14 Q-band (left) and X-band (right) EPR spectra of powdered samples of (from top to bottom) $[Fe^{III}L_3]$, **16**, and **15** at 5 K (**-**), and calculated spectra (**-**), with $D = 0.08$ cm^{-1} ($|E/D| = 1/3$) for $[Fe^{III}L_3]$, and $D = 0.20$ cm^{-1} ($|E/D| = 1/3$) for **16** (with 400 G Gaussian linewidths and 10-20% *D*-strain).

Theoretical Studies

In order to independently verify the large zero-field splitting parameter of Co^{II}, we have performed complete active space self-consistent field (CASSCF) calculations on the three unique Co^{II} sites of **15** (Table 3.5).

Table 3.5 CASSCF calculated zero-field splitting of the *S* = 3/2 state of the three Co^{II} sites in **15**.

Site	Co1	Co2	Co3	Average
D (cm^{-1})	-11.8	-19.1	-11.9	-14
E (cm^{-1})	1.51	1.27	1.51	1.4
$\lvert E/D \rvert$	0.128	0.066	0.127	0.1

The results suggest D_{Co} = -14 cm^{-1} and E/D = 0.1, which is entirely consistent with the magnetometry and heat capacity data (*vide infra*). The calculations also suggest that the principal axes of the local zero-field splitting tensors are approximately orientated perpendicular to the Fe^{III}-Fe^{III} axis and are positioned approximately 120° with respect to one another in the plane (Fig. 3.15).

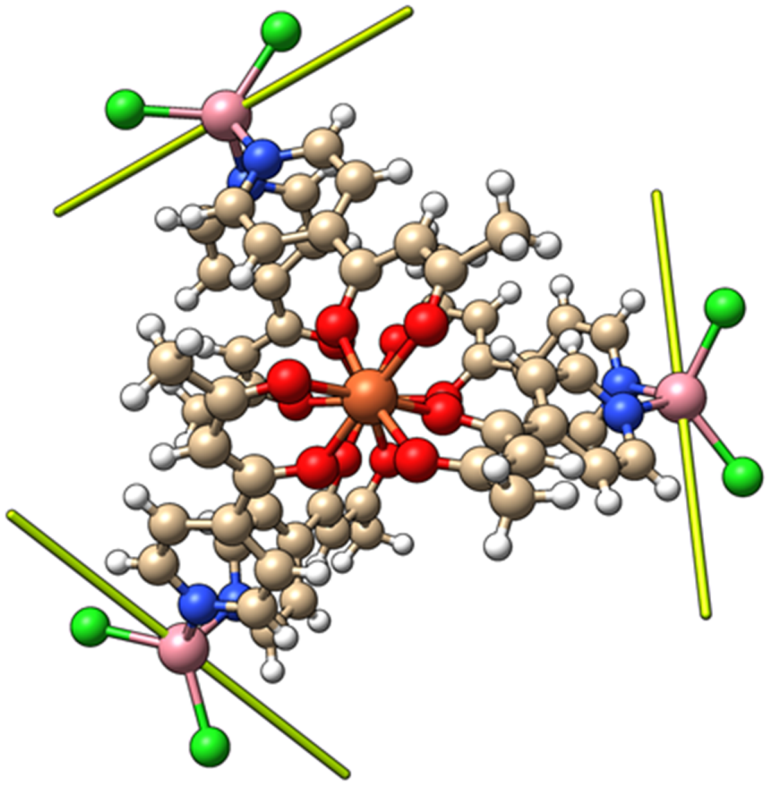

Figure 3.15 Orientation of the principal anisotropy axis for the Co^{II} sites in **15** (yellow rods). Colour code: Fe^{III} – Orange, Co^{II} – Pink, Cl^{-} – Bright Green, N – Blue, O – Red, C – Beige, H – White.

Heat Capacity Measurements

Fig. 3.16 shows the collected heat capacity data, normalised to the gas constant, c_p/R of **15** as a function of temperature (≈ 0.3-30 K) for zero-applied magnetic field. Lattice vibrations contribute predominantly to c_p as the temperature is increased to above that of liquid-helium temperature, which is not uncommon for molecular magnetic materials.[30] The lattice contribution can be described by the Debye model (dotted line in Fig. 3.16), which simplifies to a $c_p/R = aT^3$ dependence at the lowest temperatures, where $a = 7.6 \times 10^{-3}$ K^{-3} for **15**.

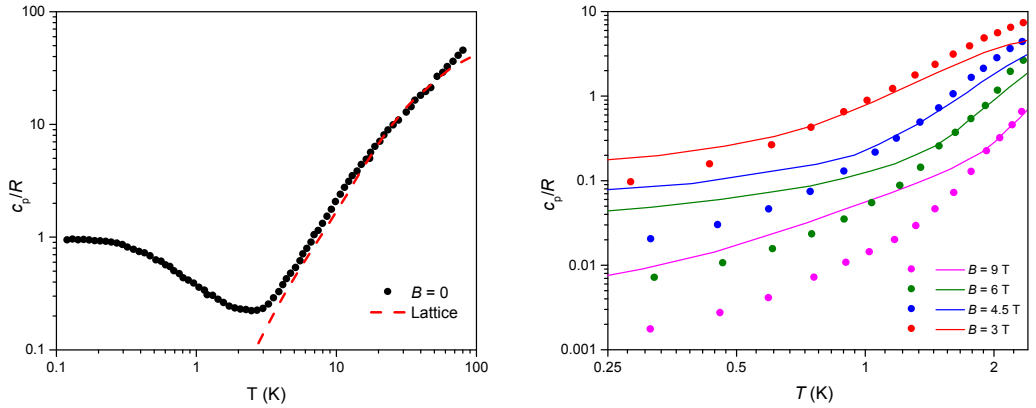

Figure 3.16 Temperature dependence of the zero-field heat capacity c_p, normalised to the gas constant R, for **15** (•), with the lattice contribution (---, left). Temperature dependence of c_p/R of **15** for T < 2 K and B ≥ 3 T (right) with experimental data (•) and best-fit data (-).

Below ≈3 K and in zero-field, we see a bump-like anomaly which corresponds to the splitting of the spin levels by crystal field effects and magnetic interactions. At these low temperatures, the magnetic measurements are very sensitive to the applied magnetic field, and there are significant deviations away from expected values for fields of 3 T and higher (Fig. 3.16). As a result of the small value of $J_{Fe\text{-}Co}$ (-0.04 cm^{-1}), and the high magnetic field, the centres can undergo full decoupling, meaning that for applied magnetic fields ≥3 T we can negate the presence of $J_{Fe\text{-}Co}$ and probe the influence of crystal fields on **15**. These measurements will allow us to examine temperatures down to ≈0.3 K, which are significantly lower than that of the magnetisation measurements (2 K).

Calculations using the spin-Hamiltonian (7) and the best-fit parameters from the magnetothermal and spectroscopic data, and the theoretical calculations (D_{Co} = -14 cm^{-1} and the here-negligible $J_{Fe\text{-}Co}$ = -0.04 cm^{-1}), gave the solid curves in Fig 3.16. The agreement between experimental and calculated data is good, but not outstanding, even when D_{Fe} (-0.2 cm^{-1}) is included. The fit is particularly unsatisfactory below ≈1 K which can be explained by the wider broadening of the low-lying energy spectrum, likely induced by higher-order anisotropy terms not included in (7).

3.4 Conclusions

Changing our acceptor from that of Chapter 2 has allowed us to synthesise five new $[M^{III}_2M^{II}_3L_6]^{n+}$ trigonal biyramids using pyridyl-based $[M^{III}L_3]$ metalloligands. The cages have been crystallised, and their behaviour characterised by a battery of physical techniques, both in solution and in the solid-state.

The fully magnetic complex **15** represents the first example of such a cage (outhwith cyanometalate chemistry) containing only paramagnetic metal ions. SQUID magnetometry, EPR spectroscopy, heat capacity measurements, and CASSCF calculations are all in agreement with each other, revealing weak antiferromagnetic exchange interations between the Fe^{III} and Co^{II} ions, and zero-field splitting parameters of $|D_{Co}|$ = 14 cm^{-1}, and $|D_{Fe}|$ = 0.2 cm^{-1}. CASSCF calculations also show that the principal axes of the local zero-field splitting tensors are located perpendicular to the Fe^{III}-Fe^{III} axis, and are positioned approximately 120° with respect to one another in the plane.

The self-assembly process occurs with high stereoselectivity, with **18** and **19** revealing unusual heterochiral ΛΔ configurations, and **15**-**17** revealing racemic ΛΛ or ΔΔ configurations about the M^{III} ion. ^{1}H NMR spectroscopy on **19** reveals some interesting features about the self-assembly process, showing amplification of the *fac*-geometrical isomer, through the rearrangement of the *mer*-isomer, upon formation of the trigonal bipyramidal structure.

The ability to easily change our acceptor in order to access other structurally analogous, but physically different coordination capsules, once again highlights how applicable the metalloligand approach is in the creation of novel magnetic cages.

3.5 References

(1) Chakrabarty, R.; Mukherjee, P. S.; Stang, P. J. *Chem. Rev.* **2011**, *111* (11), 6810.

(2) Wang, M.; Vajpayee, V.; Shanmugaraju, S.; Zheng, Y.-R.; Zhao, Z.; Kim, H.; Mukherjee, P. S.; Chi, K.-W.; Stang, P. J. *Inorg. Chem.* **2011**, *50* (4), 1506.

(3) Sun, X.; Johnson, D. W.; Caulder, D. L.; Raymond, K. N.; Wong, E. H. *J. Am. Chem. Soc.* **2001**, *123* (12), 2752.

(4) Hiraoka, S.; Sakata, Y.; Shionoya, M. *J. Am. Chem. Soc.* **2008**, *130* (31), 10058.

(5) Sakata, Y.; Hiraoka, S.; Shionoya, M. *Chem. - A Eur. J.* **2010**, *16* (11), 3318.

(6) Van Langenberg, K.; Batten, S. R.; Berry, K. J.; Hockless, D. C. R.; Moubaraki, B.; Murray, K. S. *Inorg. Chem.* **1997**, *36* (22), 5006.

(7) Wang, C. F.; Zuo, J. L.; Bartlett, B. M.; Song, Y.; Long, J. R.; You, X. Z. *J. Am. Chem. Soc.* **2006**, *128* (22), 7162.

(8) Bartlett, B. M.; Harris, T. D.; DeGroot, M. W.; Long, J. R. *Zeitschrift für Anorg. und Allg. Chemie* **2007**, *633* (13–14), 2380.

(9) Yao, M.-X.; Wei, Z.-Y.; Gu, Z.-G.; Zheng, Q.; Xu, Y.; Zuo, J.-L. *Inorg. Chem.* **2011**, *50* (17), 8636.

(10) Fujita, M.; Yazaki, J.; Ogura, K. *J. Am. Chem. Soc.* **1990**, *112* (14), 5645.

(11) Wu, H.-B.; Wang, Q.-M. *Angew. Chem. Int. Ed.* **2009**, *48* (40), 7343.

(12) Aquilante, F.; Autschbach, J.; Carlson, R. K.; Chibotaru, L. F.; Delcey, M. G.; De Vico, L.; Fdez. Galván, I.; Ferré, N.; Frutos, L. M.; Gagliardi, L.; Garavelli, M.; Giussani, A.; Hoyer, C. E.; Li Manni, G.; Lischka, H.; Ma, D.; Malmqvist, P. Å.; Müller, T.; Nenov, A.; Olivucci, M.; Pedersen, T. B.; Peng, D.; Plasser, F.; Pritchard, B.; Reiher, M.; Rivalta, I.; Schapiro, I.; Segarra-Martí, J.; Stenrup, M.; Truhlar, D. G.; Ungur, L.; Valentini, A.; Vancoillie, S.; Veryazov, V.; Vysotskiy, V. P.; Weingart, O.; Zapata, F.; Lindh, R. *J. Comput. Chem.* **2016**, *37* (5), 506.

(13) Roos, B. O.; Lindh, R.; Malmqvist, P.-Å.; Veryazov, V.; Widmark, P.-O. *J. Phys. Chem. A* **2005**, *109* (29), 6575.

(14) Coles, S. J.; Gale, P. A. *Chem. Sci.* **2012**, *3*, 683.

(15) Rigaku Oxford Diffraction. In *CrystalClear-SM Expert 3.1 b27*; 2012.

(16) Rigaku Oxford Diffraction. In *CrysAlisPro 1.171.38.41*; 2015.

(17) Rigaku Oxford Diffraction. In *CrysAlisPro*; 2016.

(18) Palatinus, L.; Chapuis, G. *J. Appl. Crystallogr.* **2007**, *40* (4), 786.

(19) Sheldrick, G. M. *Acta Crystallogr. Sect. A Found. Crystallogr.* **2007**, *64* (1), 112.

(20) Sheldrick, G. M. *Acta Crystallogr. Sect. C Struct. Chem.* **2015**, *71* (1), 3.

(21) Dolomanov, O. V.; Blake, A. J.; Champness, N. R.; Schröder, M. *J. Appl. Crystallogr.* **2003**, *36* (5), 1283.

(22) Spek, A. L. *Acta Crystallogr. Sect. C Struct. Chem.* **2015**, *71* (1), 9.

(23) Roberts, D. A.; Castilla, A. M.; Ronson, T. K.; Nitschke, J. R. *J. Am. Chem. Soc.* **2014**, *136* (23), 8201.

(24) Dabb, S. L.; Fletcher, N. C. *Dalton Trans.* **2015**, *44* (10), 4406.

(25) Riddell, I. A.; Smulders, M. M. J.; Clegg, J. K.; Hristova, Y. R.; Breiner, B.; Thoburn, J. D.; Nitschke, J. R. *Nat. Chem.* **2012**, *4* (10), 860.

(26) Pastor, A.; Martínez-Viviente, E. *Coord. Chem. Rev.* **2008**, *252* (21–22), 2314.

(27) Press, W. H.; Flannery, B. P.; Teukolsky, S. A.; Vetterling, W. T. *Numerical Recipes in C: The Art of Scientific Computing*, 2nd ed.; Cambridge University Press: Cambridge, 1992.

(28) Collison, D.; Powell, A. K. *Inorg. Chem.* **1990**, *29* (23), 4735.

(29) Barra, A. L.; Caneschi, A.; Cornia, A.; Fabrizi de Biani, F.; Gatteschi, D.; Sangregorio, C.; Sessoli, R.; Sorace, L. *J. Am. Chem. Soc.* **1999**, *121* (22), 5302.

(30) Evangelisti, M.; Luis, F.; de Jongh, L. J.; Affronte, M. *J. Mater. Chem.* **2006**, *16* (26), 2534.

Chapter 4: Imine-Based $[M^{III}_2M^{II}_3L^{im}_3]^{n+}$ and Amide-Based $[M^{III}_2L^{am}_3]$ Trigonal Bipyramids

4.1 Introduction

The previous two chapters showed how the combination of a $[M^{III}L_3]$ metalloligand (M^{III} = Cr, Fe, and Al; HL = 1-(4-pyridyl)butane-1,3-dione) and a "naked" octahedral or *cis*-capped/tetrahedral metal salt gives rise to a coordination cube or trigonal bipyramid, respectively. The development of these type of discrete cages is not limited to the exploitation of the simple interaction observed with the pyridyl-based ligand however, with the development of a new type of metalloligand allowing us access to the field of magnetic dynamic covalent chemistry. The use of reversible covalent reactions should allow for the self-correction required within the self-assembly process, with the type of reaction limited only by the functional groups appended on the building block.

As discussed in Chapter 1, Nitschke and co-workers have heavily employed dynamic covalent Schiff-base reactions between 2-pyridinecarboxaldehyde and a range of amines to create coordination capsules, including magnetic Co^{II} or Ni^{II} M_4L_6 tetrahedra.[1,2] Kaifer and co-workers have also used the reagent 2-pyridinecarboxaldehyde to make a Ni^{II} M_4L_6 structure, with the inclusion of a urea group in the *bis*(amine) allowing for hydrogen bonding driven cage formation through the encapsulation of a sulfate ion.[3] This urea group is similar to that of a *bis*(amide) group, a functional group that has been employed for the encapsulation of guests by groups such as Puddephatt and co-workers, who have encapsulated triflate and trifluorocarboxalate ions inside their Pd^{II} "lantern complexes".[4] The *bis*(amide) group, synthesised through the reaction of 3-aminopyridine and isophthaloyl chloride, is a common motif within the field of dynamic covalent chemistry, and is of a stronger nature than the aforementioned imine bond.[5] Indeed, isophthaloyl chloride has been heavily employed by groups such as Leigh and co-workers in the synthesis of cantenanes and rotaxanes,[6–8] some of which act as molecular motors.[9,10] These molecular motors have generated a lot of interest in recent years, with Sauvage, Stoddart, and Feringa winning the Nobel Prize in 2016 for their work on "nano-machines".[11–13]

Herein, we present the synthesis and characterisation of a new series of magnetic trigonal bipyramids synthesised by Schiff-base reactions, or amide-formation reactions, using the aniline-based metalloligand $[Fe^{III}L^{NH2}{}_3]$ (Fig. 4.1; HL^{NH2} = 1-(4-aminophenyl)butane-1,3-dione) and 2,6-pyridinedicarboxaldehyde or isophthaloyl chloride, respectively. In the previous chapter it was shown that metalloligands of this type are configurationally dynamic in solution, with the rearrangement of the *mer*-geometrical isomer to the *fac*-isomer in order to form the entropically favoured trigonal bipyramid.

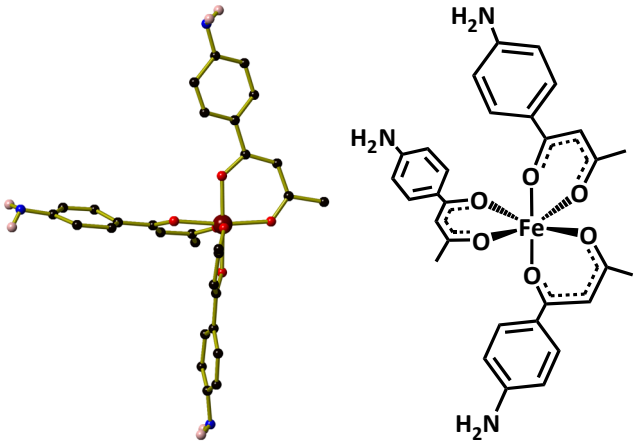

Figure 4.1 The molecular structure of *mer*-[$Fe^{III}L^{NH2}_3$] with some hydrogen atoms removed for clarity (left), and a skeletal representation for clarity (right). Colour code: Fe^{III} – Maroon, O – Red, N – Blue, C – Black, H – Pale Pink.

4.2 Experimental

4.2.1 Materials and Instrumentation

All reactions were performed under aerobic conditions. Solvents and reagents were used as received from commercial suppliers. Elemental analyses were carried out by Medac Ltd. NMR spectra were recorded on a 500 MHz Bruker Advance NMR spectrometer. Magnetisation measurements were carried out on a Quantum Design SQUID MPMS-XL magnetometer, operating between 1.8 and 300 K for dc applied magnetic fields ranging from 0 to 7 T.

4.2.2 Syntheses

Preparation of 1-(4-aminophenyl)butane-1,3-dione (HL^{NH2})

To a solution of 4'-aminoacetophenone (8.121 g, 60.08 mmol) and sodium *tert*-butoxide (17.322 g, 180.24 mmol) in THF (500 mL), was added EtOAc (17.61 mL, 180.24 mmol) in THF (50 mL). The reaction was stirred at 65 °C for 5 hours, after which time the orange precipitate was collected and washed with THF (10 mL) and diethyl ether (10 mL). The solid was dissolved in water and the pH was adjusted to 7 using acetic acid. The yellow precipitate that formed was collected by filtration and washed with water (10 mL) and diethyl ether (10 mL) The yellow solid was dissolved in a solution of HCl in MeOH (37% HCl, 1:19 v/v, 230 mL) and heated to 60 °C for 6 hours. The solution was cooled to 0 °C before the pH was adjusted to 7 using a saturated aqueous solution of $NaHCO_3$. MeOH was removed under reduced pressure and the product extracted with EtOAc, before being dried over anhydrous $MgSO_4$. Removal of EtOAc under reduced pressure

yielded HL^{NH2} as an orange oil (4.651 g, 43.14 %). ^{1}H NMR ($CDCl_3$, 500 MHz): δ 7.76 (m, 2H, Ar-*H*), 6.70 (m, 2H, Ar-*H*), 6.09 (s, 1H, COC*H*CO), 4.02 (bs, 2H, NH_2), 2.17 (s, 3H, CH_3) ppm.

Synthesis of *tris*{1-(4-aminophenyl)acetylacetonato}iron(III), $[Fe^{III}L^{NH2}{}_3]$

$FeCl_3$ (0.162 g, 1.0 mmol), HL^{NH2} (0.620 g, 3.5 mmol) and sodium methoxide (0.189 g, 3.5 mmol) were dissolved in MeOH/H_2O (1:1 v/v, 100 mL), and left to stir until a red product precipitated (≈6 h). The precipitate was filtered and washed with water, before the crude product was extracted with CH_2Cl_2, and dried over anhydrous $MgSO_4$. The CH_2Cl_2 was removed under reduced pressure to afford the product as a red solid (0.446 g, 76 %). Elemental analysis (%) calculated (found) for $C_{30}H_{33}N_3O_6Fe$ (587.45 g mol^{-1}): C 61.34 (61.18), H 5.66 (5.57), N 7.15 (7.09).

$[Fe^{III}{}_2Ni^{II}{}_3L^{im}{}_3(H_2O)_9]Cl_6$ (20)

To a solution of $[Fe^{III}L^{NH2}{}_3]$ (29.2 mg, 0.05 mmol) in MeCN (10 mL), was added 2,6-pyridinedicarboxaldehyde (10.1 mg, 0.075 mmol) and $NiCl_2$ (97.2 mg, 0.075 mmol). HOTf (8.8 μL, 0.01 mmol, 10% in MeCN) was added, and the solution was stirred for 2 hours at 60 °C, before being filtered and allowed to stand. Red X-ray quality crystals were obtained from the diffusion of methyl *tert*-butyl ether into the solution after 3 days. Yield (35 mg, 69 %). Elemental analysis (%) calculated (found) for $C_{81}H_{79}N_9O_{21}Cl_6Fe_2Ni_3$ (2015.06 g mol^{-1}): C 48.28 (48.02), H 3.95 (3.87), N 6.26 (6.19).

$[Fe^{III}{}_2Co^{II}{}_3L^{im}{}_3(H_2O)_9](BF_4)(OTf)$ (21)

To a solution of $[Fe^{III}L^{NH2}{}_3]$ (29.2 mg, 0.05 mmol) in MeCN (10 mL), was added 2,6-pyridinedicarboxaldehyde (10.1 mg, 0.075 mmol) and $Co(BF_4)_2{\cdot}6H_2O$ (25.5 mg, 0.075 mmol). HOTf (8.8 μL, 0.01 mmol, 10% in MeCN) was added, and the solution was stirred for 2 hours at 60 °C, before being filtered and allowed to stand. Red X-ray quality crystals were obtained from the diffusion of methyl *tert*-butyl ether into the solution after 3 days. Yield (35 mg, 69 %). Elemental analysis (%) calculated (found) for $C_{82}H_{81}BF_7N_9O_{24}SFe_2Co_3$ (2040.91 g mol^{-1}): C 48.26 (48.15), H 4.00 (3.94), N 6.18 (6.09).

$[Fe^{III}{}_2Co^{II}{}_3L^{im}{}_3(H_2O)_9][CoCl_4]$ (22)

To a solution of $[Fe^{III}L^{NH2}{}_3]$ (29.2 mg, 0.05 mmol) in MeCN (10 mL), was added 2,6-pyridinedicarboxaldehyde (10.1 mg, 0.075 mmol) and $CoCl_2$ (97.4 mg, 0.075 mmol). HOTf (8.8 μL, 0.01 mmol, 10% in MeCN) was added, and the solution was stirred for 2 hours at 60 °C, before being filtered and allowed to stand. Red X-ray quality crystals were obtained from the diffusion of diisopropyl ether into the solution after 5 days. Yield (32 mg, 63 %). Elemental analysis (%) calculated (found) for $C_{81}H_{63}N_9O_{15}Cl_8Fe_2Co_4$ (2033.42 g mol^{-1}): C 47.84 (47.75), H 3.12 (3.09), N 6.20 (6.17).

$[Fe^{III}_2L^{am}_3]•Cl_2$ (23)

To a solution of $[Fe^{III}L^{NH2}_3]$ (29.2 mg, 0.05 mmol) in CH_2Cl_2/MeCN (10 mL), was added isophthaloyl chloride (15.2 mg, 0.075 mmol). Triethylamine (21 μL, 0.15 mmol) was added, and the solution was stirred for 14 hours, before being filtered and allowed to stand. Red X-ray quality crystals were obtained from the diffusion of diisopropyl ether into the solution after 2 days. Yield (30 mg, 52 %). Elemental analysis (%) calculated (found) for $C_{115}H_{127}N_{17}O_{18}Cl_4Fe_2$ (2288.83 g mol^{-1}): C 60.35 (60.29), H 5.59 (5.50), N 10.40 (10.36).

$[Fe^{III}_2L^{am}_3]$ (24)

To a solution of $[Fe^{III}L^{NH2}_3]$ (29.2 mg, 0.05 mmol) in CH_2Cl_2/MeCN (10 mL), was added isophthaloyl chloride (15.2 mg, 0.075 mmol). Triethylamine (21 μL, 0.15 mmol) was added, and the solution was stirred for 14 hours, before being filtered. Silver hexafluorophosphate (37.9 mg, 0.15 mmol) was added, and the solution was stirred for 5 hours, in which time a precipitate was formed. The red solid product was isolated by filtration and dissolved in DMF. Red X-ray quality crystals were obtained from the diffusion of methyl *tert*-butyl ether into the solution after 2 days. Yield (28 mg, 51 %). Elemental analysis (%) calculated (found) for $C_{116}H_{142}N_{10}O_{26}Fe_2$ (2204.09 g mol^{-1}): C 63.21 (63.13), H 6.49 (6.41), N 6.35 (6.30).

$[Fe^{III}_2L^{am}_3]•Cl_3$ (25)

To a solution of $[Fe^{III}L^{NH2}_3]$ (29.2 mg, 0.05 mmol) in CH_2Cl_2/MeCN (10 mL), was added isophthaloyl chloride (15.2 mg, 0.075 mmol). Triethylamine (21 μL, 0.15 mmol) was added, and the solution was stirred for 14 hours, before being filtered. $(Bu_4N)_2[ReCl_6]$ (96.2 mg, 0.15 mmol) was added, and the solution was stirred for 3 hours, before being filtered and allowed to stand. Dark red X-ray quality crystals were obtained from the diffusion of diethyl ether into the solution after 4 days. Yield (39 mg, 57 %). Elemental analysis (%) calculated (found) for $C_{149}H_{199.5}N_{17.5}O_{18}Cl_3Fe_2$ (2741.80 g mol^{-1}): C 65.27 (65.21), H 7.33 (7.29), N 8.94 (8.89).

4.2.3 Crystal Structure Information

For complexes **20**-**22** single-crystal X-ray diffraction data were collected at T = 100 K on a Rigaku AFC12 goniometer equipped with an enhanced sensitivity (HG) Saturn 724+ detector mounted at the window of a FR-E+ Superbright MoKα (λ = 0.71075 Å) rotating anode generator with HF Varimax optics (100 μm focus) using Rigaku Crystal Clear and CrysalisPro software for data collection and reduction.[14–16]

The crystal structures of **20**-**22** were solved using Intristic Phasing as implemented in SHELXT.[17] All structures were refined on F_o^2 by full-matrix least-squares refinements using ShelXL within the OLEX2 suite.[18,19] All non-hydrogen atoms were refined with anisotropic displacement

parameters, and all hydrogen atoms were added at calculated positions and refined using a riding model with isotropic displacement parameters based on the equivalent isotropic displacement parameter (U_{eq}) of the parent atom. In **20** the water molecules coordinated to Ni2 shows positional disorder over special positions (2-fold axis). In **21**, the heavily disordered triflate ion has been refined as isotropic only. In **22** one of the L^{2-} ligands coordinated to Fe1 and Co2, and the water molecules coordinated to Co2, are disordered. DFIX restraints were used to maintain reliable molecular geometry. SIMU, DELU and RIGU restraints were applied to model appropriately atomic displacement parameters (ADP).

All crystal structures contain accessible voids and channels that are filled with diffuse electron density belonging to non-coordinated solvent, whose electron contribution was accounted for by the PLATON/SQUEEZE routine.[20,21] Crystals of complexes **20**-**22** were sensitive to solvent loss and diffracted poorly, which is reflected in the higher values of R_{int} and R_1.

For complexes **23**-**25**, a suitable crystal was selected and mounted on a MITIGEN holder in Paratone oil on a Rigaku Oxford Diffraction SuperNova diffractometer. Using Olex2,[22] the structure was solved with the ShelXT structure solution program,[23] using the Intrinsic Phasing solution method. The model was refined with version 2016/6 of ShelXL using Least Squares minimisation.[18]

The molecular formulae for complexes **20**-**25** are tabulated below for convenience (Table 4.1), and a crystallographic summary with structure refinement details are presented in Tables 4.2 and 4.3.

Table 4.1 Molecular formulae for complexes **20**-**25**. Additional solvent molecules of crystallisation and counterions have been removed from the molecular formulae for clarity.

Complex	Molecular formula
20	$[Fe^{III}_2Ni^{II}_3L^{im}_3(H_2O)_9]Cl_6$
21	$[Fe^{III}_2Co^{II}_3L^{im}_3(H_2O)_9](BF_4)(OTf)$
22	$[Fe^{III}_2Co^{II}_3L^{im}_3(H_2O)_9][CoCl_4]$
23	$[Fe^{III}_2L^{am}_3]\bullet Cl_2$
24	$[Fe^{III}_2L^{am}_3]$
25	$[Fe^{III}_2L^{am}_3]\bullet Cl_3$

Table 4.2 Crystallographic details for **20**-**22**.

Complex	20	21	22
Empirical formula	$C_{81}H_{79}Cl_6N_9O_{21}Fe_2Ni_3$	$C_{82}H_{81}BF_7N_9O_{24}SFe_2Co_3$	$C_{81}H_{63}Cl_8N_9O_{15}Fe_2Co_4$
Formula weight	2015.06	2040.91	2033.42
Colour	Red	Red	Red
Shape	Plate	Plate	Prism
Temperature, K	100.0	100.0	100.0
Crystal system	Monoclinic	Triclinic	Monoclinic
Space group	*I*12/*a*1	*P*-1	*P*12/*n*1
***a*, Å**	28.6659(14)	15.3967(14)	20.2134(6)
***b*, Å**	17.0846(9)	18.2132(14)	18.0881(6)
***c*, Å**	26.8865(15)	23.892(2)	20.8732(7)
***α*, °**	90.0	82.952(7)	90.0
***β*, °**	99.703(5)	73.678(8)	99.819(3)
***γ*, °**	90.0	84.412(7)	90.0
Volume, Å^3	12979.1(12)	6367.2(10)	7519.9(4)
Z	4	2	2
Density (calculated), mg m^{-3}	1.029	1.065	0.898
Absorption coefficient, mm^{-1}	0.820	0.687	0.800
Reflections collected	60609	62326	72896
Unique reflections	11441	22408	13261
Data/restraints/parameters	11441/1136/582	22408/2299/1136	13261/1566/651
Goodness-of-fit	1.587	0.890	0.988
R_{int}	0.1324	0.1880	0.0438
Final R_1	0.1716	0.1210	0.0852
Final wR_2	0.4556	0.3009	0.2669
CCDC Number			

Table 4.3 Crystallographic details for **23**-**25**.

Complex	23	24	25
Empirical formula	$C_{115}H_{127}Cl_4N_{17}O_{18}Fe_2$	$C_{116}H_{142}N_{10}O_{26}Fe_2$	$C_{149}H_{199.5}Cl_3N_{17.5}O_{18}Fe_2$
Formula weight	2288.83	2204.09	2741.80
Colour	Dark Red	Red	Dark Red
Shape	Block	Block	Block
Temperature, K	120.0	120.0	120.0
Crystal system	Triclinic	Monoclinic	Triclinic
Space group	*P*-1	*I*2/a	*P*-1
***a*, Å**	15.2552(4)	24.7630(10)	18.4659(4)
***b*, Å**	17.1217(4)	20.1439(5)	19.9774(5)
***c*, Å**	22.8788(5)	26.3684(13)	22.1077(6)
***α*, °**	84.558(2)	90	112.396(2)
***β*, °**	73.711(2)	117.130(6)	92.035(2)
***γ*, °**	86.464(2)	90	106.288(2)
Volume, Å^3	5706.3(2)	11706.0(10)	7144.0(3)
Z	2	4	2
Density (calculated), mg m^{-3}	1.332	1.251	1.275
Absorption coefficient, mm^{-1}	3.498	2.602	2.708
Reflections collected	85352	55205	110108
Unique reflections	21450	6135	26153
Data/restraints/parameters	21450/90/1242	6135/51/601	26153/238/1645
Goodness-of-fit	1.018	1.047	1.036
R_{int}	0.0836	0.0783	0.0843
Final R_1	0.0904	0.0746	0.0769
Final wR_2	0.2839	0.2205	0.2282
CCDC Number	1568874	1568872	1568875

4.3 Results and Discussion

4.3.1 Solid-State Structural Descriptions

For clarity, the structural descriptions will be separated into the two families of trigonal bipyramids, namely the imine-based $[Fe^{III}_2M^{II}_3L^{im}_3]^{n+}$ structures (**20**-**22**), and the amide-based $[Fe^{III}_2L^{am}_3]$ structures (**23**-**25**).

$[Fe^{III}_2M^{II}_3L^{im}_3]^{n+}$ Trigonal Bipyramids

The heterometallic cages $[Fe^{III}_2Ni^{II}_3L^{im}_3(H_2O)_9]Cl_6$ (**20**), $[Fe^{III}_2Co^{II}_3L^{im}_3(H_2O)_9](BF_4)(OTf)$ (**21**), and $[Fe^{III}_2Co^{II}_3L^{im}_3(H_2O)_9][CoCl_4]$ (**22**) were prepared by Schiff base reactions of $[Fe^{III}L^{NH2}_3]$ with 2,6-pyridinedicarboxaldehyde in the presence of a catalytic amount of trifluoromethanesulfonic acid, and the templating metal salts $NiCl_2$, $Co(BF_4)_2{\cdot}6H_2O$, and $CoCl_2$, respectively. Each $[Fe^{III}_2M^{II}_3]^{n+}$ skeleton is described by two Fe^{III} ions and three M^{II} ions occupying the axial and equatorial sites of the trigonal bipramid, respectively (Fig. 4.2). The Fe^{III} ions in all structures are all six-coordinate and are of $\{FeO_6\}$ octahedral geometry, with Fe^{III}-O distances in the range 1.91-2.06 Å, and O-Fe^{III}-O *cis*/*trans* angles in the ranges 85.52-99.61° and 171.13-177.03°, respectively. The approximate dimensions of the trigonal bipyramidal structures are $Fe^{III}\cdots M^{II}$ (9.30-9.63 Å), $Fe^{III}\cdots Fe^{III}$ (14.86-15.42 Å), and $M^{II}\cdots M^{II}$ (8.52-10.26 Å).

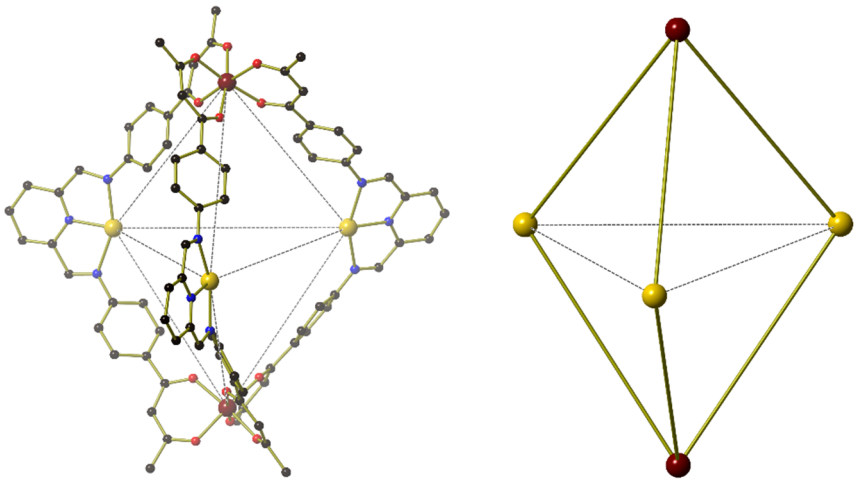

Figure 4.2 Example of an $[Fe^{III}_2M^{II}_3L_6]^{6+}$ trigonal bipyramid (left), with the ligands removed to show the metallic skeleton (right). All hydrogen atoms, counterions, and solvent molecules have been removed for clarity. Colour code: Fe^{III} – Maroon, M^{II} – Gold, N – Blue, O – Red, C – Black.

The Ni^{II} ions in **20** are all six-coordinate, with three nitrogen atoms of the ligand bonded to the Ni^{II} ions in a *mer*-fashion, with Ni^{II}-N bond distances and N-Ni^{II}-N *cis* angles in the ranges 1.97-2.12 Å and 76.71-87.67°, respectively. The coordination sphere is completed by three water molecules, with Ni^{II}-O bond distances and O-Ni^{II}-O *cis* angles in the ranges 1.96-2.03 Å and 77.74-93.87°, respectively. The overall charge of the complex is 6+, with charge balancing chloride ions hydrogen bonded to the water molecules on Ni^{II} (HO-H···Cl 2.68-2.83 Å), creating an aesthetically pleasing extended network of columns of trigonal bipyramids (Fig. 4.3).

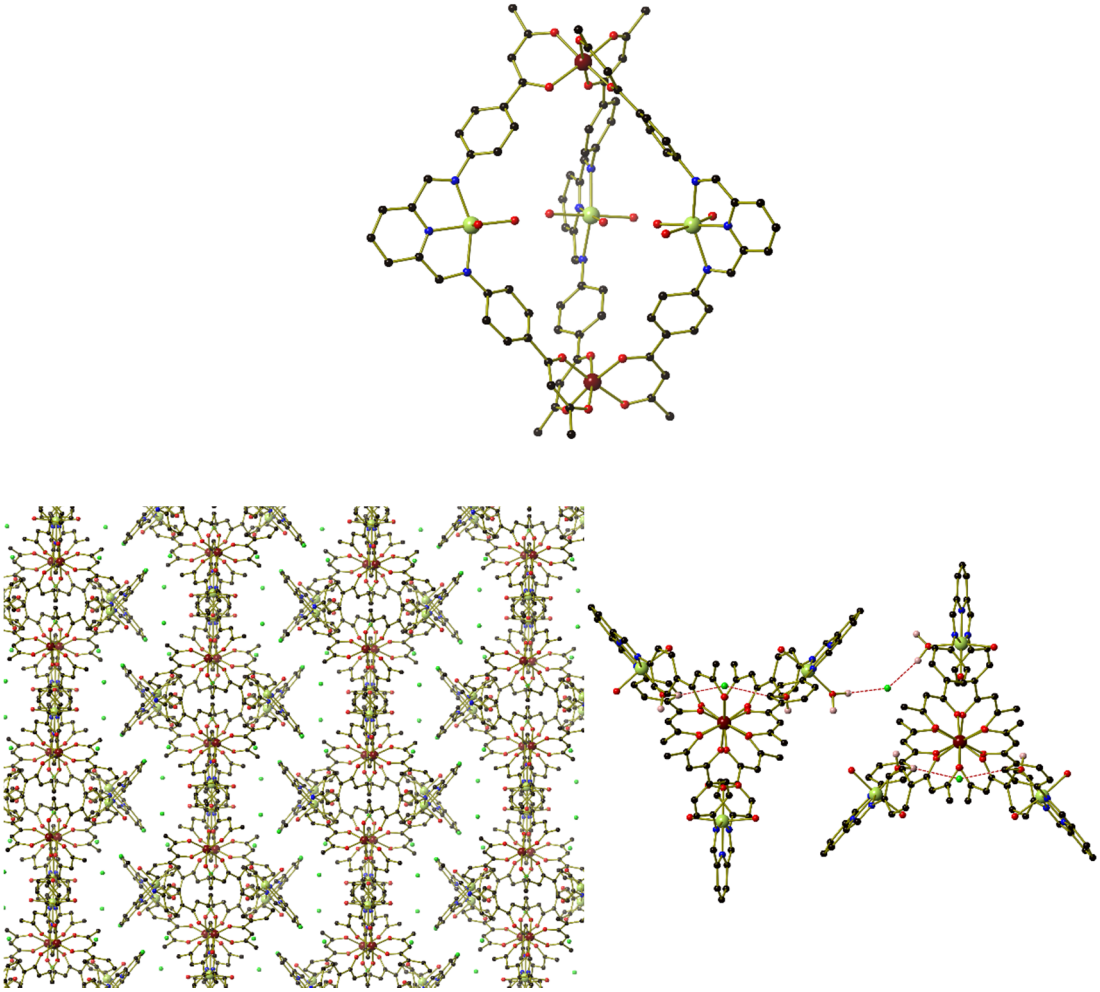

Figure 4.3 Structure of **20** (top), with the packing as viewed down the *c*-axis (left), and an example of the intermolecular interactions (---) between trigonal bipyramids and the chloride counterions (right). Some hydrogen atoms and counterions have been removed for clarity. Colour code: Fe^{III} – Maroon, Ni^{II} – Light Green, Cl^{-} – Bright Green, N – Blue, O – Red, C – Black, H – Pale Pink.

On first inspection complexes **21** and **22** look structurally analogous but there are significant differences between the structures, including both the overall charge of the complex, and the geometry of the Co^{II} ions (Fig. 4.4).

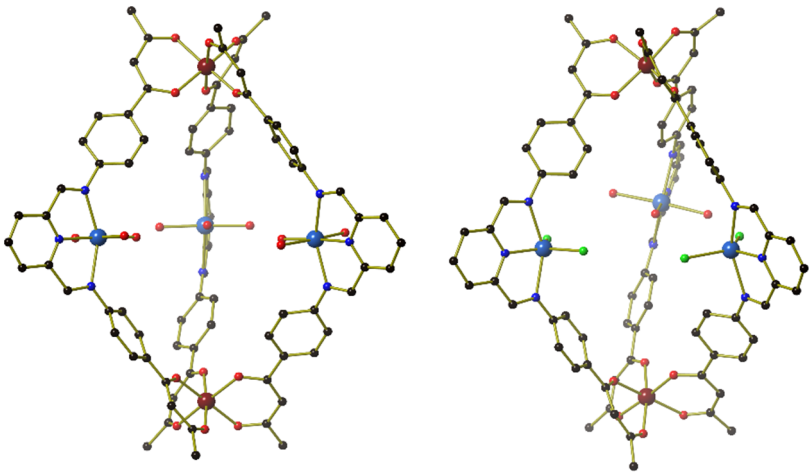

Figure 4.4 Structures of the cations of **21** (left) and **22** (right), with hydrogen atoms and non-coordinated counterions removed for clarity. Colour code: Fe^{III} – Maroon, Co^{II} – Royal Blue, Cl^- – Green, N – Blue, O – Red, C – Black.

The coordination sphere of the Co^{II} ions in **21** is similar to that of **20**, with Co^{II}-N bond distances and N-Co^{II}-N *cis* angles in the ranges 2.03-2.27 Å and 74.75-76.09°, respectively, and Co^{II}-O bond distances and O-Co^{II}-O *cis* angles in the ranges 2.03-2.12 Å and 84.35-88.28°, respectively. The overall charge of **21** is also 6+, with a mixture of charge balancing tetrafluoroborate and triflate ions hydrogen bonding to the coordinated aqua ligands within the cage (Fig. 4.5), and between cages (HO-H···O-SO_2CF_3 1.92-2.48 Å; HO-H···F-BF_3 1.96-2.66 Å).

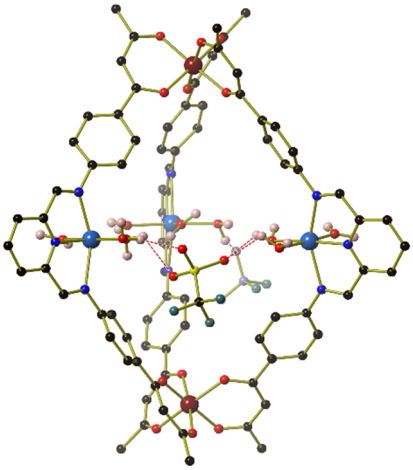

Figure 4.5 Example of intermolecular interactions (---) between the cationic cage and triflate and tetrafluoroborate counterions in **21**. Some hydrogen atoms have been removed for clarity. Colour code: Fe^{III} – Maroon, Co^{II} – Royal Blue, F^- – Turquoise, B – Dark Blue, S – Yellow, N – Blue, O – Red, C – Black, H – Pale Pink.

In **22**, two of the Co^{II} ions are five-coordinate and are of distorted trigonal bipyramidal geometry, with two coordinated chloride ions charge balancing the Co^{II} ions. For these centres, Co^{II}-N bond distances and N-Co^{II}-N *cis* angles are in the ranges 2.04-2.27 Å and 74.44-76.83°, respectively, with Co^{II}-Cl bond distances in the range 2.23-2.26 Å, and the Cl-Co^{II}-Cl *cis* angle 122.61°. The third Co^{II} site is disordered over two positions, and is six-coordinate, with three water molecules completing the coordination sphere. Co^{II}-N bond distances for this site are in the range 1.99-2.22 Å and N-Co^{II}-N *cis* angles are 76.83°, with Co^{II}-O bond distances angles in the range 2.34-2.26 Å and O-Co^{II}-O *cis* angles 75.92°. The overall charge of **22** is 2+ which is balanced by a tetrachlorocobaltate ion located outside of the cage (Fig. 4.6), the chlorides of which hydrogen bond with the L^{2-} ligand (OCC-H···Cl ≈2.84 Å; Ar-H···Cl ≈2.74 Å; NC-H···Cl ≈2.74 Å).

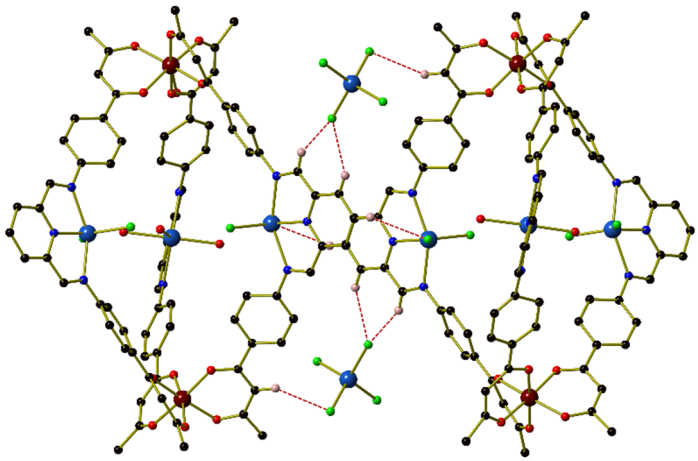

Figure 4.6 Example of intermolecular interactions (---) between the cationic cage and tetrachlorocobaltate counterions in **22**. Some hydrogen atoms have been removed for clarity. Colour code: Fe^{III} – Maroon, Co^{II} – Royal Blue, N – Blue, O – Red, C – Black, H – Pale Pink.

$[Fe^{III}_2L^{am}_3]$ Trigonal Bipyramids

The homometallic cages $[Fe^{III}_2L^{am}_3]\bullet Cl_2$ (**23**), $[Fe^{III}_2L^{am}_3]$ (**24**), and $[Fe^{III}_2L^{am}_3]\bullet Cl_3$ (**25**), were formed from the reaction of $[Fe^{III}L^{NH2}_3]$ with isophthaloyl chloride in the presence of triethylamine, with a silver salt added to **24**, and a tetrabutylammonium rhenium salt added to **25**. These cages are described by two Fe^{III} ions in the axial positions of the trigonal bipyramid (Fig. 4.7), with $Fe^{III}\cdots Fe^{III}$ distances in the range 15.88-16.43 Å, Fe^{III}-O distances in the range 1.96-2.01 Å, and Fe^{III}-O *cis*/*trans* angles in the ranges 83.77-98.96° and 167.60-177.37°, respectively.

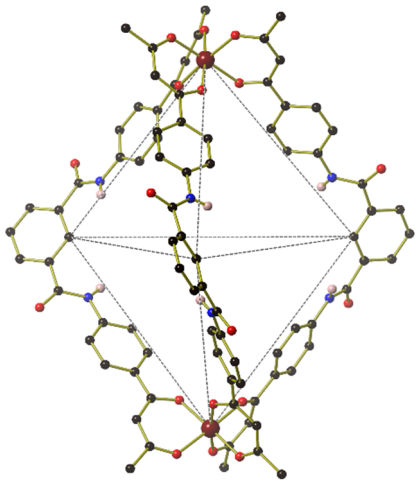

Figure 4.7 Example of an $[Fe^{III}_2L^{am}_3]$ trigonal bipyramid. Some hydrogen atoms have been removed for clarity. Colour code: Fe^{III} – Maroon, N – Blue, O – Red, C – Black, H – Pale Pink.

There are numerous intermolecular interactions in the extended structure of **23**, the most notable of which are hydrogen bonds between the chloride ions and the protons of the *bis*(amide) group (N-H···Cl ≈2.49 Å). Each chloride ion is counterbalanced by a triethylammonium cation which is formed *in-situ*, and hydrogen bonds to the chloride ion (Fig. 4.8; N-H···Cl ≈2.12 Å). The chloride ions also interact with acetonitrile and dichloromethane solvent molecules, the latter of which are situated in the internal cavity of the cage, "linking" the two chloride ions at a distance of ≈2.89 Å. Complex **23** is heterochiral with respect to Fe^{III}, and the twisting of one arm allows intermolecular hydrogen bonding to occur, the shortest distance of which is N-H···O-C ≈2.16 Å (Fig. 4.8).

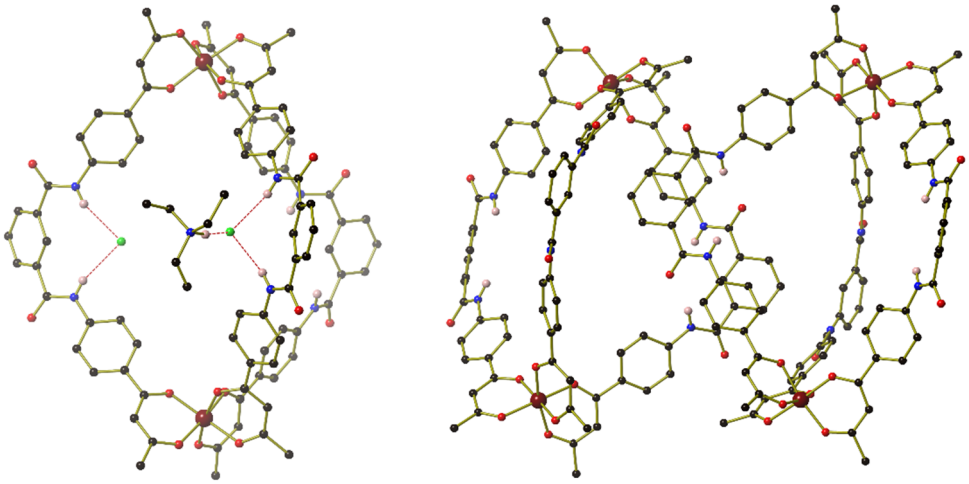

Figure 4.8 Examples of intermolecular interactions (---) in **23** (left), with the twisting of the cage allowing for intercluster overlap (right). Some hydrogen atoms have been removed for clarity. Colour code: Fe^{III} – Maroon, Cl^{-} – Green, N – Blue, O – Red, C – Black, H – Pale Pink.

There are also numerous intermolecular interactions in the crystal of **24**, with two dimethylformamide solvent molecules hydrogen bonding to the *bis*(amide) groups (Fig. 4.9; N-H···O ≈2.06 Å), which "connect" two of the clusters. There are also direct intermolecular interactions between the aromatic protons of the phenyl-*bis*(amide) group and the acac-based group of the L^{2-} ligand, with distances as short as 2.47 Å.

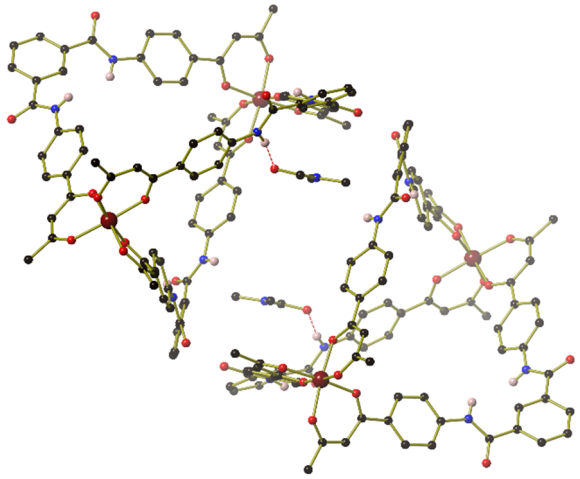

Figure 4.9 Examples of intermolecular interactions (---) in **24**. Some hydrogen atoms and solvent molecules have been removed for clarity. Colour code: Fe^{III} – Maroon, N – Blue, O – Red, C – Black, H – Pale Pink.

The replacement of the chloride ions with the larger hexachlororhenate ions was attempted through the addition of tetrabutylammonium hexachlororhenate into a solution of **23** in acetonitrile and dichloromethane. However, this resulted in the tetrabutylammonium ions replacing the triethylammonium ions to give complex **25** (Fig. 4.10). In this complex, the protons of all three *bis*(amide) groups are hydrogen bonded to a chloride ion (N-H···Cl ≈2.46 Å), the charge of which is balanced by a tetrabutylammonium cation. These cations "link" two neighbouring cages through a total of over twenty hydrogen bonds, the shortest contact of which is ≈2.05 Å (Fig. 4.10).

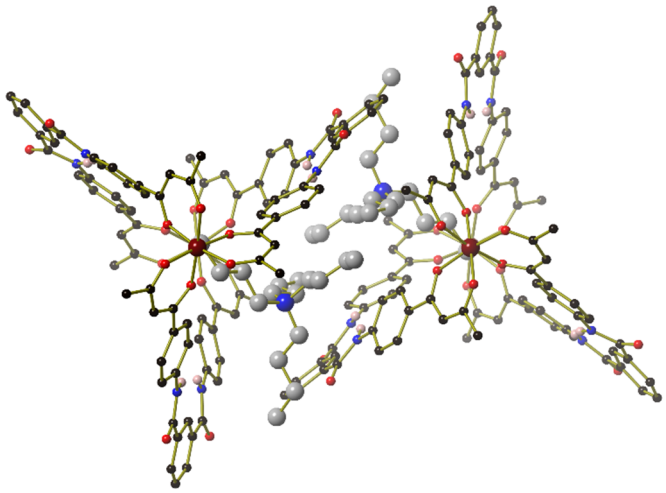

Figure 4.10 Two trigonal bipyramids of **25**, showing the tetrabutylammonium cation which helps "link" the two structures. The carbons of the cation have been coloured grey and hydrogen atoms have been removed for clarity. Colour code: Fe^{III} – Maroon, N – Blue, O – Red, C – Black/Grey, H – Pale Pink.

As opposed to **23**, complexes **24** and **25** crystallise as homochiral racemates (Fig. 4.11). There are a number of possible reasons that could account for this. In contrast to the imine-based structures, the amide-based structures do not have a templating M^{II} salt, meaning there is no initial preference for forming either a homo- or a heterochiral cage. As the chloride ions are released during amide formation, they hydrogen bond to the *bis*(amide) groups, essentially locking these groups into a specific configuration. If the cages are heterochiral, such as in **23**, the additional enthalpy gained from the ability to form four direct intercluster hydrogen bonds means that there is no reason for it to rearrange to the homochiral cage. Complex **25** has an additional chloride ion which may be favourable in forming the homochiral isomer because of the introduction of the tetrabutylammonium cation, which allows additional intercluster and intercation interactions. The ability of the dimethylformamide molecules to "connect" neighbouring cages in **24** reinforces the concept that these enthalpically-favoured intermolecular interactions are key for the formation of either a homo- or heterochiral cage. Importantly, it should be noted that this reasoning is based on solid-state effects, and indeed both homo- and heterochiral forms of **23**, **24**, and **25**, could exist in solution.

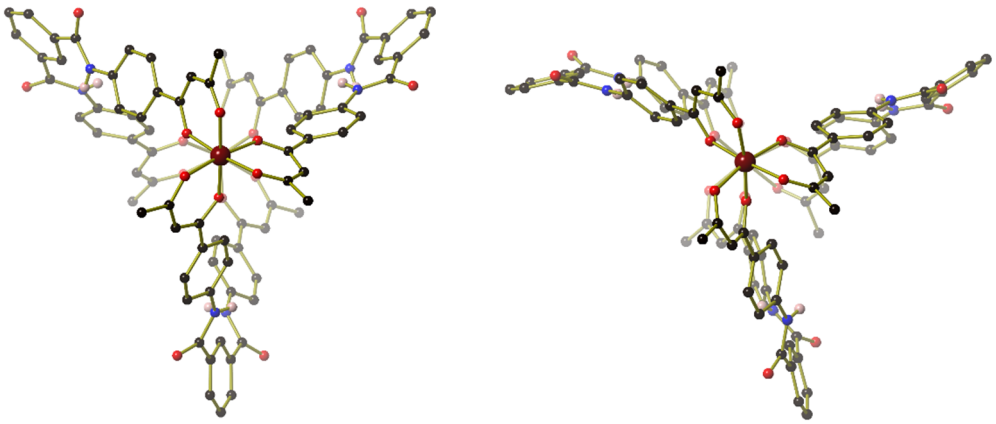

Figure 4.11 Example of a homochiral ΛΛ cage (**24**, left) and a ΛΔ heterochiral cage (**23**, right), as viewed down the Fe^{III}-Fe^{III} axis. Additional molecules and some hydrogen atoms have been removed for clarity. Colour code: Fe^{III} – Maroon, N – Blue, O – Red, C – Black, H – Pale Pink.

4.3.2 Magnetic Studies

SQUID Magnetometry

The dc (direct current) molar magnetic susceptibility, χ_M, of polycrystalline samples of **20** and **21** were measured in an applied magnetic field, B, of 0.1 T, over the 2-300 K temperature, T, range. The experimental results are shown in Fig. 4.12 in the form of the $\chi_M T$ product, where $\chi_M = M/B$, and M is the magnetisation of the sample.

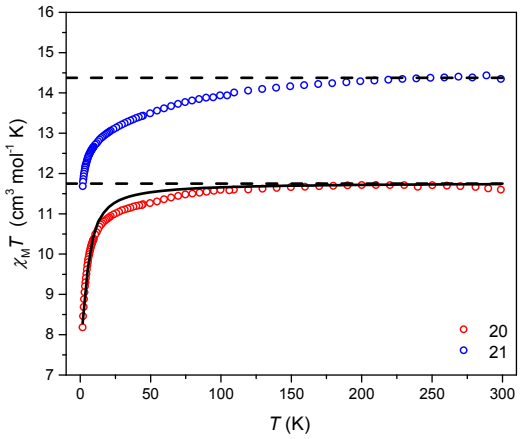

Figure 4.12 Plot of $\chi_M T$ vs T for **20** and **21**, with experimental data (•), the sum of the Curie constants of uncorrelated ions (---), and the best-fit data (**-**).

Due to the loss of lattice solvent during the evacuation of the sample chamber of the SQUID magnetometer, leading to an uncertainty in the molar mass of the measured sample, the 300 K $\chi_M T$ products of **20** and **21** were scaled to values 11.75 $cm^3\ mol^{-1}\ K$ and 14.40 $cm^3\ mol^{-1}\ K$, respectively. These are the expected values from the sum of Curie constants for $[Fe^{III}_2Ni^{II}_3]$ and $[Fe^{III}_2Co^{II}_3]$ units, respectively, with $g_{Fe} = g_{Ni} = g_{Co} = 2.0$, where g_{Fe}, g_{Ni}, and g_{Co} are the g-factors of Fe^{III}, Ni^{II}, and Co^{II}, respectively.

Upon cooling, the value of $\chi_M T$ for **20** remains essentially constant down to approximately 150 K, where it begins to decrease, reaching a minimum of ≈8.15 $cm^3\ mol^{-1}\ K$ at 2 K. This behaviour is consistent with the presence of weak antiferromagnetic coupling between Fe^{III} and Ni^{II} ions, and/or the zero-field splitting of the Ni^{II} ions. The continuous decrease in the value of $\chi_M T$ observed in **21** is likely due to the same reasons, though we note here that the zero-field splitting of the Co^{II} ions might be very large.

In order to fit the experimental susceptibility data of **20** we used the program *PHI* and spin-Hamiltonian (8):[24]

$$\hat{H} = -2\sum_{i,j<i} J_{ij}\hat{S}_i \cdot \hat{S}_j + \mu_B B\sum_i g_i \hat{S}_i + \sum_i D_i\left[\hat{S}^2_{i,z} - S_i(S_i+1)/3\right] \qquad (8)$$

where the summation indexes i, j run through the constitutive metal centres, g_i is the g-factor of the i^{th} centre, $\hat{S}$ is a spin operator, J is the isotropic exchange interaction parameter, D is the uniaxial anisotropy parameter, and S is the total spin. For simplicity, we assume that $g_{Fe} = g_{Ni} = 2$, $S_{Fe} = 5/2$, $S_{Ni} = 1$, and $D_{Fe} = 0$ ($D_{Fe} << D_{Ni}$). The best fit parameters, shown as the solid black line in Fig. 4.12, were obtained with $J_{Fe\text{-}Ni} = -0.12\ cm^{-1}$ and $D_{Ni} = 8.93\ cm^{-1}$. It should be noted that due to highly anisotropic nature of the three Co^{II} ions present in **21**, the associated spin-Hamiltonian matrix for complex **21** is too large to fit using the *PHI* program.

4.4 Conclusions

The development of the new aniline-based metalloligand $[Fe^{III}L^{NH2}{}_3]$ has allowed us to gain access to six new trigonal bipyramidal structures through dynamic covalent chemistry.

The imine-based $[Fe^{III}{}_2M^{II}{}_3L^{im}{}_3]^{n+}$ structures were synthesised through Schiff-base reactions of the metalloligand with 2,6-pyridinedicarboxaldehyde in the presence of a catalytic amount of acid, and a templating M^{II} salt. Complexes **20** and **21** possess octahedral M^{II} ions, with charge balancing anions located both inside and outside the cavity of the cage. As opposed to **20** and **21**, complex **22** contains two five-coordinate Co^{II} ions, with a charge balancing tetrachlorocobaltate ion located outside the cavity of the cage. Magnetic studies on **20** indicate weak antiferromagnetic exchange interactions between Fe^{III} and Ni^{II} ions, with $J_{Fe\text{-}Ni}$ = -0.12 cm^{-1} and D_{Ni} = 8.93 cm^{-1}.

The amide-based $[Fe^{III}{}_2L^{am}{}_3]$ structures were synthesised through amide-formation reactions of the metalloligand with isophthaloyl chloride in the presence of trimethylamine. Complexes **23**-**25** initially appear structurally analogous, but there are distinct stereochemical differences between the three complexes, with the formation of a heterochiral (**23**) or homochiral (**24** and **25**) cage governed by the enthalpic gain originating from a plethora of intermolecular interactions. The *bis*(amide) groups found in complexes **23**-**25** should allow for application in host-guest chemistry, or in the synthesis of catenanes or rotaxanes.

The ability to easily modify the metalloligands of Chapters 2 and 3 has allowed us to create two new families of trigonal bipyramids through dynamic covalent chemistry. The generation of these two families highlights the applicability and versatility of the metalloligand approach in the synthesis of cages containing paramagnetic transition metal ions.

4.5 References

(1) Riddell, I. A.; Smulders, M. M. J.; Clegg, J. K.; Hristova, Y. R.; Breiner, B.; Thoburn, J. D.; Nitschke, J. R. *Nat. Chem.* **2012**, *4* (10), 860.

(2) Ronson, T. K.; Giri, C.; Kodiah Beyeh, N.; Minkkinen, A.; Topić, F.; Holstein, J. J.; Rissanen, K.; Nitschke, J. R. *Chem. - A Eur. J.* **2013**, *19* (10), 3374.

(3) Yi, S.; Brega, V.; Captain, B.; Kaifer, A. E. *Chem. Commun.* **2012**, *48* (83), 10295.

(4) Yue, N.; Qin, Z.; Jennings, M. C.; Eisler, D. J.; Puddephatt, R. J. *Inorg. Chem. Commun.* **2003**, *6* (9), 1269.

(5) Jin, Y.; Yu, C.; Denman, R. J.; Zhang, W. *Chem. Soc. Rev.* **2013**, *42* (16), 6634.

(6) Heim, C.; Udelhofen, D.; Vgtle, F. In *Molecular Catenanes, Rotaxanes and Knots*; Wiley-VCH Verlag GmbH: Weinheim, Germany, 2007; pp 177–222.

(7) Gil-Ramírez, G.; Leigh, D. A.; Stephens, A. J. *Angew. Chemie Int. Ed.* **2015**, *54* (21), 6110.

(8) Baggerman, J.; Haraszkiewicz, N.; Wiering, P. G.; Fioravanti, G.; Marcaccio, M.; Paolucci, F.; Kay, E. R.; Leigh, D. A.; Brouwer, A. M. *Chem. - A Eur. J.* **2013**, *19* (18), 5566.

(9) Hernandez, J. V.; Kay, E. R.; Leigh, D. A. *Science.* **2004**, *306* (5701), 1532.

(10) Wilson, M. R.; Solà, J.; Carlone, A.; Goldup, S. M.; Lebrasseur, N.; Leigh, D. A. *Nature* **2016**, *534* (7606), 235.

(11) Kolesnichenko, I. V.; Anslyn, E. V. *Chem. Soc. Rev.* **2017**, *46* (9), 2385.

(12) Astumian, R. D. *Chem. Sci.* **2017**, *8* (2), 840.

(13) Erbas-Cakmak, S.; Leigh, D. A.; McTernan, C. T.; Nussbaumer, A. L. *Chem. Rev.* **2015**, *115* (18), 10081.

(14) Coles, S. J.; Gale, P. A. *Chem. Sci.* **2012**, *3* (3), 683.

(15) Rigaku Oxford Diffraction. In *CrystalClear-SM Expert 3.1 b27*; 2012.

(16) Rigaku Oxford Diffraction. In *CrysAlisPro 1.171.38.41*; 2015.

(17) Sheldrick, G. M. *Acta Crystallogr. Sect. A Found. Crystallogr.* **2007**, *64* (1), 112.

(18) Sheldrick, G. M. *Acta Crystallogr. Sect. C Struct. Chem.* **2015**, *71* (1), 3.

(19) Dolomanov, O. V.; Blake, A. J.; Champness, N. R.; Schröder, M. *J. Appl. Crystallogr.* **2003**, *36* (5), 1283.

(20) Spek, A. L. *Acta Crystallogr. Sect. D Biol. Crystallogr.* **2009**, *65* (2), 148.

(21) Spek, A. L. *Acta Crystallogr. Sect. C Struct. Chem.* **2015**, *71* (1), 9.

(22) Dolomanov, O. V.; Bourhis, L. J.; Gildea, R. J.; Howard, J. A. K.; Puschmann, H. *J. Appl. Crystallogr.* **2009**, *42* (2), 339.

(23) Sheldrick, G. M. *Acta Crystallogr. Sect. A Found. Crystallogr.* **2007**, *64* (1), 112.

(24) Chilton, N. F.; Anderson, R. P.; Turner, L. D.; Soncini, A.; Murray, K. S. *J. Comput. Chem.* **2013**, *34* (13), 1164.

Chapter 5: Conclusions and Future Outlook

The aim of this thesis was to make high-nuclearity magnetic structures with predictable magnetic behaviour through the use of metalloligands.

In Chapter 2, it was shown how the combination of a *tris*{1-(4-pyridyl)acetylacetonato}-metallogligand with a "naked" M^{II} salt led to the formation of fourteen tetradecanuclear $[M^{III}_8M^{II}_6L_{24}]^{n+}$ coordination cubes, in which the eight M^{III} ions occupy the vertices of the cube and the six M^{II} ions occupy the faces. All fourteen structures are homochiral racemates with respect to the M^{III} centre, with the stereochemical information communicated through the rigid pyridyl-ligands, which act like propellers twisting about the M^{II} ion. With the exception of the Pd^{II}-based cube, all of the structures show magnetic exchange interactions in which the magnetic information is communicated through the negatively-charged pyridyl-based ligand. The Cr^{III}-based cubes show ferromagnetic exchange interactions between the Cr^{III} and $Cu^{II}/Co^{II}/Ni^{II}$ ions, whereas the Fe^{III}-based cubes show antiferromagnetic exchange interactions between the Fe^{III} and Cu^{II}/Ni^{II} ions. Due to the enormous size of the associated matrices of these $[M^{III}_8M^{II}_6L_{24}]^{n+}$ systems, the fitting of the magnetic data has been carried out using the computational technique of statistical spectroscopy, in which the moments of the Hamiltonian are exploited to calculate any relevant thermodynamic properties. EPR spectroscopy showed a small increase in the zero-field parameter, D, of the Fe^{III} ion upon formation of the cube. Volume calculations, performed using the *³V Volume Assessor* program, confirmed an internal volume of **3** of ≈1400 Å³. The inclusion of guests can be expected when the total volume of the guest are ≈770 Å³ which corresponds with the inclusion of four sulfate ions (668 Å³) encapsulated inside **3**.

In Chapter 3, it was shown how changing the acceptor to one with an angle between 90-109.5° led to the formation of five pentanuclear $[M^{III}_2M^{II}_3L_6]^{n+}$ trigonal bipyramids in which the M^{III} ions occupy the axial positions, and the M^{II} ions occupy the equatorial positions. The fully magnetic complex **15** represents the first example of such a cage synthesised through the use of pyridyl-based metalloligands. SQUID magnetometry, EPR spectroscopy, heat capacity measurements, and CASSCF calculations are all in agreement, revealing weak antiferromagnetic exchange interactions between the Fe^{III} and Co^{II} ions, and zero-field splitting parameters of $|D_{Co}|$ = 14 cm^{-1}, and $|D_{Fe}|$ = 0.2 cm^{-1}. ^1H NMR spectroscopy confirms that the self-assembly process is dynamic upon the formation of the trigonal bipyramidal structure, showing amplification of the *fac*-geometrical isomer, through rearrangement of the *mer*-isomer in solution.

In Chapter 4, the simple modification of our metalloligand allowed access to the field of magnetic dynamic covalent chemistry. Through the use of Schiff-base or amide-formation reactions we have been able to produce three imine-based $[Fe^{III}_2M^{II}_3L^{im}_3]^{n+}$ or three amide-based $[Fe^{III}_2L^{am}_3]$ trigonal bipyramids, respectively. For the imine-based cages, the M^{II} ion has acted as a template for the formation of the trigonal bipyramid, occupying the equatorial sites, while the M^{III} ion from

the metalloligand occupies the axial sites. Magnetic studies on **20** indicate weak antiferromagnetic exchange interactions between Fe^{III} and Ni^{II} ions, with $J_{Fe\text{-}Ni}$ = -0.12 cm^{-1} and D_{Ni} = 8.93 cm^{-1}. Complexes **23**-**25** initially appear structurally analogous, but there are distinct stereochemical differences between the three complexes, with the formation of a heterochiral (**23**) or homochiral (**24** and **25**) cage governed by the enthalpic gain originating from a plethora of intermolecular interactions. The *bis*(amide) groups found in **23**-**25** should allow for application in host-guest chemistry, or in the synthesis of catenanes or rotaxanes.

The ability to simply modify the identity of the metalloligand or acceptor throughout these three chapters has shown just how applicable and versatile the metalloligand approach is in the development of families of high-nuclearity magnetic clusters, with predictable magnetic behaviour. The modular assembly of magnetic coordination capsules with internal cavities capable of hosting magnetic and redox- active guests is an under-explored field of research that can be exploited for the construction of tuneable, multifunctional molecular magnets with potential application in information storage and molecular spintronics. The ability to control and manipulate (switch on, switch off) magnetic exchange between metal ions in the host framework and between the host and guest(s) *via* the use of redox-active (radical) ligands in the framework of the host, and/or redox-active/paramagnetic guests held within the cavities, remains an attractive target for future exploration. The construction of said capsules in a manner amenable to exohedral functionalization such that the organic sheath surrounding the capsules are easily derivatised post-synthetically to modify and tune solubility, magnetic behaviour, reactivity, stability and substrate specificity would also make the cages suitable for materials applications.

Appendix: Publications

Heterometallic Cages

Deutsche Ausgabe: DOI: 10.1002/ange.201501041
Internationale Ausgabe: DOI: 10.1002/anie.201501041

$[Cr^{III}_8M^{II}_6]^{12+}$ Coordination Cubes (M^{II} = Cu, Co)**

Sergio Sanz, Helen M. O'Connor, Eufemio Moreno Pineda, Kasper S. Pedersen, Gary S. Nichol, Ole Mønsted, Høgni Weihe, Stergios Piligkos, Eric J. L. McInnes,* Paul J. Lusby,* and Euan K. Brechin**

Abstract: *$[Cr^{III}_8M^{II}_6]^{12+}$ (M^{II} = Cu, Co) coordination cubes were constructed from a simple $[Cr^{III}L_3]$ metalloligand and a "naked" M^{II} salt. The flexibility in the design proffers the potential to tune the physical properties, as all the constituent parts of the cage can be changed without structural alteration. Computational techniques (known in theoretical nuclear physics as statistical spectroscopy) in tandem with EPR spectroscopy are used to interpret the magnetic behavior.*

Molecules containing exchange-coupled paramagnetic metal ions represent a class of materials with potential applications across a breadth of scientific disciplines, with particular recent focus on information storage, quantum computation, and molecular spintronics.[1–6] The bottom-up design of magnetic materials for such applications is attractive, as molecules are inherently monodisperse, reproducible, orientable, and chemically tuneable. Synthetic strategies that target magnetic coordination compounds span the entire spectrum from the serendipitous self-assembly of coordinatively flexible metal ions and organic ligands capable of bridging in multiple ways, through to the design of structurally predictable cages using rigid linker ligands in combination with metal precursors that possess a limited number of coordination sites free for reaction.[7] This 'rational design' strategy has also been widely utilized for the preparation of numerous diamagnetic coordination capsules, the interest in these systems stemming from host–guest chemistry that has been exploited for catalysis, drug delivery, or the stabilization of reactive intermediates.[8] Heterometallic coordination capsules have also been accessed using preprogrammed self-assembly approaches, occasionally using one-pot, self-sorting strategies with thermodynamically orthogonal metal–ligand motifs,[9] or more commonly through a stepwise approach that takes advantage of kinetically robust intermediate complexes that possess pendant donor tectons, often referred to as metalloligands.[10–15] However, only a handful of these heterometallic systems possess paramagnetic centers,[13] and even fewer have been reported to display intramolecular magnetic exchange.[15]

Herein we discuss the structures and magnetic properties of the heterometallic cages $[Cr^{III}_8Cu^{II}_6L_{24}(H_2O)_{10}(NO_3)_2](NO_3)_{10}$ (**1**) and $[Cr^{III}_8Co^{II}_6L_{24}(H_2O)_{12}](ClO_4)_{12}$ (**2**), which were built using the simple metalloligand $[Cr^{III}L_3]$ (HL = 1-(4-pyridyl)butane-1,3-dione) and the metal salts $Cu(NO_3)_2\cdot 3H_2O$ and $Co(ClO_4)_2\cdot 6H_2O$, respectively. The metallic skeleton of both cages (Figure 1, see also Figures S1 and S2 in the Supporting Information) describes a simple $[Cr^{III}_8M^{II}_6]^{12+}$ cube with the Cr^{III} ions of the $[Cr^{III}L_3]$ metalloligands occupying the corners of the cube, and the M^{II} ions capping the square faces. The former are six-coordinate and in regular

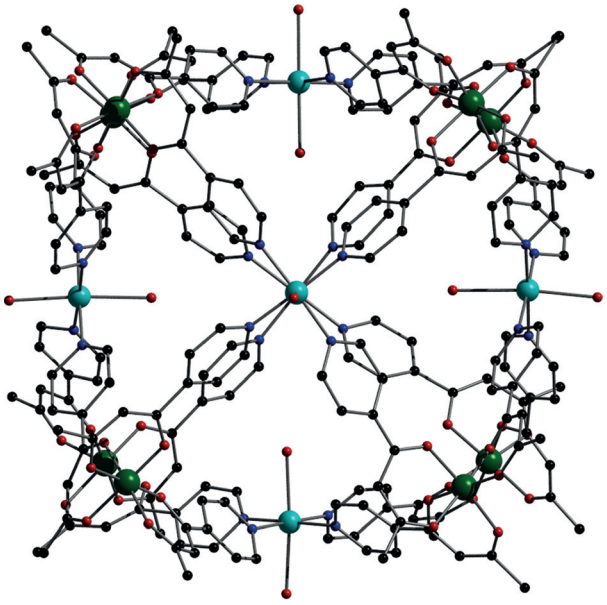

Figure 1. Molecular structure of the cation of **1**. Color code: Cr = green, Cu = light blue, O = red, N = blue, C = black. The terminally bound oxygen atoms originate from both water and nitrate molecules (see text for details).

[*] Dr. S. Sanz, H. M. O'Connor, Dr. G. S. Nichol, Dr. P. J. Lusby, Prof. E. K. Brechin
EaStCHEM School of Chemistry, The University of Edinburgh
David Brewster Road, Edinburgh, EH9 3FJ (UK)
E-mail: Paul.Lusby@ed.ac.uk
E.Brechin@ed.ac.uk
E. M. Pineda, Prof. E. J. L. McInnes
School of Chemistry, The University of Manchester
Oxford Road, Manchester M13 9PL (UK)
E-mail: eric.mcinnes@manchester.ac.uk
Dr. K. S. Pedersen, Dr. O. Mønsted, Dr. H. Weihe, Dr. S. Piligkos
Department of Chemistry, University of Copenhagen
Universitetsparken 5, 2100 Copenhagen (Denmark)
E-mail: piligkos@kiku.dk

[**] The authors acknowledge the EPSRC for funding, including the National EPR Facility at Manchester. S.P. thanks the Danish Ministry of Science, Innovation and Higher Education for a Sapere Aude Fellowship (10-081659).

Supporting information for this article is available on the WWW under http://dx.doi.org/10.1002/anie.201501041.

{CrO_6} octahedral geometry, with Cr–O distances between 1.88–2.04 Å, and *trans* angles in the range 175–179°. In **1**, the Cu^{II} ions are also six coordinate, but in Jahn–Teller distorted {CuN_4O_2} coordination geometries (Cu-N, ≈2 Å) with the O-Cu-O vector (Cu-O, ≈2.31–2.58 Å) describing the elongated axis (d_{z^2}), perpendicular to the equatorial CuN_4 plane ($d_{x^2-y^2}$) in the face of the cube. Ten of these axial ligands are H_2O molecules, but two (on opposing sides of the cube) are NO_3^- anions. In the extended structure (Figure S2), these link to neighboring cages, which results in the formation of a square sheet of cubes in the *bc* plane. The remaining ten, nonbonded, charge-balancing NO_3^- anions, and solvent molecules of crystallization, are located both within the cage cavity and in the void spaces between the cubes.

In complex **2** (Figure S1) the face-capping Co^{II} ions possess the same, albeit regular, octahedral {CoN_4O_2} geometry with Co–O bonds in the range 2.04–2.12 Å. Here, all the terminally coordinated ligands are water molecules. In the solid state, the cations of **2** pack in a brickwork-like fashion (Figure S3) with the closest intercage contacts being between the corners of neighboring cubes through a plethora of close contacts, primarily mediated by the L ligands: CH···O, ≈3.1 Å; CH_3···π, ≈3.6 Å; CH_3···CH, ≈4.0 Å; O···O, 4.3 Å; CH_3···CH_3, 4.5 Å. The twelve charge-balancing ClO_4^- anions, and solvent molecules of the crystallization, are again located both within the cage cavity and in the void spaces between cubes. The Cr···Cr distance between nearest neighbors along each edge of the cubes measures approximately 12 Å, creating an internal cavity volume close to 1000 $Å^3$ (Figure S4), thus suggesting that anions with a total volume of around 550 $Å^3$ could be accommodated.[11] Future studies will examine potential host–guest chemistry as a means of creating multifunctionality and additional magnetic exchange. The analogous diamagnetic $[Al^{III}_8Pd^{II}_6]^{12+}$ cage has been reported previously,[12] though its lack of solubility precluded the investigation of any host–guest chemistry, while similar structure types, albeit with different ligands, have been observed in the complex $[Cu^{II}_6Fe^{III}_8L_8]^{12+}$ (H_3L = tris{[2-{(imidazole-4-yl)methylid-ene}amino]ethyl}amine),[13] for which no magnetic data were reported, the spin crossover species $[\{Cu^{I}(Tp4py)(CH_3CN)\}_8\{Fe^{II}(NCS)_2\}_{10/3}\{Fe^{II}(NCS)(CH_3CN)\}_{8/3}](ClO_4)_{8/3}(CH_3CN)_n$ (Tp4py = tris{3-(4-pyridyl)-pyrazol-1-yl}hydroborate),[14] and in molecular Prussian blue species such as $[(Tp)_8(H_2O)_6Cu^{II}_6Fe^{III}_8(CN)_{24}]^{4+}$ (where Tp^- = hydrotris(pyrazolyl)borate).[15]

The direct current (d.c.) molar magnetic susceptibility, χ_M, of polycrystalline samples of complexes **1** and **2** were measured in an applied magnetic field, *B*, of 0.1 T, over the 5–280 K temperature, *T*, range (Figure 2, where $\chi = M/B$, and *M* is the magnetization). At 280 K, the $\chi_M T$ products of **1** and **2** have values of 17.7 and 26.3 $cm^3 mol^{-1} K$, respectively. These values are in excellent agreement with those expected from the spin-only contributions to the magnetism of a $[Cr^{III}_8Cu^{II}_6]$ unit (17.6 $cm^3 mol^{-1} K$), with $g_{Cr} = 2.00$ and $g_{Cu} = 2.15$, and of a $[Cr^{III}_8Co^{II}_6]$ unit (26.3 $cm^3 mol^{-1} K$), with $g_{Cr} = g_{Co} = 2.00$, where g_{Cr}, g_{Cu}, and g_{Co} are the *g*-factors of Cr^{III}, Cu^{II}, and Co^{II}, respectively. Upon cooling, the $\chi_M T$ product of **1** remains essentially constant down to 30 K, below which a fast increase is observed, reaching 19.1 $cm^3 mol^{-1} K$ at 5 K. This behavior is indicative of weak ferromagnetic exchange interactions. Upon cooling, the $\chi_M T$ product of **2** decreases continuously, reaching a plateau value of 21.5 $cm^3 mol^{-1} K$ at 8 K, before slightly increasing upon further cooling to 21.7 $cm^3 mol^{-1} K$ at 5 K. The analysis of this behavior is complicated by the combination of the ligand-field splitting of the Co^{II} ion and weak exchange interactions. The tetragonal symmetry ligand field of the {$Co(py)_4(H_2O)_2$} site removes the degeneracy of the $^4T_{1g}$ term, breaking it into ^4E_g and $^4A_{2g}$ terms, with the latter lower in energy.[16] Spin-orbit coupling (SOC) then further removes the degeneracy of the $^4A_{2g}$ term, breaking it into two Kramers doublets, the energy splitting of which can be parameterized as a zero-field splitting (*D*) of the $^4A_{2g}$ term. The fact that the high temperature $\chi_M T$ product of **2** agrees well with the expected spin-only value supports the dominance of the axial ligand field splitting over SOC.

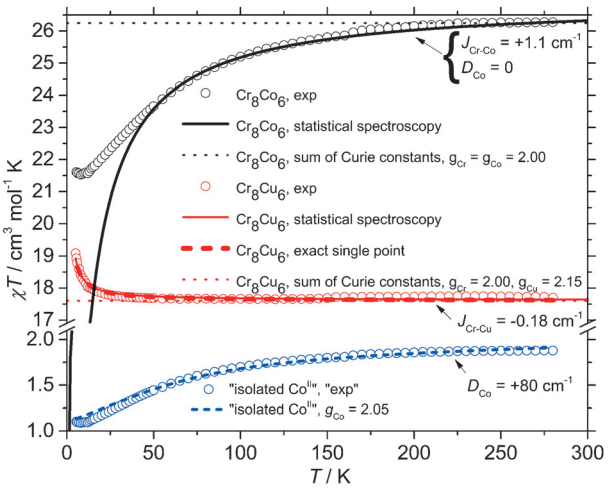

Figure 2. $\chi_M T$ products of **1** and **2**. The experimental data are shown as open circles. The curves obtained by statistical spectroscopy are shown as solid lines. The sums of the Curie constants of uncorrelated ions in **1** and **2** are shown as dotted lines. The results from matrix diagonalization of the blocked spin-Hamiltonian (1) for **1** and the best fit curve for "isolated Co^{II}", as explained in the text, for **2**, are shown as thick dashed lines.

For the quantitative interpretation of the magnetic properties of **1** and **2**, we used two limiting models: 1) with $D_M = 0$ and $J_{Cr\text{-}M} \neq 0$ (an isotropic model) and 2) with $J_{Cr\text{-}M} = 0$ and $D_M \neq 0$, where M = Cu^{II} or Co^{II}, and $J_{Cr\text{-}M}$ is the isotropic exchange parameter between Cr and M centers (where M = Cu for **1** and Co for **2**). In both limiting models, we neglected the single-ion anisotropy of Cr^{III}, D_{Cr}, as this is usually of the order of 1 cm^{-1}.[17] Given that $D_{Cu} = 0$, we only applied the isotropic model for the analysis of **1**. We started with the isotropic model for both **1** and **2**. To describe the magnetic properties we used the following isotropic spin-Hamiltonian (1)

$$\hat{H}_{iso} = J_{Cr-M} \sum_{\text{all Cr–M pairs}} \hat{S}_{Cr} \bullet \hat{S}_M + \mu_B Bg \sum_i \hat{S}_{z,i} \qquad (1)$$

with *i* running over all constitutive metal centers, $\hat{S}$ a spin operator, μ_B the Bohr magneton, *B* the applied magnetic field, and *g* the isotropic *g*-factor common to both Cr and M. Modelling the data using traditional matrix diagonalization is impractical for **1** and impossible for **2**, because of the large

dimension (4,194,304 for **1** and 268,435,456 for **2**) of the associated spin-Hamiltonian matrices. The isotropic Heisenberg Hamiltonian (1) applied to these spin systems permits blocking of the spin-Hamiltonian matrix with respect to the total spin value, *S*. To model the magnetic properties of **1** and **2**, we have adapted computational techniques known in theoretical nuclear physics as statistical spectroscopy,[18] which exploit the moments of the Hamiltonian to calculate relevant thermodynamic properties. We calculated the temperature-dependent magnetic susceptibility of **1** and **2** by use of the van Vleck equation (2), derived from (1)

$$\chi = \frac{N_A g^2 \mu_B^2}{k_B T} \frac{\sum_S (2S+1)^{\frac{S(S+1)}{3}} \exp(-\frac{E_S}{k_B T})}{\sum_S (2S+1) \exp(-\frac{E_S}{k_B T})} \quad (2)$$

with N_A Avogadro's number, k_B the Boltzmann constant, and T the temperature. We approximated the energy dependence of the $(2S+1)$ factor in the denominator by a continuous density of states, $\rho(E)$. Similarly, we approximated the energy dependence of the $(2S+1)S(S+1)/3$ factor on the nominator, by a continuous density, $\rho_C(E)$, which we designated the Curie-constant density. These two densities may be obtained from moments of an appropriate Hamiltonian,[19] here (1). The moments are related to the traces of powers of the Hamiltonian.[19] The density $\rho(E)$ is determined from the moments of a Hamiltonian containing only the Heisenberg terms of (1), whereas the density $\rho_C(E)$ is determined from the bivariate moments of (1), that is, those obtained from a Hamiltonian containing both Heisenberg and Zeeman terms. Once these moments, up to order 14 in our case, had been computed, the densities were conveniently determined following the method described in references [20,21]. Using this approach, and by successive simulations of the temperature dependence of the $\chi_M T$ product of **1** and **2**, we determined $J_{Cr\text{-}Cu} = -0.18\ cm^{-1}$ with a common isotropic *g* factor $g_1 = 2.021$, for **1**, and $J_{Cr\text{-}Co} = +1.10\ cm^{-1}$ with a common isotropic *g*-factor $g_2 = 2.0$, for **2**. In our analysis, we neglected all Cr–Cr and M–M exchange interactions, because these centers are not connected as first neighbors. The results were in excellent agreement with experiment in the case of **1** (Figure 2). For **2**, they agreed well with the experimental data down to approximately 45 K. The observed deviation below this temperature could be attributed to the lack of anisotropy terms in (1). With these parameters, the ground spin state of **1** is an $S = 15$ state and the ground spin state of **2** would be an $S = 3$ state. To verify the validity of our theoretical approach, we calculated the $\chi_M T$ product of **1** by full matrix diagonalization of the blocked spin-Hamiltonian matrix of **1**, by use of the determined spin-Hamiltonian parameters. The resulting curve (Figure 2, thick dashed line) is in excellent agreement with the one obtained with the theoretical approach based on the moments of the spin-Hamiltonian.

In the analysis using model (2) for **2**, we assumed $J_{Cr\text{-}Co} = 0$. From the experimental $\chi_M T$ product of **2**, we subtracted the calculated $\chi_M T$ value ($15\ cm^3\,mol^{-1}\,K$) for eight uncoupled Cr^{III} ions (the small D_{Cr} parameter made no difference to the high temperature data), and divided the result by six, to generate the $\chi_M T$ curve for an "isolated" Co^{II} site (Figure 2). We then attempted to fit the $\chi_M T$ product of the "isolated" Co^{II} site to an anisotropic single-ion spin-Hamiltonian:

$$\hat{H}_{aniso} = D_{Co}\left[\hat{S}^2_{z,Co} - S_{Co}(S_{Co}+1)/3\right] + \mu_B B g_{Co} \hat{S}_{Co} \quad (3)$$

with $S_{Co} = 3/2$, reflecting the $^4A_{2g}$ ground term of Co^{II}. A reasonable, but not perfect, agreement was found for $g_{Co} = 2.0$ and $D_{Co} = +80\ cm^{-1}$ (Figure 2). With these parameters, only the ground ($|m| = {}^1/_2$) Kramers doublet would be populated at low temperatures. Given that the observed low-temperature $\chi_M T$ value for an "isolated" Co^{II} is of the order of $1.1\ cm^3\,K\,mol^{-1}$, the calculated low-temperature paramagnetic $\chi_M T$ limit for **2** would be about $21.6\ cm^3\,K\,mol^{-1}$, in good agreement with the observed low-temperature plateau value of $21.5\ cm^3\,mol^{-1}\,K$, at 8 K.

The nature of the weak exchange interactions in **1** and **2** was further probed by Q- and W-band EPR spectroscopy (34 and 94 GHz, respectively). Spectra of $[Cr^{III}L_3]$, that is, the isolated corner fragment of **1** and **2** at 5 K are those of an $S_{Cr} = 3/2$ ($g_{Cr} = 1.97$) with near axial ZFS parameters of $D_{Cr} = -0.55$ and $E_{Cr} = 0.025\ cm^{-1}$, in the range found for other [Cr(diketonate)$_3$] complexes[17] (Figures S5 and S3; simulated[22] with a Gaussian linewidth of 60 mT and a 10% D-strain).

Spectra of **1** at 5 K are severely broadened compared with $[Cr^{III}L_3]$, with linewidths approaching 400 mT (Figure S6), consistent with $|J_{Cr\text{-}Cu}|$ being smaller than $|D_{Cr}|$ and with an upper bound given by the linewidth; also consistent with $J_{Cr\text{-}Cu}$ as determined from statistical spectroscopy methods. The lack of structure prevents any further analysis. Spectra of **2** are also broadened but structured (Figure 3), resembling those of $[Cr^{III}L_3]$ with noticeable shifts in resonance fields and new resonances at around 1400 mT (at W-band) because of the Co^{II} sites. This implies $|J_{Cr\text{-}Co}| < |D_{Co}|$. The matrix dimension of **2** is far too large for simulation using the full Cr_8Co_6 spin system, while the weak exchange limit precludes handling the problem by low-energy subspace methods.[23] Hence, we attempted to model the spectra of **2** as a simple $Cr^{III}Co^{II}$ dimer, of which the parameters for Cr^{III} are defined experimentally from $[Cr^{III}L_3]$, and those for Co^{II} are fixed from the "isolated" $S_{Co} = 3/2$ Co^{II} model (Figure 2). We also fixed the relative orientation of the principal axes of the D_{Cr} and D_{Co} ZFS tensors to 54.7°, which is the angle between the C_4 (face-normal, defining the unique axis of Co^{II} in **2**) and C_3 (body-diagonal, defining the unique axis of Cr^{III} in **2**) axes of a cube. Thus, the only variable is $J_{Cr\text{-}Co}$. The calculated spectra were very sensitive to small $J_{Cr\text{-}Co}$ (e.g. Figure S7), and we could reproduce the experimental resonances reasonably with $J_{Cr\text{-}Co} = -0.3\ cm^{-1}$ (Figure 3, bottom, and S7). Note that the determined $J_{Cr\text{-}Co}$ value is not that of **2** but for the fictitious $Cr^{III}Co^{II}$ dimer. The isotropic exchange parameter, $J_{Cr\text{-}Co}$, of **2** is likely smaller in magnitude.

Variable-temperature-and-variable-field (VTVB) magnetization studies of complexes **1** and **2** (Figure S8) were consistent with weak exchange in both cases. For **1**, the saturation magnetic moment of 30.8 μ_B at 5 T and 2 K, was as expected for full spin alignment. In the case of **2**, the magnetic moment was also 30.8 μ_B at 5 T and 2 K. If only the lower Kramers doublet of Co^{II} (which has $g_{eff,x} = 4$, $g_{eff,y} = 4$, $g_{eff,z} = 2$)

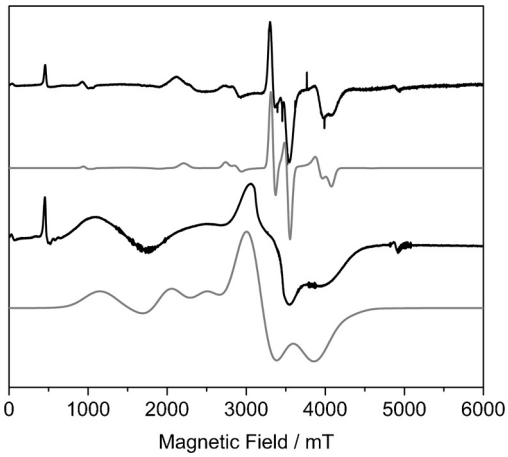

Figure 3. W-band EPR spectra of $[Cr^{III}L_3]$ (top) and **2** (bottom) in the solid state and 5 K (black lines). Calculated spectra (grey lines) 1) for $S_{Cr}=3/2$, $g_{Cr}=1.97$, $D_{Cr}=+0.55$ and $E_{Cr}=0.025$ cm^{-1} (top), and 2) for a $Cr^{III}Co^{II}$ dimer, with $S_{Cr}=S_{Co}=3/2$, $g_{Cr}=1.97$, $g_{Co}=2.05$, $D_{Cr}=-0.55$ cm^{-1}, $E_{Cr}=0.025$ cm^{-1}, $D_{Co}=+80$ cm^{-1}, $J_{Cr\text{-}Co}=-0.3$ cm^{-1} and an angle between the D_{zz}^{Cr} and D_{zz}^{Co} vectors of 54.7° (bottom; 400 mT Gaussian linewidth).

is populated in this regime ($D_{Co} \gg kT$), then the theoretical maximum magnetization is 34 μ_B, in reasonable agreement with the experimental data, given the simplicity of the model.

The flexibility in the design and construction of these $[M^{III}{}_8M^{II}{}_6]^{12+}$ cages offers enormous scope for tuning their physical properties. The corner ions can potentially be any M^{III} ion, as long as the precursor ML_3 can be prepared; the face-capping metal ions can be any M^{II} ion that can adopt square-planar, square-pyramidal, or octahedral geometry. The 12+ charge on the cage suggests that the anions can be varied and can be innocent or non-innocent, and the solvent bonded terminally to the M^{II} ions should be easily replaced, thus allowing the attachment of a host of different species and/or the assembly of the cubes into higher-order structures. The large internal cavity suggests that the cage could play host to different species, and indeed one can imagine constructing magnetic coordination capsules capable of hosting magnetic and/or redox-active guests, exerting control over (switching on and off) magnetic exchange between metal ions in the host framework and between the host and guest(s). Post-synthetic exohedral functionalization and simple changes to ligand design will also allow the modification of the magnetic properties, but additionally can be manipulated to tune solubility, reactivity, stability, and substrate specificity.

Keywords: EPR spectroscopy · heterometallic cages · magnetometry · molecular magnetism · transition metals

How to cite: *Angew. Chem. Int. Ed.* **2015**, *54*, 6761–6764
Angew. Chem. **2015**, *127*, 6865–6868

[1] S. Thiele, F. Balestro, R. Ballou, S. Klyatskaya, M. Ruben, W. Wernsdorfer, *Science* **2014**, *344*, 1135.
[2] M. Ganzhorn, S. Klyatskaya, M. Ruben, W. Wernsdorfer, *Nat. Nanotechnol.* **2013**, *8*, 165.
[3] G. A. Timco, E. J. L. McInnes, R. E. P. Winpenny, *Chem. Soc. Rev.* **2013**, *42*, 1796.
[4] A. Cornia, M. Mannini, P. Sainctavit, R. Sessoli, *Chem. Soc. Rev.* **2011**, *40*, 3076.
[5] G. Aromí, D. Aguila, P. Gamez, F. Luis, O. Roubeau, *Chem. Soc. Rev.* **2012**, *41*, 537.
[6] J. Lehmann, A. Gaita-Ariño, E. Coronado, D. Loss, *Nat. Nanotechnol.* **2007**, *2*, 312.
[7] a) G. Aromí, E. K. Brechin, *Struct. Bonding (Berlin)* **2006**, *122*, 1; b) C. J. Milios, R. E. P. Winpenny, *Struct. Bond.* **2014**, DOI: 10.1007/430_2014_149; c) J.-N. Rebilly, T. Mallah, *Struct. Bonding (Berlin)* **2006**, *122*, 103–131.
[8] a) T. Murase, Y. Nishijima, M. Fujita, *J. Am. Chem. Soc.* **2012**, *134*, 162–164; b) C. Zhao, Q.-F. Sun, W. M. Hart-Cooper, A. G. DiPasquale, F. D. Toste, R. G. Bergman, K. N. Raymond, *J. Am. Chem. Soc.* **2013**, *135*, 18802–18805; c) F. Schmitt, J. Freudenreich, N. P. E. Barry, L. Juillerat-Jeanneret, G. Süss-Fink, B. Therrien, *J. Am. Chem. Soc.* **2012**, *134*, 754–757; d) P. Mal, B. Breiner, K. Rissanen, J. R. Nitschke, *Science* **2009**, *324*, 1697–1699.
[9] M. M. J. Smulders, A. Jiménez, J. R. Nitschke, *Angew. Chem. Int. Ed.* **2012**, *51*, 6681–6685; *Angew. Chem.* **2012**, *124*, 6785–6789.
[10] a) S. Hiraoka, Y. Sakata, M. Shionoya, *J. Am. Chem. Soc.* **2008**, *130*, 10058–10059; b) S.-L. Huang, Y.-J. Lin, T. S. A. Hor, G.-X. Jin, *J. Am. Chem. Soc.* **2013**, *135*, 8125–8128; c) H. Li, Y.-F. Han, Y.-J. Lin, Z.-W. Guo, G.-X. Jin, *J. Am. Chem. Soc.* **2014**, *136*, 2982–2985; d) A. J. Metherell, M. D. Ward, *Chem. Commun.* **2014**, *50*, 6330; e) H.-B. Wu, Q.-M. Wang, *Angew. Chem. Int. Ed.* **2009**, *48*, 7343; *Angew. Chem.* **2009**, *121*, 7479; f) M. B. Duriska, S. M. Neville, B. Moubaraki, J. D. Cashion, G. J. Halder, K. W. Chapman, C. Balde, J.-F. Létard, K. S. Murray, C. J. Kepert, S. R. Batten, *Angew. Chem. Int. Ed.* **2009**, *48*, 2549; *Angew. Chem.* **2009**, *121*, 2587; g) M. B. Duriska, S. M. Neville, J. Lu, S. S. Iremonger, J. F. Boas, C. J. Kepert, S. R. Batten, *Angew. Chem. Int. Ed.* **2009**, *48*, 8919; *Angew. Chem.* **2009**, *121*, 9081; h) J. L. Heinrich, P. A. Berseth, J. R. Long, *Chem. Commun.* **1998**, 1231.
[11] a) S. Mecozzi, J. Rebek, *Chem. Eur. J.* **1998**, *4*, 1016; b) N. R. Voss, M. Gerstein, *Nucleic Acids Res.* **2010**, *38*, W555.
[12] H.-B. Wu, Q.-M. Wang, *Angew. Chem. Int. Ed.* **2009**, *48*, 7343; *Angew. Chem.* **2009**, *121*, 7479.
[13] F. Reichel, J. K. Clegg, K. Gloe, J. J. Weigand, J. K. Reynolds, C.-G. Li, J. R. Aldrich-Wright, C. J. Kepert, L. F. Lindoy, H.-C. Yao, F. Li, *Inorg. Chem.* **2014**, *53*, 688.
[14] M. B. Duriska, S. M. Neville, B. Moubaraki, J. D. Cashion, G. J. Halder, K. W. Chapman, C. Balde, J.-F. Létard, K. S. Murray, C. J. Kepert, S. R. Batten, *Angew. Chem. Int. Ed.* **2009**, *48*, 2549; *Angew. Chem.* **2009**, *121*, 2587.
[15] See for example a) J. J. Sokol, M. P. Shores, J. R. Long, *Angew. Chem. Int. Ed.* **2001**, *40*, 236; *Angew. Chem.* **2001**, *113*, 242; b) S. Wang, J.-L. Zuo, H.-C. Zhou, H. J. Choi, Y. Ke, J. R. Long, X.-Z. You, *Angew. Chem. Int. Ed.* **2004**, *43*, 5940; *Angew. Chem.* **2004**, *116*, 6066.
[16] L. L. Lohr, J. C. Miller, R. R. Sharp, *J. Chem. Phys.* **1999**, *111*, 10148; A. Bencini, C. Benelli, D. Gatteschi, C. Zanchini, *Inorg. Chem.* **1980**, *19*, 1301.
[17] G. Elbers, S. Remme, G. Lehmann, *Inorg. Chem.* **1986**, *25*, 896.
[18] S. S. M. Wong, *Nuclear Statistical Spectroscopy*, Oxford University Press and Clarendon Press, Oxford, **1986**.
[19] G. S. Rushbrooke, P. J. Wood, *Mol. Phys.* **1958**, *1*, 257.
[20] a) L. R. Mead, N. Papanicoaou, *J. Math. Phys.* **1984**, *25*, 2404; b) S. M. Grimes, T. N. Massey, *Fusion Eng. Des.* **1997**, *37*, 89.
[21] S. M. Grimes, T. N. Massey, *Phys. Rev. C* **1995**, *51*, 606.
[22] Simulations performed with EasySpin software: S. Stoll, A. Schweiger, *J. Magn. Reson.* **2006**, *178*, 42.
[23] S. Piligkos, E. Bill, D. Collison, E. J. L. McInnes, G. A. Timco, H. Weihe, R. E. P. Winpenny, F. Neese, *J. Am. Chem. Soc.* **2007**, *129*, 760.

Received: February 3, 2015
Published online: April 20, 2015

Angewandte Chemie
Eine Zeitschrift der Gesellschaft Deutscher Chemiker

Supporting Information

German Edition: DOI:

$[Cr^{III}_8M^{II}_6]^{12+}$ Coordination Cubes ($M^{II} = Cu, Co$)**

Sergio Sanz, Helen M. O'Connor, Eufemio Moreno Pineda, Kasper S. Pedersen, Gary S. Nichol, Ole Mønsted, Høgni Weihe, Stergios Piligkos, Eric J. L. McInnes,* Paul J. Lusby,* and Euan K. Brechin**

ange_201501041_sm_miscellaneous_information.pdf

Experimental Procedures

1-(4-pyridyl)butane-1,3-dione (HL) was prepared by published procedures.[1] Solvents and reagents were used as received from commercial suppliers.

Synthesis of tris{1-(4-pyridyl)acetylacetonato}chromium(III), CrL_3
$CrCl_3 \cdot 6H_2O$ (530 mg, 2 mmol) and urea (500 mg, 8 mmol) were dissolved in 50 mL of distilled water. To this solution, 1-(4-pyridyl)butane-1,3-dione, HL, (1.07 g, 6.6 mmol) was added, and the solution stirred for two days at 90°C. The resultant light-brown precipitate was filtered and washed with water. The crude product was extracted with $CHCl_3$ and dried over anhydrous $MgSO_4$. The $CHCl_3$ was removed under reduced pressure to afford the product as a light-brown solid. Purification was performed using flash column chromatography (CH_2Cl_2/acetone 1:1) to yield a light-brown product (0.7 g, 65%). Elemental analysis (%) calculated (found) for $C_{27}H_{24}CrN_3O_6$ (538.50 g/mol): C 60.22 (60.06), H 4.49 (4.19), N 7.80 (7.68). ESI-MS (positive-ion detection): *m/z* = 539.1173 {27%, $[M + H]^+$}, 561.0978 {92%, $[M + Na]^+$}, 701.1850 {100%, $[M + HL - e]^+$}, 914.1614 {45%, $[2M - L]^+$}, 1099.2083 {27%, $[2M + Na]^+$}.

Synthesis of $[Cr_8Cu_6L_{24}(H_2O)_{10}(NO_3)_2](NO_3)_{10}$ (1)
To a solution of metalloligand CrL_3 (108 mg, 0.2 mmol) in 10 mL of dichloromethane was added a solution of $Cu(NO_3)_2$ 3 H_2O (48 mg, 0.2 mmol) in 10 mL of methanol. The solution is stirred for 1 hour, before being filtered and allowed to stand. Dark-brown X-ray quality crystals were obtained after room temperature evaporation of the mother liquid during 5 days. Elemental analysis (%) calculated (found) for $C_{216}H_{208}N_{36}O_{92}Cr_8Cu_6$ (5325.32): C 48.72 (48.57), H 3.94 (3.86), N 4.73 (4.58).

Synthesis of $[Cr_8Co_6L_{24}(H_2O)_{12}](ClO_4)_{12}$ (2)
To a solution of metalloligand CrL_3 (108 mg, 0.2 mmol) in 10 mL of dichloromethane was added a solution of $Co(ClO_4)_2$ 6 H_2O (73 mg, 0.2 mmol) in 10 mL of methanol/nitromethane (1:1 *v*/*v*). The solution is stirred for 1 hour, before being filtered and allowed to stand. Small dark-brown rod-like X-ray quality crystals were obtained after room temperature evaporation of the mother liquid during 5 days. Elemental analysis (%) calculated (found) for $C_{216}H_{216}N_{24}O_{108}Cl_{12}Cr_8Co_6$ (6071.13): C 42.73 (42.47), H 3.59 (3.43), N 5.54 (5.31).

Crystallographic details:
Crystal data for **1**: $C_{216}H_{208}N_{36}O_{92}Cr_8Cu_6$, M = 5325.32, orthorhombic, space group $Pca2_1$, a = 38.1763(6), b = 31.3516(5), c = 29.1087(7) Å, α = 90, β = 90, γ = 90°, V = 34839.9(10) $Å^3$, Z = 4, Absorption coefficient = 3.717 mm^{-1}, D_c = 1.205 Mg / m^3, 171353 reflections collected, 33419 unique (R_{int} = 0.0805), final R_1 = 0.0538, wR_2 = 0.1385, *GoF* = 0.983, data/restraints/parameters = 33419/1281/3240. A suitable crystal (0.20 × 0.16 × 0.12 mm^3) was selected and mounted on a MITIGEN holder in Paratone oil on a Agilent Technologies SuperNova diffractometer using CuK_α radiation. The crystal was kept at T = 120.01(10) K during data collection. Using **Olex2** the structure was solved with the ShelXT structure solution program, using the Direct Methods solution method. The model was refined with version 2014/6 of **ShelXL** using Least Squares minimisation.[2], [3] CCDC 1026380.
Crystal data for **2**: $C_{216}H_{216}N_{24}O_{108}Cl_{12}Cr_8Co_6$, M = 6071.10, tetragonal, space group P4/n, a = 30.5293(4), b = 30.5293(4), c = 20.7384(4) Å, α = 90, β = 90, γ = 90°, V = 19328.9(7) $Å^3$, Z = 2, Absorption coefficient = 5.072 mm^{-1}, D_c = 1.043 Mg / m^3, 124556 reflections collected, 9954 unique (R_{int} = 0.1317), final R_1 = 0.0672, wR_2 = 0.1922, *GoF* = 1.068, data/restraints/parameters = 9954/4/723. A suitable crystal (0.39 × 0.07 × 0.05 mm^3) was selected and mounted on a MITIGEN holder in Paratone oil. on a Agilent Technologies SuperNova diffractometer using CuK_α radiation. The crystal was kept at T = 120.0 K during data collection. Using **Olex2** the structure was solved

with the ShelXT structure solution program, using the direct methods solution method. The model was refined with version of **ShelXL** using Least Squares minimisation.[2], [3] CCDC 1026379.

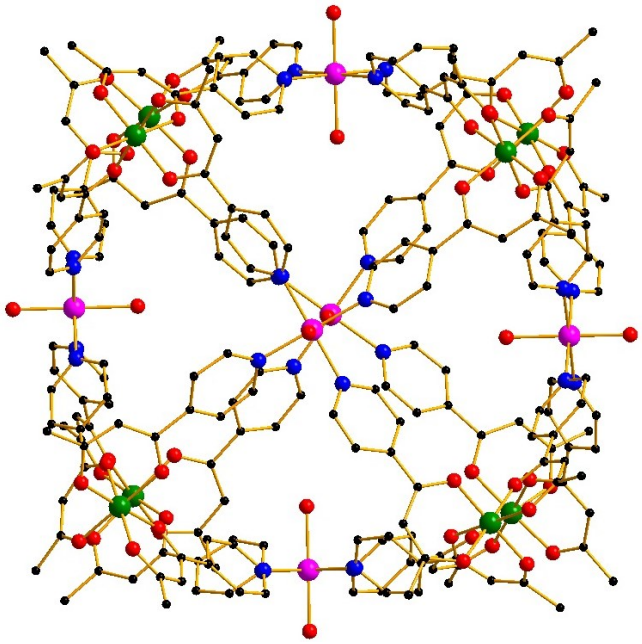

Figure S1. The structure of the cation of complex **2**. Colour code: Cr = green, Co = pink, O = red, N = blue, C = black. Anions and H-atoms omitted for clarity.

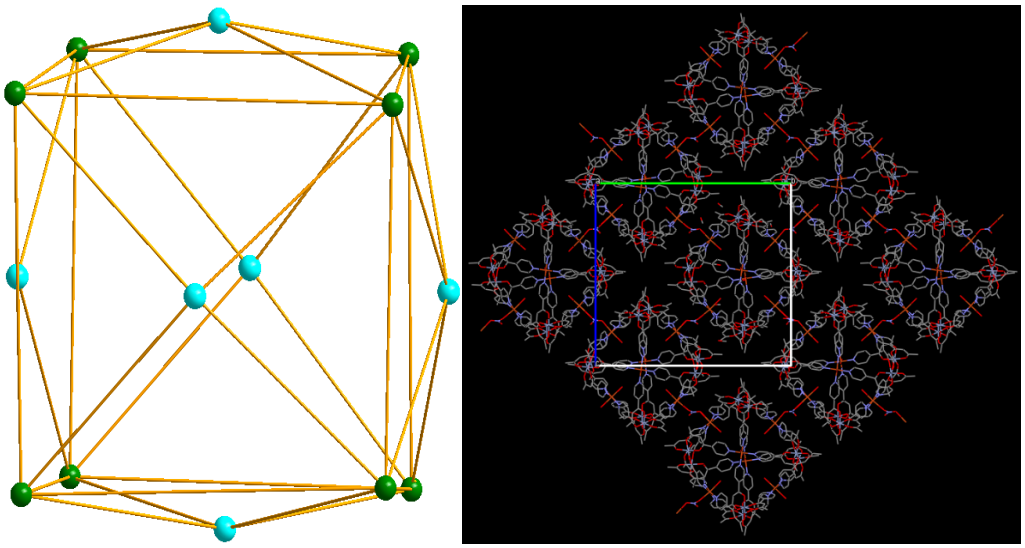

Figure S2. (Left) The metallic skeleton of the cationic cage common to both **1** and **2**. Colour code: Cr = green, Cu/Co = pale blue. (Right) The packing of the cations of **1** in the crystal as viewed down the *a*-axis. The clusters are connected to each other through bridging nitrate ions. Each cube has two nitrates, resulting in the formation of a square sheet of cages in the *bc*-plane. H-atoms and the non-bonded nitrate anions omitted for clarity.

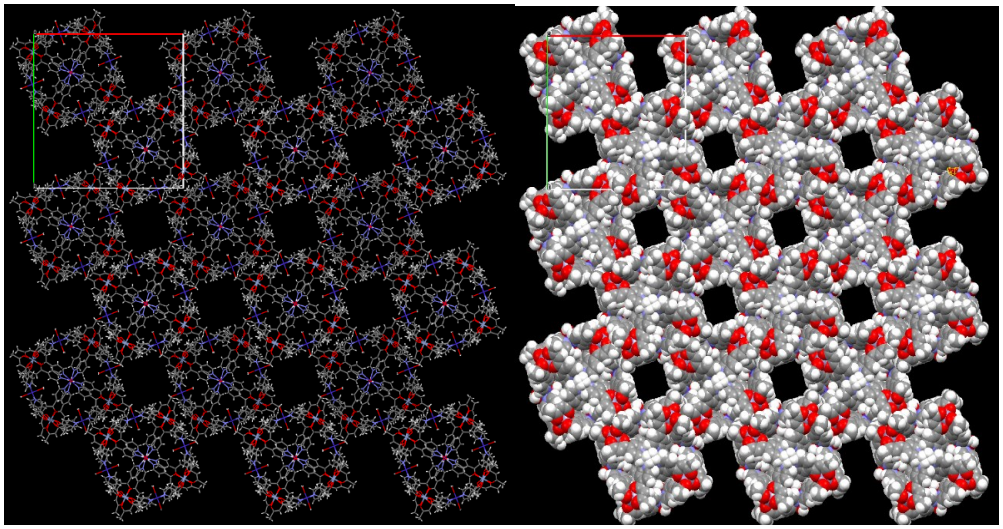

Figure S3. Packing of the cations of **2** in the crystal, viewed down the c-axis in both wireframe (left) and spacefill (right) representations. Anions are omitted for clarity.

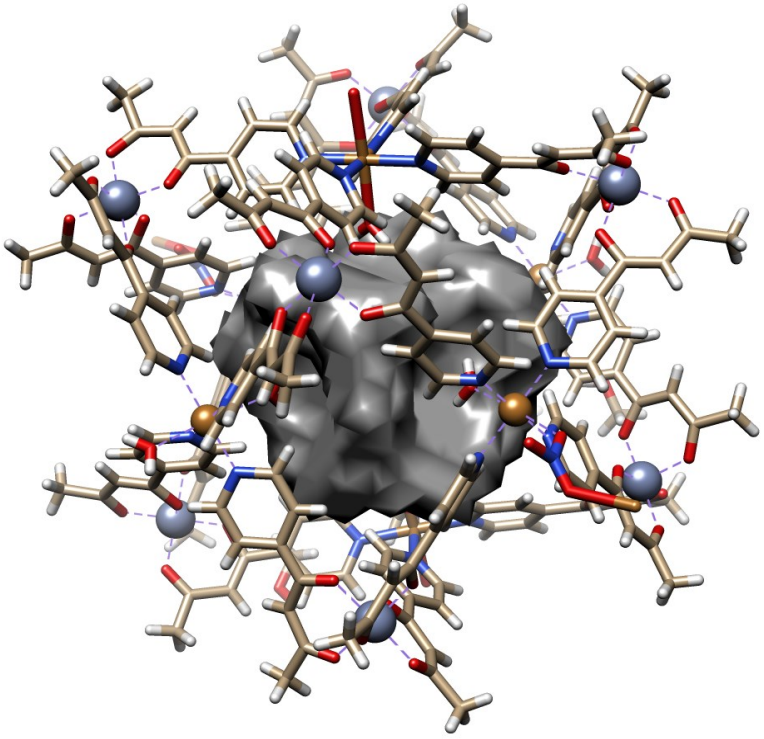

Figure S4. Representation of the available internal cavity space in complex **2**. A volume of 966 $Å^3$ was calculated employing an outer probe of 8.0 Å and an internal probe of 1.9 Å on a model in which the terminally bonded solvent molecules on the M(II) had been removed. See reference 11b in the main text for details.

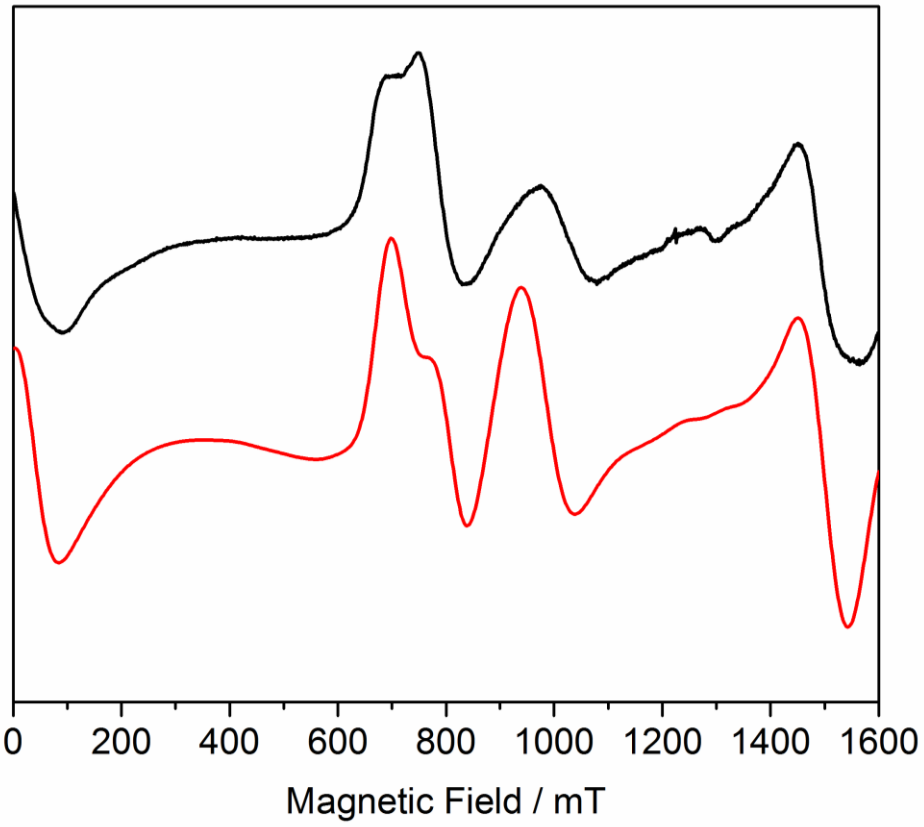

Figure S5. Q-band EPR spectrum of $[Cr^{III}L_3]$ in the solid state at 5 K (black), and simulation (red) with $S_{Cr} = 3/2$, $g_{Cr} = 1.97$, $D_{Cr} = +0.55$ and $E_{Cr} = 0.025$ cm^{-1}, with a 60 mT Gaussian linewidth and 10 % *D*-strain.

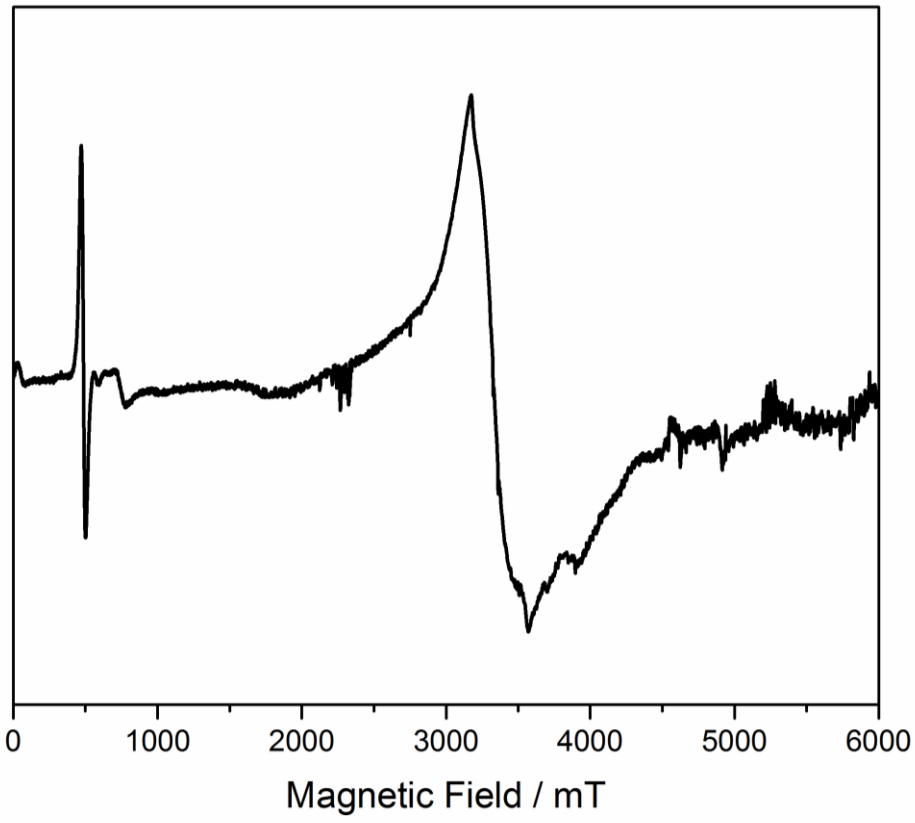

Figure S6. W-band EPR spectrum of **1** in the solid state at 5 K.

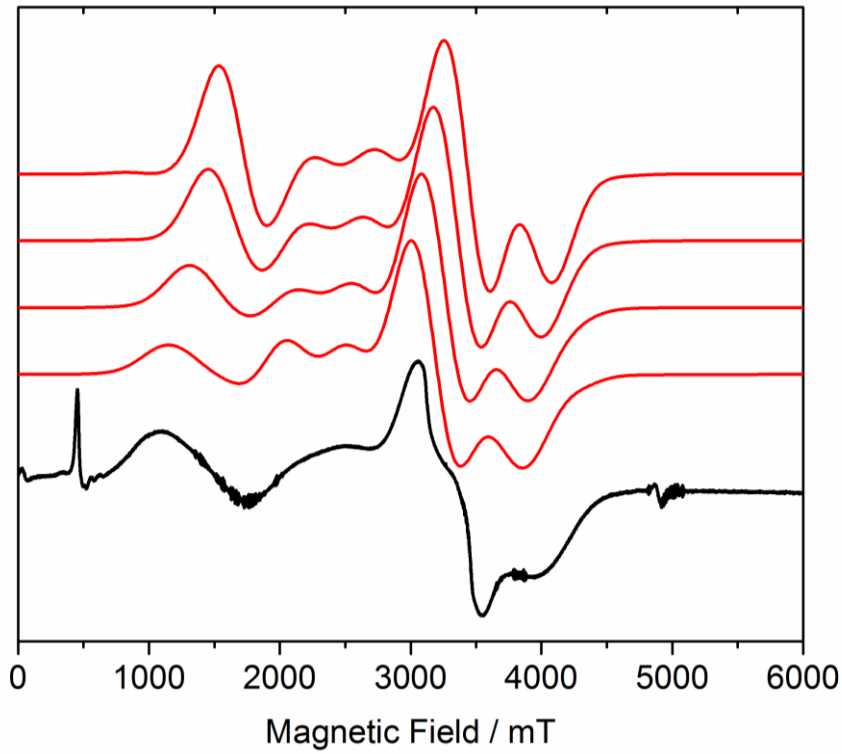

Figure S7. W-band EPR spectrum of **2** in the solid state at 5 K (black), and calculated spectra (red) for a CrCo dimer, with $S_{Cr} = S_{Co} = 3/2$, $g_{Cr} = 1.97$, $g_{Co} = 2.05$, $D_{Cr} = -0.55$ cm^{-1}, $E_{Cr} = 0.025$ cm^{-1}, $D_{Co} = +80$ cm^{-1} and an angle between the D_{zz}^{Cr} and D_{zz}^{Co} vectors of 54.7º. From top-to-bottom, $J_{CrCo} = 0$, -0.1, -0.2 and -0.3 cm^{-1}. A Gaussian linewidth of 400 mT was used.

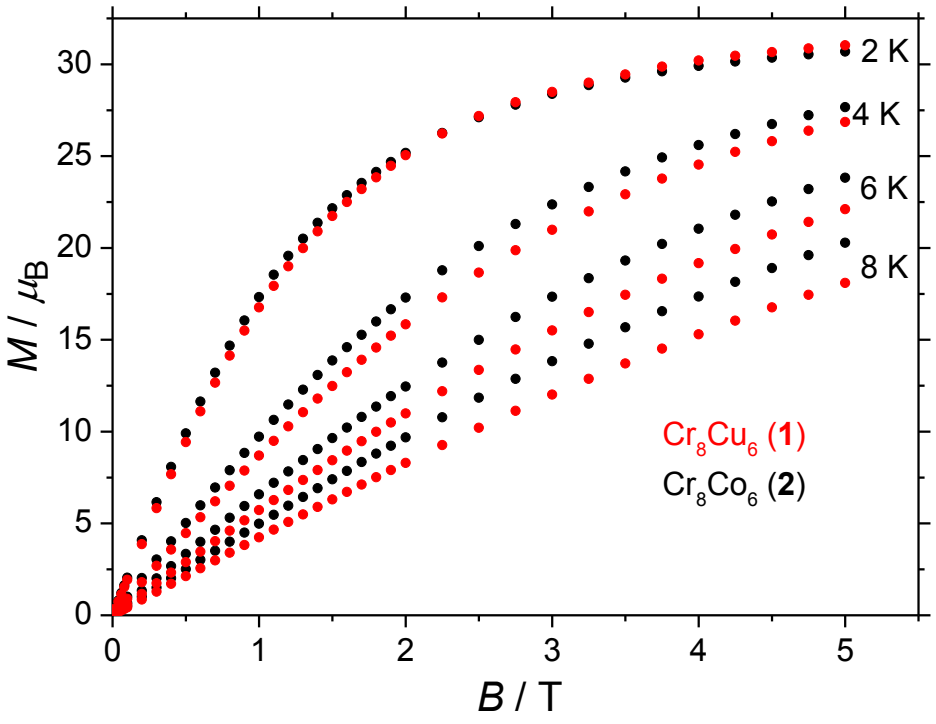

Figure S8. Variable-temperature-and-variable-field (VTVB) magnetisation studies on complexes **1** and **2** in the temperature range 2 to 8 K and in magnetic fields from 0.02 to 5.00 T.

References

[1] B. Singh, G. Y. Lesher, K. C. Pluncket, E. D. Pagani, D. C. Bode, R. G. Bentley, M. J. Connell, L. T. Hamel, P. J. Silver, *J. Med. Chem.* **1992**, *35*, 4858-4865.
[2] O.V. Dolomanov, L. J. Bourhis, R. J. Gildea, J. A. K. Howard, H. Puschmann, Olex2: A complete structure solution, refinement and analysis program, *J. Appl. Cryst.* **2009**, *42*, 339-341.
[3] G. M. Sheldrick, A short history of ShelX, *Acta Cryst.* **2008**, *A64*, 339-341.

Volume 18 | Number 26 | 14 July 2016 | Pages 4877–5052

CrystEngComm

www.rsc.org/crystengcomm

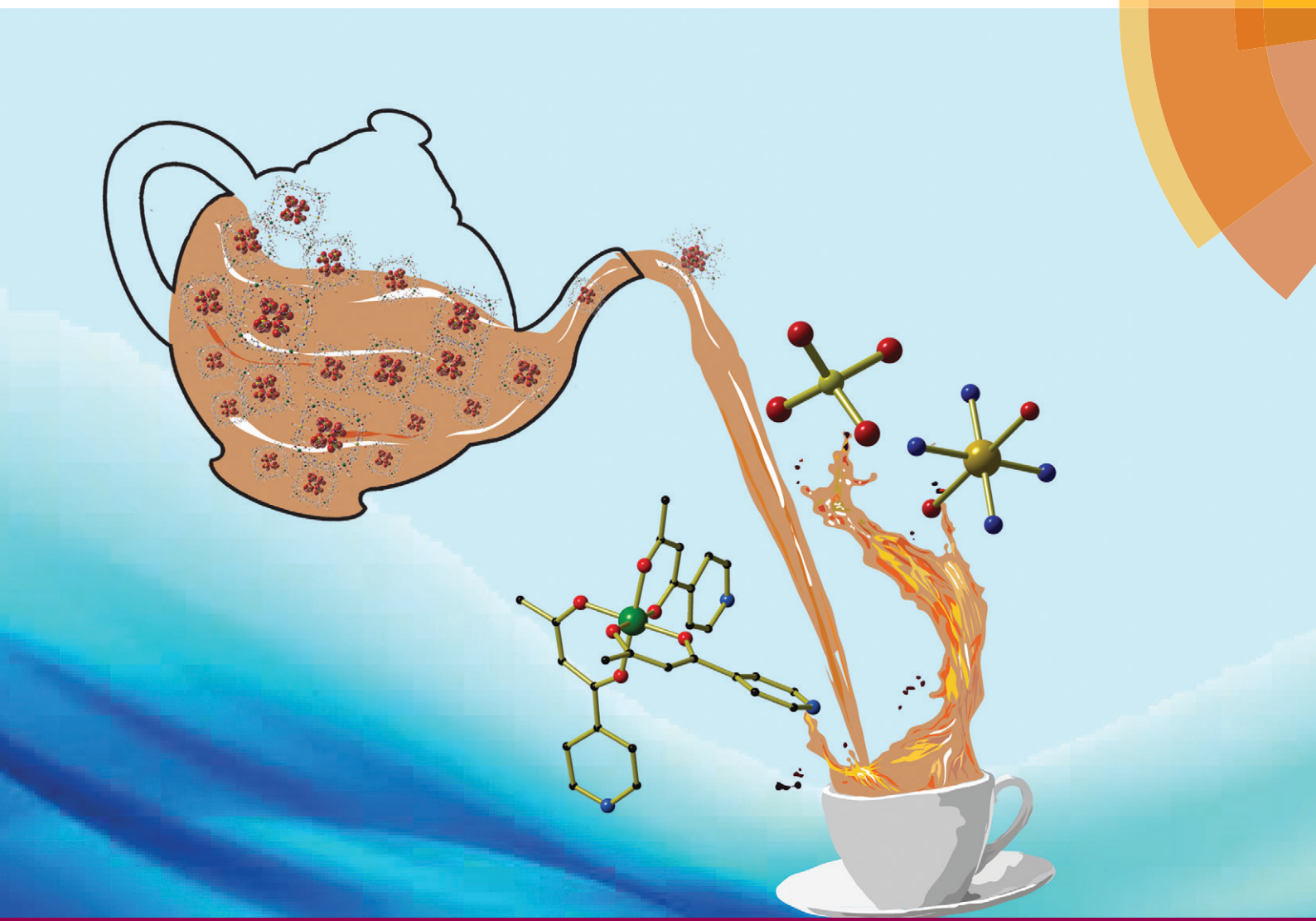

Themed issue: Form and Function of Molecular Cups and Capsules

ROYAL SOCIETY OF CHEMISTRY

PAPER
S. Sanz, P. J. Lusby, E. K. Brechin *et al.*
$[Cr^{III}_{8}M^{II}_{6}]^{n+}$ (M^{II} = Cu, Co) face-centred, metallosupramolecular cubes

175 YEARS

CrystEngComm

PAPER

View Article Online
View Journal | View Issue

Cite this: *CrystEngComm*, 2016, **18**, 4914

$[Cr^{III}_8M^{II}_6]^{n+}$ (M^{II} = Cu, Co) face-centred, metallosupramolecular cubes†

H. M. O'Connor,‡[a] S. Sanz,‡*[a] M. B. Pitak,[b] S. J. Coles,[b] G. S. Nichol,[a] S. Piligkos,[c] P. J. Lusby*[a] and E. K. Brechin*[a]

Received 23rd March 2016,
Accepted 18th April 2016

DOI: 10.1039/c6ce00654j

www.rsc.org/crystengcomm

Four $[Cr^{III}_8M^{II}_6]^{n+}$ (M^{II} = Cu, Co) coordination cubes of formulae $[Cr_8Co_6L_{24}Cl_{12}]$ (**1**), $[Cr_8Co_6L_{24}(SCN)_{12}]$ (**2**), $[Cr_8Cu_6L_{24}(H_2O)_{12}](SO_4)_6$ (**3**), and $[Cr_8Cu_6L_{24}Cl_{12}]$ (**4**) (where HL is 1-(4-pyridyl)butane-1,3-dione), were synthesised using the $[Cr^{III}L_3]$ metalloligand in combination with a variety of M^{II} salts. The metallic skeleton of each cage describes a cube in which the $[Cr^{III}L_3]$ moieties occupy the eight vertices and the M^{II} ions lie at the centre of the six faces. The axial coordination sites of the M^{II} cations are occupied by either H_2O molecules or Cl^-/SCN^- anions originating from the M^{II} salt used in the synthesis, resulting in neutral **1**, **2** and **4** and the cage in **3** being a 12+ cation; the charge-balancing SO_4^{2-} anions accommodated both inside and outside the cube. Magnetic susceptibility and magnetisation measurements reveal weak exchange between nearest neighbour metal ions, mediated *via* the L^- ligands. The modular assembly of the cubes suggests that any combination of $[M^{III}L_3]$ metalloligand and M^{II} salt will work, potentially resulting in an enormous family of supramolecular assemblies. The charge of the cubes is controlled by the nature of the ligand occupying the axial sites on the M^{II} ions, suggesting trivial ligand exchange may offer control over, amongst others, solubility, reactivity, post-synthetic modification and substrate specificity. The large internal cavities of the cubes also suggest host–guest chemistry may be a fruiful route to encapsulating magnetic and/or redox active guests which could be employed to control magnetic behaviour, and the construction of multifunctional materials.

Introduction

Metallosupramolecular chemistry relies on the use of dynamic metal–ligand bonds for the construction of multinuclear coordination assemblies.[1,2] From a design perspective, the selection of a particular metal ion can have numerous implications on the outcome of any given assembly reaction because they provide differing coordination geometry preferences, and a range of binding strengths, which often show a strong correlation with substitutional lability.[3] Given this potential variation in metal-ion component and the capacity to readily access multitopic ligands with differing coordination vectors, it is perhaps not surprising that this rational design approach has yielded a vast array of discrete nanostructures of varying shape, size and nuclearity.[4,5] Often, the combination of highly directional metal–ligand bonding and the rigid nature of the ligand framework creates a molecular scaffold that defines the boundaries of a permanent internal cavity.[2,4,5] These discrete void areas impart unique properties to the structure allowing for numerous applications[6] in areas such as gas adsorption,[7,8] stabilisation of reactive molecules,[9] catalysis,[10] biochemical and biomedical applications,[11] separation of species from a mixture,[12] and development of magnetic materials.[8,13]

In the field of molecular magnetism the systematic exploration of ligand design, metal identity and reaction conditions is employed to build families of structurally related complexes whose subsequent physical characterisation reveals the underlying principles behind the magneto-structural relationship.[14] Geometric and molecular symmetry, for example, defines a range of fascinating, and potentially useful low temperature physics, ranging from spin-frustrated molecules to anisotropic metal cages behaving like nanoscale magnets.[15,16] Judicious ligand design is the first stage of the synthetic process,[17] and the use of rigid ligands with fixed coordination modes allows for the construction of cages with

[a] *EaStCHEM School of Chemistry, The University of Edinburgh, David Brewster Road, Edinburgh, EH9 3FJ, UK. E-mail: S.Calvo@ed.ac.uk, Paul.Lusby@ed.ac.uk, E.Brechin@ed.ac.uk*
[b] *UK National Crystallography Service, Chemistry, University of Southampton, Southampton, Highfield Campus, SO17 1BJ, UK*
[c] *Department of Chemistry, University of Copenhagen, Universitetsparken 5, Copenhagen, DK-2100, Denmark*

† CCDC 1457376–1457380. CCDC Crystallographic data (including structure factors) for **1**–**4** have been deposited with the Cambridge Crystallographic Data Centre. For crystallographic data in CIF or other electronic format see DOI: 10.1039/c6ce00654j

‡ S. Sanz and H. M. O'Connor contributed equally to this work.

predictable topologies,[18] and potentially those that possess cavities capable of binding guest molecules. However, while the host–guest chemistry of diamagnetic coordination capsules has been widely studied and exploited, magnetic coordination capsules and the study of the interaction between magnetic hosts and guests has largely been ignored.[8,19]

Recently we embarked on a new project that would enable heterometallic paramagnetic coordination cages to be accessed in a modular and predictable fashion,[20] an approach centred around the tritopic "metalloligand" $[M^{III}L_3]$ (HL = 1-(4-pyridyl)butane-1,3-dione), which features a tris(acac) octahedral transition metal core pendant functionalised with three *p*-pyridyl donor groups (Fig. 1).

In the case of the *fac*-isomer, the N-donor groups are aligned in a tripodal array such that the entropically-favoured smallest assembly that ensures maximum-site occupancy with a square-planar connector would be a cubic system.[20] As such, we would be able to use pre-designed self-assembly to position one metallic [and paramagnetic] ion at the eight cube vertices and another at the centre of the six faces. Herein, we report the preparation and structural data of four heterometallic $[Cr^{III}{}_8M^{II}{}_6]^{n+}$ molecular cubes, where M^{II} = Cu, Co, along with a discussion of their magnetic behaviour.

Experimental section

Syntheses

1-(4-Pyridyl)butane-1,3-dione (HL) and the metalloligand $[CrL_3]$ were prepared according to previously published procedures.[20,21] All reactions were performed under aerobic conditions. Solvents and reagents were used as received from commercial suppliers. Variable-temperature, solid-state direct current (dc) magnetic susceptibility and variable-temperature-and-variable-field (VTVB) magnetisation data down to T = 2 K were collected on a Quantum Design MPMS-XL SQUID magnetometer equipped with a 7 T dc magnet.

$[Cr_8Co_6L_{24}Cl_{12}]$ (1)

To a solution of the metalloligand $[CrL_3]$ (108 mg, 0.2 mmol) in 20 mL of dichloromethane/tetrahydrofuran (1 : 1 v/v) was added $CoCl_2$ (20 mg, 0.15 mmol). The solution was stirred for 14 hours, before being filtered and allowed to stand. Brown, X-ray quality crystals were obtained after room temperature evaporation of the mother liquor after 5 days. Elemental analysis (%) calculated (found): C 51.84 (51.61), H 4.20 (4.09), N 6.25 (6.54). Yield = 63%.

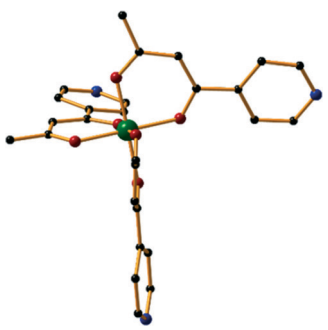

Fig. 1 The molecular structure of $[Cr^{III}L_3]$. Colour code: Cr = green, O = red, N = blue, C = black. H = atoms omitted.

$[Cr_8Co_6L_{24}(SCN)_{12}]$ (2)

To a solution of the metalloligand $[CrL_3]$ (108 mg, 0.2 mmol) in 20 mL of dichloromethane/methanol (1 : 1 v/v) was added $Co(SCN)_2$ (35 mg, 0.2 mmol). The solution was stirred for 2 hours, before being filtered and allowed to stand. Brown, X-ray quality crystals were obtained after room temperature evaporation of the mother liquor after 5 days. Elemental analysis (%) calculated (found): C 53.63 (53.26), H 3.79 (3.51), N 4.94 (5.13). Yield = 77%.

$[Cr_8Cu_6L_{24}(H_2O)_{12}](SO_4)_6$ (3)

To a solution of the metalloligand $[CrL_3]$ (108 mg, 0.2 mmol) in 20 mL of dichloromethane/methanol (1 : 1 v/v) was added a solution of $Cu(SO_4)\cdot 5H_2O$ (50 mg, 0.2 mmol) in 3 mL of water. The solution was stirred for 1 hour, before being filtered and allowed to stand. Green X-ray quality crystals were obtained after room temperature evaporation of the mother liquor after 5 days. Elemental analysis (%) calculated (found): C 47.33 (47.12), H 3.97 (3.83), N 6.13 (5.97). Yield = 59%.

$[Cr_8Cu_6L_{24}Cl_{12}]$ (4)

To a solution of the metalloligand $[CrL_3]$ (108 mg, 0.2 mmol) in 20 mL of dichloromethane/methanol (1 : 1 v/v) was added a solution of $CuCl_2\cdot 2H_2O$ (34 mg, 0.2 mmol) in 2 mL of water. The solution was stirred for 5 minutes before being filtered and allowed to stand. Green-brown, X-ray quality crystals were obtained after room temperature evaporation of the mother liquor after 5 days. Elemental analysis (%) calculated (found): C 50.72 (50.43), H 3.78 (3.45), N 6.57 (6.64). Yield = 68%.

Crystal structure information

For compounds **1**, **2** and **4** single-crystal X-ray diffraction data were collected at T = 100 K on a Rigaku AFC12 goniometer equipped with an enhanced sensitivity (HG) Saturn 724+ detector mounted at the window of an FR-E+ Superbright MoKα rotating anode generator with HF Varimax optics (70 μm focus)[22] using Rigaku Crystal Clear and CrysalisPro software[23,24] for data collection and reduction. For compound **3** and $[Cr^{III}L_3]$ single crystal X-ray diffraction data were measured on a Rigaku Oxford Diffraction SuperNova diffractometer using Mo (for $[Cr^{III}L_3]$) or Cu (for **3**) radiation at T = 120 K. The CrysalisPro software package was used for instrument control, unit cell determination and data reduction.[25] Unit cell parameters in all cases were refined against all data. Crystal structures were solved using the charge flipping method implemented in SUPERFLIP[26] (**1**, **2**, and **4**), Olex2 ($[Cr^{III}L_3]$), or by direct methods with ShelXS (**3**). All structures were refined on F_o^2 by full-matrix least-squares refinements using ShelXL[27] within the OLEX2 suite.[28] All non-hydrogen

atoms were refined with anisotropic displacement parameters, and all hydrogen atoms were added at calculated positions and refined using a riding model with isotropic displacement parameters based on the equivalent isotropic displacement parameter (U_{eq}) of the parent atom.

Crystal data for $[Cr^{III}L_3]$. $C_{27}H_{24}N_3O_6Cr$, M_r = 538.49, trigonal, a = 17.6411(3) Å, b = 17.6411(3) Å, c = 27.0463(4) Å, α = 90.0°, β = 90.0°, γ = 120.0°, V = 7289.3(2) Å^3, Z = 12, $R\bar{3}$, D_c = 1.472 g cm^{-3}, μ = 0.520 mm^{-1}, T = 120 K, 5148 unique reflections (R_{int} = 0.0473), 4803 with $F^2 > 2\sigma$, $R(F, F^2 > 2\sigma)$ = 0.0561, R_w (F^2, all data) = 0.1096.

Crystal data for 1. $C_{232}H_{224}N_{24}O_{52}Cl_{12}Cr_8Co_6$, M_r = 5375.43, triclinic, a = 28.265(4) Å, b = 29.830(4) Å, c = 31.290(5) Å, α = 72.023(16)°, β = 71.093(15)°, γ = 63.981(13)°, V = 21 995(7) Å^3, Z = 2, $P\bar{1}$, D_c = 0.812 g cm^{-3}, μ = 0.526 mm^{-1}, T = 100(2) K, 73 957 unique reflections (R_{int}= 0.0635), 49 534 with $F^2 > 2\sigma$, $R(F, F^2 > 2\sigma)$ = 0.1299, R_w (F^2, all data) = 0.4175.

Crystal data for 2. $C_{228}H_{192}N_{36}O_{48}S_{12}Cr_8Co_6$, M_r = 5106.41, tetragonal, a = 41.7282(5) Å, b = 41.7282(5) Å, c = 30.6665(7) Å, $\alpha = \beta = \gamma$ = 90.0°, V = 53 397.9(18) Å^3, Z = 4, $I4_122$, D_c = 0.667 g cm^{-3}, μ = 0.420 mm^{-1}, T = 100(2) K, 23 556 unique reflections (R_{int} = 0.1250), 10 357 with $F^2 > 2\sigma$, $R(F, F^2 > 2\sigma)$ = 0.0457, R_w (F^2, all data) = 0.0941.

Crystal data for 3. $C_{216}H_{216}N_{24}O_{84}S_6Cr_8Cu_6$, M_r = 5481.79, tetragonal, a = 28.79166(19) Å, b = 28.79166(19) Å, c = 24.4854(3) Å, $\alpha = \beta = \gamma$ = 90.0°, V = 20 297.4(4) Å^3, Z = 2, $P4/n$, D_c = 0.897 g cm^{-3}, μ = 2.782 mm^{-1}, T = 120 K, 16 958 unique reflections (R_{int} = 0.0762), 11 352 with $F^2 > 2\sigma$, $R(F, F^2 > 2\sigma)$ = 0.1208, R_w (F^2, all data) = 0.3932.

Crystal data for 4. $C_{216}H_{192}N_{24}O_{48}Cl_{12}Cr_8Cu_6$, M_r = 5114.68, tetragonal, a = 41.329(14) Å, b = 41.329(14) Å, c = 31.056(10) Å, $\alpha = \beta = \gamma$ = 90.0°, V = 53 046(40) Å^3, Z = 4, $I4_122$, D_c = 0.640 g cm^{-3}, μ = 0.486 mm^{-1}, T = 100(2) K, 23 152 unique reflections (R_{int} = 0.1250), 11 046 with $F^2 > 2\sigma$, $R(F, F^2 > 2\sigma)$ = 0.0424, R_w (F^2, all data) = 0.1118.

CCDC 1457376-1457380.

Crystallography discussion

Crystals of all samples were very sensitive to solvent loss, which resulted in rapid crystal delamination and poor quality X-ray diffraction data. To slow down this crystal degradation, crystals of compounds **1**, **2** and **4** were 'cold mounted' on MiTeGen Micromounts™ at T = 203 K using Sigma-Aldrich Fomblin Y® LVAC (3300 mol. wt.) with the X-Temp 2 (ref. 29) crystal cooling system attached to the microscope. This procedure protected crystal quality and permitted collection of usable X-ray data. All four structures contain large accessible voids and channels that are filled with diffuse electron density belonging to uncoordinated solvent, whose electron contribution was accounted for by the SMTBX solvent masking routine as implemented in OLEX2 software. The crystal structure of **1** exhibits a significant amount of positional disorder, whereby part of the complex adopts two positions along the Cl3–Co2–Cl4 axis. This disorder has been modelled over two sites with a 60 : 40 ratio. Several geometrical constraints (DFIX, AFIX 66, FLAT) have been used to maintain sensible molecular geometry.

Crystal structures **2** and **4** (both in the tetragonal $I4_122$ space group) have been refined as two-component inversion twins with 81 : 19 and 58 : 42 ratios, respectively. Global SIMU, RIGU and DELU restraints were used to model atomic displacement parameters. For structure **3**, the measured data were consistently of poor quality. This structure has been modelled as far as is reasonable and practical, given the poor quality of the data set. The ShelX weighting scheme could not be optimized. The Cu_6Cr_8 cage was identified easily from the initial structure solution and refines well without restraints. Overall the cube carries a total charge of 12+. This is balanced by six sulphate anions. Peaks in the difference map corresponding to three crystallographically inequivalent sulphate anions per asymmetric unit were identified. Of these, two are inside the cube (S2 and S3) and one (S1) is outside the cube. The geometry of the S1 anion is the most stable, and thus S2 and S3 anions were modelled to have similar geometries to S1. S1 and S2 were refined anisotropically with displacement ellipsoid restraints; S3 was refined using an isotropic model. Each sulphate anion was modelled as half-occupied, and each is disordered around a crystallographic four-fold rotation axis so that the charges balance. Bond distance and displacement similarity restraints (SADI and RIGU) were used, as shown in the .res file embedded within the CIF shelx_res_file. Close O···O contacts between sulphate anions are flagged by PLATON; this is inevitable given the disordered nature of the anions. The copper centres are assumed to have axial aqua ligands, with the H atoms on these ligands placed for the sake of chemical completeness. The SQUEEZE routine of PLATON[30] was used to remove the remaining electron density, corresponding to 2934 electrons per unit cell. It is not good practice to attempt to ascribe this much electron density to either of the two solvents employed, methanol and dichloromethane, or to adventitious water molecules, as the ratio of solvents cannot be established by any other means. There is one residual peak of approximately 6.6 electrons located in the centre of the cube. There is no chemically plausible model for this, given the reagents and solvents used.

Results and discussion

The heterometallic cages $[Cr^{III}_8Co^{II}_6L_{24}Cl_{12}]$ (**1**), $[Cr^{III}_8Co^{II}_6L_{24}(SCN)_{12}]$ (**2**), $[Cr^{III}_8Cu^{II}_6L_{24}(H_2O)_{12}](SO_4)_6$ (**3**) and $[Cr^{III}_8Cu^{II}_6L_{24}Cl_{12}]$ (**4**) were all prepared in a similar manner by addition of an M^{II} salt to the metalloligand $[Cr^{III}L_3]$ (HL = 1-(4-pyridyl)butane-1,3-dione) in a mixed solvent system (either CH_2Cl_2/MeOH or CH_2Cl_2/THF, see the Experimental section for full details). The resultant reactions were stirred for a period of 1–14 hours, before being filtered; crystals were obtained by slow evaporation of the mother liquor at room temperature over several days. All four structures (Fig. 2 and 3) reveal a similar pseudo-cubic metallic skeleton $[Cr^{III}_8M^{II}_6]^{12+}$ where each M^{II} (M^{II} = Co, Cu) ion is situated slightly above (1.2–1.4 Å) the centre of a square face of approximate

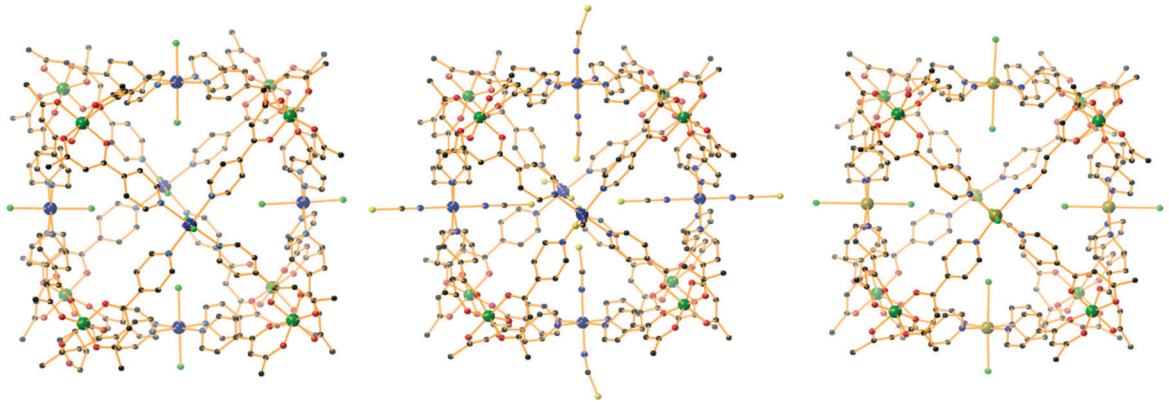

Fig. 2 From left to right, molecular structures of **1**, **2** and **4**. Colour code: Cr = green, Co = blue, Cu = olive, O = red, N = blue, S = yellow, Cl = light-green, C = black. H-atoms omitted for clarity.

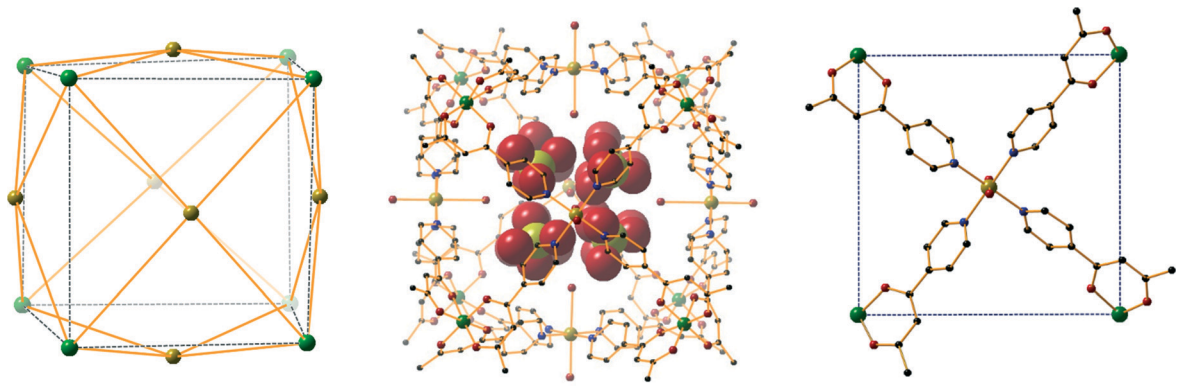

Fig. 3 Metallic skeleton of the cation of complex **3** (left). The distance between nearest neighbour Cr^{III} and Cu^{II} ions is approximately 8.8 Å. The molecular structure of **3** (centre) highlighting the encapsulation of four SO_4^{2-} molecules in the internal cavity of the cage. H-atoms and external SO_4^{2-} anions have been omitted for clarity. Representation of one of the six faces of the cube (right), highlighting the coordination geometry of the Cu^{II} ion. The Cu^{II} ion is six coordinate with a $\{CuN_4O_2\}$ coordination sphere; the Jahn–Teller distortion lying along the O–Cu–O vector, perpendicular to the face of the cube. Colour code: Cr = green, Cu = olive, O = red, N = blue, C = black.

dimensions 12 Å, defined by four Cr ions. Each $[Cr^{III}L_3]$ corner unit consists of a six-coordinate Cr ion with regular $\{CrO_6\}$ octahedral geometry, with Cr–O distances between 1.86–2.01 Å and *cis*/*trans* angles in the range 85.6–94.2° and 176.3–179.5°, respectively. The face-centred linkage of each corner fragment is achieved by the coordination of the four pyridyl donors to the equatorial positions of the six-coordinate M^{II} metal ions, with M^{II}–N distances in the range 2–2.2 Å. For **1**, **2** and **4**, the remaining apical sites of each M^{II} ion are occupied by the anions present in the starting cobalt or copper salts (*i.e.* Cl^- or SCN^-) giving overall charge neutral cages. However, with **3**, the apical sites are occupied by water molecules (arising from either the hydrated metal salt or from the non-dried solvent), which gives an assembly with overall +12 charge. Charge balance is maintained through the presence of a total of six SO_4^{2-} anions, four inside and two outside the cube (Fig. 3). The Jahn–Teller axis of each Cu^{II} ion in **3** and **4** lies perpendicular to the face it sits in.

All four structures reveal that **1**–**4** crystallise as homochiral racemates, *i.e.* each cube possesses eight $[Cr^{III}L_3]$ stereocentres of the same Λ or Δ chirality. While it is possible that this could simply be a packing effect from a complex and dynamic diastereomeric mixture, solution-based self-sorting of assemblies that contain multimetallic stereocenters is a common,[31] if not universal,[32] occurrence. The energetic preference for a single diastereomer is a sign that stereochemical information between adjacent metal vertices is efficiently transmitted through the ligand framework. In the case of **1**–**4**, the $[Cr^{III}L_3]$ stereocentres communicate *via* the tetrapyridyl-M^{II} coordination motif, which exhibit pronounced propeller-like twists (rather than idealised D_{4h} symmetry). Interestingly, the sense of this twist is conserved over the six connected faces of each individual assembly; the opposite holds for connecting $[Cr^{III}L_3]$ fragments of alternate stereochemistry.

Cr···Cr distances between nearest neighbours along the edges of the cubes measure approximately 12 Å, creating an internal volume of ~1400 $Å^3$ per cage. Volume calculations performed on all four complexes with the ^{3}V Volume Assessor programme,[33] which operates by rolling a virtual probe on the surface of a macromolecule, confirm this. A representation of the available internal cavity space in **2** is shown in

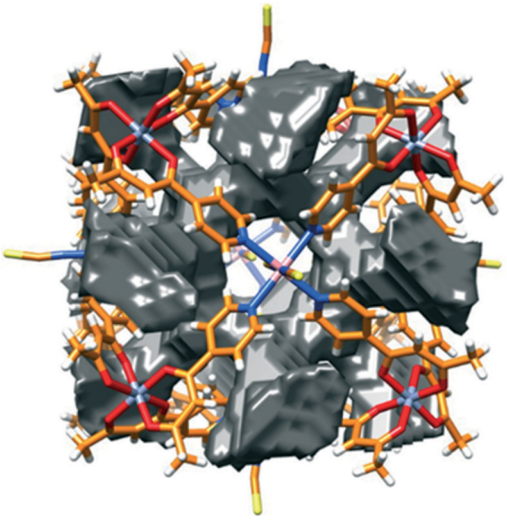

Fig. 4 Representation of the available internal cavity space in complex **2**. A volume of 1471 Å^3 was calculated employing an outer probe of 8.0 Å and an internal probe of 1.5 Å. See ref. 33 for details.

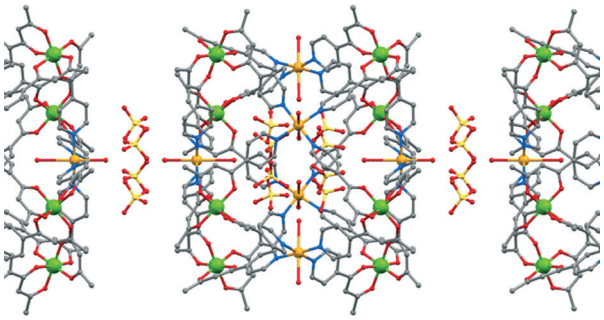

Fig. 5 The packing of three molecules of compound **3** in the crystal, highlighting the H-bonded chains of cubes along the *c*-axis of the cell.

Fig. 4 as an example. The binding of molecules of suitable dimensions in the internal cavity of a molecular receptor in solution can be expected when the packing coefficient, that is, the ratio of the guest volume to the host volume, is approximately 0.55.[34] This suggests that guests with a total volume of ~770 Å^3 could be accommodated in compounds **1–4**. Indeed this is in accordance with the encapsulation of four SO_4^{2-} anions, with total volume of 668 Å^3, inside the cavity of complex **3** (Fig. 3). Future work will focus on examining the host–guest chemistry of these cages, since their large internal cavities could potentially play host to an array of different species. For example, one can imagine constructing magnetic coordination capsules capable of hosting magnetic and/or redox-active guests, exerting control over magnetic superexchange between metal ions in the host framework and between the host and guest.

There are several close intermolecular contacts between the cages in the extended structures of **1–4**. In **1** the closest intercluster contacts are between the halide ions on one cube and the L^- ligands of the neighbouring cage with Cl···C distances in the range 3.6–3.9 Å, while for **2** the closest contact is between the O- and C-atoms of the L^- ligands, with distances as short as 3.3 Å. Similar ligand–ligand interactions also occur between the corners of the cubes in **3** and **4**, but in addition the externally located SO_4^{2-} ions in **3** H-bond to the terminally bonded H_2O molecules on the M^{II} ions (O···O, 2.7 Å), directing the formation of chains of clusters along the *c*-axis of the cell (Fig. 5).

Magnetic studies

Quantitatively analysing the magnetic behaviour of such large heterometallic species using traditional matrix diagonalisation techniques is non-trivial, and often impossible, due to the enormous dimensions of the associated spin-Hamiltonian matrices. For complexes **1** and **2** analysis is further hindered by the presence of the highly anisotropic octahedral Co^{II} ion. As such we do not attempt fits of the susceptibility and magnetisation data, but instead simply compare the experimental data to the detailed magnetothermal and spectroscopic investigation of the structurally similar complexes $[Cr^{III}{}_8Co^{II}{}_6L_{24}(H_2O)_{12}](ClO_4)_{12}$ (**5**) and $[Cr^{III}{}_8Cu^{II}{}_6L_{24}(H_2O)_{10}(NO_3)_2](NO_3)_{10}$ (**6**) reported in ref. 20, in which computational techniques known in theoretical nuclear physics as statistical spectroscopy were employed. The dc (direct current) molar magnetic susceptibility, χ_M, of polycrystalline samples of complexes **1–4** were measured in an applied magnetic field, *B*, of 0.1 T, over the *T* = 5–300 K temperature range (Fig. 6); where $\chi_M = M/B$, and *M* is the magnetisation. At room temperature, the $\chi_M T$ products of **1–2** and **3–4** have values of 26.3 and 17.7 cm^3 mol^{-1} K, respectively, in excellent agreement with that expected from the spin-only contributions to the magnetism of a $[Cr^{III}{}_8Co^{II}{}_6]$ unit (26.3 cm^3 mol^{-1} K) with $g_{Cr} = g_{Co} = 2.00$, and of a $[Cr^{III}{}_8Cu^{II}{}_6]$ unit (17.6 cm^3 mol^{-1} K), with $g_{Cr} = 2.00$ and $g_{Cu} = 2.15$, where g_{Cr}, g_{Co}, and g_{Cu} are the *g*-factors of Cr^{III}, Co^{II} and Cu^{II}, respectively. Upon cooling, the $\chi_M T$ values of **1–2** decrease continuously reaching a low temperature value of ~20 cm^3 mol^{-1} K. The behaviour of complexes **3–4** appears, at least upon initial inspection, to be somewhat different. Upon cooling, the $\chi_M T$ products of both remain essentially constant down to *T* = 20 K, below which there is an increase to a value of ~18.5 cm^3 mol^{-1} K. Qualitatively the magnetic behaviour of **3** and **4** is straightforward: the exchange between the Cr^{III} and Cu^{II} ions is very weak and ferromagnetic in nature. One can also come to the same conclusion for compounds **1** and **2** [and **5**] if one assumes the high temperature decrease in $\chi_M T$ is due solely to the anisotropy of the octahedral Co^{II} ion. Indeed, the data for **5** shows a low temperature increase in $\chi_M T$ which is consistent with a weakly ferromagnetic Cr^{III}–Co^{II} interaction. Clearly, however, other models invoking an antiferromagnetic interaction could explain the variable temperature susceptibility.[20] Variable-temperature-and-variable-field (VTVB) magnetisation studies are consistent with the presence of weak exchange interactions in all cases (Fig. 6, bottom), with the saturation magnetic moment at *T* = 2 K and *B* = 7 T being close to that expected for a fully parallel alignment of the spins in the case of the Cr–Cu cages. For the Cr–Co cages

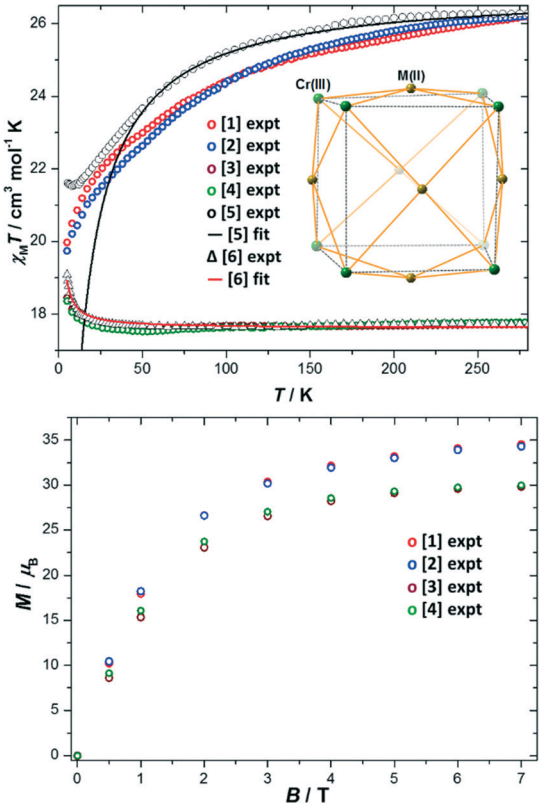

Fig. 6 Plot of the $\chi_M T$ product *versus* temperature for complexes **1**–**4** (top). The data for complexes **5** and **6** are added for comparison. See ref. 20 for full details of the fits for **5** and **6**. Plot of the VTVB magnetisation data for complexes **1**–**4** (bottom).

1 and **2** the saturation magnetic moments are lower than the ferromagnetic limit due to the large orbital contribution of the octahedral Co^{II} ion.[20a]

Conclusions

The modular assembly of magnetic coordination capsules with internal cavities capable of hosting magnetic and redox-active guests is an under-explored field of research that can be exploited for the construction of tuneable, multifunctional molecular magnets with potential application in information storage and molecular spintronics. The ability to control and manipulate (switch on, switch off) magnetic exchange between metal ions in the host framework and between the host and guest(s) *via* the use of redox-active (radical) ligands in the framework of the host, and/or redox-active/paramagnetic guests held within the cavities, remains an attractive target. The construction of said capsules in a manner amenable to exohedral functionalization such that the organic sheath surrounding the capsules are easily derivatised post-synthetically to modify and tune solubility, magnetic behaviour, reactivity, stability and substrate specificity would also make the cages suitable for materials applications.

Here, the simple, modular assembly of $[M^{III}_8M^{II}_6]^{n+}$ cubes [with M^{III} = Cr and M^{II} = Co, Cu] suggests that any combination of $[M^{III}L_3]$ metalloligand and M^{II} salt will work, potentially resulting in an enormous family of supramolecular assemblies. The charge of the cubes varies from neutral to 12+ and is controlled by the nature of the ligand occupying the axial sites on the M^{II} ions. Ligand substitution at these sites should be trivial and may prove a gateway to accessing a variety of new cages and polymers whereby the clusters are linked *via* di/polytopic linker ligands. Complex **3** encapsulates four SO_4^{2-} ions in its central cavity (of volume ~1400 Å^3) suggesting that cationic cages may be good hosts for different guests, such as organic radicals or simple coordination compounds containing paramagnetic metal ions.

Heterometallic Cr–Co cages are surprisingly rare. Excluding organometallic and metal–metal bonded species, a search of the Cambridge Structural Database returned just a handful of hits, and the vast majority of these are derivatives of the well-known $[Cr_7Co]$ wheels of Winpenny and Timco.[35] There are two hydroxo/alkoxo-bridged dimers,[36] linear trimers and the ubiquitous triangular basic carboxylates,[37] a Cr_2Co_2 butterfly and a Cr_3Co star,[38] and pivalate/phosphonate-bridged Cr_2Co_4, Cr_4Co_8 and Cr_4Co_4 cages.[39] Heterometallic Cr–Cu complexes are similarly dominated by Manchester wheels, but here there is a little more variety with Cr_7Cu, Cr_8Cu_2, $Cr_{10}Cu_2$ and $Cr_{12}Cu_2$ examples all being reported.[40] Beyond these there is very little else in the literature, bar a few examples of dimers, Cr_2Cu trimers, Cr_2Cu_2 butterflies and one example of a Cr_2Cu_4 cage.[41] The Cr_8Co_6 and Cr_8Cu_6 cages reported herein are therefore the largest such species yet reported.

Acknowledgements

EKB thanks the EPSRC for funding. MP and SJC thank the EPSRC for funding the UK National Crystallography service.

Notes and references

1 See for example (*a*) J.-M. Lehn, *Supramolecular Chemistry Concepts and Perspectives*, VCH, Weinheim, 1995; (*b*) J. L. Atwood, J. E. D. Davies, J.-M. Lehn, D. D. MacNicol and F. Vogtle, *Comprehensive Supramolecular Chemistry*, Pergamon, Oxford, 1996.
2 B. H. Northrop, Y.-R. Zheng, K.-W. Chi and P. J. Stang, *Acc. Chem. Res.*, 2009, **42**, 1554.
3 J. Ribas, *Coordination Chemistry*, Wiley-VCH, 2008.
4 T. R. Cook, Y. Zheng and P. J. Stang, *Chem. Rev.*, 2013, **113**, 734.
5 R. Chakrabarty, P. S. Mukherjee and P. J. Stang, *Chem. Rev.*, 2011, **111**, 6810.
6 M. Yoshizawa, J. K. Klosterman and M. Fujita, *Angew. Chem., Int. Ed.*, 2009, **48**, 3418.
7 I. A. Riddell, M. M. J. Smulders, J. K. Clegg and J. R. Nitschke, *Chem. Commun.*, 2011, **47**, 457.
8 M. B. Duriska, S. M. Neville, J. Lu, S. S. Iremonger, J. F. Boas, C. J. Kepert and S. R. Batten, *Angew. Chem., Int. Ed.*, 2009, **48**, 8919.

9 See for example (*a*) P. Mal, B. Breiner, K. Rissanen and J. R. Nitschke, *Science*, 2009, **324**, 1697; (*b*) M. M. J. Smulders and J. R. Nitschke, *Chem. Sci.*, 2012, **3**, 785.
10 See for example (*a*) M. Yoshizawa, M. Tamura and M. Fujita, *Science*, 2006, **312**, 251; (*b*) T. Murase, S. Horiuchi and M. Fujita, *J. Am. Chem. Soc.*, 2010, **132**, 2866; (*c*) S. Horiuchi, Y. Nishioka, T. Murase and M. Fujita, *Chem. Commun.*, 2010, **46**, 3460.
11 M. Hannon, *Chem. Soc. Rev.*, 2007, **36**, 280.
12 (*a*) Y. R. Hristova, M. M. J. Smulders, J. K. Clegg, B. Breiner and J. R. Nitschke, *Chem. Sci.*, 2011, **2**, 638; (*b*) S. Turega, M. Whitehead, B. R. Hall, M. F. Haddow, C. A. Hunter and M. D. Ward, *Chem. Commun.*, 2012, **48**, 2752.
13 E. Coronado and G. M. Espallargas, *Chem. Soc. Rev.*, 2013, **42**, 1525.
14 *Magneto-Structural Correlations in Exchange-Coupled Systems*, ed. D. Gatteschi, O. Kahn and R. D. Willet, D. Reidel, Dordrecht, 1985.
15 J. Schnack, *Dalton Trans.*, 2010, **39**, 4677.
16 D. Gatteschi, R. Sessoli and J. Villain, *Molecular Nanomagnets*, Oxford University Press, Oxford, 2006.
17 C. J. Milios and R. E. P. Winpenny, *Struct. Bonding*, 2015, **164**, 1.
18 J. N. Rebilly and T. Mallah, *Struct. Bonding*, 2006, **122**, 103.
19 (*a*) J. J. Sokol, M. P. Shores and J. R. Long, *Angew. Chem., Int. Ed.*, 2001, **40**, 236; (*b*) S. Wang, J. L. Zuo, H. C. Zhuo, H. J. Choi, Y. Ke, J. R. Long and X. Z. You, *Angew. Chem., Int. Ed.*, 2004, **43**, 5940; (*c*) H. Kumari, C. L. Dennis, A. V. Mossine, C. A. Deakyne and J. L. Atwood, *J. Am. Chem. Soc.*, 2013, **135**, 7110; There are several metal-organic polyhedra based on paramagnetic metal ions, but in the main these have not targeted/reported magnetic behaviour. See for example: (*d*) A. J. McConnell, C. S. Wood, P. P. Neelakandan and J. R. Nitschke, *Chem. Rev.*, 2015, **115**, 7729; (*e*) C. J. Brown, F. D. Toste, R. G. Bergman and K. N. Raymond, *Chem. Rev.*, 2015, **115**, 3012; (*f*) T. D. Hamilton, G. S. Papaefstathiou, T. Friščić, D.-K. Bucar and L. R. MacGillivary, *J. Am. Chem. Soc.*, 2008, **130**, 14366; (*g*) H. Kumari, P. Jin, S. J. Teat, C. L. Barnes, S. J. Dalgarno and J. L. Atwood, *J. Am. Chem. Soc.*, 2014, **136**, 17002.
20 (*a*) S. Sanz, H. M. O'Connor, E. M. Pineda, K. S. Pedersen, G. S. Nichol, O. Mønsted, H. Weihe, S. Piligkos, E. J. L. McInnes, P. J. Lusby and E. K. Brechin, *Angew. Chem., Int. Ed.*, 2015, **54**, 6761; (*b*) an analogous, diamagnetic cage also exists: H.-B. Wu and Q.-M. Wang, *Angew. Chem., Int. Ed.*, 2009, **48**, 7343.
21 B. Singh, G. Y. Lesher, K. C. Pluncket, E. D. Pagani, D. C. Bode, R. G. Bentley, M. J. Connell, L. T. Hamel and P. J. Silver, *J. Med. Chem.*, 1992, **35**, 4858.
22 S. J. Coles and P. A. Gale, *Chem. Sci.*, 2012, **3**, 683.
23 *CrystalClear-SM Expert 3.1 b27* (Rigaku, 2012).
24 *CrysAlisPro 1.171.38.41* (Rigaku Oxford Diffraction, 2015).
25 *CrysAlisPro*, Rigaku Oxford Diffraction, Oxford, UK, 2016.
26 L. Palatinus and G. Chapuis, *J. Appl. Crystallogr.*, 2007, **40**, 786.
27 G. M. Sheldrick, *Acta Crystallogr.*, 2015, **71**, 3.
28 O. V. Dolomanov, A. J. Blake, N. R. Champness and M. Schröder, *J. Appl. Crystallogr.*, 2003, **36**, 1283.
29 T. Kottke and D. Stalke, *J. Appl. Crystallogr.*, 1993, **26**, 615.
30 A. L. Spek, *Acta Crystallogr., Sect. C: Struct. Chem.*, 2015, **71**, 9.
31 A. M. Castilla, W. J. Ramsay and J. R. Nitschke, *Acc. Chem. Res.*, 2014, **47**, 2063.
32 O. Chepelin, J. Ujma, X. Wu, A. M. Z. Slawin, M. B. Pitak, S. J. Coles, J. Michel, A. C. Jones, P. E. Barran and P. J. Lusby, *J. Am. Chem. Soc.*, 2012, **134**, 19334.
33 N. R. Voss and M. Gerstein, *Nucleic Acids Res.*, 2010, **38**, W555.
34 S. Mecozzi and J. Rebek, *Chem. – Eur. J.*, 1998, **4**, 1016.
35 E. C. Saňudo, T. B. Faust, C. A. Muryn, R. G. Pritchard, G. A. Timco and R. E. P. Winpenny, *Inorg. Chem.*, 2009, **48**, 9811.
36 (*a*) P. Chaudhuri, M. Winter, J. Kueppers, K. Wieghardt, B. Nuber and J. Weiss, *Inorg. Chem.*, 1987, **26**, 3302; (*b*) P. Alborés, J. Seeman and E. Rentschler, *Dalton Trans.*, 2009, 7660.
37 K. M. Corbin, D. J. Hodgson, M. H. Lynn, K. Michelsen, K. M. Nielsen and E. Pedersen, *Inorg. Chim. Acta*, 1989, **159**, 129.
38 (*a*) V. V. Semenaka, O. V. Nesterova, V. N. Kokozay, R. I. Zybatyuk, O. V. Shishkin, R. Boca, C. J. Gómez-García, J. M. Clemente-Juan and J. Jezierska, *Polyhedron*, 2010, **29**, 1326; (*b*) D. J. Hodgson, K. Michelsen and E. D. Towle, *J. Chem. Soc., Chem. Commun.*, 1988, 426.
39 Y.-Z. Zheng, B. A. Breeze, G. A. Timco, F. Tuna and R. E. P. Winpenny, *Dalton Trans.*, 2010, **39**, 6175.
40 (*a*) B. Ballesteros, T. B. Faust, C.-F. Lee, D. A. Leigh, C. A. Muryn, R. G. Pritchard, D. Schultz, S. J. Teat, G. A. Timco and R. E. P. Winpenny, *J. Am. Chem. Soc.*, 2010, **132**, 15435; (*b*) L. P. Engelhardt, C. A. Muryn, R. G. Pritchard, G. A. Timco, F. Tuna and R. E. P. Winpenny, *Angew. Chem., Int. Ed.*, 2008, **47**, 924; (*c*) F. K. Larsen, J. Overgaard, S. Parsons, E. Rentschler, A. A. Smith, G. A. Timco and R. E. P. Winpenny, *Angew. Chem., Int. Ed.*, 2003, **42**, 5978; (*d*) C.-F. Lee, D. A. Leigh, R. G. Pritchard, D. Schultz, S. J. Teat, G. A. Timco and R. E. P. Winpenny, *Nature*, 2009, **458**, 314; (*e*) L. P. Engelhardt, C. A. Muryn, R. G. Pritchard, G. A. Timco, F. Tuna and R. E. P. Winpenny, *Angew. Chem., Int. Ed.*, 2008, **47**, 924.
41 See for example: (*a*) J. A. Rusanova, V. V. Semenaka, V. V. Dyakonenko and O. V. Shishkin, *Acta Crystallogr., Sect. E: Crystallogr. Commun.*, 2015, **71**, 1077; (*b*) G. Lorusso, V. Corradini, A. Candini, A. Ghirri, R. Biagi, U. D. Pennino, S. Carretta, E. Garlatti, P. Santini, G. Amoretti, G. Timco, R. G. Pritchard, R. E. P. Winpenny and M. Affronte, *Phys. Rev. B: Condens. Matter Mater. Phys.*, 2010, **82**, 144420; (*c*) J. Glerup, P. A. Goodson, D. J. Hodgson, M. H. Lynn and K. Michelsen, *Inorg. Chem.*, 1992, **31**, 4785; (*d*) S. Khanra, T. Weyhermuller and P. Chaudhuri, *Dalton Trans.*, 2007, 4675; (*e*) F. S. Delgado, J. Sanchiz, T. Lopez, F. Lloret, M. Julve and C. Ruiz-Perez, *CrystEngComm*, 2010, **12**, 2711.

Chemical Science

EDGE ARTICLE

View Article Online
View Journal | View Issue

Cite this: *Chem. Sci.*, 2017, **8**, 5526

$[M^{III}_2M^{II}_3]^{n+}$ trigonal bipyramidal cages based on diamagnetic and paramagnetic metalloligands†

S. Sanz,‡*[a] H. M. O'Connor,‡[a] V. Martí-Centelles,[a] P. Comar,[a] M. B. Pitak,[b] S. J. Coles,[b] G. Lorusso,[c] E. Palacios,[c] M. Evangelisti,[c] A. Baldansuren,[d] N. F. Chilton,[d] H. Weihe,[e] E. J. L. McInnes,*[d] P. J. Lusby,*[a] S. Piligkos*[e] and E. K. Brechin*[a]

Received 1st February 2017
Accepted 18th May 2017

DOI: 10.1039/c7sc00487g

rsc.li/chemical-science

A family of five $[M^{III}_2M^{II}_3]^{n+}$ trigonal bipyramidal cages (M^{III} = Fe, Cr and Al; M^{II} = Co, Zn and Pd; $n = 0$ for **1–3** and $n = 6$ for **4–5**) of formulae $[Fe_2Co_3L_6Cl_6]$ (**1**), $[Fe_2Zn_3L_6Br_6]$ (**2**), $[Cr_2Zn_3L_6Br_6]$ (**3**), $[Cr_2Pd_3L_6(dppp)_3](OTf)_6$ (**4**) and $[Al_2Pd_3L_6(dppp)_3](OTf)_6$ (**5**) (where HL is 1-(4-pyridyl)butane-1,3-dione and dppp is 1,3-bis(diphenylphosphino)propane) are reported. Neutral cages **1–3** were synthesised using the tritopic $[M^{III}L_3]$ metalloligand in combination with the salts $Co^{II}Cl_2$ and $Zn^{II}Br_2$, which both act as tetrahedral linkers. The assembly of the *cis*-protected $[Pd^{II}(dppp)(OTf)_2]$ with $[M^{III}L_3]$ afforded the anionic cages **4–5** of general formula $[M^{III}_2Pd^{II}_3](OTf)_6$. The metallic skeleton of all cages describes a trigonal bipyramid with the M^{III} ions occupying the two axial sites and the M^{II} ions sitting in the three equatorial positions. Direct current (DC) magnetic susceptibility, magnetisation and heat capacity measurements on **1** reveal weak antiferromagnetic exchange between the Fe^{III} and Co^{II} ions. EPR spectroscopy demonstrates that the distortion imposed on the $\{MO_6\}$ coordination sphere of $[M^{III}L_3]$ by complexation in the $\{M^{III}_2M^{II}_3\}$ supramolecules results in a small, but measurable, increase of the zero field splitting at M^{III}. Complete active space self-consistent field (CASSCF) calculations on the three unique Co^{II} sites of **1** suggest $D_{Co} \approx -14$ cm^{-1} and $E/D \approx 0.1$, consistent with the magnetothermal and spectroscopic data.

Introduction

Molecular magnetism relies on the ability of the synthetic chemist to make an enormous breadth of structurally diverse polymetallic cages spanning the d- and f-block of the periodic table.[1–10] The structural and magnetic characterisation of such species details the magneto-structural relationship and often uncovers fascinating magnetic phenomena which, in turn, feedback into the synthesis of new complexes designed to enhance and improve properties toward application.[11–18] Synthetic strategies for the design of polymetallic clusters containing multiple paramagnetic metal ions span the range from serendipitous self-assembly in which coordinatively flexible metal ions, that can often exist in multiple oxidation states, are combined with organic ligands capable of bridging in numerous ways to form complexes whose absolute structures are difficult to predict, through to a more 'supramolecular' approach whereby metal ions with defined coordination geometries are paired with rigid ligands containing donor atoms with a single, predesigned orientation preference that afford, in most cases, a predicted structure. In the field of molecular magnetism, the latter is perhaps best exemplified by cyanometalate chemistry.[19–23]

A similar synthetic approach is followed in the metallosupramolecular chemistry of diamagnetic cages and capsules where the combination of directional metal–ligand bonding and rigorously rigid ligands creates cages with permanent internal cavities capable of hosting guest molecules, constructed primarily for potential application in, for example, catalysis,[24] the stabilisation of reactive molecules[25] and photochemistry.[26] Due to the difficulties associated with performing solution-based one- and two-dimensional NMR spectroscopy on paramagnetic species, where broad signals and a wide chemical

[a]EaStCHEM School of Chemistry, The University of Edinburgh, David Brewster Road, Edinburgh, EH9 3FJ, UK. E-mail: E.Brechin@ed.ac.uk; S.Calvo@ed.ac.uk; Paul.Lusby@ed.ac.uk

[b]UK National Crystallography Service, Chemistry, University of Southampton, Highfield Campus, Southampton, SO17 1BJ, UK

[c]Instituto de Ciencia de Materiales de Aragón (ICMA), CSIC – Universidad de Zaragoza, Departamento de Física de la Materia Condensada, 50009 Zaragoza, Spain

[d]School of Chemistry, The University of Manchester, Oxford Road, Manchester, M13 9PL, UK. E-mail: eric.mcinnes@manchester.ac.uk

[e]Department of Chemistry, University of Copenhagen, Universitetsparken 5, DK-2100, Copenhagen, Denmark. E-mail: piligkos@chem.ku.dk

† Electronic supplementary information (ESI) available: Additional NMR, IR, PXRD, ICPOES, MS, EPR data and CASSCF methodology. CCDC 1520425–1520429. Crystallographic data (including structure factors) for **1–5** have been deposited with the Cambridge Crystallographic Data Centre. For ESI and crystallographic data in CIF or other electronic format see DOI: 10.1039/c7sc00487g

‡ S. Sanz and H. M. O'Connor contributed equally to this work.

shift range are commonplace,[27] it is perhaps not surprising that the majority of metallosupramolecular chemistry has focused on the use of diamagnetic metal centres, albeit with some notable exceptions.[28]

We recently initiated a project that would enable heterometallic, paramagnetic coordination cages to be accessed in a modular and predictable fashion,[29] an approach centred around the tritopic metalloligand $[M^{III}L_3]$ (where HL = 1-(4-pyridyl)butane-1,3-dione), which features a tris(acac) octahedral transition metal core functionalised with three *p*-pyridyl donor groups (Fig. 1).[30] Combination of the *fac*-isomer of $[M^{III}L_3]$ with a square-planar M^{II} connector leads to the formation of $[M^{III}_8M^{II}_6]^{n+}$ molecular cubes.[29,30] Herein we show that replacement of the square planar connector with tetrahedral or *cis*-capped square planar metal salts leads to the formation of trigonal bipyramidal $[M^{III}_2M^{II}_3]^{n+}$ cages,[31] where M^{III} = Fe, Cr, Al and M^{II} = Co, Zn, Pd. Reports of magnetic clusters based on this skeleton are rare, the only previous examples employing cyano bridging ligands.[32–34]

Experimental section

Syntheses

1-(4-Pyridyl)butane-1,3-dione (HL) and the metalloligand $[Cr^{III}L_3]$ were prepared according to previously published procedures.[29,35] All reactions were performed under aerobic conditions. Solvents and reagents were used as received from commercial suppliers. Elemental analyses were carried by Medac Ltd.

$[Fe^{III}L_3]$

$FeCl_3$ (1 mmol, 0.162 g), 1-(4-pyridyl)butane-1,3-dione (3.5 mmol, 0.57 g) and NaOMe (3.5 mmol, 0.189 g) were dissolved in 100 mL of MeOH/H_2O (1 : 1 v/v) and left to stir until a red product precipitated (~24 h). The resultant red precipitate was filtered and washed with water. The crude product was extracted with $CHCl_3$ and dried over anhydrous $MgSO_4$. The $CHCl_3$ was removed under reduced pressure to afford the product as a red solid. Yield (0.46 g, 85%). Elemental analysis (%) calculated (found): C 59.79 (59.53), H 4.46 (4.39), N 7.75 (7.67).

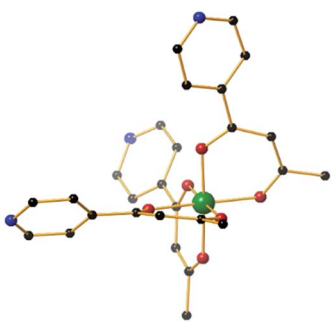

Fig. 1 The molecular structure of the *fac*-isomer of the metalloligand $[M^{III}L_3]$ (M = Fe, Cr, Al). Colour code: M^{III} = green, O = red, N = blue, C = black. Hydrogen atoms have been omitted for clarity.

$[Al^{III}L_3]$

$Al(NO_3)_3\cdot 9H_2O$ (1 mmol, 0.375 g), 1-(4-pyridyl)butane-1,3-dione (3.5 mmol, 0.57 g) and NaOMe (3.5 mmol, 0.189 g) were dissolved in 100 mL of MeOH/H_2O (1 : 1 v/v) and left to stir until a white product precipitated (~1 h). The resultant white precipitate was filtered and washed with water. The crude product was extracted with $CHCl_3$ and dried over anhydrous $MgSO_4$. The $CHCl_3$ was removed under reduced pressure to afford the product as a white solid. Yield (0.39 g, 76%). Elemental analysis (%) calculated (found): C 63.16 (63.06), H 4.71 (4.53), N 8.18 (8.11).

$[Fe_2Co_3L_6Cl_6]$ (1)

To a solution of the metalloligand $[Fe^{III}L_3]$ (108 mg, 0.2 mmol) in 35 mL of acetone, was added $CoCl_2$ (39 mg, 0.3 mmol). The resultant mixture was stirred for 30 minutes, before being filtered and layered with Et_2O. Orange, plate-shaped X-ray quality crystals were obtained after 20 days. Yield (98 mg, 67%). Elemental analysis (%) calculated for $C_{54}H_{48}N_6O_{12}Cl_6Fe_2Co_3$: C 44.00, H 3.28, N 5.70. Found: C 44.12, H 3.39, N 5.77.

$[Fe_2Zn_3L_6Br_6]$ (2)

To a solution of the metalloligand $[Fe^{III}L_3]$ (108 mg, 0.2 mmol) in 35 mL of dichloromethane/acetone (1 : 1 v/v) was added $ZnBr_2$ (67 mg, 0.3 mmol). The solution was stirred for 30 minutes, before being evaporated to dryness. The dark-red product was re-dissolved in nitromethane, filtered and allowed to stand. Dark-red, prism-shaped X-ray quality crystals were obtained after room temperature evaporation of the mother liquor after 10 days. Yield (133 mg, 76%). Elemental analysis (%) calculated for $C_{54}H_{48}N_6O_{12}Br_6Fe_2Zn_3$: C 36.85, H 2.75, N 4.77. Found: C 36.97, H 2.87, N 4.91.

$[Cr_2Zn_3L_6Br_6]$ (3)

To a solution of the metalloligand $[Cr^{III}L_3]$ (108 mg, 0.2 mmol) in 35 mL of dichloromethane was added $ZnBr_2$ (67 mg, 0.3 mmol). After 1 hour of reaction a precipitate appeared. The dark-red solid product was isolated by filtration, re-dissolved in DMF and layered with MeOH. Dark-red, prism-shaped X-ray quality crystals were obtained after 10 days. Yield (142 mg, 81%). Elemental analysis (%) calculated for $C_{54}H_{48}N_6O_{12}Br_6Cr_2Zn_3$: C 37.01, H 2.76, N 4.80. Found: C 36.92, H 2.67, N 4.67.

$[Cr_2Pd_3L_6(dppp)_3](OTf)_6$ (4)

To a solution of the metalloligand $[Cr^{III}L_3]$ (108 mg, 0.2 mmol) in 35 mL of methanol was added $[Pd(dppp)_2(CF_3SO_3)_2]$ (245 mg, 0.3 mmol; dppp is 1,3-bis(diphenylphosphino)propane). The solution was stirred for 30 minutes, before being filtered and allowed to stand. Orange, rod-shaped X-ray quality crystals were obtained after room temperature evaporation of the mother liquor after 5 days. Yield (275 mg, 78%). Elemental analysis (%) calculated for $C_{141}H_{126}O_{30}N_6F_{18}P_6S_6Cr_2Pd_3$: C 48.00, H 3.60, N 2.38. Found: C 47.89, H 3.47, N 2.27.

$[Al_2Pd_3L_6(dppp)_3](OTf)_6$ (5)

To a solution of the metalloligand $[Al^{III}L_3]$ (103 mg, 0.2 mmol) in 35 mL of acetonitrile was added $[Pd(dppp)_2(CF_3SO_3)_2]$ (245 mg, 0.3 mmol). The solution was stirred for 15 hours at 50 °C, before being filtered and layered with diethyl ether. Colourless, rod-shaped X-ray quality crystals were obtained after 5 days. Yield (288 mg, 83%). ^{1}H NMR (500 MHz, CD_3CN): δ 8.61 (bs, 12H, Py-*H*), 7.79–7.67 (m, 12H, dppp-Ar*H*), 7.48–7.44 (m, 12H, dppp-Ar*H*), 7.42–7.39 (m, 12H, dppp-Ar*H*), 7.34–7.27 (m, 12H, dppp-Ar*H*), 7.26–7.22 (m, 12H, dppp-Ar*H*), 7.18 (d, J = 6.5 Hz, 12H, Py-H), 6.13 (s, 6H, COC*H*CO), 3.28–3.11 (m, 6H, dppp-CH_2), 3.10–2.92 (m, 6H, dppp-CH_2), 2.60–2.36 (m, 3H, dppp-CH_2), 2.15 (s, 18H, CH_3), 1.93–1.75 (m, 3H, dppp-CH_2) ppm. ^{13}C NMR (126 MHz, CD_3CN): δ 198.79, 177.61, 151.26, 147.79, 134.91–134.82 (m, 2 signals), 133.70, 133.07–132.99 (m, 3 signals), 130.60–130.51 (m, 2 signals), 130.42–130.33 (m, 2 signals), 127.58–126.88 (m), 125.52–124.82 (m), 124.37, 122.06 (q, J = 321.0 Hz), 99.58, 28.10, 22.25–21.92 (m), 18.30 ppm. ^{31}P NMR (202 MHz, CD_3CN) δ 6.97 ppm. ^{19}F NMR (471 MHz, CD_3CN) δ −79.05 ppm. Diffusion coefficient (DOSY, 500 MHz, CD_3CN, 298 K) 5.99 × 10^{-10} m^2 s^{-1}, hydrodynamic radius 9.9 Å. ESI TOF HRMS *m*/*z*: found 1010.1238 $[M - 3OTf^-]^{3+}$, calculated for $[C_{138}H_{126}Al_2F_9N_6O_{21}P_6Pd_3S_3]^{3+}$ 1010.1069. Elemental analysis (%) calculated for $C_{141}H_{126}O_{30}N_6F_{18}P_6S_6Al_2Pd_3$: C 48.69, H 3.65, N 2.42. Found: C 48.42, H 3.57, N 2.35.

Crystal structure information

For compounds **1**, **2** and **3** single-crystal X-ray diffraction data were collected at T = 100 K on a Rigaku AFC12 goniometer equipped with an enhanced sensitivity (HG) Saturn 724+ detector mounted at the window of an FR-E+ Superbright MoKα rotating anode generator with HF Varimax optics (70 μm focus)[36] using Rigaku Crystal Clear and CrysalisPro software[37,38] for data collection and reduction. The crystals were sensitive to solvent loss and were therefore 'cold-mounted' using X-Temp 2 System apparatus at T = 70 °C and then quickly transferred to diffractometer.

For compounds **4** and **5** single crystal X-ray diffraction data were measured on a Rigaku Oxford Diffraction SuperNova diffractometer using Cu radiation at T = 120 K. The CrysalisPro software package was used for instrument control, unit cell determination and data reduction.[39] Unit cell parameters in all cases were refined against all data. Crystal structures were solved using the charge flipping method implemented in SUPERFLIP[40] (**1**, **2**, and **3**), or by direct methods with ShelXS (**4** and **5**). All structures were refined on F_o^2 by full-matrix least-squares refinements using ShelXL[41] within the OLEX2 suite.[42] All non-hydrogen atoms were refined with anisotropic displacement parameters, and all hydrogen atoms were added at calculated positions and refined using a riding model with isotropic displacement parameters based on the equivalent isotropic displacement parameter ($U_{eq.}$) of the parent atom. All five structures contain accessible voids and channels that are filled with diffuse electron density belonging to uncoordinated solvent, and $CF_3SO_3^-$ anions in the case of compounds **4–5**. The SQUEEZE routine of PLATON[43] was used to remove remaining electron density corresponding to solvent and anions not reported in the calculated formula. Crystallographic summary and structure refinement details are presented in Table 1. CCDC: 1520425–1520429.†

Physical measurements

Magnetisation measurements were carried out on a Quantum Design SQUID MPMS-XL magnetometer, operating between 1.8 and 300 K for DC applied magnetic fields ranging from 0 to 5 T. Microcrystalline samples were dispersed in eicosane in order to avoid torquing of the crystallites. Heat capacity measurements were carried out for temperatures down to *ca.* 0.3 K by using a Quantum Design 9T-PPMS, equipped with a ^{3}He cryostat. The experiments were performed on thin pressed pellets (*ca.* 1 mg) of a polycrystalline sample, thermalised by *ca.* 0.2 mg of Apiezon N grease, whose contribution was subtracted by using a phenomenological expression. X- and Q-band EPR spectra were collected on powdered microcrystalline samples of $[FeL_3]$ and compounds **1–4** at the UK National EPR Facility in Manchester.

Results and discussion

Solution self-assembly and structure

It could be reasonably expected that reaction of the metalloligand $[Al^{III}L_3]$ with a *cis*-protected square planar complex should yield a trigonal bipyramid. However, in the case of the archetypal 90° acceptor complex $[(en)Pd(NO_3)_2]$,[44] it had previously been shown that instead, displacement of the bidentate ethylene diamine ligand occurs to yield the $[Al_8Pd_6]^{12+}$ cube.[29b] We were thus pleased to find that when we switched to the more strongly coordinating bis(diphenylphosphino)propane (dppp), we were able to isolate the $[Al_2Pd_3]^{6+}$ trigonal bipyramidal complex, **5**, in 83% yield following reaction overnight at 50 °C between $[Al^{III}L_3]$ and $[Pd(dppp)(OTf)_2]$ in acetonitrile. All the spectroscopic data indicate that the structure of **5**, confirmed by X-ray crystallography (see below), is preserved in solution. As well as ESI-MS, which reveals the 3+ charge state corresponding to $[5 - 3OTf]^{3+}$ matching the expected isotopic distribution (see ESI†), the ^{1}H NMR spectrum of the product (Fig. 2b) shows just a single set of signals. The ^{1}H DOSY spectrum also indicates that all the resonances possess the same diffusion coefficient, which corresponds to a hydrodynamic radius of 9.9 Å, closely matching the data obtained by XRD.

It is also interesting to note that the starting metalloligand $[Al^{III}L_3]$ exists as a mixture of the *mer* and *fac* configurations, clearly evidenced by the multiplet for the acac CH and CH_3 signals in the ^{1}H NMR spectrum (Fig. 2c, resonances shown in blue and magenta), which is replaced by a singlet in the crude reaction mixture (Fig. 2d). This indicates that under the conditions of the reaction, $[Al^{III}L_3]$ is configurationally dynamic, and that the self-assembly process amplifies the proportion of the *fac* configuration through the formation of **5**. While *mer* tris(bidentate) octahedral complexes are also known to generate discrete metallosupramolecular cages,[45] the divergent disposition of the pendant donor groups create larger closed systems, which with a dynamic system such as this will rapidly rearrange

Table 1 X-ray data collection and refinement details

	1	**2**·2MeNO$_2$	**3**·2MeOH	**4**·17MeOH	**5**·6CH$_3$CN
Formula	$C_{54}H_{48}N_6O_{12}Cl_6Fe_2Co_3$	$C_{56}H_{48}Br_6Fe_2N_8O_{16}Zn_3$	$C_{56}H_{48}Br_6Cr_2N_6O_{14}Zn_3$	$C_{158}H_{194}Cr_2F_{18}N_6O_{47}P_6Pd_3S_6$	$C_{153}H_{144}N_{12}O_{30}F_{18}Al_2P_6S_6Pd_3$
MWt [g mol^{-1}]	1474.17	1876.29	1816.57	4072.56	3724.13
T [K]	100	100	100	120	120
λ [Å]	0.71075	0.71075	0.71075	1.5418	1.5418
Crystal system	Trigonal	Trigonal	Trigonal	Triclinic	Cubic
Space group	$P3_221$	$P3_221$	$P3_221$	$P\bar{1}$	$I\bar{4}3d$
Unit cell [Å/°]	$a = 12.7708(5)$ $b = 12.7708(5)$ $c = 39.0709(12)$ $\alpha = 90$ $\beta = 90$ $\gamma = 120$	$a = 12.8153(16)$ $b = 12.8153(16)$ $c = 12.8153(16)$ $\alpha = 90$ $\beta = 90$ $\gamma = 120$	$a = 13.2429(10)$ $b = 13.2429(10)$ $c = 38.380(3)$ $\alpha = 90$ $\beta = 90$ $\gamma = 120$	$a = 18.4407(9)$ $b = 22.0037(9)$ $c = 27.1925(10)$ $\alpha = 104.146(3)$ $\beta = 109.298(4)$ $\gamma = 95.522(4)$	$a = 43.73712(7)$ $b = 43.73712(7)$ $c = 43.73712(7)$ $\alpha = 90$ $\beta = 90$ $\gamma = 90$
Volume [Å^3]	5518.5(5)	5520.9(16)	5829.1(10)	9907.3(8)	83 666.3(4)
Z	3	3	3	2	16
Density (calculated) [g cm^{-3}]	1.333	1.693	1.546	1.365	1.183
μ [mm^{-1}]	1.318	4.668	4.322	4.843	3.770
Reflections collected	21 773	32 005	8827	66 752	498 156
Independent reflections	8331	6717	8827	12 021	14 608
R_{int}	0.1233	0.0627	0.0356	0.0871	0.0934
Goodness-of-fit on F^2	1.020	1.040	0.971		
Final R indices [$F^2 > 2\sigma(F^2)$]	0.0732	0.0379	0.0512	0.0806	0.0869
R indices (all data)	0.0887	0.0409	0.0605	0.1050	0.0897

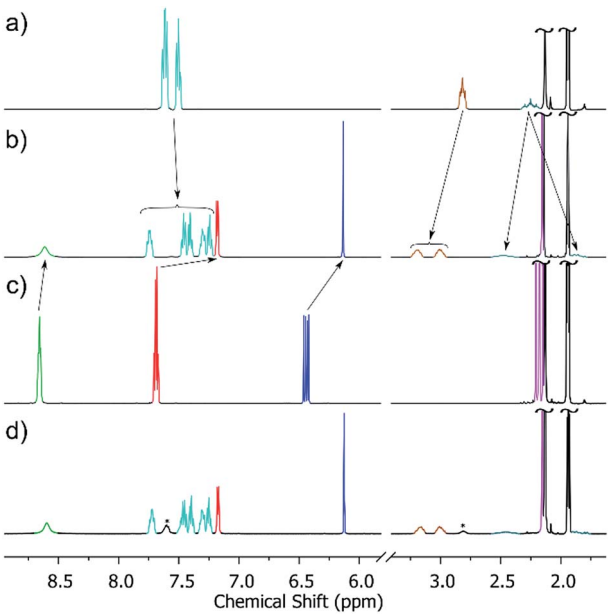

Fig. 2 Partial ^{1}H NMR spectra (CD$_3$CN, 500 MHz, 300 K) of (a) [Pd(dppp)(CF$_3$SO$_3$)$_2$]; (b) cage **5** (re-dissolved crystalline material) (c) [Al^{III}L$_3$]; (d) the crude self-assembly reaction between a slight excess of [Pd(dppp)$_2$(CF$_3$SO$_3$)$_2$] and [Al^{III}L$_3$] in CD$_3$CN (signals for excess [Pd(dppp)$_2$(CF$_3$SO$_3$)$_2$] marked *). Colour code: *o*-Py, green; *m*-Py, red; dppp ArH, turquoise; acac CH, blue; dppp-CH$_2$, brown and pale blue; acac-CH$_3$, magenta.

to give the entropically more favourable trigonal bipyramid. A comparison of the ^{1}H NMR spectra of the re-dissolved crystalline sample of **5** (Fig. 2b) and the crude reaction solution, obtained by treating a slight excess of [Pd(dppp)(OTf)$_2$] with [Al^{III}L$_3$] in CD$_3$CN (Fig. 2d), shows that this amplification is not a solid-state packing effect, rather a solution-based effect. The single set of signals in the ^{1}H NMR spectrum of the product (Fig. 2b/d) also indicates that **5** is formed with complete diastereoselectivity.[46] This represents a second tier of self-sorting, which, unusually, involves Pd-mediated heterochiral recognition of Δ and Λ-[Al^{III}L$_3$] enantiomers (see below).

Solid-state structure descriptions

The heterometallic trigonal bipyramid cages [Fe$_2$Co$_3$L$_6$Cl$_6$] (**1**), [Fe$_2$Zn$_3$L$_6$Br$_6$] (**2**), [Cr$_2$Zn$_3$L$_6$Br$_6$] (**3**), [Cr$_2$Pd$_3$L$_6$(dppp)$_3$](OTf)$_6$ (**4**) and [Al$_2$Pd$_3$L$_6$(dppp)$_3$](OTf)$_6$ (**5**) (Fig. 3 and 4) were all synthesised in a similar manner, by addition of either tetrahedral or *cis*-protected square planar M^{II} compounds to the metalloligand [M^{III}L$_3$] (M^{III} = Fe, Cr or Al) in acetone, methanol, acetonitrile or a mixed solvent system, with crystals isolated from slow evaporation of the mother liquor, or diffusion of Et$_2$O or MeOH (see the Experimental section for full details). The metallic skeletons of the cages in **1–5** describe a trigonal bipyramid with the M^{III} ions situated on the axial positions and the M^{II} ions on the equatorial sites. The approximate dimensions of the $[M^{III}_2M^{II}_3]^{n+}$ metallic skeleton are M^{III}···M^{II} (8.77–8.99 Å), M^{II}···M^{II} (11.72–12.80 Å) and M^{III}···M^{III} (10.75–11.20 Å).

Each of the three M^{II} metal ions is coordinated by two N donors from the pyridyl groups of [M^{III}L$_3$]. The N–M^{II}–N angle of the tetrahedral CoN$_2$Cl$_2$/ZnN$_2$Br$_2$ moiety for compounds **1–3** lies in the range 90.63–103.57°; in **4–5** the equivalent N–Pd–N angle is in the range 84.40–85.39°. Each [M^{III}L$_3$] corner unit consists of a six-coordinate M^{III} ion with regular {MO$_6$} octahedral geometry. For the three different [M^{III}L$_3$] metalloligands used in the synthesis the M^{III}–O distances and angles are: Fe–O 1.98–

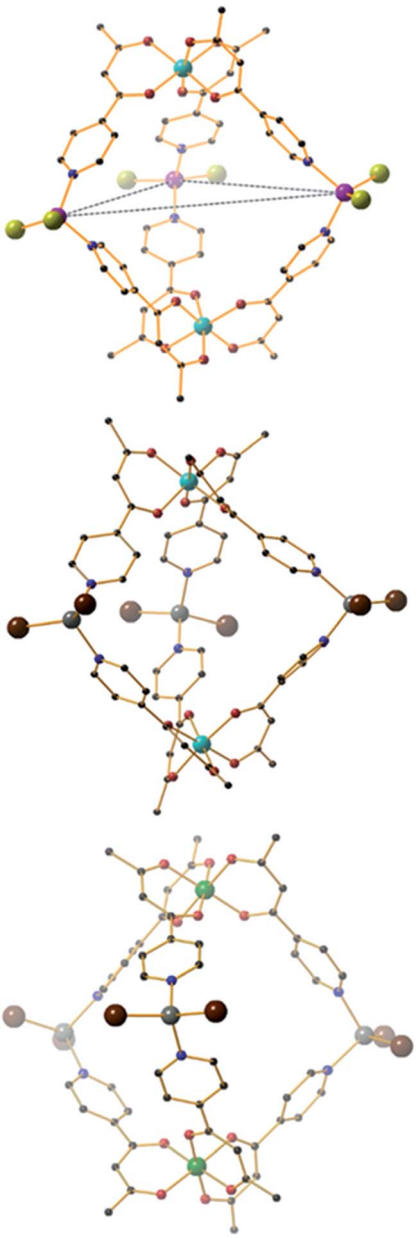

Fig. 3 From top to bottom, molecular structures of (ΛΛ)-**1**, **2** and **3**. Colour code: Fe = cyan, Co = magenta, Cr = green, Zn = grey, O = red, N = blue, Cl = green, Br = brown, C = black. H-atoms omitted for clarity. The dashed blue line in the upper figure highlights the trigonal plane of M^{II} ions.

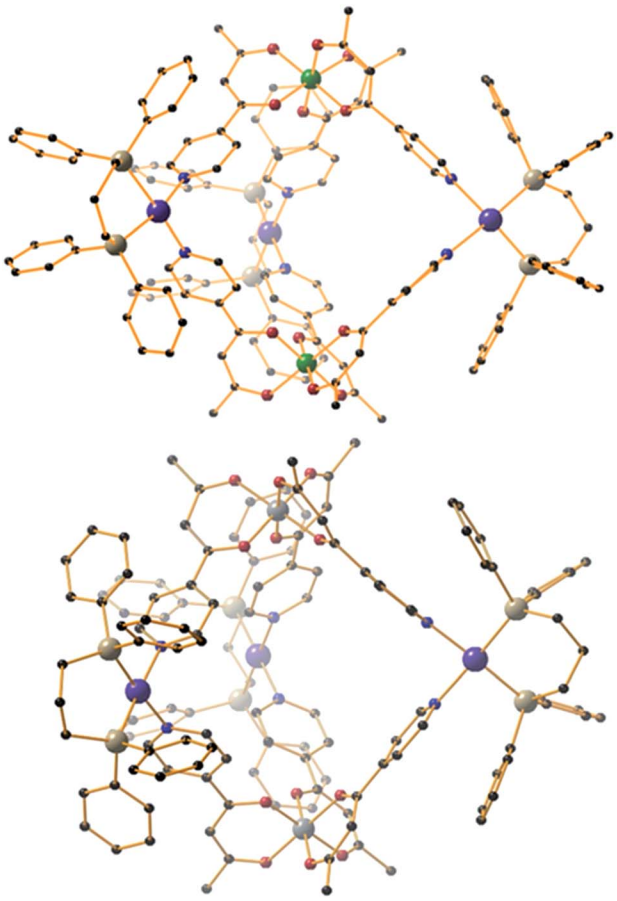

Fig. 4 Molecular structures of (ΛΔ)-**4** (top) and **5** (bottom). Colour code: Cr = green, Al = grey, Pd = magenta, P = silver, O = red, N = blue, C = black. H-atoms and OTf^- counteranions omitted for clarity.

2.02 Å, Fe–O *cis*/*trans* angles 83.48–95.17° and 169.99–178.40°, respectively; Cr–O 1.91–1.98 Å, Cr–O *cis*/*trans* angles 86.82–94.04° and 176.35–179.85°, respectively; Al–O 1.86–1.89 Å, Al–O *cis*/*trans* angles 88.84–91.43° and 179.03–179.54°, respectively. The Co^{II} and Zn^{II} ions lie in distorted tetrahedral environments with bond distances in the range 2.05–2.35 Å (Co–Cl ~ 2.23 Å, Co–N ~ 2.05 Å, Zn–Br ~ 2.35 Å and Zn–N ~ 2.06 Å) and bond angles around the metal centres ranging from 90.62° to 120.08°. In compounds **4** and **5**, the Pd^{II} ion is 90° *cis*-blocked through the use of the dppp ligand (Pd–P bond distance ~ 2.27 Å). The coordination of Pd to $[M^{III}L_3]$ through the use of Pd–N bonds (ranging from 2.08–2.14 Å) creates a distorted square planar geometry around the Pd centre with *cis*/*trans* bond angles in the range 84.40–93.50° and 165.49–178.57°, respectively. While complexes **1–3** are neutral, charge balance is maintained in **4** and **5** through the presence of a total of six $CF_3SO_3^-$ anions, lying outside the cage.

While the intrametallic distances of the five trigonal bipyramids are similar, there is nonetheless a distinct diastereomeric difference between structures **1–3** and **4–5**. Whereas **1–3** are all homochiral racemates in which each intact capsule features two $[M^{III}L_3]$ units that possess the same Λ or Δ chirality, in contrast structures **4** and **5** are both the achiral heterodiastereomer. While sorting of chiral octahedral metal motifs has been frequently observed in metallosupramolecular assembly reactions, for the vast majority homochiral assemblies are energetically preferred.[47] The commonality of the [Pd(dppp)] unit in both **4** and **5** that feature different $[M^{III}L_3]$ metalloligands would suggest that either the small change in angle between pyridine donors at each M^{II} connector and/or the interactions of the dppp protecting ligand with these donors cause the change in diastereomeric preference. Solution studies with **5** would also indicate this is not simply due to selective crystallization from a complex mixture (see above). Outwith cyanometalate

chemistry,[32–34] compounds **1–4** represent the first examples of trigonal bipyramids built with paramagnetic metal ions, and join a small family of analogous compounds containing diamagnetic metal ions.[48–52]

SQUID magnetometry

The dc (direct current) molar magnetic susceptibility, χ, of a polycrystalline sample of **1** was measured in an applied magnetic field, B, of 0.1 T, over the 2–300 K temperature, T, range. The experimental results are shown in Fig. 5 in the form of the χT product, where $\chi = M/B$, and M is the magnetisation of the sample. At room temperature, the χT product of **1** has a value of 14.4 cm^3 K mol^{-1}, in good agreement with the sum of Curie constants for a $[Fe^{III}_2Co^{II}_3]$ unit (14.375 cm^3 K mol^{-1}, $g_{Fe} = g_{Co} = 2.0$). Note that the estimation of the g-value of the Co^{II} ions here is an approximation and subject to error (*e.g.* lattice solvent lost upon sample drying will result in a variation of the samples diamagnetism), and a better measure comes from the EPR spectroscopy, which is consistent with $g_{Co} = 2.3$ (*vide infra*). Upon cooling, the χT product of **1** remains essentially constant down to approximately 100 K, wherefrom it decreases upon further cooling to 9.5 cm^3 K mol^{-1} at 2 K. Given that the anisotropy of Fe^{III} is negligible, this behaviour is consistent with a relatively large single-ion magnetic anisotropy for the Co^{II} centres and/or an antiferromagnetic exchange interaction between the Fe^{III} and Co^{II} centres. To better define the low-temperature magnetic properties of **1**, low temperature variable-temperature-and-variable-field (VTVB) magnetisation data were measured in the temperature and magnetic field ranges $T = 2$–12 K and $B = 0$–5 T (Fig. 5). At the highest investigated field (5 T) and the lowest investigated temperature (2 K), the magnetisation of **1** is of 13.7 μ_B (μ_B is the Bohr magneton). Furthermore, when the VTVB data of **1** are plotted against the reduced quantity $\mu_B B/kT$, little nesting of the VTVB data is observed. This observation indicates that the part of the energy spectrum of **1** probed under these experimental conditions does not present significant anisotropy splitting with respect to the temperature of measurement at zero magnetic field.

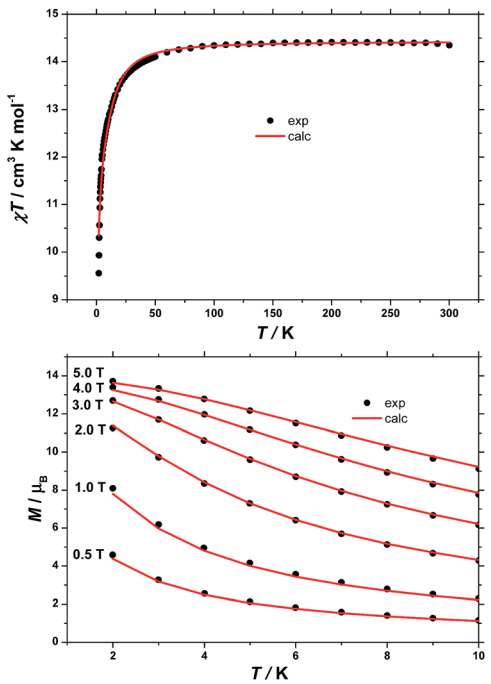

Fig. 5 (Top) Temperature dependence of the χT product of a polycrystalline sample of **1** with $B = 0.1$ T. (Bottom) VTVB magnetisation data of **1** in the field and temperature ranges 0.5 to 5 T and 2 to 10 K, respectively. Solid lines are the best-fit curves, see text for details.

For the quantitative interpretation of the magnetisation data, we used spin-Hamiltonian (1)

$$\hat{H} = \mu_B B \sum_i g_i \hat{S}_i - 2 \sum_{i,j<i} J_{ij} \hat{S}_i \cdot \hat{S}_j + \sum_i D_i \left[\hat{S}_{i,z}{}^2 - S_i(S_i+1)/3 \right] \quad (1)$$

where the summation indexes i, j run through the constitutive metal centres, g_i is the g-factor of the i^{th} centre, $\hat{S}$ is a spin operator, J is the isotropic exchange interaction parameter, D is the uniaxial anisotropy parameter and S is the total spin.

In our spin-Hamiltonian model, we assume for simplicity that all g-factors are equal to 2, $S_{Fe^{III}} = 5/2$, $S_{Co^{II}} = 3/2$, we only consider exchange interactions between Co^{II} and Fe^{III} centres, and neglect the single-ion anisotropy of Fe^{III}. Furthermore, we fix the uniaxial anisotropy of Co^{II} to $D_{Co} = -14$ cm^{-1}, as extracted from the modelling of the EPR data and theoretical calculations, which are discussed further in the following sections. Thus, at this point our model contains only one free parameter, namely, the isotropic exchange between Fe^{III} and Co^{II}, $J_{Fe\text{–}Co}$. The χT product of **1** was fitted to spin-Hamiltonian (1) by full matrix numerical diagonalisation of the spin-Hamiltonian of the full system of dimension 2304 by 2304, through use of the Levenberg–Marquardt algorithm.[53] This resulted in the best-fit parameter $J_{Fe\text{–}Co} = -0.04$ cm^{-1}. In order to verify the validity of our model, $J_{Fe\text{–}Co}$ was fixed to the determined best-fit value, $J_{Fe\text{–}Co} = -0.04$ cm^{-1}, and D_{Co} was maintained fixed at -14 cm^{-1}. At this point our model contains no free parameters. Thereafter, the VTVB data of **1** were simulated by use of spin-Hamiltonian (1). The simulated curves are shown as solid red lines in Fig. 5. With these parameters, the energy spectrum of **1** consists of four groups of densely packed states, each separated by approximately $2D_{Co}$ (Fig. 6). It is interesting to note that multiple ground level crossings simultaneously occur at approximately 0.47 T when the magnetic field is applied parallel to the quantisation axis.

Heat capacity

Fig. 7 shows the collected heat capacity data, normalised to the gas constant, c_p/R of **1** as a function of temperature (between *ca.* 0.3 K and 30 K) for zero-applied magnetic field. As is typical for molecular magnetic materials,[54] lattice vibrations contribute predominantly to c_p as a rapid increase above liquid-helium temperature. The lattice contribution can be described by the Debye model (dotted line in Fig. 7), which simplifies to a $c_p/R = aT^3$ dependence at the lowest temperatures, where $a = 7.6 \times 10^{-3}$ K^{-3} for **1**.

For $T <$ *ca.* 3 K, the zero-field c_p shows a wide bump-like anomaly, which we attribute to the splitting of the spin levels

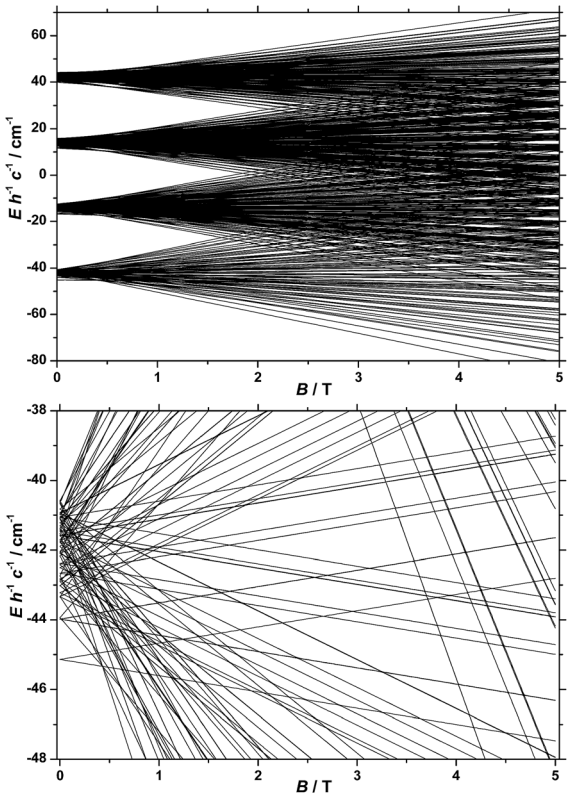

Fig. 6 (Top) Energy spectrum of **1** determined with the best-fit parameters (see text) and the magnetic field applied along the quantisation axis. (Bottom) Low-lying states of the energy spectrum of **1**, determined as described in the text.

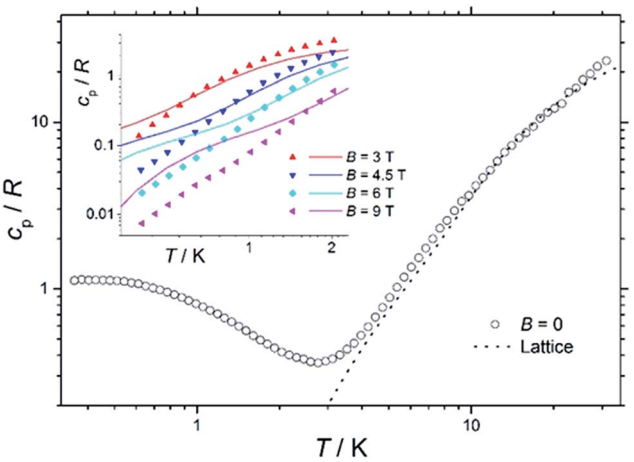

Fig. 7 Temperature dependence of the zero-field heat capacity c_p, normalised to the gas constant R, for a polycrystalline sample of **1**. The dotted line is the lattice contribution. Inset: temperature dependence of c_p/R of **1** for $T < 2$ K and $B \geq 3$ T. Solid lines are the best-fit curves, see text for details.

by zero-field splitting and magnetic interactions. At such low temperatures, the magnetic measurements are very sensitive to the applied magnetic field, as seen in the experimental behaviour for fields of 3 T and higher (inset of Fig. 7). Such large intensities of the applied magnetic field are sufficient for promoting full decoupling between the individual spin centres (we recall that the exchange interaction is as small as $J_{Fe-Co} = -0.04$ cm^{-1} on the basis of the fit of the magnetometry data). Therefore, the temperature and field dependence of the c_p data in Fig. 7 (inset), collected for $B \geq 3$ T, are particularly suitable for probing the influence of crystal fields on **1**, down to temperatures significantly lower than the ones obtained in the magnetisation measurements.

The solid lines in Fig. 7 are the curves calculated for Hamiltonian (1), using the best-fit parameters from the magnetothermal and spectroscopic data and theoretical calculations, *i.e.*, $D_{Co} = -14$ cm^{-1} and the here-negligible $J_{Fe-Co} = -0.04$ cm^{-1}. The agreement with the experimental data is good, though not outstanding. Anticipating the discussion on the EPR spectra (*vide infra*), we have checked that adding a zero-field splitting (ZFS) of $D_{Fe} = -0.2$ cm^{-1} at the Fe^{III} sites does not improve the fit. The discrepancy is most evident below *ca.* 1 K, where the experimental data have lower values than the calculated ones. This behaviour can be explained by a wider broadening of the low-lying energy spectrum, likely induced by higher-order anisotropy terms, which are not taken into account in Hamiltonian (1).

EPR spectroscopy

We previously reported EPR spectra of [CrL$_3$], giving the ZFS of the Cr^{III}, $s = 3/2$ ion as $D = -0.55$ cm^{-1} with a small rhombicity of $|E/D| = 0.045$.[29] Q-Band spectra of **3** and **4** are similar to that of [Cr^{III}L$_3$], and give $D = -0.64$ and -0.61 cm^{-1}, respectively (Fig. S11;† $|E/D| = 0.03$–0.04).[55] Hence, the distortion imposed on the {CrO$_6$} coordination sphere of [Cr^{III}L$_3$] by complexation in the {Cr$^{III}_2$M$^{II}_3$} supramolecules results in a small, but measurable, increase of the ZFS at Cr^{III}. The {CrO$_6$} metric parameters do not appear to be very different.

Such an increase in D is also found for the Fe^{III} ($s = 5/2$) systems. X- and Q-band EPR spectra of [Fe^{III}L$_3$] reveal a rather small ZFS of $D = 0.08$ cm^{-1} with $|E/D| = 1/3$ (Fig. 8 and S12;† note the sign of D has no significance with a fully rhombic D-tensor). These values are similar to those reported for [Fe(acac)$_3$] ($|D| = 0.16$ cm^{-1}, $E/D = 0.3$)[56] and [Fe(dpm)$_3$] (dpm = dipivaloylmethane; $D = -0.20$ cm^{-1}, $|E/D| = 0.25$).[57] On incorporation into the {Fe$^{III}_2$Zn$^{II}_3$} complex **2**, a much richer spectrum is observed (Fig. 8 and S12), giving $D = 0.20$ cm^{-1} ($E/D = 1/3$). Angular overlap model studies on [Fe(acac)$_3$] and [Fe(dpm)$_3$] show D to be very sensitive to the trigonal distortion at Fe^{III},[57] and there is a more significant structural difference in the {Fe^{III}O$_6$} coordination spheres when bound in {Fe$^{III}_2$Zn$^{II}_3$}, with longer Fe–O bonds and wider O–Fe–O angles in the {py}$_3$ face, than in the equivalent Cr^{III} systems.

The {Fe$^{III}_2$Co$^{II}_3$} complex **1** gives Q-band EPR spectra with very broad features at *ca.* 5, 9 and 12 kG that line up with the main features of the spectrum of the {Fe$^{III}_2$Zn$^{II}_3$} complex **2**. Hence, the ZFS at Fe^{III} must be similar. The very large ZFS at Co^{II} means that only transitions within the ground Kramers doublet of this ion are observed (the microwave energy, $h\nu \ll |D|$), and there must be a significant rhombicity in order for these transitions to

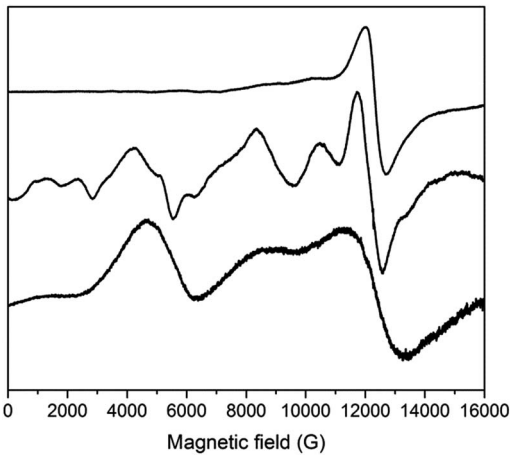

Fig. 8 Q-Band EPR spectra of powdered samples of (from top to bottom) [FeL_3], **2** and **1** at 5 K.

fall within the observed features. The spectra also show that the J_{FeCo} exchange interaction must be very weak, resulting only in severe broadening of the peaks. Test calculations on a simple $\{Fe^{III}Co^{II}\}$ model, with fixed ZFS at the $s = 5/2$ and 3/2 spins (the latter taking $D = -14$ cm^{-1} with $E/D = 0.1$; averaging the results of CASSCF calculations – see below) suggest that if $|J_{FeCo}| >$ *ca.* 0.02 cm^{-1} then additional features would be observed in the Q-band EPR spectrum. Note that the limit for the full, five-spin system would be different.

The D_{Fe} values obtained from EPR would have a negligible effect on the calculated $\chi T(T)$ and $c_p(T,B)$ curves for **1**, and a negligible effect on the global level structure in Fig. 6a, because both $|D_{Fe}|$ and $|J_{FeCo}|$ are $\ll|D_{Co}|$. However, it would affect the detail of the states within each of the densely packed multiplets of Fig. 6a, because $|D_{Fe}|$ and $|J_{FeCo}|$ are of similar magnitude.

Theoretical studies

In order to independently verify the large ZFS of Co^{II} we have performed complete active space self-consistent field (CASSCF) calculations on the three unique Co^{II} sites of **1**, see the SI for details. The results suggest $D_{Co} = -14$ cm^{-1}, $E/D = 0.1$ (Table S1†) which is entirely consistent with the magnetometry and heat capacity data. The calculations also suggest that the principal axes of the local ZFS tensors are oriented roughly perpendicular to the Fe^{III}–Fe^{III} axis and canted approximately 120° with respect to one another in the plane (Fig. 9). Accounting for the non-collinearity in spin-Hamiltonian (1) did not improve the quality of the fits to the magnetometry or heat capacity data.

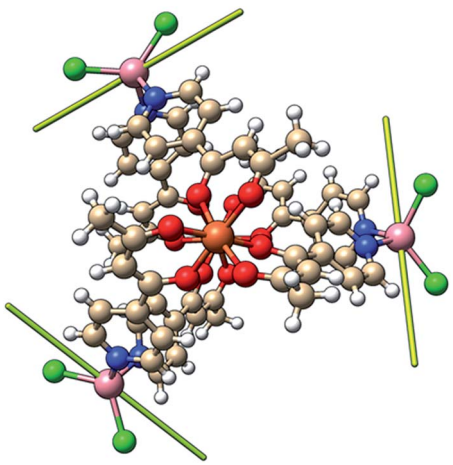

Fig. 9 Orientation of the principal anisotropy axis for the Co^{II} sites in **1** (yellow rods); orange = Fe, pink = Co, green = Cl, red = O, blue = N, beige = C, white = H.

Conclusions

Complexes **1–5** represent a novel, and unusual family of trigonal bipyramidal cage complexes, built with the tritopic $[ML_3]$ metalloligand, featuring a tris(acac) octahedral transition metal core functionalised with three *p*-pyridyl donor groups, and a series of transition metal salts. Outwith cyanometalate chemistry, compound **1** represents the first example of such a cage containing paramagnetic metal ions. Complementary studies investigating the diamagnetic variants using ^{1}H NMR spectroscopy reveal some interesting features about the solution self-assembly process. Firstly, the $[M^{III}L_3]$ metalloligand is a highly dynamic tritopic building block as evidenced by *fac* configurational isomer being amplified at the expense of the *mer* during the course of cage formation. The self-assembly process also occurs with high and unusual stereoselectivity wherein the trigonal bipyramids are formed exclusively from twisted pyramidal components of opposite Δ/Λ-handedness. Solution stability of the cage is also confirmed *via* mass spectrometry. SQUID magnetometry and heat capacity measurements on **1** reveal weak antiferromagnetic exchange between the Fe^{III} and Co^{II} ions, with $|D_{Co}| = 14$ cm^{-1}. EPR spectroscopy reveals that the distortion imposed on the $\{MO_6\}$ coordination sphere of $[M^{III}L_3]$ by complexation in the $\{M^{III}_2M^{II}_3\}$ supramolecules results in a small, but measurable, increase of the zero field splitting at M^{III}. CASSCF calculations on the three unique Co^{II} sites of **1** suggest that the principal axes of the local ZFS tensors are oriented perpendicular to the Fe^{III}–Fe^{III} axis, but canted ∼120° with respect to each other.

Acknowledgements

EKB thanks the EPSRC for funding, and the Velux Foundations for a Villum Visiting Professor Programme Grant. PJL thanks the Leverhulme Trust (RPG-2015-232). GL, EP and ME thank the Spanish Ministry of Economy, Industry and Competitiveness (MAT2013-44063-R and MAT2015-68204-R). We thank the EPSRC for funding the UK National Crystallography service and the UK National EPR Facility. NFC thanks the Ramsay Memorial Trust for a Research Fellowship.

Notes and references

1 A. Fernandez, J. Ferrando-Soria, E. Moreno Pineda, F. Tuna, I. J. Vitorica-Yrezabal, C. Knappke, J. Ujma, C. A. Muryn,

G. A. Timco, P. E. Barran, A. Ardavan and R. E. P. Winpenny, *Nat. Commun.*, 2016, **7**, 10240.
2 D. Aguilà, L. A. Barrios, V. Velasco, O. Roubeau, A. Repollés, P. J. Alonso, J. Sesé, S. J. Teat, F. Luis and G. Aromí, *J. Am. Chem. Soc.*, 2014, **136**, 14215–14222.
3 M. Manoli, S. Alexandrou, L. Pham, G. Lorusso, W. Wernsdorfer, M. Evangelisti, G. Christou and A. J. Tasiopoulos, *Angew. Chem., Int. Ed.*, 2016, **55**, 679–684.
4 K. E. R. Marriott, L. Bhaskaran, C. Wilson, M. Medarde, S. T. Ochsenbein, S. Hill and M. Murrie, *Chem. Sci.*, 2015, **6**, 6823–6828.
5 J. Martinez-Lillo, J. Faus, F. Lloret and M. Julve, *Coord. Chem. Rev.*, 2015, **289–290**, 215–237.
6 M. Ibrahim, V. Mereacre, N. Leblanc, W. Wernsdorfer, C. E. Anson and A. K. Powell, *Angew. Chem., Int. Ed.*, 2015, **54**, 15574–15578.
7 K. R. Meihaus, M. E. Fieser, J. J. Corbey, W. J. Evans and J. R. Long, *J. Am. Chem. Soc.*, 2015, **137**, 9855–9860.
8 S. T. Liddle and J. van Slageren, *Chem. Soc. Rev.*, 2015, **44**, 6655–6669.
9 S. K. Langley, D. P. Wielechowski, V. Vieru, N. F. Chilton, B. Moubaraki, L. F. Chibotaru and K. S. Murray, *Chem. Sci.*, 2014, **5**, 3246–3256.
10 M. Atzori, L. Tesi, E. Morra, M. Chiesa, L. Sorace and R. Sessoli, *J. Am. Chem. Soc.*, 2016, **138**, 2154–2157.
11 S. Thiele, F. Balestro, R. Ballou, S. Klyatskaya, M. Ruben and W. Wernsdorfer, *Science*, 2014, **344**, 1135–1138.
12 M. Ganzhorn, S. Klyatskaya, M. Ruben and W. Wernsdorfer, *Nat. Nanotechnol.*, 2013, **8**, 165–169.
13 M. L. Baker, T. Guidi, S. Carretta, J. Ollivier, H. Mutka, H. U. Güdel, G. A. Timco, E. J. L. McInnes, G. Amoretti, R. E. P. Winpenny and P. Santini, *Nat. Phys.*, 2012, **8**, 906–911.
14 Y. Rechkemmer, F. D. Breitgoff, M. van der Meer, M. Atanasov, M. Hakl, M. Orlita, P. Neugebauer, F. Neese, B. Sarkar and J. van Slageren, *Nat. Commun.*, 2016, **7**, 10467.
15 G. Lorusso, O. Roubeau and M. Evangelisti, *Angew. Chem., Int. Ed.*, 2016, **55**, 3360–3363.
16 L. Tesi, E. Lucaccini, I. Cimatti, M. Perfetti, M. Mannini, M. Atzori, E. Morra, M. Chiesa, A. Caneschi, L. Sorace and R. Sessoli, *Chem. Sci.*, 2016, **7**, 2074–2083.
17 H. Atkinson, R. Inglis, E. del Barco and E. K. Brechin, *Phys. Rev. Lett.*, 2014, **113**, 087201.
18 M. Shiddiq, D. Komijani, Y. Duan, A. Gaita-Ariño, E. Coronado and S. Hill, *Nature*, 2016, **531**, 348–351.
19 J.-N. Rebilly and T. Mallah, *Struct. Bonding*, 2006, **122**, 103–131.
20 V. Marvaud, C. Decroix, A. Scuiller, F. Tuyèras, C. Guyard-Duhayon, J. Vaissermann, J. Marrot, F. Gonnet and M. Verdaguer, *Chem.–Eur. J.*, 2003, **9**, 1692–1705.
21 M. Nihei, Y. Sekine, N. Suganami, K. Nakazawa, A. Nakao, H. Nakao, Y. Murakami and H. Oshio, *J. Am. Chem. Soc.*, 2011, **133**, 3592–3600.
22 J. M. Zadrozny, D. E. Freedman, D. M. Jenkins, T. D. Harris, A. T. Iavarone, C. Mathonière, R. Clérac and J. R. Long, *Inorg. Chem.*, 2010, **49**, 8886–8896.
23 T. Glaser, *Chem. Commun.*, 2011, **47**, 116–130.
24 C. Zhao, F. D. Toste, K. N. Raymond and R. G. Bergman, *J. Am. Chem. Soc.*, 2014, **136**, 14409–14412.
25 P. Mal, B. Breiner, K. Rissanen and J. R. Nitschke, *Science*, 2009, **324**, 1697–1699.
26 O. Chepelin, J. Ujma, X. Wu, A. M. Z. Slawin, M. B. Pitak, S. J. Coles, J. Michel, A. C. Jones, P. E. Barran and P. J. Lusby, *J. Am. Chem. Soc.*, 2012, **134**, 19334–19337.
27 A. Pastor and E. Martínez-Viviente, *Coord. Chem. Rev.*, 2008, **252**, 2314–2345.
28 See for example: W. Cullen, K. A. Thomas, C. A. Hunter and M. D. Ward, *Chem. Sci.*, 2015, **6**, 4025–4028.
29 (*a*) S. Sanz, H. M. O'Connor, E. M. Pineda, K. S. Pedersen, G. S. Nichol, O. Mønsted, H. Weihe, S. Piligkos, E. J. L. McInnes, P. J. Lusby and E. K. Brechin, *Angew. Chem., Int. Ed.*, 2015, **54**, 6761–6764; an analogous cage of diamagnetic metals has also been published, 2009, see: (*b*) H.-B. Wu and Q.-M. Wang, *Angew. Chem., Int. Ed. Engl.*, 2009, **48**, 7343–7345.
30 H. M. O'Connor, S. Sanz, M. B. Pitak, S. J. Coles, G. S. Nichol, S. Piligkos, P. J. Lusby and E. K. Brechin, *CrystEngComm*, 2016, **18**, 4914–4920.
31 R. Chakrabarty, P. S. Mukherjee and P. J. Stang, *Chem. Rev.*, 2011, **111**, 6810–6918.
32 K. Van Langenberg, S. R. Batten, K. J. Berry, D. C. R. Hockless, B. Moubaraki and K. S. Murray, *Inorg. Chem.*, 1997, **36**, 5006–5015.
33 (*a*) C. F. Wang, J. L. Zuo, B. M. Bartlett, Y. Song, J. R. Long and X. Z. You, *J. Am. Chem. Soc.*, 2006, **128**, 7162–7163; (*b*) B. M. Bartlett, T. D. Harris, M. W. DeGroot and J. R. Long, *Z. Anorg. Allg. Chem.*, 2007, **633**, 2380–2385.
34 M.-X. Yao, Z.-Y. Wei, Z.-G. Gu, Q. Zheng, Y. Xu and J.-L. Zuo, *Inorg. Chem.*, 2011, **50**, 8636–8644.
35 B. Singh, G. Y. Lesher, K. C. Pluncket, E. D. Pagani, D. C. Bode, R. G. Bentley, M. J. Connell, L. T. Hamel and P. J. Silver, *J. Med. Chem.*, 1992, **35**, 4858–4865.
36 S. J. Coles and P. A. Gale, *Chem. Sci.*, 2012, **3**, 683–689.
37 Rigaku Oxford Diffraction, in *CrystalClear-SM Expert 3.1 b27*, 2012.
38 Rigaku Oxford Diffraction, in *CrysAlisPro 1.171.38.41*, 2015.
39 Rigaku Oxford Diffraction, in *CrysAlisPro*, 2016.
40 L. Palatinus and G. Chapuis, *J. Appl. Crystallogr.*, 2007, **40**, 786–790.
41 G. M. Sheldrick, *Acta Crystallogr., Sect. C: Struct. Chem.*, 2015, **71**, 3–8.
42 O. V. Dolomanov, A. J. Blake, N. R. Champness and M. Schröder, *J. Appl. Crystallogr.*, 2003, **36**, 1283–1284.
43 A. L. Spek, *Acta Crystallogr., Sect. C: Struct. Chem.*, 2015, **71**, 9–18.
44 M. Fujita, J. Yazaki and K. Ogura, *J. Am. Chem. Soc.*, 1990, **112**, 5647–5648.
45 I. A. Riddell, M. M. J. Smulders, J. K. Clegg, Y. R. Hristova, B. Breiner, J. D. Thoburn and J. R. Nitschke, *Nat. Chem.*, 2012, **4**, 751–756; A. J. Metherell and M. D. Ward, *Chem. Sci.*, 2016, **7**, 910–915.
46 While a single set of signals could also indicate dynamic exchange of the components relative to the NMR timescale, this is unlikely with a Pd-based system.

Furthermore, *in situ* monitoring of the self-assembly reaction in CD_3CN with excess Pd salt using ^1H NMR spectroscopy (*e.g.* Fig. 2d), showed this not to be in fast exchange.

47 A. M. Castilla, W. J. Ramsay and W. J. J. R. Nitschke, *Acc. Chem. Res.*, 2014, **47**, 2063–2073.

48 N. R. Voss and M. Gerstein, *Nucleic Acids Res.*, 2010, **38**, 555–562.

49 M. Wang, V. Vajpayee, S. Shanmugaraju, Y. R. Zheng, Z. Zhao, H. Kim, P. S. Mukherjee, K. W. Chi and P. J. Stang, *Inorg. Chem.*, 2011, **50**, 1506–1512.

50 X. Sun, D. W. Johnson, D. L. Caulder, K. N. Raymond and E. H. Wong, *J. Am. Chem. Soc.*, 2001, **123**, 2752–2763.

51 S. Hiraoka, Y. Sakata and M. Shionoya, *J. Am. Chem. Soc.*, 2008, **2**, 1–15.

52 Y. Sakata, S. Hiraoka and M. Shionoya, *Chem.–Eur. J.*, 2010, **16**, 3318–3325.

53 W. H. Press, S. A. Teukolsky, W. T. Vetterling and B. P. Flannery, *Numerical recipes in C: The Art of Scientific Computing*, 2nd edn, Cambridge University Press, Cambridge, 1992.

54 M. Evangelisti, F. Luis, L. J. de Jongh and M. Affronte, *J. Mater. Chem.*, 2006, **16**, 2534–2549.

55 H. Weihe, *SIM-EPR*, Copenhagen University.

56 D. Collison and A. K. Powell, *Inorg. Chem.*, 1990, **29**, 4735–4746.

57 A.-L. Barra, A. Caneschi, A. Cornia, F. Fabrizi de Biani, D. Gatteschi, C. Sangregorio, R. Sessolia and L. Sorace, *J. Am. Chem. Soc.*, 1999, **121**, 5302–5310.

Dalton Transactions

COMMUNICATION

View Article Online
View Journal | View Issue

Cite this: *Dalton Trans.*, 2015, **44**, 20839

Received 30th October 2015,
Accepted 13th November 2015

DOI: 10.1039/c5dt04264j

www.rsc.org/dalton

A room temperature spin crossover ionic liquid†

Anthony J. Fitzpatrick, Helen M. O'Connor and Grace G. Morgan*

Two new paramagnetic ionic liquids (ILs) comprising a mononuclear iron(III) or manganese(III) complex cation, charge balanced by a dicyanamide anion are reported which show a range of spin states. Both are liquids at room temperature and the Fe(III) based IL exhibits a spin crossover close to 300 K. The spin crossover profile is independent of the solvation, and is both air and moisture stable.

The molecular switching phenomenon of SCO has great potential in data storage and molecular switching and sensing.[1] However there is a need to have a processable, malleable material whose properties are less dependent on crystalline morphology. Recently there has been an interest in the investigation of the effects of crystalline defects in solid SCO materials.[2] The "breathing" of SCO molecules can propagate across a whole domain resulting in a macroscopic change in the lattice. Apart from breaking or damaging the sample, the presence of microscopic defects may strongly influence the way the SCO propagates at the macroscopic level.

One method to overcome crystalline defects could be the use of ionic liquid (IL) design strategies. Most of the work in SCO in the past 80 years has been carried out in the solid state but with increasing interest in development of processable spin switchable materials, there is a move towards investigation of the phenomenon in soft matter.[3–10] ILs are salts with melting temperatures below 373 K and room temperature liquids (RTILs) offering a promising vehicle to add flexibility to develop the range of SCO applications *e.g.* thermochromic inks or spin switchable reaction media. The main design criterion for an IL of a bulky asymmetric cation charge balanced by a bulky anion, offers much scope for combinations of cation and anion which in turn allows for a great variety of tunable interactions and applications. The negligible vapour pressure, wide temperature liquid range, high thermal stability, high ionic conductivity, wide electrochemical window, and ability to solvate compounds of widely varying polarity have seen their increased use in organic synthesis,[11,12] magnetism,[13] physical and analytical chemistry,[14–16] and, most prevalently, catalysis.[17–20]

In 2013 Okuhata *et al.* published the first and so far only example of a SCO IL,[21] utilising a terdentate equatorial $N_2O_2^{2-}$ donor set around iron(III) with exogenous axial *n*-butylimidazole ligands. However the complex gradually decomposes by desorption of the axial ligands and hence is not suitable for further processing. Here we present a route to synthesising stable SCO complexes with RTIL characteristics. This is achieved by the covalent addition of bulky asymmetric cationic groups to two different types of hexadentate Schiff base ligands, R-Sal$_2$222 which facilitates SCO in Fe(III),[22–27] and R-Sal$_2$323, known to promote SCO in Mn(III),[28–34] Fig. 1.

The parent ligands were modified by appending *N*-butyl imidazolium groups to the salicylaldehyde ligand precursor. This was achieved by reaction of *N*-butyl imidazole with 5-(methylchloro)salicylaldehyde,[35] to yield compound (**1**), Scheme 1.

The *N*-butylimidazolium functionalised salicylaldehyde, (**1**), was then reacted with triethylenetetramine (222) or *N*,*N*′-bis(3-aminopropyl)ethylenediamine (323), to form the Schiff base and the appropriate metal chloride was added directly to the solution. Anion metathesis was effected by addition of sodium dicyanamide to form complexes [Fe(L1)][$(CN)_2N)_3$·3H_2O (**2**) and [Mn(L2)][$(CN)_2N)_3$, (**3**) as clean viscous liquids in good

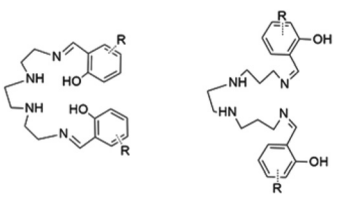

H_2R-Sal$_2$222 H_2R-Sal$_2$323

Fig. 1 Schiff base ligands known to promote SCO in Fe(III), (H_2R-Sal$_2$222) and Mn(III), (H_2R-Sal$_2$323).

School of Chemistry, Belfield, Dublin 4, Ireland. E-mail: grace.morgan@ucd.ie

†Electronic supplementary information (ESI) available. See DOI: 10.1039/c5dt04264j

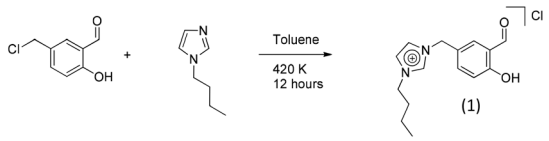

Scheme 1 Synthesis of substituted salicylaldehyde, (**1**).

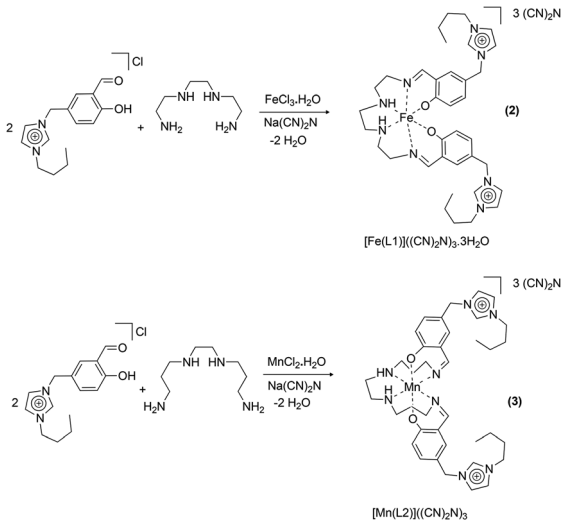

Scheme 2 Synthesis of complexes (**2**) and (**3**).

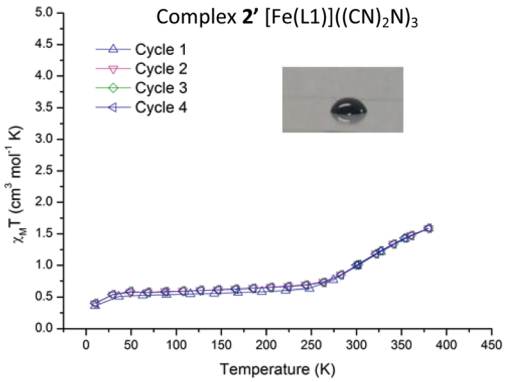

Fig. 2 $\chi_M T$ *vs.* T plot for **2′**. Inset: one drop of **2** at RT.

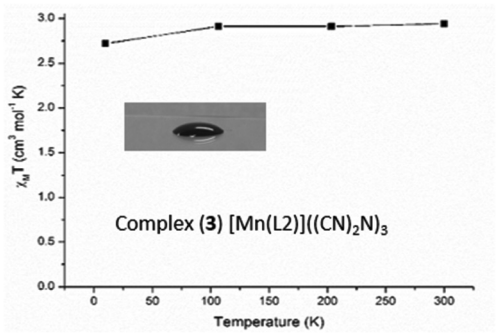

Fig. 3 $\chi_M T$ *vs.* T plot for [Mn(L2)](($CN)_2N)_3$, (**3**). Inset: one drop of (**3**) at RT.

yield (Scheme 2). As both (**2**) and (**3**) are liquids at room temperature it was not possible to obtain the glass transition temperatures on our current experimental setup but these will reported separately as our low temperature studies develop.

The hydrated complex (**2**), [Fe(L1)](($CN)_2N)_3·3H_2O$, and its dehydrated analogue (**2′**) [Fe(L1)](($CN)_2N)_3$ both exhibit a gradual and incomplete SCO between 10–380 K, shown for four cycles of heating and cooling at 5 K min^{-1} for (**2′**) in Fig. 2. The initial scan on [Fe(L1)](($CN)_2N)_3·3H_2O$, (**2**), resulted in loss of water and a change in molar mass but no difference in the magnetic profile, (see Fig. S1 in the ESI†) or physical state, *i.e.* the liquid character is retained and the spin switching is impervious to solvation in contrast to what is normally observed in solid state SCO.[36–38]

The moment of *circa* 0.5 cm^3 mol^{-1} K between 10–250 K, is as expected for S = 1/2, *i.e.* low spin Fe(III).[22] Above 250 K the moment starts to rise indicating onset of a switch to S = 5/2 ($\chi_M T$ = 4.38 cm^3 mol^{-1} K) reaching a value of $\chi_M T$ = 1.58 cm^3 mol^{-1} K (36% HS) at the maximum recorded temperature. The liquid did not display an obvious colour change over this temperature range but electronic absorption spectra collected in methanol solution between 278–323 K showed a decrease in intensity on warming, Fig. S3.†

Complex (**3**), [Mn(L2)](($CN)_2N)_3$, is also a RTIL, however no SCO is observable between 300–10 K, Fig. 3. The $\chi_M T$ value between 100–300 K is close to 3 cm^3 mol^{-1} K, *i.e.* high spin Mn(III), S = 2.[29,32] The slight decrease in the $\chi_M T$ value at low temperatures is attributed to zero-field splitting.

A recent experimental study on the structural fatigability of crystalline SCO complex by Guionneau *et al.*[39] showed that after numerous thermal SCO cycles (HS → LS→ HS) the mosaicity of the crystal significantly increases. The mosaic model describes a crystal as an ordered domain in an array of slightly misaligned tiles. Even after one cycle the mosaicity increases and the increase continues after every cycle until at 20 cycles there is a plateau. This highlights the potential structural instability of crystalline SCO complexes for use in applications, although in this case the magnetic properties were not affected. However the complex used in Guionneau's study only exhibits a gradual SCO which shows very low cooperativity. Structural fatigability, is expected to have greater consequences for hysteretic transitions that are dependent on solid state interactions to improve cooperativity. Here a route which overcomes structural fatigability has been employed whereby the spin active centres are present in liquid form rather than as components in a crystalline lattice. Work is ongoing to introduce design features which may promote more abrupt spin state switching in such media.

In conclusion, a novel route to the synthesis of robust and chemically stable magnetically switchable room temperature ionic liquids, is reported here. The addition of large cationic groups to the SCO promoting ligands was successfully used to confer liquid characteristics on the resulting complexes with

room temperature spin state switching observed in one example. The potential tunability of this system is great as many known SCO families comprise ionic salts and we have shown here that through relatively facile transformations liquid character can be conferred with very little change to the immediate coordination sphere of the metal ion. This method of depressing the melting point of solid complexes to become intrinsic liquids by ligand design has a wide array of applications from catalysis to materials chemistry.

Experimental section

Synthesis of (1)

Under a nitrogen atmosphere, 5-chloromethyl-2-hydroxybenzaldehyde (4.824 g, 28.3 mmol) was added to 1-butylimidazole (4.46 mL, 33.9 mmol) in toluene (30 mL). The resulting yellow solution was stirred for 24 hours before washing with deionised water, drying with Na_2SO_4, and removing the solvent using rotary evaporation to yield a yellow viscous liquid in 83% yield. ^{1}H: δ_H (300 MHz; $CDCl_3$) 0.9 (t, 3H), 1.3 (m, 2H), 1.8 (m 2H), 4.2 (t, 2H), 5.7 (s, 2H), 6.9–7.5 (m 3H), 10.0 (s, 1H).

Synthesis of (2)

Ligand (**1**), (1 mmol, 0.294 g) was dissolved in CH_2Cl_2/MeOH (25 mL/5 mL) before triethylenetetramine (0.07 mL, 0.5 mmol) was added and stirred for 10 minutes at room temperature. The formation of the Schiff-base ligand was indicated by the yellow solution that formed. $FeCl_3{\cdot}6H_2O$ (0.135 g, 0.5 mmol) was then added which led to formation of the complex as indicated by the colour change from yellow to brown/black. Anion exchange was performed using sodium dicyanamide (0.178 g, 2 mmol) and the solution was stirred for 30 minutes at room temperature. The resulting solution was filtered and placed into a round-bottom flask and the solvent was removed by rotary evaporation. The dark liquid that remained was extracted using CH_2Cl_2 before being dried over sodium sulfate and filtered. Removal of the solvent afforded complex (**2**) as a dark brown/red coloured liquid. Yield = 70%, Elemental Analysis: Calc. for $[Fe(L1)][(CN)_2N)_3]{\cdot}3H_2O$, $C_{42}H_{50}FeN_{17}O_2{\cdot}3H_2O$, Theory: C, 55.02; H, 5.94; N, 25.97, Found: C, 54.99; H, 5.84; N, 25.83.

Synthesis of (3)

Ligand (**1**), (1 mmol, 0.294 g) was dissolved in CH_2Cl_2/MeOH (25 mL/5 mL) before *N*,*N*′-bis(aminopropyl)ethanediamine (0.09 mL, 0.5 mmol) was added and stirred for 10 minutes at room temperature. The formation of the Schiff-base ligand was indicated by the yellow solution that formed. $MnCl_2{\cdot}4H_2O$ (0.099 g, 0.5 mmol) was then added which led to formation of the complex as indicated by the colour change from yellow to brown. Anion exchange was performed using sodium dicyanamide (0.178 g, 2 mmol) and the solution was stirred for 30 minutes at room temperature. The resulting solution was filtered and placed into a round-bottom flask and the solvent was removed by rotary evaporation. The liquid that remained was extracted using CH_2Cl_2 before being dried over sodium sulfate and filtered. Removal of the solvent afforded complex (**3**) as a dark brown coloured liquid. Yield = 64%, Elemental Analysis: Calc. for $[Mn(L2)][(CN)_2N)_3]$, $C_{44}H_{54}$-$MnN_{17}O_2$, Theory: C, 54.88; H, 6.38; N, 24.73, Found: C, 54.57; H, 6.40; N, 24.68.

We thank the following for their generous support: Science Foundation Ireland for Investigator Project Award 12/IP/1703 (G. G. M), the EU-COST action on spin state reactivity (CM1305) (G. G. M.), the National University of Ireland and the Cultural Service of the French Embassy in Ireland for scholarships (A. J. F) and the Irish Higher Education Authority for funding a SQUID magnetometer. We thank Dr James Sullivan at the UCD School of Chemistry for the use of TGA facilities. All authors acknowledge the generous support of University College Dublin.

Notes and references

1 (*a*) M. A. Halcrow, *Spin-crossover materials: properties and applications*, John Wiley & Sons, 2013; (*b*) P. Gütlich, A. B. Gaspar and Y. Garcia, *Beilstein J. Org. Chem.*, 2013, **9**, 342–391.
2 P. Guionneau, *Dalton Trans.*, 2014, **43**, 382–393.
3 P. Grondin, O. Roubeau, M. Castro, H. Saadaoui, A. Colin and R. Clérac, *Langmuir*, 2010, **26**, 5184–5195.
4 C. Gandolfi, N. Miyashita, D. G. Kurth, P. N. Martinho, G. G. Morgan and M. Albrecht, *Dalton Trans.*, 2010, **39**, 4508–4516.
5 A. B. Gaspar, M. Seredyuk and P. Gütlich, *Coord. Chem. Rev.*, 2009, **253**, 2399–2413.
6 O. Roubeau, A. Colin, V. Schmitt and R. Clérac, *Angew. Chem., Int. Ed.*, 2004, **43**, 3283–3286.
7 O. Roubeau, B. Agricole, R. Clérac and S. Ravaine, *J. Phys. Chem. B*, 2004, **108**, 15110–15116.
8 Y. Galyametdinov, V. Ksenofontov, A. Prosvirin, I. Ovchinnikov, G. Ivanova, P. Gütlich and W. Haase, *Angew. Chem., Int. Ed.*, 2001, **40**, 4269–4271.
9 H. Soyer, E. Dupart, C. J. Gómez-García, C. Mingotaud and P. Delhaès, *Adv. Mater.*, 1999, **11**, 382–384.
10 H. Soyer, C. Mingotaud, M.-L. Boillot and P. Delhaes, *Thin Solid Films*, 1998, **327–329**, 435–438.
11 O. Green, S. Grubjesic, S. Lee and M. A. Firestone, *Polym. Rev.*, 2009, **49**, 339–360.
12 K. C. Lethesh, K. Van Hecke, L. Van Meervelt, P. Nockemann, B. Kirchner, S. Zahn, T. N. Parac-Vogt, W. Dehaen and K. Binnemans, *J. Phys. Chem. B*, 2011, **115**, 8424–8438.
13 Y. Funasako, T. Mochida, T. Inagaki, T. Sakurai, H. Ohta, K. Furukawa and T. Nakamura, *Chem. Commun.*, 2011, **47**, 4475–4477.
14 F. Endres and S. Zein El Abedin, *Phys. Chem. Chem. Phys.*, 2006, **8**, 2101–2116.
15 M. Koel, *Crit. Rev. Anal. Chem.*, 2005, **35**, 177–192.

16 M.-D. Bermudez, A.-E. Jimenez, J. Sanes and F.-J. Carrion, *Molecules*, 2009, **14**, 2888–2908.
17 J. Dupont, R. F. de Souza and P. A. Suarez, *Chem. Rev.*, 2002, **102**, 3667–3692.
18 M. J. Earle and K. R. Seddon, *Pure Appl. Chem.*, 2000, **72**, 1391–1398.
19 T. Welton, *Coord. Chem. Rev.*, 2004, **248**, 2459–2477.
20 A. J. Carmichael, M. J. Earle, J. D. Holbrey, P. B. McCormac and K. R. Seddon, *Org. Lett.*, 1999, **1**, 997–1000.
21 M. Okuhata, Y. Funasako, K. Takahashi and T. Mochida, *Chem. Commun.*, 2013, **49**, 7662–7664.
22 M. F. Tweedle and L. J. Wilson, *J. Am. Chem. Soc.*, 1976, **98**, 4824–4834.
23 P. N. Martinho, Y. Ortin, B. Gildea, C. Gandolfi, G. McKerr, B. O'Hagan, M. Albrecht and G. G. Morgan, *Dalton Trans.*, 2012, **41**, 7461–7463.
24 P. N. Martinho, C. J. Harding, H. Müller-Bunz, M. Albrecht and G. G. Morgan, *Eur. J. Inorg. Chem.*, 2010, 675–679.
25 C. Gandolfi, C. Moitzi, P. Schurtenberger, G. G. Morgan and M. Albrecht, *J. Am. Chem. Soc.*, 2008, **130**, 14434–14435.
26 R. Pritchard, S. A. Barrett, C. A. Kilner and M. A. Halcrow, *Dalton Trans.*, 2008, 3159–3168.
27 I. Nemec, R. Herchel, I. Salitros, Z. Travnicek, J. Moncol, H. Fuess, M. Ruben and W. Linert, *CrystEngComm*, 2012, **14**, 7015–7024.
28 G. G. Morgan, K. D. Murnaghan, H. Müller-Bunz, V. McKee and C. J. Harding, *Angew. Chem., Int. Ed.*, 2006, **45**, 7192–7195.
29 P. N. Martinho, B. Gildea, M. M. Harris, T. Lemma, A. D. Naik, H. Müller-Bunz, T. E. Keyes, Y. Garcia and G. G. Morgan, *Angew. Chem., Int. Ed.*, 2012, **51**, 12597–12601.
30 B. Gildea, L. C. Gavin, C. A. Murray, H. Müller-Bunz, C. J. Harding and G. G. Morgan, *Supramol. Chem.*, 2012, **24**, 641–653.
31 K. Pandurangan, B. Gildea, C. Murray, C. J. Harding, H. Müller-Bunz and G. G. Morgan, *Chem. – Eur. J.*, 2012, **18**, 2021–2029.
32 B. Gildea, M. M. Harris, L. C. Gavin, C. A. Murray, Y. Ortin, H. Müller-Bunz, C. J. Harding, Y. Lan, A. K. Powell and G. G. Morgan, *Inorg. Chem.*, 2014, **53**, 6022–6033.
33 S. Wang, M. Ferbinteanu, C. Marinescu, A. Dobrinescu, Q. D. Ling and W. Huang, *Inorg. Chem.*, 2010, **49**, 9839–9851.
34 S. Wang, Y.-H. Li and W. Huang, *Eur. J. Inorg. Chem.*, 2015, **2015**, 2237–2244.
35 S. T. Chew, K. M. Lo, S. K. Lee, M. P. Heng, W. Y. Teoh, K. S. Sim and K. W. Tan, *Eur. J. Med. Chem.*, 2014, **76**, 397–407.
36 S. Hayami, Z.-z. Gu, H. Yoshiki, A. Fujishima and O. Sato, *J. Am. Chem. Soc.*, 2001, **123**, 11644–11650.
37 D. J. Harding, D. Sertphon, P. Harding, K. S. Murray, B. Moubaraki, J. D. Cashion and H. Adams, *Chem. – Eur. J.*, 2013, **19**, 1082–1090.
38 I. Nemec, R. Herchel and Z. Travnicek, *Dalton Trans.*, 2015, **44**, 4474–4484.
39 P. Guionneau, S. Lakhloufi, M.-H. Lemée-Cailleau, G. Chastanet, P. Rosa, C. Mauriac and J.-F. Létard, *Chem. Phys. Lett.*, 2012, **542**, 52–55.

Chemistry Education Research and Practice

PAPER

View Article Online
View Journal | View Issue

Cite this: *Chem. Educ. Res. Pract.*, 2017, **18**, 403

Developing laboratory skills by incorporating peer-review and digital badges

Michael K. Seery,* Hendra Y. Agustian, Euan D. Doidge, Maciej M. Kucharski, Helen M. O'Connor and Amy Price

Laboratory work is at the core of any chemistry curriculum but literature on the assessment of laboratory skills is scant. In this study we report the use of a peer-observation protocol underpinned by exemplar videos. Students are required to watch exemplar videos for three techniques (titrations, distillations, preparation of standard solutions) in advance of their practical session, and demonstrate the technique to their peer, while being reviewed. For two of the techniques (titrations and distillations), the demonstration was videoed on a mobile phone, which provide evidence that the student has successfully completed the technique. In order to develop digital literacy skills, students are required to upload their videos to a video sharing site for instructor review. The activity facilitated the issuing of digital badges to students who had successfully demonstrated competency. Students' rating of their knowledge, experience, and confidence of a range of aspects associated with each technique significantly increased as a result of the activity. This work, along with student responses to questions, video access, and observations from implementation are reported in order to demonstrate a novel and useful way to incorporate peer-assessment of laboratory skills into a laboratory programme, as well as the use of digital badges as a means of incorporating and documenting transferable skills on the basis of student generated evidence.

Received 4th January 2017,
Accepted 24th January 2017

DOI: 10.1039/c7rp00003k

rsc.li/cerp

Introduction

Purpose of laboratory work

The first teaching laboratory in chemistry in Britain was established at the University of Edinburgh in 1807, although the notion of associating practical work with a chemistry curriculum dates back further. William Cullen, who held the first independent chemistry lectureship in Britain and Ireland, and was from 1756 Professor of Chemistry at Edinburgh, made laboratories available to his students, so that they might explore some of the concepts he discussed in his lectures (Anderson, 1978).

Since then, practical work has grown to become a core component of the chemistry curriculum (Kirschner and Meester, 1988; Hofstein and Lunetta, 2004; Reid and Shah, 2007). Chemistry courses accredited by the Royal Society of Chemistry list as one of their requirements that "students must develop a range of practical skills" and chemistry courses at Bachelor level need to demonstrate that at least 300 hours are assigned to practical work, excluding undergraduate research (RSC, 2015). In the US, work over the last decade has gauged what chemistry faculty consider goals of practical work in chemistry (Bruck *et al.*, 2010; Bruck and Towns, 2013). These include engaging in the scientific process, developing critical thinking skills, communication skills, and mastery of laboratory techniques and skills. There is therefore a general sense that practical work is important, and that there is a value placed on the "hands-on" skills students achieve in the laboratory.

While the value of practical work is considered paramount by professional societies and faculty, there have long been calls for reform in teaching laboratories both at school and university level (Hofstein and Lunetta, 2004; Reid and Shah, 2007). Some of this has been in response to the challenge of whether practical work should be carried out at all, given its cost and time requirement (Hawkes, 2004). Recently, interesting work on the student perception of practical work has emerged. This highlighted that students in earlier years are more likely to be driven by affective aspects of work, such as finishing the practical quickly (DeKorver and Towns, 2015). Outcomes of a study involving students in upper-level undergraduate laboratories included the finding that there was substantial misalignment with faculty goals and student goals of practical work, and also emphasised the desire students at this level had to complete the practical work as quickly as possible (DeKorver and Towns, 2016). This is likely a reflection of one continuing and central failure of much of the laboratory work in chemistry curricula: that the laboratory work is not itself assessed.

EaStCHEM School of Chemistry, University of Edinburgh, Joseph Black Building, Edinburgh, UK. E-mail: michael.seery@ed.ac.uk

Assessment of laboratory work

Despite the value placed on laboratory work by faculty and professional bodies, there are few reports on the direct assessment of laboratory work or on demonstration of competencies and skills. Assessment tends to focus on the laboratory report or on some outcome of the laboratory work, such as yield or product purity (Graham *et al.*, 2008). Some recent reports directly describing the assessment of practical skills are described below.

The development of a rubric to assess undergraduate organic chemistry laboratory activities has been described (Chen *et al.*, 2013). Acknowledging the fact that many large institutions rely on demonstrators (also called graduate teaching assistants) to assess student work, their rubric aimed to provide a systematic method to assess the tasks students needed to complete in several organic syntheses reactions. Their rubric considered particular skills required (*e.g.* refluxing), and identified sub-skills that students needed to demonstrate to achieve these skills (*e.g.* use of clamp, use of condenser). These sub-skills aligned with benchmark statements so that markers could determine whether the sub-skill requirements were fully or partially met, or neglected.

In the context of laboratory skills, there is an argument that there is a gap between what graduates leave university education with and what industrial employers report that they need (Kirton *et al.*, 2014). These authors argue that measurement of academic competence (as reported by examination grades) does not necessarily indicate students have high proficiency in laboratory work. They describe their adaptation of the objective structural clinical examination approach used in healthcare education, to develop what they term structured chemistry examinations. These consisted of a laboratory session dedicated to students demonstrating their competencies in six areas, two of which included core laboratory practical skills. These were assessed according to a scoring sheet, which checked that students could complete the practical and quantitative aspects of various practical tasks (*e.g.* weighing using an analytical balance).

The use of video recordings for assessment of students completing a pipetting task (Towns *et al.*, 2015) and, more recently, a burette task (Hensiek *et al.*, 2016) has been described. Students are required to submit their video for assessment to their virtual learning environment, where they are graded according to a range of criteria (*e.g.* bringing the meniscus to the line in the pipette) using a rubric aligned with the instructions students were given. As well as feedback on their videos, students who successfully demonstrated the technique were also awarded a digital badge.

The work outlined above has informed the design of activities used in the approach described in this work. It is worth mentioning here that other authors that have described the assessment of practical work include the assessment of practical work in high school settings using several stations, (Rhodes, 2010) and a practical exam where students must have competencies to complete the tasks required (Neeland, 2007). However, the direct observation of practical skills for the purpose of assessment appears to be limited to very few reports. In her report, Towns writes that the assessment of hands-on practical work needs more research.

The approaches for assessing laboratory skills described above illustrate interesting and innovative ways to allow students demonstrate their competencies and skills under valid testing conditions. Although they take different forms, three components are common: (1) the clear description of what is expected of students; (2) an alignment of assessment processes with these expectations; and (3) a means to authenticate and validate the assessment of the activity. In our work in designing assessment of laboratory skills, it was evident that these components needed to be part of the design framework.

Formative assessment

Most assessment at university level comes after the corresponding teaching event. Students are assessed on their lecture content after lectures by examinations, and typically on their laboratory work by means of a laboratory report after they have completed the work. The methods described for assessment of laboratory skills above were also summative; students are given feedback after the event. Hendry challenges the notion of ''loading up'' feedback; that is feedback that is stored up and provided to students after their work has been completed (Hendry, 2013). This approach typically gives students information on how they might do the task better, and highlight any errors made. An issue with this mode of feedback is that its relevance is lost to students; the task it refers to is complete and there is no mechanism for students to demonstrate that they have engaged with this feedback or to demonstrate that they can recomplete the task with the feedback in mind.

Hendry argues for the use of exemplars – examples of work or activities of a particular quality – so that students have a much clearer sense of what is required of them in advance of the task, rather than relying for feedback after the event. This is also described as scaffolding, which provides an overall structure for students, presented so that they can develop their own work alongside it, and at points where they are unsure, use the scaffold to push beyond their zone of proximal development, as described by Vygotsky in his theory on social constructivism. The literature on exemplars does not intend to dismiss *post hoc* feedback; rather it argues that educators should provide a scaffold (in the form of an exemplar) for students before they complete their task, allow them to complete it, and then provide feedback on their work, again using the scaffold as a basis.

A connected concept is that of formative assessment, involving the use of activities enabling learners to bridge the gap between their current level of understanding or competence and the desired level. One aspect of formative assessment, is the engagement of students in self-evaluation (Black and Wiliam, 2006). Of course this connection between formative assessment and feedback was outlined by Sadler (emphasis added):

''A key premise is that for students to be able to improve, they must develop the capacity to *monitor the quality of their own*

work during actual production. This in turn requires that students possess *an appreciation of what high quality work is*, that they *have the evaluative skill necessary for them to compare* with some objectivity the quality of what they are producing in relation to the higher standard, *and that they develop a store of tactics or moves* which can be drawn upon to modify their own work.'' (Sadler, 1989)

Connecting Sadler's concepts to the previous discussion, it is clear that exemplars offer students an opportunity to ''possess an appreciation of what high quality work is''. Thus in designing a laboratory skills assessment protocol within Sadler's framework, it is necessary to, along with the provision of exemplars, enable students ''monitor the quality of their own work during production'', ''have the evaluative skills'' so that they may compare to the exemplars, and ''develop. . .tactics'' to modify their work.

Four reasons to incorporate self- and peer-assessment are suggested (Sadler and Good, 2006). It offers a *logistical* advantage in providing a large group of students with feedback more quickly and in more detail. There is a *pedagogical* benefit in considering another student's work, which can prompt an opportunity to change ideas or further develop skills. It develops *metacognitive* skills beyond the subject specific content by using higher order thinking skills to offer judgement and prompt self-evaluation (Zoller *et al.*, 1997) Finally, there is an *affective* component, as the process of peer evaluation can prompt a more productive, friendlier and cooperative learning environment, by encouraging a shared ownership of the learning process (Weaver II and Cotrell, 1986).

Pre-laboratory work

The discussion of exemplars, above, can be related to the work on pre-laboratory activities, which is extensive in chemistry education literature. Pre-laboratory videos and simulations have been described as a means of preparing students for laboratory work by reducing the cognitive load in laboratory time (Winberg and Berg, 2007; Jolley *et al.*, 2016). Recent work published in this journal suggested that pre-laboratory activities on their own did not have a significant change on student perceptions of laboratory work, but when this preparatory work was explicitly acted on in the laboratory, students negative feelings towards laboratory work decreased (Spagnoli *et al.*, 2017).

This literature on pre-laboratory work guides the approach in this study. Exemplar work, in this case in the form of pre-laboratory demonstrations, may have some value, but this value can be enhanced by explicitly relating to it in laboratory time. In the framework devised here, there is of course a clear and obvious link between pre-laboratory and in-laboratory work, due to the nature of the activity (technique demonstrations). This point is highlighted as it attempts to align the general literature on exemplars with that on pre-laboratory work.

Digital badges

One way of acknowledging student competence in particular skills is to issue them with a digital badge. Digital badges are of increasing interest in education as a means of ''micro-accreditation''; issuing an institutional acknowledgement for coursework where the student has displayed evidence for stated achievements. Students may display these badges on their own social media or personal profiles, websites, *etc.* (Casilli and Hickey, 2016). There are a growing number of examples of the practice of issuing digital badges with positive findings, including recent work in English education (Yang *et al.*, 2015), medical education (Mehta *et al.*, 2013), and secondary STEM education (Elkordy, 2016).

An advantage of digital badging is that they can give enhanced visibility to the many formal and informal learning scenarios students engage with during the course of their studies, but which may not be immediately obvious to someone reading a degree transcript.

Digital badges are often proposed as a means of motivating students. By linking with concepts popular in computer gaming, or on some review websites that wish to reward contributors of different levels, advocates argue that the desire to achieve badges and build up on a collection is a useful extrinsic motivator. However critics of the approach argue that it is essentially a behaviourist approach to reward learning, shifting the focus to the goal rather than to the learning activities themselves (Elkordy, 2016). In response to this criticism, Elkordy cites Goldberg, who has argued that badges will have benefit when they are incorporated into a context that socially supports them, and where users understand their purpose and significance (Goldberg, 2012). Indeed, results from a study in a high school STEM context suggests that use of badges was motivating both in terms of the learning goal, and also in task performance.

The use of digital badges in university chemistry laboratory education has been presented by Towns *et al.*, whose work was described above. In this case, as well as assessment of the completion a laboratory technique (pipetting, use of burette), the videos submitted by students of their completion of the technique was used as evidence to demonstrate their competency, and subject to demonstration of competency, they were issued with a digital badge for pipetting. This work has formed the basis of the present study, with modifications to incorporate guidance from the literature on exemplars and peer review, as well as in the desire to develop students' digital literacy (discussed below).

Description of peer-assessment protocol for assessment of laboratory skills

The literature presented above underpins the framework for the design of peer assessment protocols for laboratory skills. The following describes how it was implemented for three techniques: performing titrations; explaining a distillation procedure; and making up a standard solution from solid. A dedicated laboratory session was allocated for this activity. This approach was taken over the alternative (where students

demonstrate it at some stage over their laboratory course) as it was felt that students who were least confident and had least experience may struggle to find time in the otherwise busy laboratory programme.

The peer assessment protocol for laboratory skills is described in full below, but briefly it involved the following.

(1) Before the lab: students were asked to watch exemplar videos for the techniques they will demonstrate in advance of the lab. The techniques involved were titrations (requiring students to know how to pipette correctly), setting up distillation apparatus and explaining the distillation procedure, and preparing a standard solution from solid. The exemplar videos students were asked to watch are publicly available (Doidge *et al.*, 2016; Kucharski and Seery, 2016a, 2016b, 2016c).

(2) During the lab: students demonstrated each technique to each other in the laboratory. During the demonstration, their peer used an observation sheet to check that each step was correctly completed. For two out of the three techniques (titration and distillation), students videoed their peer on a mobile phone as they were demonstrating. Students could review the peer observation sheet feedback in the laboratory, and opt to reshoot a video if they wished based on this feedback. Peers and demonstrators signed off on the form once all involved were satisfied that the technique had been successfully demonstrated.

(3) After the lab: students uploaded their video to a video sharing website (*e.g.* YouTube or an internal University sharing site) for the two techniques which they had video evidence for. Students submitted links to their videos to the virtual learning environment. After review, those videos which provided evidence that the student had demonstrated competency in the technique were issued with a digital badge in that technique (Fig. 1).

Pre lab work

Sadler highlights the need to have an appreciation of what high quality work is, and the literature on exemplars demonstrate that this is a suitable approach to provide this information. Therefore, in advance of laboratory classes, students are required to watch video demonstrations of the techniques they will be asked to perform in the laboratory class. These exemplar videos are intended to allow students see what will be required of them, in their own laboratory setting. This differs from previous reported approaches, where students viewed teaching assistant demonstrations in the laboratory. The rationale for this approach was to formalize the concept of exemplars, so that students know that there is an expectation that they should review the procedure in advance of the laboratory class. It was also evident in the preparation of exemplar videos that there were a wide range of views on what "correct technique" was, and therefore we wished to document a fully correct, literature-based, approach as a reference for all involved in the laboratory activity.

Fig. 1 Digital badges designed for titration, distillation, and standard solution techniques. In the implementation described in this work, badges for titration and distillation technique were issued.

In lab peer demonstration and review

To structure in-lab work, we were keen to align with a common theme from earlier reports of assessing laboratory work – that students have a clear description of what is expected. Therefore, we developed the Peer Observation Sheets to structure student activity in the lab (Appendix 1). These described, for each technique in turn, the steps students should take, as well as points for the peer to consider when providing feedback. These aimed to address Sadler's point about enabling students to evaluate their work by comparing to the exemplar. They also defined the points at which students should start and end videoing. Thus the Peer Observation Sheets were used to structure the overall flow of the laboratory session.

Previous work on assessment of laboratory skills defined the format of the Peer Observation Sheets; which were essentially rubrics of activities students should complete in each stage of the demonstration (Chen *et al.*, 2013). In addition, space was provided for peers to write feedback based on these rubric prompts. These were subsequently intended to act as discussion prompts during the peer review. For example, students have the option to review the video to check on a particular protocol step on the basis of peer review discussions. This aimed to allow students to address the final points highlighted by Sadler: to monitor the quality of their own work during production and to develop a capacity to modify and improve their work.

Once students had completed their demonstrations and peer review forms, these were signed off by the demonstrators and submitted for final review by the instructor. As the purpose and main learning outcome of the activity was that students demonstrated a technique to each other and reviewed their peer's techniques, the submission of three complete and signed peer review forms meant that they had successfully completed their requirements.

Post lab review of work

The third and final theme arising from previous work on assessment of laboratory skills was a means to authenticate and validate the assessment of the activity. This was achieved by reviewing student videos and providing them with feedback on issues aligning with those raised in the Peer Observation Sheets. Students uploaded their videos to a video sharing site (*e.g.* YouTube, Vimeo, university's own hosting site) and submitted the URL links to their videos (titration demonstration and distillation explanation) into an assignment area in

their virtual learning environment. Once their assignment had been viewed, students received individual feedback based on the technique displayed in their videos, and assuming the video displayed an appropriate level of competency, they were issued with a digital badge *via* the virtual learning environment, which they could push out to their own Open Badge Backpack (https://backpack.openbadges.org/). The backpack is an independent hosting site for badges, which allows learners collect and display badges from wherever they may earn them. As it is not dependent on any institution, the purpose of the backpack is that learner's can access and control their badges once they have moved on from any institution where their badges were issued (*e.g.* in this case, the university). Students also received feedback on the answers noted on their Peer Observation Sheets, in relation to the number of significant figures, and their standard solution calculations.

Combination of effects: developing transferable skills

Much of the innovation and reform regarding practical work has capitalised on the opportunities the laboratory environment offers in terms of addressing a wider set of transferable and professional skills. Outcomes of practical work have been grouped into three broad themes: practical skills, transferable skills, and intellectual skills (Carnduff and Reid, 2003). Transferable skills considered included aspects such as team working, organisation, time management, communication, presentation, information retrieval, data processing, numeracy, designing strategies, and problem solving.

We consider that the laboratory activity described herein incorporates the development of several transferable skills. In order to prepare their demonstration, students are required to watch the video and organise in advance what they are going to do. As mentioned above, the process of peer review can develop metacognitive skills beyond subject specific content.

In addition to these, this activity offers students scope to develop their information technology skills. They are required to record video and upload that video to a sharing website. An important consideration in this is managing their digital footprint; the process of submitting a link to a video hosted elsewhere rather than just the video itself means that students have to make decisions about how they wish to control access to that video. As most of the formal online interactions between educators and students occur within their virtual learning environment (VLE), there is little or no opportunity for educators to support students in developing a professional online identity outwith the VLE, and which they are responsible for managing. Indeed it is argued that there is an onus on educators to formally consider this support and development within their curricula (Ng, 2015; Seery, 2016).

Research questions

The aim of the research study is to explore some factors around assessment and learning of practical laboratory skills. In particular, we were keen to explore the following.

(1) To what extent did students watch exemplar videos prior to their laboratory session?

(2) How do students consider their own ability had changed as a result of completing the activity?

(3) What were the observations about the implementation of the lab-skills activity in practice?

Methodology

A quantitative approach is used to address these research questions. The advantages of this include that we are able to readily determine data regarding the access and use of our exemplar videos, as well as quantify changes in the pre-/post survey data described below. This data is used to give a sense of the interaction and outcomes in the circumstances observed in this particular case. The laboratory session and its associated work are an unusual format in relation to the general scheme used for the remainder of the sessions which students experience over the course of their first year laboratories. These tend to follow a more traditional format, where students answer some general pre-laboratory questions, complete the laboratory session, and prepare a worksheet or short report for assessment. However as an early session is used (the second session out of ten in the semester), it is assumed that from the student perspective, recently arrived at university, that the uniqueness of the session is not apparent at this stage. We use the pre-/post survey described below to gain a sense of how students perceive their knowledge, experience, and confidence changing as a result of the activities. Details of how this is conducted are outlined below.

Methods

Ethical approval was secured from the School's Research Committee in line with institutional guidelines. In accordance with British Education Research Association guidelines (BERA, 2011), students were informed about the research prior to completion of survey, as well as being offered the right to withdraw their contributions at any time. Students who completed the survey but opted not to have their results considered in the analysis were removed from the dataset ($n = 3$). The survey was conducted on the Bristol Online Surveys platform which is fully compliant with UK data protection laws. Data was only held on University-secured computers and was not transferred electronically by other means.

A pre-/post survey was used to examine students' perception of their knowledge, confidence, and experience in several aspects to do with each procedure, based on the approaches used in previous reports on badging activities (Towns *et al.*, 2015; Hensiek *et al.*, 2016). Full surveys are in Appendix 2. Students ranked on a Likert scale of 1–5, where 1 represented a low value (no knowledge, no experience, not confident) and 5 represented a high value (very knowledgeable, very experienced, very confident). The procedural protocol steps also mirrored the approach of developing statements to be used in the rubric

by Chen *et al.* (2013), by identifying key procedural steps to be considered in the demonstration.

For pre-/post-analysis, the averages of the totals for each technique for knowledge, confidence, and experience were compared. Analysis was conducted with SPSS and Microsoft Excel programmes. Students were also asked three questions in the survey. These questions related to each technique: students were asked: (1) to read a burette when provided with a close-up picture of liquid in a burette; (2) when they would change a flask to collect a second fraction during a distillation; and (3) to calculate a concentration having been given a mass and molar mass. The answers to these were categorised as follows. For burette readings, answers were categorised as correct if the correct reading was given, and it was given to two decimal places. It was categorised as incorrect if the reading was incorrect or if it was given to one decimal place. For distillation, the answers were categorised as correct if students correctly explained when to change the flask, otherwise it was categorised as incorrect. For standard solution concentration calculations, answers were categorised as correct if students gave the correct concentration to the correct number of significant figures. Otherwise, it was categorised as incorrect, noting whether it was an incorrect calculation or whether the number of significant figures was wrong. The aim of this categorisation is to provide an additional source of data to put the student responses by way of looking at relationships between students' knowledge, experience and confidence, and their answers to these questions.

For each pre- and post-laboratory data, descriptive statistics were presented and analysed in order to look at the central tendency, which was done with median values. At this point, the data was treated as it was. Missing values are reported but all valid responses are included. For pre-/post-analysis, the data was cleaned so that only matching pairs of responses were considered. The total responses reduced from 148 to 120. They were analysed with paired *t*-test, Cohen's *d* and effect size. This process involves the averaging of Likert responses to generate one overall pre-score and one overall post-score for each of the knowledge, experience, and confidence values for each technique, and the subsequent analysis of the differences between these scores. Averaging Likert scales is subject to some discussion in the education literature as it involves the averaging of ordinal values. In a discussion of this kind of analysis, Lalla writes that parametric tests can be used if it is assumed that the ordinal variable is an approximate measurement process, which evaluates a continuous underlying variable (Lalla, 2017). However, being aware of the criticisms of this approach, we place our pre-/post-analysis in the context of an initial exploration of the quantification of actual responses themselves, and subsequently use statistical analysis of pre-/post-scores to summarise any observed differences quantitatively. The total number of students who completed the practical session is 158.

Analysis of viewing figures and length of video viewed was obtained from YouTube analytics dashboard. The analytics dashboard allows viewership to be filtered by date range and also by geographic region (*i.e.* UK). Analytics also provide information on the viewing platform (PC, mobile, *etc.*). This information was exported from the YouTube analytics dashboard and subsequently processed in Microsoft Excel. In order to provide a combined overview of viewing of the video in the time prior to the labs, a ''weighted frequency'' was calculated from the product of the number of viewers on a particular day and the length of time the video was viewed for on that particular day.

The analytics dashboard also provides information on viewer retention over the course of a video. This information is not available to export, and hence for each video, within the date range and geographic filters considered, a screen-shot was taken of the analytics dashboard.

Results and discussion

Research Question 1: To what extent did students watch exemplar videos prior to their laboratory session?

Students completed the laboratory activity during their third week (second laboratory session) of first year at university. Because of the size of the class, laboratory sessions run in three 3 hour sessions: Tuesday mornings and afternoons, and Wednesday afternoons. Videos were made available prior to the sessions. YouTube access statistics for the three videos for the 6 days prior to the lab sessions, and the lab session days themselves are summarized in Table 1. Access before this time and after this time was negligible. Given that fact, and that the majority of views were UK only, it is assumed that essentially all views are associated with this activity. 158 students completed the laboratory activity and while it is not possible to say all students watched the videos in advance of the practical class,

Table 1 Summary of YouTube analytic data for the three exemplar videos

	Titration	Distillation	Standard solution
URL	http://bit.ly/skillstitrating	http://bit.ly/skillsdistillation	http://bit.ly/skillsstandardsoln
Video length (m:ss)	4:57	7:15	5:57
All views/UK views	269/267	300/295	264/243
Average view duration m:ss (%)	4:08	5:09	4:17
	83%	71%	72%
Viewing platform	Computer: 91%	Computer: 90%	Computer: 92%
	Mobile: 7.2%	Mobile: 8.1%	Mobile: 6.6%
	Tablet: 1.5%	Tablet: 2%	Tablet: 1.6%

the number of views (267 titration, 295 distillation, 243 standard solution) suggest that most did, with many students watching repeatedly.

An important consideration is the extent of the video that students watched. Average view times are shown, along with percentages of the entire video. For titrations, the % of video viewed averaged at 83%, for distillations, it was 71%, and for standard solutions, it was 72%.

These figures will automatically include students who re-watch a video but only a segment of it. Hence, of more interest is the retention of a student viewer over the course of a video. The YouTube analytics platform provides this information graphically, and the plots for the three videos are shown in Appendix 3. These illustrate a remarkable stability in viewing across almost the entire length of video, suggesting that students who started to watch tended to watch almost all of the video. ''Drop-offs'' were noted at the end of each video, at times 4:40, 5:40, and 5:20 for titration, distillation, and standard solution respectively. These times correspond on the videos to finishing notes about the video: confirmation of calculation, repeated statement about distillation, and the method of concentration calculation in standard solutions. The drop-off periods do not relate to the lab skills part of the video. These end of video drop-offs also distort the average viewing times, by reducing the average due to the component of the video not viewed at the end of the timeline.

Finally YouTube analytics provides information on the viewing platform. These data show that the dominant viewing platform was a personal computer, which was used over 90% of the time. The next choice was mobile phones (6–8%), followed by tablets. The % figures do not add up to 100%, probably because there were some views where the platform was not recognised.

Fig. 2 aims to represent the YouTube viewing data graphically, This compares a ''weighted frequency'' of views, accounting for the number of views and the average viewing time across all platforms for the days (−6 to −1) running up to the laboratory sessions, which are identified as days 1 and 2. Platform viewing data tended to mimic these data, although the highest use of mobile and tablet platforms were on the lab days themselves, reflecting the fact that students reviewed these videos in the laboratory session itself. This was facilitated by making short URLs available to students (as indicated in Table 1) so that they could easily call up the video if required. Access to dynamic information *in situ* has been proposed as a means of reducing in-lab cognitive load (Kolk *et al.*, 2012).

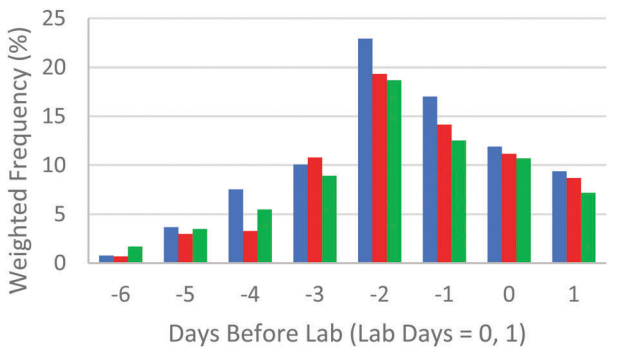

Fig. 2 Viewings of videos in advance on lab (days −6 to −1) and on lab days (day 0 = Tuesday, 1 = Wednesday) represented as weighted frequency, the product of the fraction of total views and the viewing time on a particular day. Bars from left to right represent: titration (blue), distillation (red) and standard solution (green) videos.

In addition to the three main exemplar videos, students were also referred in the titration video to review a video on how to pipette (http://bit.ly/skillsvolpipette). This link was also directly provided in their pre-laboratory links. This video showed a very similar access profile to the main laboratory videos: 219 UK views, with an average view of 3:29 of 4:15, corresponding to 82%. Interestingly, this video's retention remained uniform over the course of its length (Appendix 3), and did not show the drop-off that other videos displayed. This adds weight to the conclusion that drop-off in the other videos is probably due to the fact that they finished with a section not directly related to the actual lab skill, whereas the pipetting video finished at the end of the skill demonstration without lingering on other considerations.

The above data aims to show that in general, students completing the practical session involving demonstration of laboratory skills watch the exemplary videos in advance.

Research Question 2: How do students consider their own ability had changed as a result of completing the activity?

Students were surveyed before and after the laboratory activity in a manner similar to that described previously (Towns *et al.*, 2015; Hensiek *et al.*, 2016). These surveys asked students to rate their knowledge, confidence and experience on a 5-point Likert scale, prior to and after the laboratory session (Appendix 2). The pre-test survey highlighted some interesting observations. In general students reported the highest previous knowledge, confidence, and experience of standard solutions, followed by titrations, with the lowest scores for distillations. For example, the median value for knowledge of ''weighing out a solid onto a balance'' was 5 in the pre-lab survey. In contrast, the median value for experience of ''correctly greasing glassware'' in distillation was 1.

Self-rating of knowledge, confidence, and experience

We analyse the pre-/post-survey data in two ways. Firstly, we counted the number of responses in each point on the scale in each category before and after the lab. The change in the number of responses allows us to consider the changing levels of student perception on their levels of knowledge, confidence, and experience. The data summarised graphically in Fig. 3. In all cases, we see a decrease in the number of responses in the lower numbered Likert categories, with an increase in the number of responses in the higher number Likert points, especially point 5. This is reflecting a growth in the number of students choosing 5 in responses to the survey questions after the laboratory, indicating that they consider their levels of

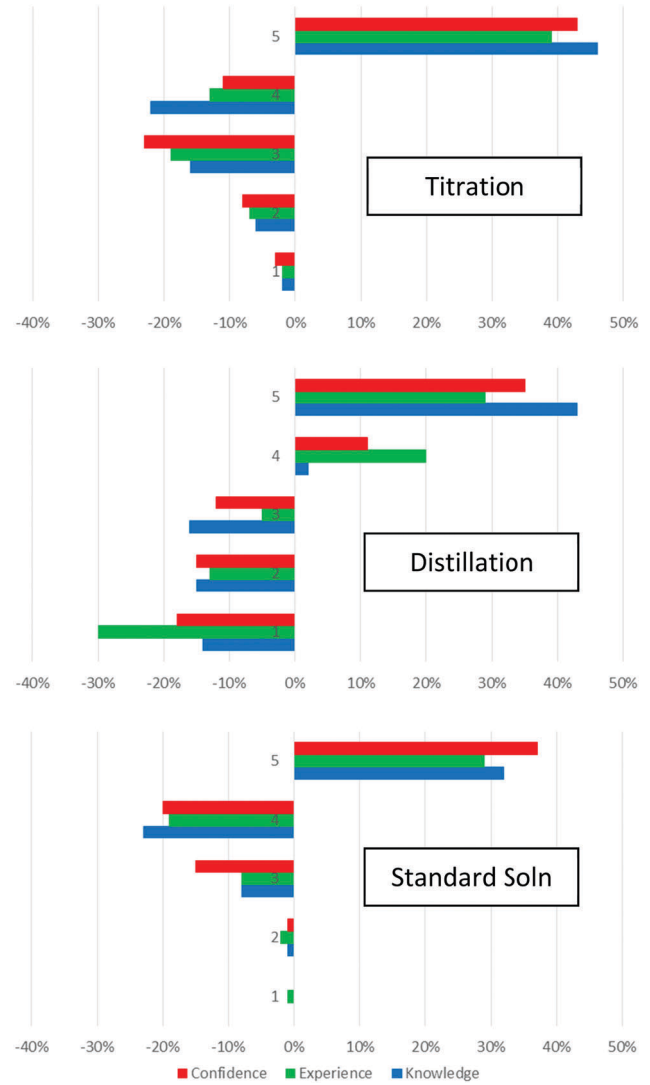

Fig. 3 % change in number of responses to survey for all answers in titrations (top), distillations (middle) and standard solutions (bottom). Percentage changes in responses for knowledge (blue bottom bar), experience (green middle bar), and confidence (red top bar) are shown.

knowledge, confidence, and experience to have increased (Fig. 3). The increase in number of students selecting choice "5" was observed across all three experiments: titration, distillation, and standard solutions. By monitoring the consequent decrease in the other scales, we can obtain a sense of the shift in changing perceptions of self-evaluated knowledge, confidence, and experience.

In the case of titrations, students' high ratings prior the laboratory increased further, and the changes show a decrease in the number of responses rated "3" and "4", and an increase in the number of responses rated "5". The most substantial changes were observed for distillations; students rated their experience much lower than their knowledge prior to the lab, reflecting that many of them would have learned about distillation in school but not performed one, due to the cost of the distillation apparatus. Therefore large changes are observed across all three categories, but student experience sees the largest shift; the largest decrease is in the number of responses rated "1". The pre-lab ratings for standard solutions were the highest, reflecting that students have likely learned about and completed many standard solution preparations in their school work. Thus the largest shift here is ratings of "4", with the subsequent increase in ratings of "5".

As well as counting directly the number of responses, it is possible to conduct a pre-/post statistical test to ascertain whether there is any significant difference in the means of the responses before and after the laboratory activity. A sum of the pre-lab means and post-lab means for each of the series of statements for the three techniques are shown. As there are 6 statements for titrations, 7 for distillation, and 4 for standard solutions, the maximum possible score for these techniques is 30, 35, and 20 respectively. After the data was cleaned as described in the Methods section, a paired t-test was conducted on matching pairs before and after the laboratory activity. This data is shown in Table 2. In all cases, there is a significant difference ($p < 0.001$) between the pre- and post-mean scores for each knowledge, experience, and confidence scale. By calculating the Cohen's d value, these differences were all calculated to have a large or very large effect size (Sawilowsky, 2009), with the exception of "experience" of standard solutions. Although the median values of distillation were among the lowest in the pre-laboratory group, the effect size of the increase was the highest compared to that of the other techniques.

Pre- and post-laboratory questions

As well as self-rated perceptions, students were also asked a question in the pre- and post laboratory surveys relating to the laboratory skill. For titrations, students were shown a picture of a burette and asked to note the reading (required to two decimal places); for distillations students were asked to explain when they would change a flask to collect a second fraction, and for standard solutions, students were asked to calculate a solution concentration given a particular mass. The numbers

Table 2 Accumulated mean pre- and post-laboratory activity scores for students rating of their knowledge, experience, and confidence in titrations (6 sub-scales), distillation (7 sub-scales) and preparing standard solutions (4 sub-scales)

Technique	Pre-lab mean	Post-lab mean	Cohen's d (effect size)
Titration (30)			
Knowledge	23.44	28.18	1.41 (v. large)
Experience	22.03	26.88	1.08 (large)
Confidence	22.25	27.51	1.27 (v. large)
Distillation (35)			
Knowledge	21.61	30.85	1.55 (v. large)
Experience	16.09	26.32	1.48 (v. large)
Confidence	19.99	29.03	1.32 (v. large)
Standard solution (20)			
Knowledge	17.39	19.08	0.82 (large)
Experience	16.47	18.17	0.56 (medium)
Confidence	16.00	18.57	0.80 (large)

Table 3 Categorisation of responses to a question for each of the techniques pre- and post-laboratory work

Question	Pre-lab	Post lab
Burette reading	Correct: 34% Incorrect: 1 Decimal: 48% Reading: 18%	Correct: 66% Incorrect: 1 Decimal: 23% Reading: 10%
Distillation procedure	Correct: 43% Incorrect: 43% Don't know: 14%	Correct: 75% Incorrect: 24% Don't know: 1%
Concentration calculation	Correct: 31% Incorrect: Sig. fig.: 45% Calculation: 22%	Correct: 32% Incorrect: Sig. fig.: 53% Calculation: 13%

given in the question meant that the answer should be reported to two significant figures. The post lab questions were the same, but involved a different burette reading and a different concentration calculation. Responses to these questions are shown in Table 3.

As well as total responses, it was noted that percentage of students who gave an incorrect burette reading and whose self rating average exceeded 3/5 for titrations was 13% in the pre-lab survey and 9% in the post-lab survey. The proportion who incorrectly answered the distillation question and whose self-rating average exceeded 3/5 was 15% in the pre-lab survey and 20% in the post lab survey. Finally the proportions who answered the molarity calculation incorrectly but who had a higher than 3/5 average self-rating was 21% in the pre-lab survey and 16% in the post-lab survey.

The above data aims to demonstrate, that for titrations and distillations, both students' perceptions of their laboratory competency and external measures of some aspects of these competencies, improved over the project.

The exception is with the data on standard solutions. While students' self-perceptions increased as a result of the activity, there was little change observed in the responses to the calculation question, aside from a reduction in the number of incorrect responses. The reason for this can only be speculated from the available data. This protocol differed from others; students were not required to video each other doing this activity, merely to observe each other. In practice (as indicated below) we noted that many students did not undergo peer observation as there was no explicit need – the absence of a requirement for a video meant that peers could work on their own individually if they wished.

Another reason may be that the peer observation sheet does not explicitly mention significant figures as a consideration, merely that the student should add a label to their flask ''with appropriate details.'' Therefore significant figures might not have been considered, or indeed it might have been perceived that this was not a consideration. It will be interesting to observe whether this changes in a future iteration where significant figures are explicitly mentioned.

Research Question 3: What were the observations about the implementation of the lab-skills activity in practice?

The laboratory sessions were structured around the Peer Observation Sheets (Appendix 1), with students being given space to provide feedback on their peer's video demonstration. These sheets also indicated which components of the demonstration students should record on their video.

Recording and submitting videos

There were no difficulties reported in terms of students not wishing to be videoed or not having a mobile phone to record their video. As part of the demonstrator induction, it was made clear that if students did not wish to be recorded, then they could complete the demonstration with a demonstrator present for the purpose of showing their competency and to complete the laboratory activity. In this case, the student would not receive the digital badge, as this was based on the evidence produced. However, all students in this implementation successfully recorded and submitted their two videos (titration and distillation). Students were required to upload their video to a video sharing site and submit the link to the virtual learning environment for review, within 48 hours of their laboratory session.

As mentioned above, students were not required to video the standard solution preparation. This was partly due to the fact that this involved two significant tasks: weighing out a solid correctly, and making up the solution after transferring the solid. It was felt that this may take too much time to video. The absence of a requirement to video meant that observations of students not completing the peer review, and just preparing their solutions themselves, were reported. This may explain the small change in pre-post survey question responses for this technique, but regardless, demonstrates the necessity for some evidence of peer review for this approach. A future iteration plans to separate the weighing and standard solution procedures, so that they can be videoed and afforded a digital badge.

Suggestions for sites to submit their video included YouTube, Vimeo, and the university's own video sharing site. Students opted to upload their videos in order of preference to the university's own video sharing site (58%), YouTube (40%), Vimeo (1%), and a Dropbox or similar link (1%).

The submission of links to videos rather than videos themselves to the virtual learning environment was required. The purpose of this was to develop students' digital literacy, and awareness about digital footprint. Students were informed that they should submit their video and list it publicly or have it unlisted (available to anyone with the link) as they chose. They were informed that private videos could not be viewed, but that they could make their videos private after instructor review. A surprise finding was that most students chose the university's own video site to host their videos. No data on the reason for this was collected, but anecdotally, several students commented that they saw this work as ''academic'' and therefore was better placed there instead of a site such as YouTube. Other students considered the university website more secure for their academic work. In reviewing some videos again as part of the research project after instructor review, it was noted that some students had exercised the option to change their video

settings to private. These kinds of options and choices mean that students are developing the ability to control their own digital footprint.

Feedback on performance

Students were required to complete the Peer Observation Sheets to provide feedback on their lab partner's performance. Analysis of these sheets however indicated that there was very little written feedback provided; comments such as "nicely demonstrated" or "well done" were common. In a small number of instances (~10%) some instances of feedback on technique was provided. These typically were along the lines of suggestions on how to improve, for example in a titration feedback sheet, some feedback was "add liquid more slowly near endpoint". However, this was not typical.

Students also received feedback on the aspects of the Peer Observation Sheet that they needed to complete themselves, namely the titration readings and average titre and the standard solution concentration calculation. 17% of student reports marked did not record one or more of their titration figures to two decimal places, while the remainder did. 16% of students did not complete the calculation of their standard solution correctly. By far the most common mistake was the correct number of significant figures, 59% of students did not enter in the correct number of significant figures for their standard solution calculations, in line with the responses observed for the post-lab survey quiz, also involving significant figures.

Finally, students received feedback on their videos. For titrations, this tended to focus on specific issues which may affect the accuracy of results. While not prevalent, the most common error was not washing the burette tip after each dropwise addition close to the endpoint, followed by not reading burette to two decimal places either at the start or the end of the titration. Distillation feedback was less rich; students tended to set-up and explain the distillation very well. Typical comments, when required, were regarding the correct arrangement for the condenser tubing.

Digital badges

Students' videos were reviewed, and assessed holistically to determine whether competency was displayed in the technique. In almost all cases, students were issued with a digital badge. Students were awarded five points for submitting each video, with a point deducted for issues which affected accuracy or operation. Students who received more than three points out of five were awarded with the badge automatically by the virtual learning environment. In the VLE used (Blackboard), this is managed by setting criteria: a check to see if student submitted their assignment, which would detail the video link, and a check to see if the score awarded exceeded 3/5. Once these criteria were met, students were awarded the badge (called an "achievement" in Blackboard). They had the option to "push" (publish) this badge to the open badges backpack; the independent platform for hosting badges. Because of data protection issues, the student must be offered this choice, and thus we were not able to secure data on how many students opted to publish their badge, nor indeed what role the badges had in motivating students to do well in the activity, if any. Therefore the framework proposed incorporates badging as a means to package the entire exercise, and our future work will focus on these motivational aspects, and interests in display of badges. Some hints came through anecdotal feedback from students, regarding queries about "getting the badge" during the lag time between video submission and assessment.

Limitations

In this study, the use of pre-lab exemplar videos, in-lab demonstration with videoing (for two of three techniques), and in-lab peer review was used to facilitate the learning of laboratory skills. The entire process involved the production of evidence-based competencies, which meant that it could be packaged up in the awarding of digital badges. Because of the combination of approaches, it is not clear whether one or of these approaches leads to the observed improvements in students' perceptions of their knowledge, confidence, and experience of the techniques, or if it is a combination, what the relative weighting is of those different components which are having an effect. For example, the literature on pre-laboratory activity cited above illustrates that this can have benefit in terms of reducing cognitive load in the laboratory. Little is known about the motivation aspects of digital badges. However the purpose was not to isolate each component involved but to show that the combination, which was designed in accordance with the framework proposed by Sadler, has some merit.

Another limitation in our study is that all of our participants had studied chemistry in school and likely had some practical experience. Therefore it cannot be concluded that the approach taken here is appropriate for teaching techniques *ab initio*, although the results from the distillation experiment suggest that even without prior experience in the practical technique, the framework proposed works well.

Conclusions

Peer-review of laboratory techniques incorporating peer-recorded video has enabled a useful *in situ* feedback method for students in the development of their laboratory skills. Exemplar videos provided in advance of the laboratory class provide students with information on the correct protocol. For demonstration of technique, students and their peers use a peer-observation sheet which allows the feedback to be structured and aligned with the exemplar videos. Video recording is valuable as a means of prompting this feedback and ensuring peer dialogue – a fact noted in the third technique where peer review was not required – and also acts as evidence for competency. This evidence is awarded by means of a digital badge, acknowledging students ability to complete the technique. The activity described provides a useful means of facilitating peer assessment, as well as documenting and acknowledging transferable skill development by means of digital badges.

Appendices

Appendix 1a: peer observation sheet – titrations

Lab Skills: Peer Observation Checklist
Part A: Pipetting and Titrations

Chemistry 1A

Name		Date	
Matric No		Lab Session	
Demonstrator		Group	

Instructions

Use the form below to assess your lab partner while they carry out a technique. Record the steps indicated on their phone so they can submit their video for assessment. Use the spaces to offer some helpful feedback when reviewing the technique. Submit this form to your demonstrator at the end of the lab.

	Protocol Step	☑	Lab Partner Comments / Feedback
1	**Collect the necessary glassware and ensure it is clean** *To check: washing of glassware with water and small amounts of solution. Drying off any drops.*		
2	**Pipette 10 cm^3 ~0.1 M HCl into flask** *To check: compressing of pipette bulb prior to attaching to pipette; attaching with hands close together; drawing up liquid into pipette but not into bulb; lowering to the line; releasing liquid while holding pipette vertically, touch last drop to surface of solution.*		
	Begin videoing the demonstration at this point		
3	**Adding ~0.1 M NaOH to the burette** *To check: holding funnel above burette, do not add to zero mark, removing funnel.*		
4	**Stating initial volume of liquid (camera zoom)** *To check: clear picture of initial value and stating reading to two decimal places.*		
5	**Adding indicator and beginning titration** *To check: adding 2 – 3 drops **only**, presence of white tile, adding titrant while shaking flask, noting rate of colour change.*		
6	**Adding liquid dropwise towards end point** *To check: adding dropwise, washing burette tip and sides of flask with small amounts of water, successfully reaching end-point.*		
7	**Stating final volume of liquid (camera zoom) and note on sheet** *To check: clear picture of final value and stating reading to two decimal places; stating titration volume.*		
	End videoing the demonstration at this point		

Titration	Rough	Accurate 1	Accurate 2	Accurate 3 (video)
Start Volume (cm^3)				
End Volume (cm^3)				
Amount Added (cm^3)				

Peer Reviewer Signature	
Demonstrator Signature	

Appendix 1b: peer observation sheet – distillations

Lab Skills: Peer Observation Checklist

Part B: Setting up Quickfit® distillation

Chemistry 1A

Name		Date	
Matric No		Lab Session	
Demonstrator		Group	

Instructions

Use the form below to assess your lab partner while they carry out a technique. Record the steps indicated on their phone so they can submit their video for assessment. Use the spaces to offer some helpful feedback when reviewing the technique. Submit this form to your demonstrator at the end of the lab.

	Protocol Step	☑	Lab Partner Comments / Feedback
1	**Assemble the necessary glassware and ensure it is clean** *To check: presence of round bottom flask (25 mL), still head, thermometer with adaptor, condenser, receiver adaptor and beaker, clamp.*		
	There is no need to grease joints for the demonstration, but if you wish to practice, you may.		
2	**Connect rubber tubing to water supply and condenser** *To check: sequence of connection to tap, water in (bottom of condenser), water out (top), tubing goes over the widest part of the connector.*		
3	**Assemble apparatus** *To check: flask with the connected still head in the heating mantle, condenser clamping securely but without strain, collection beaker in place, wiring to the heating mantle is in a sensible position. DO NOT PLUG IN HEATING MANTLE.*		
	Begin videoing the demonstration at this point		
4	**Introduce yourself and apparatus** *To check: explaining overall arrangement, noting position of thermometer, cables and tubing away from heat source. Turning on water and showing steady water flow. State that you would add 2 – 3 bumping granules.*		
5	**Explain the distillation process** *To check: liquid would be added via funnel (remove stillhead), heated until boiling, temperature rise noted until steady, collect fraction until temperature rises again, replace flask until temperature steadies again, replace flask. Clear statement of what each flask would contain.*		
6	**When to finish and cooling down the apparatus** *To check: statement regarding leaving some liquid in the flask to avoid explosion, waiting until liquid cools, shutting down water.*		
	End videoing the demonstration at this point		

Peer Reviewer Signature	
Demonstrator Signature	

Appendix 1c: peer observation sheet – standard solutions

Lab Skills: Peer Observation Checklist

Part C: Preparing a standard solution

Chemistry 1A

Name		Date	
Matric No		Lab Session	
Demonstrator		Group	

Instructions

Use the form below to assess your lab partner while they carry out a technique. Use the spaces to offer some helpful feedback when reviewing the technique. **This technique is not videoed.**

	Protocol Step	☑	Lab Partner Comments / Feedback
1	**Weighing out solid sodium carbonate into weigh boat** *To check: adding solid from container to beaker while on tissue, moving to balance to weigh, tidy working, final mass close to required value.*		
2	**Transferring solid to beaker** *To check: adding solid from weigh boat and washing weigh boat into beaker, aid dissolving with glass rod, washing glass rod, taking care not to exceed final desired volume.*		
3	**Transfer to volumetric flask** *To check: transfer of solution, washing of beaker and bringing final volume close to mark.*		
4	**Making up to the mark** *To check: careful addition of water dropwise using a plastic pipette, bottom of meniscus exactly on graduation line. Stoppering and inverting solution. Adding a label with appropriate details.*		
	If the liquid level goes above the meniscus, the solution should be discarded and the procedure restarted.		

Calculations

Mass of Na_2CO_3 (g)	
Concentration of solution prepared (mol dm^{-3})	

Peer Reviewer Signature	
Demonstrator Signature	

Hand in this form to your demonstrator at the end of the lab.

Appendix 2: pre-/post-survey questions

Name

Student ID

Lab group (Day/time)

You are asked in these questions to rate between 1–5 your own ability in terms of knowledge, experience and confidence in various aspects of completing techniques.

- 1 is a low value (little knowledge, no experience, not confident).
- 5 is a high value (very knowledgeable, lots of experience, very confident).
- **Your ratings do not affect your lab score in any way!**

Titrations

Rate your knowledge, experience, and confidence of the following aspects of titrations:

1. Adding liquid to burette
2. Where initial level of liquid in burette should be
3. Amount of indicator to add
4. What to do to analyte in conical flask when adding solution from burette
5. Steps to take when near end point (dropwise adding, washing)
6. Reading a burette to correct number of decimal places

A picture of a burette with some liquid is shown. What is the correct reading of this value?

Quickfit distillation

1. Identify the necessary glassware for distillation
2. Correct sequence to connect rubber tubing to condenser
3. Know how to correctly grease glassware
4. Correct assembly of apparatus including placement of clamp and thermometer.
5. Arrangement of cables and tubing in a safe manner
6. Correct method for adding liquid and required number of bumping granules
7. Protocol for collecting different fractions

In a short statement, explain how you would know when to transfer flasks after you collect your first fraction during a distillation.

Preparing a standard solution

1. Weighing out a solid onto a balance.
2. Transferring solid to beaker and solvating
3. Transferring solution to volumetric flask
4. Making up a solution to the mark in a volumetric flask

[x] g of Na_2CO_3 is weighed out and made up to 250 cm^3 of water. What concentration would you write on the label of this flask?

Appendix 3: YouTube retention plots (taken directly from YouTube analytics dashboard)

Titration video: http://bit.ly/skillstitrating

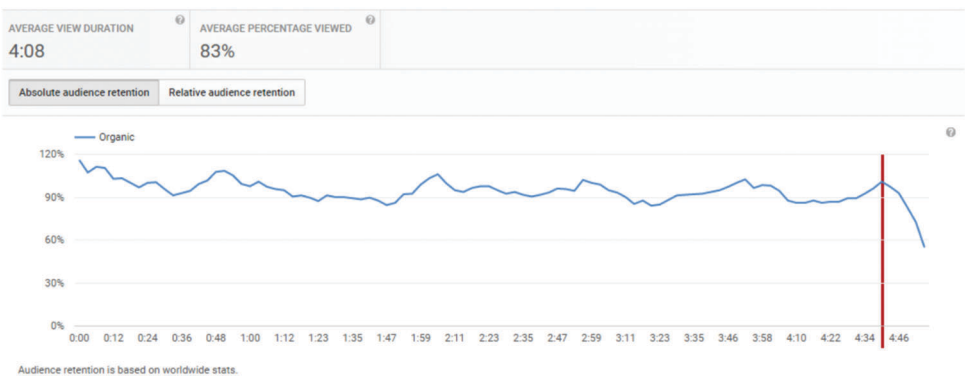

Distillation video: http://bit.ly/skillsdistillation

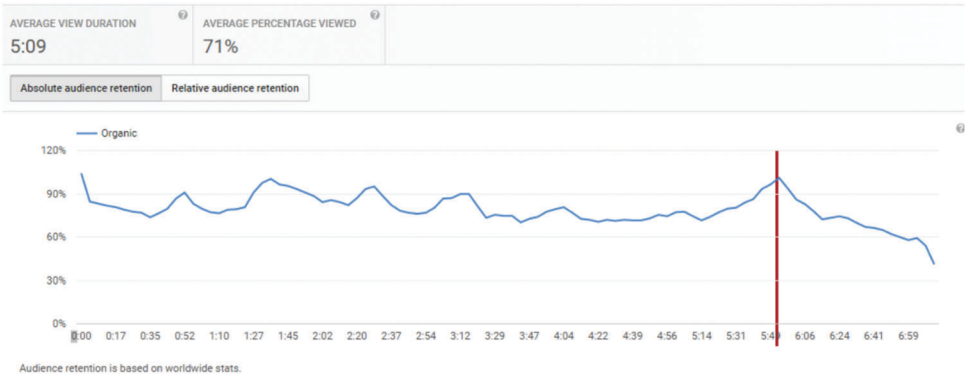

Standard solution video: http://bit.ly/skillsstandardsoln

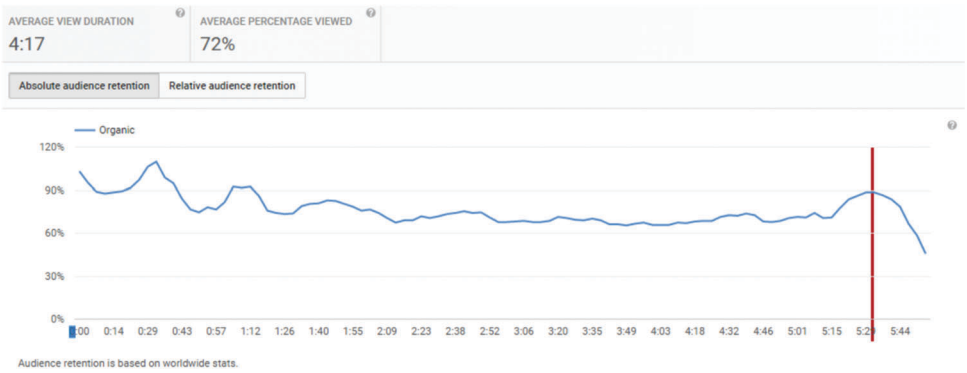

Pipetting video: http://bit.ly/skillsvolpipette

Acknowledgements

MKS and MMK wish to acknowledge the Institute for Academic Development Principal's Teaching Award Scheme. EDD, HMO'C and AP acknowledge the Principal's Career Development Scholarships, University of Edinburgh.

References

Anderson G. W., (1978), *The Playfair Collection and the Teaching of Chemistry at the University of Edinburgh 1713–1858*, Edinburgh: The Royal Scottish Museum.

BERA, (2011), *Ethical Guidelines for Educational Research*.

Black P. and Wiliam D., (2006), *Inside the black box: raising standards through classroom assessment*, Granada Learning.

Bruck A. D. and Towns M., (2013), Development, Implementation, and Analysis of a National Survey of Faculty Goals for Undergraduate Chemistry Laboratory, *J. Chem. Educ.*, **90**(6), 685–693, DOI: 10.1021/ed300371n.

Bruck L. B., Towns M. and Bretz S. L., (2010), Faculty Perspectives of Undergraduate Chemistry Laboratory: Goals and Obstacles to Success, *J. Chem. Educ.*, **87**(12), 1416–1424, DOI: 10.1021/ed900002d.

Carnduff J. and Reid N., (2003), *Enhancing undergraduate chemistry laboratories: pre-laboratory and post-laboratory exercises*, Royal Society of Chemistry.

Casilli C. and Hickey D., (2016), Transcending conventional credentialing and assessment paradigms with information-rich digital badges, *Inf. Soc.*, **32**(2), 117–129, DOI: 10.1080/01972243.2016.1130500.

Chen H.-J., She J.-L., Chou C.-C., Tsai Y.-M. and Chiu M.-H., (2013), Development and Application of a Scoring Rubric for Evaluating Students' Experimental Skills in Organic Chemistry: An Instructional Guide for Teaching Assistants, *J. Chem. Educ.*, **90**(10), 1296–1302, DOI: 10.1021/ed101111g.

DeKorver B. K. and Towns M. H., (2015), General Chemistry Students' Goals for Chemistry Laboratory Coursework, *J. Chem. Educ.*, **92**(12), 2031–2037, DOI: 10.1021/acs.jchemed.5b00463.

DeKorver B. K. and Towns M. H., (2016), Upper-level undergraduate chemistry students' goals for their laboratory coursework, *J. Res. Sci. Teach.*, **53**(8), 1198–1215, DOI: 10.1002/tea.21326.

Doidge E. D., O'Connor H. M., Price A. and Seery M. K., (2016), *Using a volumetric pipette correctly*, retrieved from https://www.youtube.com/watch?v=yL5XZhrWZ6I.

Elkordy A., (2016), Development and Implementation of Digital Badges for Learning Science, Technologly, Engineering and Math (STEM) Practices in Secondary Contexts: A Pedagogical Approach with Empirical Evidence, in *Foundation of Digital Badges and Micro-Credentials*, Springer, pp. 483–508.

Goldberg D. T., (2012), *Badges for Learning: Threading the Needle Between Skepticism and Evangelism*, retrieved from http://dmlcentral.net/badges-for-learning-threading-the-needle-between-skepticism-and-evangelism/.

Graham K. J., Johnson B. J., Jones T. N., McIntee E. J. and Schaller C. P., (2008), Designing and Conducting a Purification Scheme as an Organic Chemistry Laboratory Practical, *J. Chem. Educ.*, **85**(12), 1644, DOI: 10.1021/ed085p1644.

Hawkes S. J., (2004), Chemistry Is Not a Laboratory Science, *J. Chem. Educ.*, **81**(9), 1257, DOI: 10.1021/ed081p1257.

Hendry G., (2013), Integrating feedback with classroom teaching, in Merry S., Price M., Carless D. and Taras M. (ed.), *Reconceptualising Feedback in Higher Education: Developing Dialogue with Students*, Routledge, pp. 133–134.

Hensiek S., DeKorver B. K., Harwood C. J., Fish J., O'Shea K. and Towns M., (2016), Improving and Assessing Student Hands-On Laboratory Skills through Digital Badging, *J. Chem. Educ.*, **93**(11), 1847–1854, DOI: 10.1021/acs.jchemed.6b00234.

Hofstein A. and Lunetta V. N., (2004), The laboratory in science education: foundations for the twenty-first century, *Sci. Educ.*, **88**(1), 28–54, DOI: 10.1002/sce.10106.

Jolley D. F., Wilson S. R., Kelso C., O'Brien G. and Mason C. E., (2016), Analytical Thinking, Analytical Action: Using Prelab Video Demonstrations and e-Quizzes To Improve Undergraduate Preparedness for Analytical Chemistry Practical Classes, *J. Chem. Educ.*, **93**(11), 1855–1862.

Kirschner P. A. and Meester M. A. M., (1988), The laboratory in higher science education: problems, premises and objectives, *High. Educ.*, **17**(1), 81–98, DOI: 10.1007/bf00130901.

Kirton S. B., Al-Ahmad A. and Fergus S., (2014), Using Structured Chemistry Examinations (SChemEs) As an Assessment Method To Improve Undergraduate Students' Generic, Practical, and Laboratory-Based Skills, *J. Chem. Educ.*, **91**(5), 648–654, DOI: 10.1021/ed300491c.

Kolk K. V. D., Beldman G., Hartog R. and Gruppen H., (2012), Students Using a Novel Web-Based Laboratory Class Support System: A Case Study in Food Chemistry Education, *J. Chem. Educ.*, **89**(1), 103–108, DOI: 10.1021/ed1005294.

Kucharski M. M. and Seery M. K., (2016a), *Completing a Distillation*, November 2016, retrieved from https://www.youtube.com/watch?v=qZRRRXlZexg.

Kucharski M. M. and Seery M. K., (2016b), *Preparing a standard solution*, November 2016, retrieved from https://www.youtube.com/watch?v=MeOAPbMvubE.

Kucharski M. M. and Seery M. K., (2016c), *Titration Exemplar Video*, November 2016, retrieved from https://www.youtube.com/watch?v=rK7Egs-SJus.

Lalla M., (2017), Fundamental characteristics and statistical analysis of ordinal variables: a review, *Quality & Quantity*, **51**(1), 435–458.

Mehta N. B., Hull A. L., Young J. B. and Stoller J. K., (2013), Just Imagine: New Paradigms for Medical Education, *Academic Medicine*, **88**(10), 1418–1423, DOI: 10.1097/ACM.0b013e3182a36a07.

Neeland E. G., (2007), A One-Hour Practical Lab Exam for Organic Chemistry, *J. Chem. Educ.*, **84**(9), 1453, DOI: 10.1021/ed084p1453.

Ng W., (2015), *New digital technology in education: conceptualizing professional learning for educators*, Springer.

Reid N. and Shah I., (2007), The role of laboratory work in university chemistry, *Chem. Educ. Res. Pract.*, **8**(2), 172–185, DOI: 10.1039/B5RP90026C.

Rhodes M. M., (2010), A Laboratory Practical Exam for High School Chemistry, *J. Chem. Educ.*, **87**(6), 613–615, DOI: 10.1021/ed100200k.

RSC, (2015), *Accreditation of Degree Programmes*.

Sadler D. R., (1989), Formative assessment and the design of instructional systems, *Instructional Science*, **18**(2), 119–144.

Sadler P. M. and Good E., (2006), The impact of self-and peer-grading on student learning, *Educ. Assess.*, **11**(1), 1–31.

Sawilowsky S. S., (2009), New effect size rules of thumb, *J. Mod. Appl. Stat. Methods*, **8**(2), 597–599.

Seery M. K., (2016), CVs for the 21st Century, *Educ. Chem.*, **53**(2), 32.

Spagnoli D., Wong L., Maisey S. and Clemons T. D., (2017), Prepare, do, review: a model used to reduce the negative feelings towards laboratory classes in an introductory chemistry undergraduate unit, *Chem. Educ. Res. Pract.*, **18**(1), 26–44.

Towns M., Harwood C. J., Robertshaw M. B., Fish J. and O'Shea K., (2015), The Digital Pipetting Badge: A Method To Improve Student Hands-On Laboratory Skills, *J. Chem. Educ.*, **92**(12), 2038–2044, DOI: 10.1021/acs.jchemed.5b00464.

Weaver II R. L. and Cotrell H. W., (1986), Peer evaluation: a case study, *Innovative High. Educ.*, **11**(1), 25–39.

Winberg T. M. and Berg C. A. R., (2007), Students' cognitive focus during a chemistry laboratory exercise: effects of a computer-simulated prelab, *J. Res. Sci. Teach.*, **44**(8), 1108–1133.

Yang J. C., Quadir B. and Chen N.-S., (2015), Effects of the Badge Mechanism on Self-Efficacy and Learning Performance in a Game-Based English Learning Environment, *J. Educ. Comput. Res.*, **54**(3), 371–394, DOI: 10.1177/0735633115620433.

Zoller U., Tsaparlis G., Fatsow M. and Lubezky A., (1997), Student self-assessment of higher-order cognitive skills in college science teaching, *J. Coll. Sci. Teach.*, **27**(2), 99.